# THE RHYTHM OF RIVERS

## On Dune Dynamics and Hydraulic Roughness

Sjoukje I. de Lange

## Propositions

1 | Roughness is scale dependent.
(this thesis)

2 | Two-dimensional phase diagrams oversimplify reality.
(this thesis)

3 | Delegating data collection harms data interpretation.

4 | Buzzword-driven research hampers scientific neutrality and research quality.

5 | The best way to develop individually is through collaboration.

6 | Rigidly adhering to project goals is less important than embracing serendipity.

7 | We are nature.

8 | A lack of curiosity killed the cat.

Propositions belonging to the thesis, entitled:

*The Rhythm of Rivers - On Dune Dynamics and Hydraulic Roughness*

Sjoukje I. de Lange
Wageningen, 8 May 2024

# The Rhythm of Rivers

## On Dune Dynamics and Hydraulic Roughness

Sjoukje Irene de Lange

**Thesis committee**

**Promotor**
Prof. Dr A. J. F. Hoitink
Personal chair, Hydrology and Environmental Hydraulics
Wageningen University & Research

**Co-promotor**
Dr K. Waldschläger
Assistant professor, Hydrology and Environmental Hydraulics
Wageningen University & Research

**Other members**
Dr C. C. van Heerwaarden, Wageningen University & Research
Prof. Dr J. Best, University of Illinois, Urbana, USA
Dr A. Lefebvre, University of Bremen, Germany
Dr A. W. Baar, TU Delft

This research was conducted under the auspices of the Graduate School for Socio-Economic and Natural Sciences of the Environment (SENSE).

# The Rhythm of Rivers

## On Dune Dynamics and Hydraulic Roughness

Sjoukje Irene de Lange

**Thesis**
submitted in fulfilment of the requirements for the degree of doctor
at Wageningen University
by the authority of the Rector Magnificus,
Prof. Dr C. Kroeze
in the presence of the
Thesis Committee appointed by the Academic Board
to be defended in public
on 8 May 2024
at 1:30 p.m. in the Omnia Auditorium.

S. I. de Lange
The Rhythm of Rivers - On Dune Dynamics and Hydraulic Roughness
xiii+234 pages.

PhD thesis, Wageningen University, Wageningen, the Netherlands (2024)
With references, with summaries in English and Dutch

DOI 10.18174/648604
© 2024 S. I. de Lange

# Summary

River deltas located in the Fluvial-to-Tidal-Transition-Zone (FTTZ) experience a complex interaction of river and tidal currents, driving the delta morphology. Deltas worldwide face the threat of absolute sea level rise, increased peak discharge from the rivers, and subsidence of the subsurface, putting their dense population in danger. Operational water management of the rivers in the delta and prediction of the complex morphological behaviour of the system is essential. Water management depends on hydraulic models, which simplify complex processes into overarching parameters to run effectively. One of these parameters is hydraulic roughness, which is the resistance the water experiences by protruding objects. The main source of this roughness was thought to be subaqueous undulations of the river bed: bedforms. Bedforms, especially dunes, can impact water levels via their roughness, are also important for sediment transport, fairway depth maintenance, ecology, and sedimentary rock record interpretation. Understanding what drives the size and shape of bedforms in river deltas, and how they impact the bedform-generated roughness, is crucial for improving hydraulic models. Therefore, this thesis aims to determine how environmental factors in the FTTZ alter bedform geometry, and how these bedforms in turn impact the hydraulic roughness in the FTTZ (Chapter 1).

The first part of this thesis assesses environmental factors that are characteristic of the FTTZ and that may impact bedform geometry. These factors include, but are not limited to, the presence of mixed bed sediment (Chapter 3), flocculated sediment (Chapter 4), and high flow velocities (Chapter 5). However, accurate and robust measurements of mixed and flocculated particle size distributions are needed, hence we first discuss the corresponding measurement practices (Chapter 2). The second part of the thesis assesses the hydraulic roughness from dunes. First, ways to derive hydraulic roughness from field data are assessed, after which we explore the predictive capacity of well-established roughness predictors in a riverine system (Chapter 6), and a tidally-influenced system (Chapter 7). Finally, we determine which factors contribute to the variance in reach-scale hydraulic roughness.

In **Chapter 2**, we explored how mixed suspended particle size distributions (PSDs) can best be measured. We assessed measurement practices, such as storing and stirring the sample, and determined the measurement time required to obtain a reliable PSD. We found that particle size measurements do not yield absolute numbers, but depend on the measurement method. There is a large difference in PSDs of suspended sediments measured by laser diffraction in situ (in the field) and ex situ (in the laboratory), caused by ex situ altering of the (flocculated) particles. Additionally, careful time-averaging of the PSD data is required, and more measurement time is needed for coarser field samples with a wider distribution. These findings impact current measurements practices and stress the need for unified measurement protocols.

Following up on this, in **Chapter 3**, the impact of mixed bed sediments on bedform geometry is assessed via laboratory experiments. Different mixtures of sediment were tested, including mixtures with various degrees of cohesion. Adding finer, non-cohesive material to a base material of medium sand leads to an increase in mobility of the base material, caused by the hiding-exposure effect, which leads to an increase in dune length and an increase or decrease in dune height depending on the starting point. However, when the added fine material is (slightly) cohesive, the mobility of the mixture is decreased, which hampers dune formation. The study indicates that detailed knowledge of the bed sediment size distribution is needed for accurate prediction of bedform geometry.

Not only the bed sediment can be mixed, but flocculated particles in the water column and on the bed could interact with the bed and the bedforms as well. In **Chapter 4** we show with laboratory experiments that the geometry of the bedforms is not affected by flocculated clay. However, we show for the first time that flocs interacted with the bed by being buried in the leeside of the bedforms and released from the stoss. Although this did not impact bedform geometry, it has significant implications for sediment transport budgets and interpretation of rock records.

High flow conditions can occur in the FTTZ when river discharge and ebb outflow coincide. In **Chapter 5**, we assess the impact of high flow on dunes by reanalysing previously published laboratory data. We observed that during the transition from dunes to upper stage plane bed (USPB) the bed becomes unstable, shown by an increase in standard deviation in dune height with increasing transport stage. The accompanying increase in bimodality indicates that the unstable behaviour could be attributed to a critical transition. Unlike the generally assumed smooth transition from dunes to USPB, we observe flickering at the tipping point. Flickering at high transport stages can have severe implications for the resulting hydraulic roughness, and it calls for reassessment of field monitoring and laboratory experimental design, where many measurements are needed to derive the average bed stage.

In **Chapter 6**, the hydraulic roughness from dunes in the Waal River (the Netherlands) is determined, using various field methods and roughness predictors. We found that conventional roughness predictors explain only 1/3rd of the variance in friction factor that was found from examining water surface profiles. Additionally, there was no link found between various leeside angle statistics and roughness. Instead, the bed level gradient fluctuates in counter phase with the friction factor, indicating the importance of larger-scale multi-kilometre bed-level undulations.

Finally, the bedforms and hydraulic roughness in the FTTZ of the Fraser River (Canada) are studied in **Chapter 7**. In the dynamic conditions of the FTTZ, the spatial variability of bedform geometry was assessed, and a hydraulic model was employed to estimate the influence of bedform geometry on the hydraulic roughness. The spatial

variability in bedform geometry was well-captured by the shear stresses from the hydrodynamic model, but the prediction of the absolute bedform height with empirical equations was poor. Furthermore, we found that hydraulic roughness can be well-predicted from bedform geometry. However, unlike previously thought, details in the geometry, such as the leeside angle, do not matter for the reach-scale roughness.

This thesis underlines the importance of previously ignored environmental stressors and their influence on spatiotemporal variability in bedform geometry. Neglecting local-scale variability impedes the accurate prediction of bedform geometry. However, although details in bedform geometry are important for many other fields, they are not needed to determine reach-scale roughness, and hydraulic models could be tuned by focusing on larger-scale roughness elements. Future research should focus on: (1) causes of spatial variability in bedform fields and the implementation of these in phase diagrams, (2) scale-dependency of roughness and the relative contribution of different roughness components, and (3) critical transitions within geomorphology.

# Samenvatting

Wereldwijd worden delta's bedreigd door absolute zeespiegelstijging, bodemdaling, en een toename van de piekafvoer van rivieren. Dit vormt een gevaar voor de dichtbevolkte gebieden in delta's. De morfologie van rivierdelta's gelegen in de Fluviale-Marine-Transitiezone (FMTZ) wordt beïnvloed door complexe rivier- en getijstromen. Operationeel waterbeheer van de riviertakken in de delta en voorspelling van het complexe morfologische gedrag van het systeem zijn essentieel. Om de rivieren in de delta te beheren en het complexe morfologische gedrag van het systeem te voorspellen, worden hydraulische modellen gebruikt. Deze modellen versimpelen complexe processen in overkoepelende parameters voor optimale prestatie. Eén van deze parameters is hydraulische ruwheid: de weerstand die het water ondervindt door uitstekende objecten. De belangrijkste bron van deze ruwheid werd verondersteld onderwaterduinen op de rivierbodem te zijn, die daarmee indirect de waterstanden beïnvloeden. Ze zijn ook belangrijk voor sedimenttransport, het onderhoud van de vaardiepte, ecologie en interpretatie van sedimentgesteente. Het begrijpen van welke factoren de grootte en vorm van bodemvormen in rivierdelta's bepalen, en hoe ze de door bodemvormen gegenereerde ruwheid beïnvloeden, is cruciaal voor het verbeteren van hydraulische modellen. Dit proefschrift heeft als doel te bepalen hoe factoren in de FMTZ de bodemvormgeometrie veranderen, en hoe deze bodemvormen op hun beurt de hydraulische ruwheid in de FMTZ beïnvloeden (Hoofdstuk 1).

Het eerste deel van dit proefschrift gaat over omgevingsfactoren die kenmerkend zijn voor de FMTZ en die bodemvormgeometrie kunnen beïnvloeden. Deze factoren omvatten, maar zijn niet beperkt tot, de aanwezigheid van gemengd bodemsediment (Hoofdstuk 3), van geflocculeerd sediment (Hoofdstuk 4) en van hoge stroomsnelheden (Hoofdstuk 5). Nauwkeurige en robuuste metingen van gemengde en geflocculeerde deeltjesgrootteverdelingen zijn noodzakelijk, dus de bijbehorende meetmethodes worden eerst besproken (Hoofdstuk 2). Het tweede deel van het proefschrift behandelt de hydraulische ruwheid vanuit duinen. Eerst worden manieren om hydraulische ruwheid uit veldgegevens te halen bediscussieerd, waarna we de voorspellende capaciteit van veelgebruikte ruwheidsvoorspellers onderzoeken in een riviersysteem (Hoofdstuk 6) en een getijdenbeïnvloed systeem (Hoofdstuk 7). Tot slot bepalen we welke factoren bijdragen aan de variantie in de grootschalige hydraulische ruwheid.

In **Hoofdstuk 2** onderzochten we hoe gemengde gesuspendeerde deeltjesgrootteverdelingen (DGV) het beste kunnen worden gemeten. We vergeleken diverse meetmethoden, zoals het bewaren en roeren van het monster, en bepaalden de benodigde meettijd om een betrouwbare DGV te verkrijgen. We ontdekten dat de deeltjesgroottemetingen geen absolute getallen opleveren, maar afhankelijk zijn van de meetmethode. Er is een groot verschil in de DGV van gesuspendeerde sedimenten, gemeten door laserdiffractie, in situ (in het veld) of ex situ (in het laboratorium), veroorzaakt

door ex-situdeformatie van de (geflocculeerde) deeltjes. Bovendien is het nodig om de metingen zorgvuldig te middelen over tijd, en meer meettijd is nodig voor grovere veldmonsters met een bredere distributie. Deze bevindingen beïnvloeden de huidige meetmethoden en benadrukken de noodzaak van harmonieuze meetprotocollen.

Hierop volgend, wordt in **Hoofdstuk 3** via laboratoriumexperimenten de invloed onderzocht van verschillende type gemengde bodemsedimenten op de geometrie van bodemvormen. We testten verscheidenen sedimentmengsels, waaronder mengsels met verschillende mate van cohesie. Het toevoegen van fijner, niet-cohesief materiaal aan een basismateriaal van middelgroot zand leidt tot een toename van de mobiliteit van het basismateriaal. Dit is veroorzaakt door het *hiding-exposure-effect* en resulteert in een toename van de lengte van de duinen en een toe- of afname in duinhoogte, afhankelijk van het startpunt. Echter, wanneer het toegevoegde materiaal (licht) cohesief is, wordt de mobiliteit van het mengsel verminderd, wat de vorming van duinen belemmert. De studie geeft aan dat gedetailleerde kennis van de grootteverdeling van het bodemsediment nodig is voor een nauwkeurige voorspelling van bodemvormgeometrie.

Niet alleen het bodemsediment in de FMTZ kan gemengd zijn, maar ook geflocculeerd sediment in de waterkolom en op de bodem kan interageren met de bodem en de bodemvormen. In **Hoofdstuk 4** laten we zien met laboratoriumexperimenten dat de geometrie van de bodemvormen niet wordt beïnvloed door de geflocculeerde klei. We tonen voor het eerst aan dat kleivlokken met de bodem interageren: ze worden begraven aan de lijzijde van de bodemvormen en geërodeerd van de loefzijde. Hoewel dit de geometrie van de bodemvormen niet beïnvloedt, heeft het aanzienlijke implicaties voor sedimenttransport van klei en de interpretatie van sedimentgesteente.

Hoge stroomsnelheden kunnen voorkomen in de FMTZ wanneer de rivierafvoer en eb-uitstroom samenvallen. In **Hoofdstuk 5** bestuderen we de impact van hoge stroming op duinen, door eerder gepubliceerde laboratoriumgegevens opnieuw te analyseren. We observeerden dat bij de overgang van duinen naar een vlak bed, de bodem instabiel wordt. Dit was zichtbaar door de toename van de standaardafwijking in duinhoogte bij toenemende stroomsnelheid. De bijbehorende toename in bimodaliteit van de duinhoogteverdeling, duidt erop dat het instabiele gedrag wordt veroorzaakt door een kritische transitie. In tegenstelling tot de algemeen aangenomen geleidelijke overgang van duinen naar een vlak bed, observeerden we flikkering op het kantelpunt. Flikkeren bij hoge snelheden kan ernstige gevolgen hebben voor de resulterende hydraulische ruwheid, en het roept op tot heroverweging van het ontwerpen van veldmonitoring en experimenteel laboratoriumonderzoek: er zijn veel opnames nodig om de gemiddelde bodemtoestand te verkrijgen.

In **Hoofdstuk 6** wordt de hydraulische ruwheid vanuit duinen in de rivier de Waal (Nederland) bepaald, met behulp van verschillende veldmethoden en ruwheidsvoorspellers. We ontdekten dat conventionele ruwheidsvoorspellers slechts 1/3e van de variantie in ruwheid verklaren, die werd bepaald aan de hand van wateroppervlakteprofielen. Bovendien vonden we geen verband tussen verschillende lijzijdestatistieken en ruwheid. In plaats daarvan bleek het bodemniveau in tegenfase te zijn met de ruwheid, wat duidt op het belang van grootschalige, kilometerslange bodemgolvingen.

Ten slotte bestuderen we de bodemvormen en hydraulische ruwheid in de FMTZ van de Fraser River (Canada) in **Hoofdstuk 7**. In de dynamische omstandigheden van de FMTZ onderzochten we de ruimtelijke variabiliteit van bodemvormgeometrie, en we gebruikten een hydraulisch model om de invloed van details in bodemvormgeometrie op de hydraulische ruwheid te bepalen. De ruimtelijke variabiliteit in bodemvormgeometrie werd goed ingeschat met behulp van de schuifspanningen uit het hydrodynamische model, maar de voorspelling van de absolute duinhoogte met empirische vergelijkingen bleek onvoldoende. Bovendien vonden we dat hydraulische ruwheid goed voorspeld kan worden met de duingeometrie. In tegenstelling tot wat eerder werd gedacht, zijn details in de duingeometrie, zoals de lijzijdehoek, echter niet belangrijk voor de grootschalige ruwheid.

Dit proefschrift benadrukt het belang van omgevingsfactoren die eerder verwaarloosd werden, en hun invloed op de ruimtelijke en temporele variabiliteit in bodemvormgeometrie. Het verwaarlozen van variabiliteit op lokaal niveau belemmert de nauwkeurige voorspelling van bodemvormgeometrie. Hoewel details in bodemvormgeometrie belangrijk zijn voor veel andere vakgebieden, zijn ze niet nodig om grootschalige ruwheid te bepalen, en hydraulische modellen kunnen worden afgesteld door zich te richten op grootschalige ruwheidselementen. Toekomstig onderzoek zou zich moeten richten op: (1) oorzaken van ruimtelijke variabiliteit in bodemvormvelden en de implementatie hiervan in fasediagrammen, (2) de schaalafhankelijkheid van ruwheid en de relatieve bijdrage van verschillende ruwheidsonderdelen, en (3) kritische overgangen binnen geomorfologie.

# Contents

Summary v

Samenvatting ix

**1** | Introduction 1

**2** | Suspended particle size measurements of flocculated sediment 19

**3** | Dunes in mixed sediment 43

**4** | Floc capturing by dunes 73

**5** | On the transition from dunes to upper stage plane bed 91

**6** | The contribution of dunes to hydraulic roughness 107

**7** | Hydraulic roughness in a tidal river 137

**8** | Synthesis 173

**9** | Supplementary Information 187
Appendices 189
Bibliography 195
Supplementary Materials 217
Nomenclature 219
Acknowledgements 223
Statement of authorship contribution 227
List of publications 229
Curriculum vitae 231
Graduate school certificate 232

*Ik weet niet wat de uiterwaard*
*me wil vertellen, ik heb geen idee*
*wat de murmelende rivier me*
*toe te vertrouwen heeft.*

# 1

# Introduction

## 1.1 | Context: the importance of subaqueous dunes in (tidal) rivers

River deltas worldwide face the dual threat of absolute sea level rise and land subsidence, which increases the risk of flooding from both the river and the sea domain. In deltas, the effects of climate change and human-induced land development amplify each other (Renaud et al., 2013). More extreme climatic events can increase the risks of riverine flooding through increased peak discharges, while storm surges from the seaward domain can occur more frequently, both altering the interaction between tides and river discharge (Hoitink & Jay, 2016). In addition, human activity further modifies the system, including land reclamation for agricultural, urban development, and industry, which reduces the accommodation space of the discharge system (Hoitink et al., 2017). Embankments impede the natural aggregation of the delta plains, leading to delta subsidence (Paola et al., 2011; Giosan et al., 2013). Additionally, dredging for fairway maintenance and sand mining for building materials alter the balance between incoming and outgoing currents (Vellinga et al., 2014; Auerbach et al., 2015). All these changes make the system vulnerable and unpredictable. Understanding the morphological and hydraulic behaviour deltas is crucial to ensure livability in these densely populated areas.

The morphological and hydraulic behaviour of river deltas is not straightforward. River deltas are situated in the fluvial-to-tidal transition zone (FTTZ). The FTTZ is controlled by numerous multi-scale mechanisms that interact with one another, creating complexity that is unique to these systems. The FTTZ is influenced by both the river discharge from upstream and the tidal forces from downstream. The interaction of river flow and tides create a complicated exchange between these two forces (Buschman et al., 2009), varying on small spatiotemporal scales. Furthermore, the distribution of the bed- and the suspended sediment is far from uniform, with mixtures of sand, silt, clay, and flocculated particles. Together, these cause highly variable sediment transport rates.

To manage river deltas, computer models are employed for operational water management (e.g. controlling the opening and closing of sluices), flood prediction and forecasting, flow velocity estimations for shipping safety, determination of dredging volumes, and prediction of the morphological development of the delta. To develop these models, the inherent natural variability and complexity of the FTTZ must be simplified into overarching parameters. One of these parameters is hydraulic roughness, which quantifies the resistance to flow by objects protruding into the water column (Chow, 1959). Roughness is a combination of form drag (roughness resulting from pressure variations, by for example bed undulations) and skin friction drag (roughness caused by the shearing of the fluid particles against the sediment particles of the river bed) (Einstein, 1950). Roughness is a key parameter impacting the water level,

which is often simplified by an estimation of skin friction drag and the model is subsequently calibrated by tuning the form drag. In reality, form roughness is thought to be predominately determined by subaqueous bedforms on the river bed, such as dunes and ripples. Consequently, subaqueous bedforms play an important role in sediment transport gradients and water level dynamics (Berne et al., 1993; Venditti, 2013), which in turn determine bedform geometry. For the improvement of operational models, it is essential to enhance understanding of bedform geometry and its variability in the FTTZ, as well as the bedform-generated roughness.

In this thesis, I aim to:

- Establish and understand how environmental factors in the FTTZ alter bedform geometry.
- Determine how bedforms impact the hydraulic roughness in the FTTZ.

This chapter serves as an introduction to bedforms and bedform-generated roughness, and outlines the contents of this thesis. It starts with an overview of the types of bedforms and the environmental forces that shape them. Subsequently, hydraulic roughness is introduced, followed by a discussion on methods to estimate dune height, and the resulting hydraulic roughness, from limited data. Then, I assess methods to study bedform-generated roughness. Finally, the research question and the contents of the thesis are outlined.

## 1.2 | Background

### 1.2.1 | What are bedforms and why are they relevant?

Subaqueous bedforms are wave-like structures on the bed of a water body. They are ubiquitous in sand-bedded lowland rivers and estuaries with flows capable of moving sand. Bedforms hold relevance across a range of disciplines, including geomorphology, ecology, sedimentology, and hydraulic engineering. Bedforms are relevant to a large range of fields. Firstly, bedforms are considered the most important source of local flow resistance, on which I elaborate in Section 1.2.4. Secondly, the shear stress distribution determines sediment transport gradients, which determine bedform formation and geometry, which feeds back into the near-bed flow field and shear stress distribution (Venditti & Bradley, 2022; Best, 2005). This interplay between hydraulics, sediment transport, and morphology is referred to as the morphodynamic feedback loop. Via this feedback loop, bedforms play a crucial role in sediment transport. Thirdly, the dynamics of bedforms are essential for fairway depth management, such as dredging location and frequency (ASCE Task Force, 2002). Fourthly, the presence of bedforms is preserved in the sedimentary depositional record (Das et al., 2022). Interpreting the cross-set thickness of these records can provide an estimate of dune

heights, which, in turn, can provide an approximation of past flow depth and velocity, aiding the understanding of past climates. Finally, bedform geometry and its spatial distribution determine suitable foraging places for aquatic wildlife (Greene et al., 2020).

Various types of subaqueous bedforms can be observed. A typical sequence of bedforms emerges with increasing flow strength (shear stress) (Figure 1.1). In sub-critical flows, where the Froude number $Fr$ is lower than one ($Fr = \frac{u}{\sqrt{gh}}$, in which $u$ = flow velocity, $g$ = gravitational acceleration, and $h$ = water depth), a typical sequence develops with increasing flow strength. This includes a Lower Stage Plane Bed (no sediment movement), ripples (dimensions 0.01-0.1 m high, 0.1-1 m long) and dunes (0.1 - 1 m high, 10 - 100 m long). As the Froude number approaches unity, bedforms wash out, and an upper stage plane bed develops. For supercritical flows ($Fr > 1$), antidunes develop, but this situation is rare in lowland rivers since the Froude number hardly ever exceeds unity. This thesis focuses on dunes as they are considered the largest source of roughness in lowland rivers.

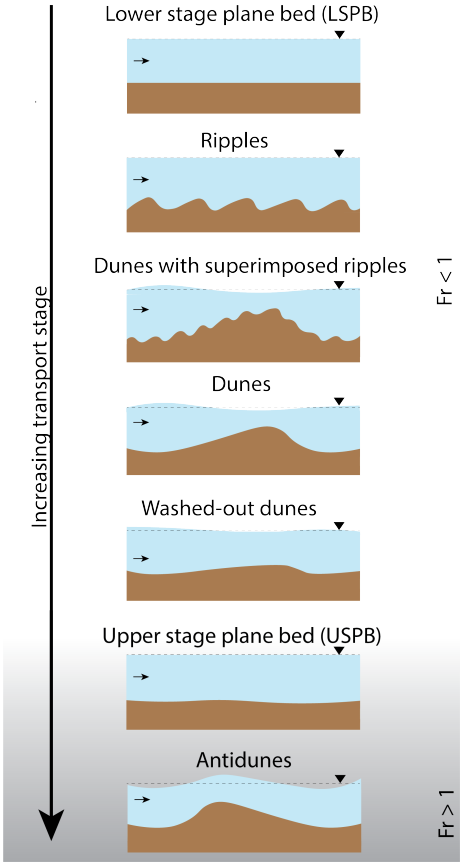


**Figure 1.1** | Sequence of sub-aqueous bedforms occurring with increasing flow strength, for sub-critical ($Fr < 1$) and supercritical ($Fr > 1$) flow. Adjusted from Venditti & Bradley (2022).

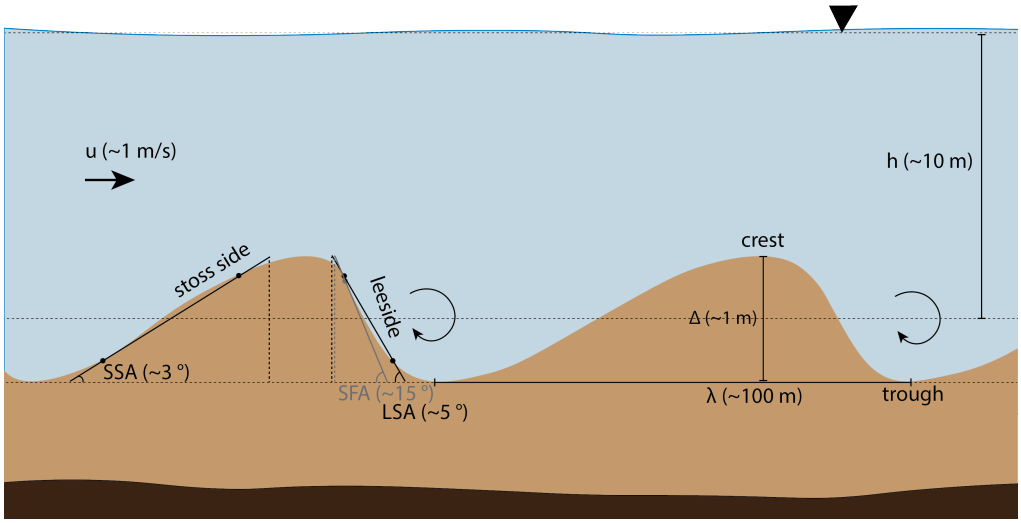


**Figure 1.2** | Dune geometry, expressed in dune height Δ, dune length $\lambda$, the angle of the leeside *LSA*, which by definition excludes the upper and lower 1/6th of the leeside, the stoss side angle (*SSA*), also excluding the upper and lower 1/6th of the stoss side, and the slip face angle (*SFA*), which is the steepest part (95 percentile) of the leeside. Exemplary values for these parameters in a lowland river are shown. Figure is not to scale.

The geometry of dunes is expressed in terms of bedform height (Δ), length ($\lambda$), leeside angle (*LSA*), stoss side angle (*SSA*) and slip face angle (*SFA*, the steepest part of the *LSA*), as well as various ratios of these measures. The definitions of these measurements are summarised in Figure 1.2.

The visualisation of bedform morphology in scientific literature generally include colourful top views or along-stream profiles, is often highly vertically exaggerated for discernability. However, vertical exaggeration can be misleading, creating the false impression of gigantic mountains on the river bed. Figure 1.3a illustrates how a real (not vertically-exaggerated) river bed would look. Some of my printed theses feature a distinctive bookmark, with a 3D-printed dune field on the back. This is a down-scaled dune field of the Fraser River, equally down-scaled in all directions (x, y, z), and is meant to get a grasp on the actual geometry of the bedforms.

### 1.2.2 | What are bedforms shaped by?

Various phase diagrams have been developed to predict the occurrence of specific bedforms. These diagrams typically feature a (dimensionless) measure of grain size on one axis, and a (dimensionless) measure of flow strength on the other, and are based on numerous field and laboratory measurements. The type of bedform is determined by flow and particle characteristics, although various phase diagrams are not in agreement about the precise boundaries. Additionally, bedforms can be superimposed on other bedforms in various configurations.

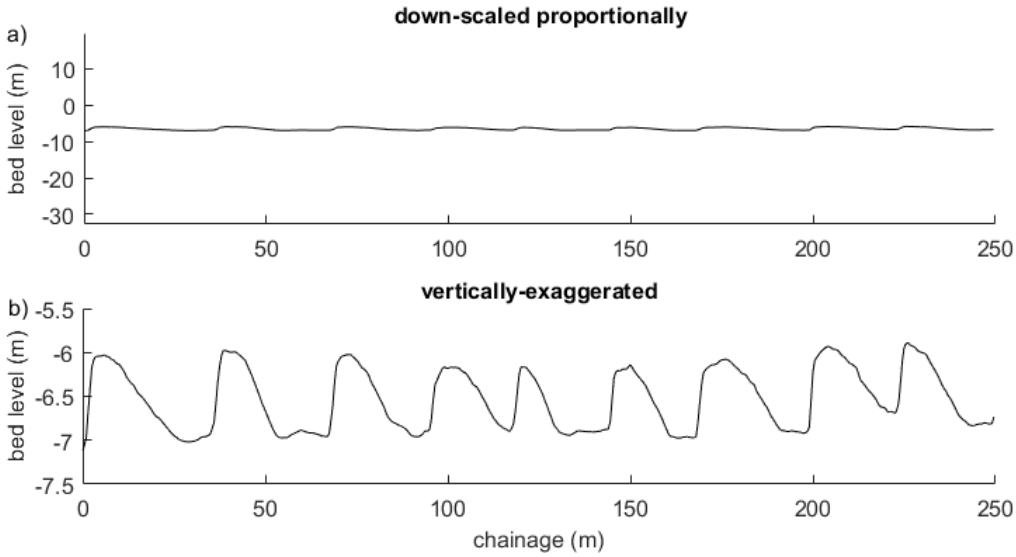


**Figure 1.3** | Example profile of a dune field of the Fraser River (flow direction right to left), which is a) equally down-scaled in all directions (x, y, z). b) vertically exaggerated for discernability.

The flow and particle characteristics that determine bedform geometry are combined in a parameter called transport stage. Transport stage is a measure of the flow strength relative to the sediment mobility, and is often expressed as the ratio between shear stress and the critical shear stress, the latter being the shear stress required to initiate sediment motion. In unidirectional flows, dune height is known to increase with an increase in transport stage, to reach a maximum, beyond which dune height decreases towards zero (upper stage plane bed) (Figure 1.1). The response of dunes to changes in flow strength is particularly relevant for areas with strong discharge seasonality. Dunes grow or may even wash out during the rising limb of the discharge peak, decay during the falling limb, and remaining relatively constant during base flow periods (Bradley & Venditti, 2021; Julien et al., 2002).

However, the relation between equilibrium dune height and transport stage is a simplified approach, and both intrinsic and extrinsic variability can induce scatter in this relationship. Especially in the FTTZ, equilibrium bedform geometry can deviate from its expected geometry and dynamics, as discussed in the following section.

### 1.2.3 | How do bedforms in the fluvial-to-tidal transition zone differ from fluvial bedforms?

Many laboratory and modelling studies have investigated the factors shaping bedform geometry (Section 1.2.2). However, these studies often focus on conditions that are not representative of the fluvial-to-tidal transition zone (FTTZ), such as a unimodal grain size and a steady flow (e.g. Best & Kostaschuk 2002; Kwoll et al. 2016; Naqshband

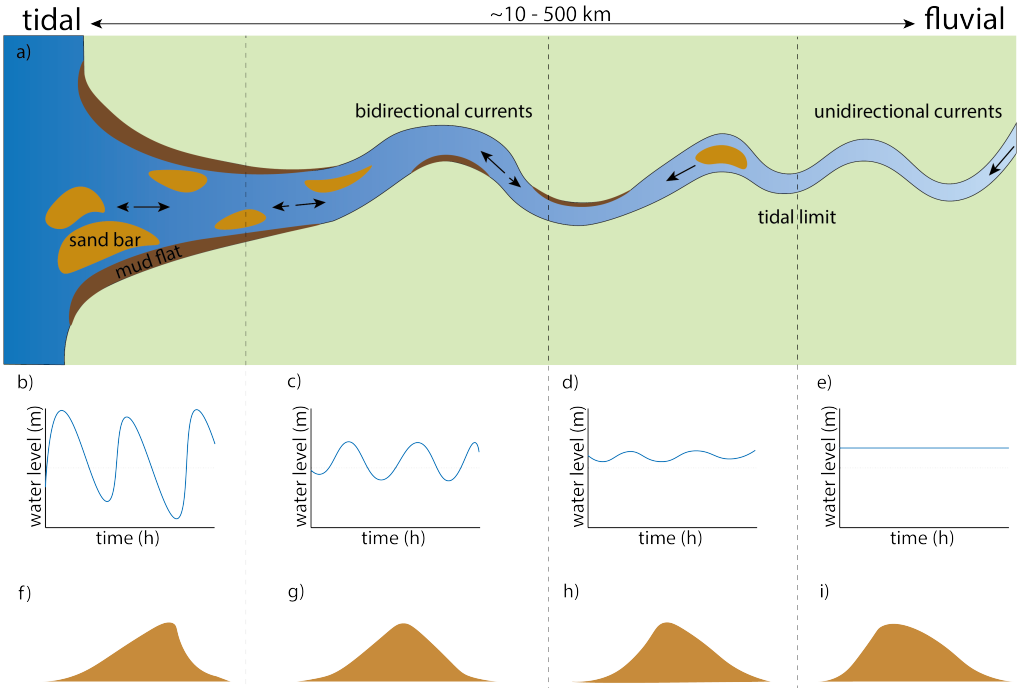


**Figure 1.4** | Schematisation of the fluvial-to-tidal transition zone (FTTZ), in which the river flow changes from a purely unidirectional flow to a bidirectional flow. The impact of tides and river flow on the water levels and dune orientation are schematised.

et al. 2014a,b, 2016, 2017; Venditti et al. 2016). These simplifications hamper the understanding of determinants of dune geometry within the FTTZ. However, from field data it is known that bedform geometry is impacted by environmental factors specific to the FTTZ (Lefebvre et al., 2021; Prokocki et al., 2022) that are less relevant to fluvial environments. For example, bedforms in the FTTZ become more symmetric with sharper crests due to the reversal of the current (Lefebvre & Winter, 2016). Below, I discuss the definition of the FTTZ and provide a summary of environmental factors characteristic of the FTTZ that might impact bed geometry.

The FTTZ is defined as the part of the river that is fully dominated by fluvial processes at its upstream boundary, and both by tidal and coastal processes at its downstream boundary (Phillips, 2022; Jones et al., 2020) (Figure 1.4). The FTTZ can extend for tens to hundreds of kilometres, with its location depending on factors such as (seasonal) discharge peaks, tidal amplitude, and the shape of the estuary (Leuven et al., 2019; Kästner et al., 2017). Generally, the FTTZ can be subdivided into four zones (Gugliotta et al., 2017). In the most landward zone, the fluvial zone, the current is unidirectional, primarily influenced by upstream discharge (Figure 1.4e). Moving seaward, in the second zone, the flow becomes increasingly affected by tides, resulting in fluctuations in the water level over time (Figure 1.4d). In the third zone, the current

may temporarily reverse (Wells, 1995) (Figure 1.4c). This zone includes the Estuarine Turbidity Maximum (ETM), which is characterised by locally-elevated suspended sediment concentrations (Postma, 1967; Glangeaud, 1938). The fourth zone, located at the river mouth, experiences the strongest tidal influence, where water levels are primarily controlled by tides (Figure 1.4b). Although the direction of the residual flow is seaward, the direction of the residual sediment flux depends on the ebb or flood dominance of the system. Due to differences in friction during low and high flow, many estuaries experience a short flood phase with a high flow magnitude, and a longer ebb face with a lower magnitude (Figure 1.4b) (Brown & Davies, 2010), resulting in a landward-directed residual sediment flux.

The changes in flow dynamics in zones one to four generally coincide with an increase in channel width and a decrease in channel slope (Parker et al., 2008; Seminara et al., 2012). Additionally, the bed sediment becomes finer (Kästner et al., 2017) (known as downstream fining) and silty and muddy sediments become present, resulting in a mixed sediment bed. The fine suspended particles can flocculate with increasing salinity (Dyer, 1989; Winterwerp, 2002; Mietta et al., 2009), and can also interact with the bed sediment (Mehta, 2014). All these changes, which are not accounted for in standard phase diagrams and geometry predictors, affect the geometry of bedforms in the FTTZ, and will be elaborated on below.

Mixed sediments in the FTTZ can have a complex, bimodal, trimodal, or wide sediment distribution, and may consist not only of sand particles, but also of silt, clay, and flocculated particles (Edmonds & Slingerland, 2010; Hughes, 2012). However, phase diagrams and geometry predictors (Section 1.2.2) are based on cohesionless, unimodal sediments, limiting their applicability in areas with mixed sediment. The effect of cohesive and mixed sediment is often not included in critical shear stress parameterisation required to determine the transport stage, while there is evidence that these kinds of distributions can significantly impact dune geometry. For example, dune dimensions are known to decrease as clay content increases (Schindler et al., 2015) due to the cohesive properties of the clay. However, it remains unknown how non-cohesive mixed sediment with a wide distribution impacts dune morphology. Contrasting studies exist about the impact of silt on the bed, either stabilising (Yao et al., 2022; Bartzke et al., 2013) or mobilising (Ma et al., 2020) the sediment bed, and the result on bedforms is unknown.

Furthermore, not only mixed bed sediment, but also suspended sediment can impact dune geometry. For example, it is suggested that high concentrations of suspended sediment, such as in the ETM, can suppress dune growth (Best & Kostaschuk, 2002; Wan, 1985). Suspended sediment does not only consist of small solid particles (primary particles), but also of aggregates of these: flocs. Although flocculated particles are also present in riverine systems (Nicholas & Walling, 1996; Bungartz

& Wanner, 2004; Lamb et al., 2020; Fettweis, 2008), they are abundant in estuarine systems worldwide (Dyer, 1989; Winterwerp, 2002; Mietta et al., 2009), as flocculation is induced by organic material and salinity. Flocs differ from solid grain particles by having a lower density and a larger diameter, altering their settling velocity and the shear stress needed for entrainment (Lamb et al., 2020). Unlike the very small primary particles, such as clay, the flocs can interact with the bed sediment (Winterwerp et al., 2021), and might be deformed by this interaction. To date, it remains unstudied how the interaction between flocs and bedforms impacts both the flocs and the bedform geometry.

To be able to study the impact of mixed sediments, including flocs, on dune geometry, scientists must be able to measure their properties. Measuring particle size is not straightforward. When measuring in the field (in situ), logistical challenges (e.g. accessibility, battery lifetime, instrument choice) come into play, while when measuring in the laboratory (ex situ) the particles are removed from their natural surroundings. The decision for in or ex situ measurements is therefore often a logistical decision, and the consequences of this decision are unknown. Flocculated sediments in particular are prone to breaking and deformation, due to the measurement instrument itself (for example through the usage of pumps during in situ measurements) and sampling and storing for ex situ measurements (Federal Interagency Sedimentation Project, 1941). The strength of these effects remains undetermined. Additionally, the time needed for an accurate measurement for different types of samples is unknown, and various studies use various measurement times (e.g. Czuba et al. 2015; Gartner et al. 2001; Andrews et al. 2010) without justification. Clear guidelines on how to measure mixed suspended particles are lacking.

Finally, the FTTZ is characterised by tidally-induced flow strength fluctuations on relatively short (hourly) time scales. This means that bedforms are exposed to continuously changing flows. The reversing flow impacts bedform height and lee angle (Hendershot et al., 2016), but this response is lagged (hysteresis). Small bedforms might reverse crest orientation, following the direction of tidal flow reversal, while larger bedforms remain oriented in the residual sediment transport direction (Ernstsen et al., 2006) (Figure 1.4f). Especially during low tide, the outgoing flow is amplified, giving rise to higher flow velocities. High flow velocities are known to cause the flattening of bedforms and the transition into the upper stage plane bed (USPB). However, various studies hinted at an increased variability with increasing flow velocity (Venditti et al., 2016; Bradley & Venditti, 2019; Saunderson & Lockett, 1983). The researchers found the bed to be alternating between different bed states, but an explanation for this is lacking.

### 1.2.4 | What are the hydraulic consequences of bedforms?

Bedforms are considered a significant contributor to roughness in channels, i.e. the friction the flow experiences, leading to energy dissipation. By influencing roughness, bedforms indirectly modify flow characteristics, which in turn affect the bedforms themselves via sediment transport. This results in a feedback loop, where continuous adjustments of bedforms to the flow and vice versa occur.

Traditionally, roughness from dunes was believed to be primarily determined by the ratio between dune height and length (van Rijn, 1984). However, recent research has revealed that factors such as crest line orientation (Lefebvre, 2019), the two or three dimensionality of the dune field (Venditti, 2007; Nelson et al., 1993), and the shape of the leeside angle (LSA), also play a significant role in flow separation (Lefebvre & Cisneros, 2023). Roughness by dunes is created in the leeside of the dune. If the leeside is steep enough ($>$ 17 - 30$^\circ$ (Kwoll et al., 2016; Lefebvre & Cisneros, 2023)), the flow will separate, creating turbulence that dissipates energy. With milder leeside angles, intermittent or no flow separation occurs, but the flow expansion and corresponding deceleration can still lead to energy losses (Best & Kostaschuk, 2002). In laboratory settings with shallow flows, bedforms have steeper leeside angles than dunes in field conditions (Cisneros et al., 2020; Kostaschuk & Venditti, 2019). This distinction has led to the terminology differentiation between High-Angled Dunes (HADs) and Low-Angled Dunes (LADs). LADs generate less form roughness than HADs because less flow separation occurs on their leeside.

In the FTTZ, the relationship between bedforms and roughness is even more complex than in unidirectional rivers and laboratory experiments. The reversal of the current can have far-reaching consequences for the hydraulic roughness, when during upstream-oriented flow the roughness is different from the roughness during downstream-oriented flow (Herrling et al., 2021; Lefebvre et al., 2013). For example, during low tide, flow separation at the leeside of the primary (and secondary) bedforms contributes to roughness. In contrast, during flood tide, when the main flow direction is landward, the primary bedforms do not have enough time to adjust to the change in current direction, and the incoming flow passes over the less steep stoss side angle, where flow separation is less likely to occur. However, smaller superimposed bedforms can adapt quicker to changes in current direction, and flow separation at their new, land-facing leeside becomes the primary source of roughness (Lefebvre et al., 2011). It remains unclear to what extent the variability in dune geometry in the FTTZ is relevant for roughness determination.

### 1.2.5 | How can bedform geometry and the resulting hydraulic roughness be predicted?



Hydraulic roughness, an essential parameter in hydraulic and morphodynamic models, demands quantification. It is used to estimate water depth, improve models for flood prediction, determine shipping safety, estimate water availability, and identify sediment transport pathways (Karim, 1995; Julien & Klaassen, 1995). Hydraulic roughness can be expressed in various parameters, all related via (empirical) equations. The most common roughness parameters include the friction factor $f$ (-), the Chézy coefficient $C$ ($m^{1/2}s^{-1}$), Manning's $n$ (s $m^{-1/3}$), and roughness length $z_0$ (m). While this thesis predominantly uses the friction factor, there may be instances where other expressions of roughness are referenced.

Quantifying roughness is challenging as it can not be directly measured in the field. Numerous methods are available to predict or estimate hydraulic roughness and the bedform geometry that contributes to this roughness. These estimates can be used to characterise the system and can be employed in modelling efforts. I have identified three methods upon which roughness estimates are based: (1) derivations from direct flow measurements, (2) empirical equations based on bedform geometry, and (3) inference from model calibration of hydraulic models.

Various assumptions underlie these methods. The first method assumes that flow characteristics, such as turbulent fluctuations, are directly related to roughness. The second method assumes that local-scale roughness, which pertains to the scale of hundreds of metres and excludes reach-scale roughness elements such as width and depth changes (van Rijn, 1984), comprises only two elements: skin drag (by grains) and form drag (by bedforms). Those two elements would collectively make up the total shear stress or hydraulic roughness and could be partitioned as such (Einstein, 1950; Engelund & Hansen, 1967; van Rijn, 1984; Nelson & Smith, 1989; Garcia & Parker, 1993; Wright & Parker, 2004). Skin drag is driven by the development of a boundary layer close to the bed. However, when bedforms are present, the shear stress is dominated by form friction. The third method runs the risk of oversimplifying the physical processes of roughness, and calibrated values might only be valid for the specific conditions used for calibration (Klemes, 1986). Below I discuss the three methods.

Direct measures of flow characteristics, impacted by both sediment and bedforms, can be used to predict roughness. Many methods are available, each with its (dis)advantages, see Biron et al. (2004) and Pope et al. (2006) for reviews. Methods include using the Karman-Prandtl "Law of the Wall", to estimate bed shear stress from logarithmic velocity profiles, the Turbulent Kinetic Energy (TKE) method, relating turbulent fluctuations in the $x$, $y$, and $z$ directions to bed shear stress, or the Reynolds stress tensor method, deriving bed shear stress from stream-wise and vertical velocity fluctuations. From these direct measures of bed shear stress, $z_0$ can be estimated

(Hoitink et al., 2009). Finally, in uniform, steady-state rivers the water surface slope along the river can be used to estimate roughness.

However, direct (continuous) measures of flow characteristics are not generally available, especially not in field studies (Vermeulen et al., 2013). Alternatively, many equations estimate hydraulic roughness from dune height and length, generally in the form of a constant multiplied by $\frac{\Delta^2}{\lambda}$ (Soulsby, 1997), in which $\Delta$ is the dune height and $\lambda$ the dune length. Input values for these roughness estimations are, among others, dune geometry (sometimes including the leeside angle to account for the difference in flow separation between HADs and LADs (Lefebvre & Winter, 2016)), sediment characteristics ($D_{50}$, $D_{90}$) and various derivations from water depth (e.g. shear stress). With the rise of better field methods, dune geometry can be derived from bathymetric measurements, which can be directly used in the hydraulic roughness predictors. It is however unknown how these different approaches compare, and to which extent the leeside angle plays a determining role.

In the absence of direct bedform geometry measurements, for example, in poorly accessible regions or during flood conditions, empirical equations to estimate dune height can be used. Input values can either be estimated based on flat-bed conditions (from grain-related friction, and up- and downstream boundary conditions) or measured values, in which the impact of dunes is implicitly included. The latter option is common, and generally includes a value for water depth or shear stress (Yalin, 1964; Allen, 1978, 1972; Karim, 1995; Venditti & Bradley, 2022). For example, the total shear stress could be derived from the depth-slope product, in which the water surface slope reflects the total hydraulic roughness of the river (Lefebvre & Winter, 2016). When using shear stress values to predict dune height, an iterative approach would be needed to estimate the hydraulic roughness based on dune geometry predictions. This results from the fact that hydraulic roughness impacts the initial shear stress that was used to estimate dune height. At first sight, the dune height predictor of van Rijn (1984) seems to avoid the iterative approach, since they use the grain-based Chézy coefficient and grain shear velocity in their estimations for hydraulic roughness. However, these values are derived from the depth-averaged flow velocity and water depth, which are also bedform impacted. Therefore, all these methods require a priori knowledge of total shear stress, and an iterative approach is required.

The feedback between water height (shear stress) and roughness poses a challenge in hydraulic modelling. When parameterising roughness in the model, it will influence the water depth (and consequently bedforms, in case of a morphodynamic model), thus affecting roughness, which, in turn, alters water depth. If the approach were solely based on predicted dune geometry (instead of measured dune geometry), an iterative approach would be necessary. This cumbersome task is often simplified, typically using a calibration constant, to align modelled output values (such as water

depth) with the corresponding measured value. An example is provided for the model of the Rhine branches (Rijntakkenmodel) (Kosters et al., 2022). In the fifth generation of this model, a simplified version of the roughness predictor of van Rijn (1984) is used, wherein dune height is substituted with dune height derived from water depth, using Julien et al. (2002). An additional constant is used for tuning/calibration, eliminating the need for iteration but establishing feedback between water height and roughness. In the sixth generation model of the Rhine branches, the need for iteration is also eliminated, but now by incorporating measured dune height from bathymetric data, which is then implemented in the roughness predictor of van Rijn (1984).



### 1.2.6 | How to study bedforms?

Studying bedforms and the associated hydraulic roughness can be done through laboratory experiments, field studies, or modelling studies, each having its own (dis)advantages. In the following section, I discuss these methods, aiming to stimulate discourse about the optimal method considering the study aim and conditions.

Laboratory experiments, for example conducted in a flume, have the advantage of having good control over the initial and boundary conditions (Hacking, 1984), enabling the systematic study of one parameter while maintaining other conditions constant. The reproducibility of experiments allows for building on previously conducted studies, which can significantly improve fundamental knowledge. Moreover, they facilitate direct monitoring and quantification of otherwise challenging (or impossible) to access regions, such as the near-bed region for studying bed shear stresses (Gomez, 1978). However, laboratory experiments are ultimately a simplified version of nature, and the researcher is unable to simulate all complex processes innate to the field. Furthermore, the problem of scaling arises, requiring parameters to be downscaled to laboratory scale. Froude scaling, generally used when studying free-surface processes such as in this thesis, is based on keeping the relative importance of gravitational forces to inertial forces in a fluid flow as close to field values as possible. Alternatively, Reynolds scaling, used for studying enclosed water bodies, such as pipes or tanks, is based on keeping the relative importance of viscous forces to inertial forces as close to field values as possible. Achieving both types of scaling simultaneously without altering gravity or fluid characteristics is impossible (Heller, 2011). Additionally, downscaling certain elements could alter their behaviour. For example, downscaled sediment particles may become less mobile and more cohesive. Consequently, the sediment is not downscaled in laboratory studies, and dunes simulated in the lab are higher and steeper than their natural counterparts (HADs in the flume, versus LADs in the field, see Section 1.2.2). Relations found in the lab cannot be one-to-one applied to the field without considering scaling. Altering sediment characteristics, for example by replacing the natural sediment with low-density polystyrene particles (Naqshband & Hoitink, 2020), could be a solution. Despite these scaling issues, Paola et al. (2009)

found that morphological processes are well captured with laboratory experiments, as morphological feedback mechanisms are reasoned to be scale-independent.

In field studies, all complex natural processes are present. While seemingly ideal, the limited control and unpredictability of nature can complicate field measurements. (Non-intrusive) measurements can be complex, and practical issues arise regarding accessibility and resource deployment versus spatiotemporal resolution. For example, bathymetric data of the riverbed from a multibeam echosounder (MBES) provides a detailed picture of the bedforms, however, the spatiotemporal resolution is limited. The measurements are dependent on water level (e.g. only possible during high tide, and not along the channel margins), they are time and resource consuming, and safety can be a concern during periods with high flow velocities. Another example is sediment sampling to determine particle size, a time-consuming and logistically complex process with subsequent challenges in laboratory sample analysis.

Finally, modelling studies are used to study dunes and hydraulic roughness. Modelling is versatile, allowing the study of a wide range of scenarios and conditions without significant resource investments. It enables simulation of scales that are hard to measure in the field, such as the turbulent flow over a single bedform, or the tidal attenuation throughout the entire FTTZ. However, computer models are based on assumptions, simplifications, and parameterisations, necessitating a trade-off between complexity (realism) and computational speed. Calibration and validation are required, and a model outcome might be right for the wrong reason.

In this thesis, the combination of methods used depends on the aim of the study. Ultimately, a thoughtful selection and interpretation of the method, while considering all its (dis)advantages, is crucial. Combining insights from all methods can be a powerful tool (Kleinhans et al., 2009).

## 1.3 | Research questions

From the literature review above it becomes clear that knowledge of dune geometry and the resulting hydraulic roughness is essential for river management, but many unknowns exist when extrapolating this knowledge to the FTTZ. In this thesis, I will assess how bedform geometry in the FTTZ can differ from riverine bedforms, and how roughness in the FTTZ is affected by these bedforms. To attain the research objectives as posed in Section 1.1, the following research questions will be answered.

*Establish and understand how environmental factors in the FTTZ alter bedform geometry.*

- How can the particle size distribution of mixed sediments, including flocs, best be measured?
- What is the impact of fine sediment in mixed sediment beds on dune geometry?
- What is the influence of flocculation on dune geometry?
- How does high flow velocity impact bedform geometry at the transition from dunes to upper stage plane bed?

*Determine how bedforms impact the hydraulic roughness in the FTTZ.*

- What is the predictive capacity of well-established roughness predictors in rivers and the FTTZ?
- What contributes to the variance in hydraulic roughness in rivers?
- How do dune geometry and hydraulic roughness spatially vary in the FTTZ?

Each chapter in this thesis addresses one or more research questions. The outline of the thesis is described in the next section.

## 1.4 | Outline of thesis

The first four chapters of this thesis (Chapters 2 - 5) evaluate factors that are characteristic of the FTTZ but not necessarily of fluvial systems, and how these impact dune geometry. The succeeding two chapters (Chapters 6 and 7) then assess the impact of the dune geometry on hydraulic roughness in a fluvial and a fluvial-tidal system.

One of the factors potentially influencing dune geometry is sediment heterogeneity, including flocculated sediments. First, to provide accurate and reliable measurements of mixed sediment characteristics, Chapter 2 explores how suspended particle size distributions can best be measured. Besides assessing measurement practises, such as storage and stirring of the sample, we demonstrate how long a sample should be measured to obtain a reliable particle size distribution.

Following up on this, in Chapters 3 and 4, the impact of various mixtures of sediments and flocculation on bedform geometry is assessed via laboratory experiments. In Chapter 3, a recirculating flume is used to simulate flow over a sediment bed of various sand-silt mixtures with distinct degrees of cohesion. In Chapter 4, various degrees of flocculation and the interaction of these flocs with the sediment bed are studied in an annular flume.

High flow conditions can occur in the FTTZ when river discharge and ebb outflow coincide. A large variability in dune height is observed during high flow conditions, which is explored further in Chapter 5. Here, previously published laboratory data is re-analysed, and a theoretical framework is developed to describe the observations at the transition from a dune-covered to a flatbed.

Chapters 6 and 7 focus on the hydraulic roughness from dunes. To measure hydraulic roughness in the field, various methods exist (Section 1.2.5). Some of these are compared in Chapter 6 in a field study of the Waal River (the Netherlands). Additionally, the variance of the hydraulic roughness is assessed, and environmental factors to explain this variance are sought. In Chapter 7, this knowledge is applied to the FTTZ of the Fraser River (Canada). In the dynamic conditions of the FTTZ, the spatial variability of dune geometry is assessed. Hereafter, a hydraulic model is employed to estimate the influence of details in dune geometry on the hydraulic roughness.

The concluding Chapter 8 provides a synthesis of the main findings of this thesis. It will give broader context to the findings, and pose future research directions to further the field of dune and roughness research.

*I would also rather be*
*in situ*
*than ex situ*

# 2

# Suspended particle size measurements of flocculated sediment

This chapter was originally published as:

de Lange, S.I. & Seghal, D., Martínez-Carreras, N., Waldschläger, K., Bense, V.F., Hissler, C., Hoitink, A.J.F. (2024). The impact of flocculation on in situ and ex situ particle size measurements by laser diffraction. Water Resources Research 60(1). DOI: 10.1029/2023WR035176

## Abstract

Accurate particle size distribution (PSD) measurements of suspended particulate matter (SPM) composed of flocs and aggregates are important to improve understanding of ecological and geomorphological processes, and for environmental engineering applications. PSDs can be measured in situ (in the field) using a submersible sensor, or ex situ (in the laboratory) using samples. The methodological choice is often guided by logistical factors, and the differences in PSDs acquired by in situ and ex situ measurements is of concern. In this study, a laser-diffraction instrument (the LISST-200X) was used to compare in situ and ex situ PSD measurements. Samples measured ex situ were stored for three consecutive weeks and measured each week in a laboratory using different stirrer speeds. We observed that ex situ measurements display a higher $D_{50}$ (median particle size) than in situ measurements of the same sample (up to 613% larger, 112% on average). Our experiments show that the difference between in situ and ex situ measurements can be explained by flocculation of the riverine sediments during the first week of storage. During the subsequent ex situ measurements, the stirring results in a significantly lower $D_{50}$. Ex situ measurements are therefore unsuitable for flocculated SPM. This study provides recommendations for optimising PSD measurements by calculating the measurement times required to obtain robust PSD measurements (exceeding three minutes per sample), which are larger for field samples with coarser particles and wider PSDs.

## 2.1 | Introduction



Accurate and robust particle size distribution (PSD) measurements of suspended particulate matter (SPM) (including mineral particles, and flocs/aggregates) are important to many environmental studies. Examples include studying pollution transport by suspended particles (Rügner et al., 2019), studying the effect of colmation on spawning sites of aquatic biota (Bilotta & Brazier, 2008), and tackling technological challenges such as calibration of optical sensors (Agrawal & Pottsmith, 2000; Sehgal et al., 2022b). Additionally, the local SPM PSDs, together with flow dynamics, may control the mud (clay and silt) fluxes in rivers (Lamb et al., 2020). Also, PSD represent an important physical characteristic controlling sediment transport models directly or indirectly through settling velocity and critical shear stress. An accurate measure of the PSD is thus important for the estimation of SPM fluxes. However, the accuracy and reliability of the SPM PSD measurements are affected by many factors, such as SPM composition, flocculation (Droppo, 2004), measurement methodology (in situ / ex situ), and the logistics around the measurement process.

The methodological choice of whether to measure the PSD in situ or ex situ often depends on the aim and logistics of the study. Measuring in situ provides a natural picture of the PSD, commonly referred to as the effective PSD (Gartner et al., 2001), and allows for continuous long-term monitoring (Andrews et al., 2010). The in situ PSD includes both the discrete (River & Richardson, 2019) and composite particles (flocs) (Droppo, 2001; Williams et al., 2008). Conversely, ex situ measurements are performed under controlled laboratory conditions, often to better understand the complex particle transport processes. In situ and ex situ PSD measurements are subject to different factors and will therefore yield different results. These differences, typically neither acknowledged nor studied, will be discussed below.

A measured PSD is also impacted by decisions made before, during, and after the measurements. These include the choice of instrument type (e.g., laser diffraction, image analysis, or sieving), measurement time to obtain a reliable average, and data (post-) processing. Even more uncertainty is introduced when measuring ex situ, where sample collection (e.g., grab sampling, using Niskin bottles, or automatic samplers), sample storage (including storage duration and temperature), sample treatment (e.g., pre-sieving, oxidation, or chemical dispersion) and transportation become necessary (Gartner et al., 2001). Many studies (Phillips & Walling, 1995; Federal Interagency Sedimentation Project, 1941; Chakraborti et al., 2009; Livsey et al., 2022; Czuba et al., 2015; Boss et al., 2018; Zhao et al., 2018) attempt to understand and quantify the individual uncertainties associated with each of the above-mentioned choices. The LISST series of instruments developed by Sequoia (LISST-100X/200X and LISST-SL) are commonly used for in situ measurements. These instruments use laser diffraction, and the resulting measurements are affected by (a) the instrument itself (measure-

ment range, optical system (number and location of the detectors) and the selected particle size distribution model (Fraunhofer, Mie)), (b) the particle properties (shape, composition and mass density) and (c) the measurement environment (turbulence and thermal fluctuations) (Czuba et al., 2015; Bieganowski et al., 2018). Hence, different laser diffraction instruments may yield different results.

Instrument-related differences become evident when comparing the PSDs of a sample measured using different measurement instruments for both in situ and ex situ. For example, Czuba et al. (2015) compared PSDs measured with an in stream LISST-SL, and physical samples using the pipette method and a Sedi-Graph (a lab based instrument). Boss et al. (2018) compared PSDs measured with a LISST-100X using an in situ flow-through chamber and physical samples using a Beckman Coulter (a lab-based instrument). Both studies found comparable PSDs in situ and ex situ, but post-measurement adjustments were necessary to account for differences in the size ranges measured with each technique. Without adjustments, Czuba et al. (2015) measured lower $D_{50}$ values in the stream than on the physical samples, whereas Boss et al. (2018) measured similar PSD shapes but a 2.5 times higher particulate volume concentration with the Beckman Coulter than with the LISST-100X. As different instruments measure at different ranges and might use different measurement principles, accurate comparison of in situ and ex situ PSD measurements is only possible using a single instrument.

An additional drawback of the laser-diffraction instruments used in the previously discussed studies is that flocculated particles can break when using a LISST-SL and a pump-controlled flow through a chamber. Breaking or deforming the flocs during measurements can result in unreliable PSD measurements (Lamb et al., 2020), as flocs get spread across multiple size classes (Chassagne et al., 2022). The (de)formation of flocs changes the particle size distribution, density and particle settling velocity (Guo & He, 2011). For example, freshwater flocs with diameters of 150–250 $\mu$m (similar to fine sand) can have similar settling velocities as 20 $\mu$m silt because of the low densities of flocs, thus affecting the theoretical SPM flux estimations (Lamb et al., 2020), although this may necessitate a deeper analysis on SPM theory to present a holistic understanding of flocs and fluxes in rivers (Hunt, 1968; McLean, 1992). Measuring in situ PSDs is therefore essential when using SPM flux estimation models (Chassagne & Safar, 2020). The in situ use of a LISST-200X, which will be used in this research, overcomes this limitation as particles pass through an open flow chamber, minimising local turbulence during both in situ and ex situ measurements. Additionally, water sampling for ex situ measurements might induce breakage of flocs or promote flocculation (Gibbs, 1981; Phillips & Walling, 1995), which eventually attain a new equilibrium with the ex situ measurement setup after sampling (Kranck, 1979).

Another factor to be taken into account when using laser diffraction to determine PSDs is that a measurement time must be chosen to obtain representative measurements. Very little is known about the influence of SPM characteristics (e.g., dominant size-class) on the required measurement times. They should be long enough to be statistically representative, while remaining time and resource efficient. In existing literature, different measurement and averaging intervals are indistinctly used. For example, measurements by Czuba et al. (2015) included an average of 16 readings taken in 2 s, while Gartner et al. (2001) averaged 16 readings taken in 20 s, and subsequently averaged this over one minute. Alternatively, Andrews et al. (2010) took 10 measurements every second, and averaged this over 100 seconds. Zhao et al. (2018) looked more critically at the averaging method. They used an average of 30 measurements, indicating little difference ($<\sim$10%) between readings, and showed that both 30 or 60 readings yield approximately the same result. It should be noted that the aforementioned authors used different LISST versions, and that there is currently a lack of guidance on how to optimise measurement times.

It is crucial to acknowledge that the measured SPM PSD of a water sample collected from a river (ex situ) may not match the actual PSD in the natural environment. This is because the existing flocs or aggregates could be altered during sampling, storage and ex situ PSD measurements, changing its SPM characteristics (Federal Interagency Sedimentation Project, 1941). Similarly, optimum measurement time lengths might vary depending on SPM characteristics. We argue that the magnitude of the alteration when using ex situ methods is largely unknown, and that this lack of knowledge hampers the formulation of clear guidelines to measure PSDs in and ex situ, affecting the multitude of disciplines depending on particle size information. In this study, we hypothesise that the change in floc size is the main cause of divergence between in and ex situ PSD measurements, and that larger measurement times are needed as floc size increases. The latter is because the PSD of flocculated sediments is likely to cover a larger number of size classes. We test this by performing in situ and ex situ PSD measurements using the same instrument, storing samples for different duration of times and at different conditions (hot and light, and cold and dark), and by investigating the relationship between statistical uncertainty, number of measurements, and PSD characteristics. The objectives are (a) to examine how the $D_{50}$ and PSD of flocculated particles changes as a function of the ex situ measurement environment (shear stress parameterised by stirring speed), (b) to determine the impact of sample storage duration on ex situ $D_{50}$/PSD measurements, and (c) to establish optimal measurement times for in situ and ex situ measurements as a function of SPM characteristics. The key novelties of this study are the quantification of the effect of flocculation on grain size distributions and the presentation of an optimised measurement time for recording PSD and calculating reliable $D_{50}$ values. The aims of this paper are conceptualised in Figure 2.1.

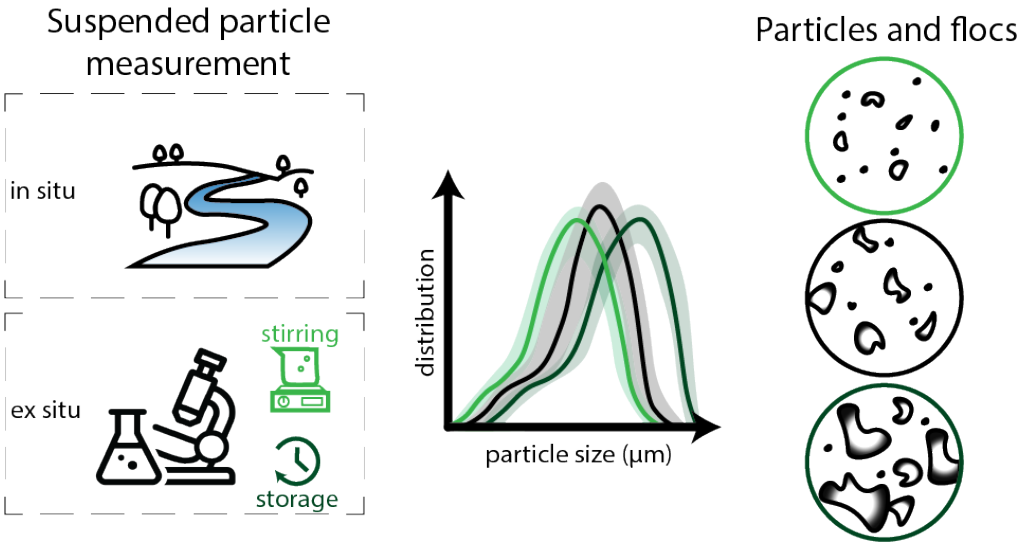


**Figure 2.1** | Graphical overview of this research

## 2.2 | Methods

PSD measurements were performed using a LISST-200X (Sequoia Scientific), hereafter referred to as a LISST, for both in situ and ex situ measurements. Additionally, a Mastersizer-3000 (Malvern Panalytical), hereafter referred to as a Mastersizer, was used to test higher stirring speeds ex situ. During ex situ analysis, microscopic images were taken to visualise particles. This allows for identification and explanation of the differences between measurement methods. Finally, requirements for the duration of the in and ex situ measurements (measurement time length) were determined.

### 2.2.1 | Particle size distribution measurements

#### 2.2.1.1 | LISST-200X

A LISST-200X is a submersible laser-diffraction based particle-size analyser. Laser diffraction instruments are based on the scattering of collimated laser light by small particles, and the subsequent detection (Agrawal & Pottsmith, 2000). The instrument projects a laser beam through a sample of particles in suspension and measures the forward scattering divided in multiple angles (Andrews et al., 2010; Czuba et al., 2015). The detector has multiple rings with logarithmically increasing radii, which correspond to a range of scattering angles (Agrawal & Pottsmith, 2000). The largest particles are detected by the innermost ring, and vice versa. The LISST has an optical path length of 2.5 cm through which the laser passes the sample. Light is scattered in 36 angles, resulting in 36 log-spaced size classes between 1.00 and 500 $\mu$m. Additionally, the laser passes through the centre of the rings, and a photo-diode behind the ring detector measures the transmission. The measured reduction in light intensity

by attenuation is used to de-attenuate the measured scattered light. It is essential to correct for attenuation since the magnitude of scattering is related to the number of particles, and therefore needed to derive the PSD (Agrawal & Pottsmith, 2000). Before the light distributions are inverted to a PSD, they must be corrected for background scattering in pure water and ageing of the laser and windows. Finally, the detected light is back-calculated to a PSD assuming a certain optical model. The LISST outputs PSD, total volume concentration, optical transmission, depth, and temperature on a desired measurement interval.



Limitations should be considered when using the LISST. First, too fine or too coarse particles outside of the instrument's range (1.00 - 500 $\mu$m) are grouped into the smaller and larger size classes, respectively, where the smallest or largest size classes are being affected the most ('rising tails') (Fettweis, 2008), which can lead to an over or underestimation of $D_{50}$. In this study, rising tails are not observed. Second, multiple scattering caused by high particle concentrations can affect the PSD measurements (Czuba et al., 2015; Sehgal et al., 2022c). However, in this study, the measured suspended particulate matter concentrations (SPMC) were below 150 mg $L^{-1}$, what lies within the recommended measuring maximum limit of the manufacturer (1332 mg $L^{-1}$ for a $D_{50}$ of 31.25 $\mu$m). Third, natural particles (including flocs) are not circular, impacting light scattering (Mikkelsen & Pejrup, 2001; Pedocchi & García, 2006; Graham et al., 2012). We therefore used the irregular particle random shape model of the LISST, which partially takes into account the non-spherical nature of particles (Agrawal et al., 2008). The model incorporates slightly irregular particles, but might not fully represent the highly irregularly-shaped flocs.

#### 2.2.1.2 | In situ measurements

The schematic diagram (Figure 2.2) summarises the steps taken to perform the measurements in situ and ex situ. In situ particle size measurements were performed in the Attert River in Useldange, Luxembourg. The Attert River enters Luxembourg from Belgium in the northwest and runs from west to east. It covers a catchment area of 247 $km^2$. The Attert River near Useldange is an example of a rural basin (Martínez-Carreras et al., 2012). The bedrock geology is dominated by Trias marls and dolomites, Lias sandstone, Devonian shales, and phyllites (Pfister et al., 2017). The sampling site has a stabilised river channel with large boulder blocks. The sampling period covered the rising limb of a runoff event (16/11/2022 - 18/11/2022). At the sampling location, a LISST was mounted on a stepladder submerged close to the riverbank. The sensor was constantly submerged, positioned 20 cm above the stream bed, and parallel to the stream channel. This reduced particle adherence and sedimentation in the measurement cells. For optimum data quality, the LISST was cleaned and the background calibration was updated 12 hours before deployment. It was programmed to measure every 30 seconds.

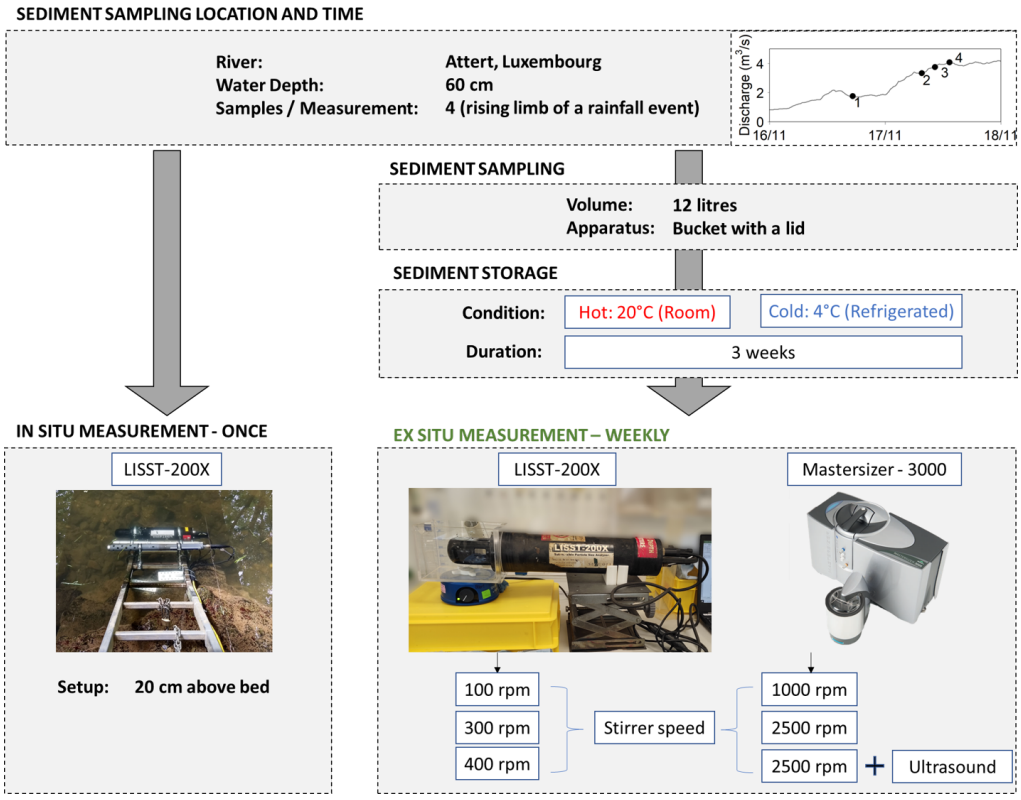


**Figure 2.2** | Summary of the sampling steps for in situ and ex situ PSD measurements using a LISST-200X and a Mastersizer-3000. The picture of the Mastersizer is taken from Malvern Panalytical (www.malvernpanalytical.com). Inset: Hydrograph of the rising limb of the sampled rainfall-runoff event between 16/11/2022 - 18/11/2022, indicating the four sampling times.

The in situ PSD of each measurement was calculated as the average of the in situ measurements recorded for 15 minutes, evenly spread around the grab sampling time. This was not the case for the first measurement (out of four) however, where it is an average of the first 7.5 minutes due to a technical failure.

#### 2.2.1.3 | Ex situ measurements

To perform ex situ measurements in the laboratory, four grab samples (12-L each; sample 1, sample 2, sample 3, and sample 4) were collected near the LISST using a 5 L plastic sampling container with a handler immersed upside down approximately 30 cm. A lid was secured before lifting the bucket out of the water. Each grab sample was split into 12 1-L bottles (hereafter called sub-samples). Out of the 12 sub-samples, six sub-samples were stored at room temperature (18-23 °C) while exposed to light, referred to as hot-stored samples, and six were refrigerated inside a dark cold-storage (4 °C), referred to as cold-stored samples.

Ex situ particle size measurements were performed in the laboratory using a LISST and a Mastersizer. Additionally, the SPMC of the samples was measured, and the samples were inspected using a microscope. This analysis was done on various subsamples, for three storage durations (1-3 weeks) and for two storage conditions (hot and cold).



The ex situ LISST PSD measurement procedure was as follows. Before doing the measurement, a background measurement was carried out with clear tap water. Then, after gentle agitation of the sediment bottle, the sample was poured into a test volume chamber provided by the LISST manufacturer (Figure 2.2). A magnetic stirrer kept particles in suspension, without air bubbles forming. Each sample was measured at three different stirrer speeds (100, 300, 400 rpm). Higher speeds were not used to avoid disalignment of the magnetic stirrer. Measurements were performed for 5 minutes. The LISST was set to average 10 recordings per second, resulting in 1 measurement per second. Measurements were taken consecutively with increasing stirring speeds starting at 100 rpm. We observed an exponential decrease in $D_{50}$ in the first minute of stirring after changing the stirrer speed. After this time, the $D_{50}$ and transmission (indication of turbidity) remained constant. We therefore excluded the data collected during the first minute. The raw data was converted to the corresponding PSD using the random-shape model (Agrawal et al., 2008). The averaged data was used to calculate the $D_{50}$ value per sample, which was done for each individual stirrer setting (100, 300, 400 rpm), storage duration (1, 2, and 3 weeks) and storage condition (hot and cold). The calculated values were subsequently used to determine the effect of storage duration and stirring on the established PSD.

Additionally, ex situ particle size measurements were performed using a Mastersizer-3000 (Malvern Panalytical Ltd., Malvern, United Kingdom), hereafter referred to as Mastersizer (MS), to test high stirrer speed settings. Three different settings were used for this purpose: 1000, 2500, and 2500 rpm along with ultrasonic vibrations (US). The procedure is detailed in the Supplementary Text S2.

A standard gravimetric method was used to measure the SPMC of all water samples after filtration through 1.2 $\mu$m Whatman GF/C glass fibre filters (General guidelines: Guy 1969). Finally, a settling column was used to visualise the SPM samples under an inverted microscope (Leica® DMR). The samples were transferred using a pipette into the settling column, where they were allowed to settle for 15 minutes. Next, a Leica-DFC 500 high-resolution digital camera (v. 3.7.0, Leica Microsystems) fitted on the microscope was used to take 2D images on a scale of 50 $\mu$m. 2D images may not reflect the spatial complexity of natural sediment and flocs, however, they provide a simple solution to infer the levels of intra-particle aggregation (Spencer et al., 2021). Here, we simply use the images to provide an example of the difference in the scale of primary particles (PPs) (clay, silt, and sand) and flocs.

#### 2.2.1.4 | Additional data sets

Additional in situ and ex situ data sets (Table 2.1, in grey) were used to calculate the required measuring time to obtain representative PSDs, with the aim of including samples with contrasting characteristics. All additional data sets were collected using the same LISST-200X.

The additional in situ data from measurements at Everlange (Luxembourg) and Rotterdam (The Netherlands) were taken from Sehgal. et al. (2022). The additional ex situ sources consist of two data sets: (1) measurements from several consecutive events sampled at Huncherange (Luxembourg), and (2) experimental data sets collected using a tank setup. Both data sets, except for a few experiments from the second data set (oxidised, tank setup), were taken from Sehgal et al. (2022a). A detailed description of the tank setup and measurement protocol is available in Sehgal et al. (2022c). The same measurement protocol and samples were used to characterise the sediment samples that were oxidised using hydrogen peroxide ($H_2O_2$) 60% at 1:1 solution ($H_2O_2$ and Mili-Q water) for 15 days, with intermittent stirring and warming at 30 °C. Measurements recorded at concentrations of 100 mg $L^{-1}$ and 1000 mg $L^{-1}$ were used. The oxidised data set was added to include PSD measurements of samples with nearly no organic matter or inter-particle cohesion.

**Table 2.1** | The list of data sets used to generate results in this study. Data set in grey is used for the Monte Carlo analysis (Section 2.3.5).

| Data set | Amount of samples | in situ LISST | ex situ LISST | | | | ex situ Mastersizer (MS) | | |
|---|---|---|---|---|---|---|---|---|---|
| | | | Stirrer speed (rpm) | | | | Stirrer speed (rpm) | | |
| | | | 100 | 300 | 350 | 400 | 1000 | 2500 | 2500* |
| **This paper** | 28 (4 in situ, 24 ex situ) | X | X | X | | X | X | X | X |
| **Tank setup (no ox)**[1] | 32 | | | | X | | | | |
| **Tank setup (oxidised)** | 28 | | | | X | | | | |
| **Huncherange**[1] | 70 | | | | | X | | | |
| **Everlange**[2] | 26 | X | | | | | | | |
| **Rotterdam**[2] | 36 | X | | | | | | | |

*Additionally, ultrasonic vibrations were applied.
[1]Sehgal et al. (2022a); [2]Sehgal. et al. (2022)

### 2.2.2 | Data analysis

#### 2.2.2.1 | Sample characterisation

We characterised the PSDs based on (a) size percentiles, (b) distribution width, and (c) bi- or multi-modality. To account for differences in volumetric concentration when visualising the data, the PSDs are normalised by dividing the area per bin by the total area under the PSD.

The particle size of the sample was parameterised by taking the 10th, 50th, or 90th percentile of the PSD, resulting in the $D_{10}$, $D_{50}$, and $D_{90}$ ($\mu$m), respectively. To group the samples, the PSD of a sample was defined as small if its $D_{50}$ was smaller than the median $D_{50}$ of all collected samples (51 $\mu$m). The PSD width was characterised as the span value, $SV$ (-):

$$SV = \frac{D_{90} - D_{10}}{D_{50}} \tag{2.1}$$



The PSD was defined as narrow if its $SV$ was smaller than the median $SV$ of all collected samples (2.38).

Finally, the bi- and multi-modality of a sample was defined by identifying local maxima (peaks) in its PSD. A local maximum is a data point in the PSD that is larger than its two neighbouring maxima. If the local maximum was at least 0.5 times the height of the concentration indicated by the global maximum (highest peak), then the sample was labelled as bi- or multi-modal.

#### 2.2.2.2 | Measuring time requirements

We studied the relation between statistical uncertainty and the number of measurements, which was used to determine how many measurements are required to obtain a representative PSD. We performed a Monte Carlo bootstrap analysis to find which subset of all collected measurements of a sample reflects the characteristics of the entire population. We assume that the entire population is not changing over time. We randomly drew a subset of measurements and calculated the $D_{50}$ of the sample. The size of the subset ranged from one measurement to all measurements in the entire set. Next, a Monte Carlo bootstrap analysis was performed 1000 times for each subset size to determine the deviation of the subset from the data set mean $D_{50}$. The minimum and maximum values were taken from each run. These simulations were performed for 233 samples (Table 2.1) with varying values of $D_{50}$, SV, modality, and measurement method (in or ex situ).

The measurement frequency (which could be more than 1 measurement per second) was used to convert the number of measurements, as calculated by the Monte Carlo bootstrap analysis, to measurement time. By studying the change in maximum deviation from the data set mean when adding more measurement readings (when measurement time increases), we gave an estimate on how many readings (and hence measurement time) were needed to give a representative estimate of the $D_{50}$ of the sample. The threshold to determine when the sample is statistically representative was defined in three different ways, and can be tailored to the researchers' needs. The first two thresholds were based on the slope of the maximum and minimum deviation from the data set mean. The slope of the deviation decreased when adding more

measurements, indicating that the information gain (or decrease in uncertainty) was decreasing when including more measurements. The first threshold is reached when the slope of the maximum and minimum deviation from the data set mean is equal or less than ± 0.05. A stricter formulation of this is used for the second threshold, where the slope should be equal to or less than ± 0.005. Finally, a maximum deviation of 5% from the data set mean is allowed for the third threshold. Different thresholds can be chosen depending on the accuracy level required.

## 2.3 | Results and Discussion

Sections 2.3.1 and 2.3.2 describe the PSD behaviour in the in situ and ex situ measuring environments. Sections 2.3.3 and 2.3.4 highlight the influence of storage and stirring on $D_{50}$ with reference to in situ $D_{50}$. Section 2.3.5 provides the minimum measurement time needed to obtain a reliable average value of $D_{50}$ for different SPM characteristics. Section 2.3.6 describes the implications of the results and recommendations for PSD measurements based on this study.

### 2.3.1 | In situ sample characterisation

Figure 2.3 shows the in situ and ex situ PSD of the 4 samples collected during the rising limb of a runoff event. In-situ measurement 1 (and sample 1) was taken during the onset of the event and measurements 2-4 were taken during the rising limb (Figure 2.2).

Discharge dynamics impact the PSDs of the samples in three different ways. First, while discharge increased with measurement number, so did the average $D_{50}$ of the in situ samples ($D_{50}$ = 26 ± 3, 47 ± 4, 53 ± 3, and 53 ± 2 $\mu$m for samples 1-4, respectively), and also in the SPMC of the samples (11, 47, 53 and 53 mg $L^{-1}$ for samples 1-4, respectively; see also Supplementary Figure S11). An absolute difference of 1.1, 3.6, 1.3 and 2.7 $\mu$m was found between the average $D_{50}$ of the in situ samples measured over 15 mins (26.2, 47.6, 52.9 and 52.5 $\mu$m) and the in situ measurements corresponding to the ex situ sampling at 7.5 minutes (27.3, 44.1, 51.6 and 49.8 $\mu$m). However, averaging of LISST data is essential (see Section 2.3.5), necessitating us to use the averaged value. With increasing discharge, the particle size and concentration increases, which can be related to remobilisation of sediment stored on the river bed (Lee et al., 2019) and the role of shear stress in altering particle size (Grangeon et al., 2012).

Second, the nature of the particles that are dominating the PSD differs per measurement. During the onset of the event (sample 1), the $D_{50}$ is smaller, and the bimodal distribution of the PSD (peaks at 6 and 22 $\mu$m) could be related to the presence of small PPs (clay) and small flocs. These peaks may represent the base flow conditions, which become less dominant as larger particles are entrained. However, these sizes

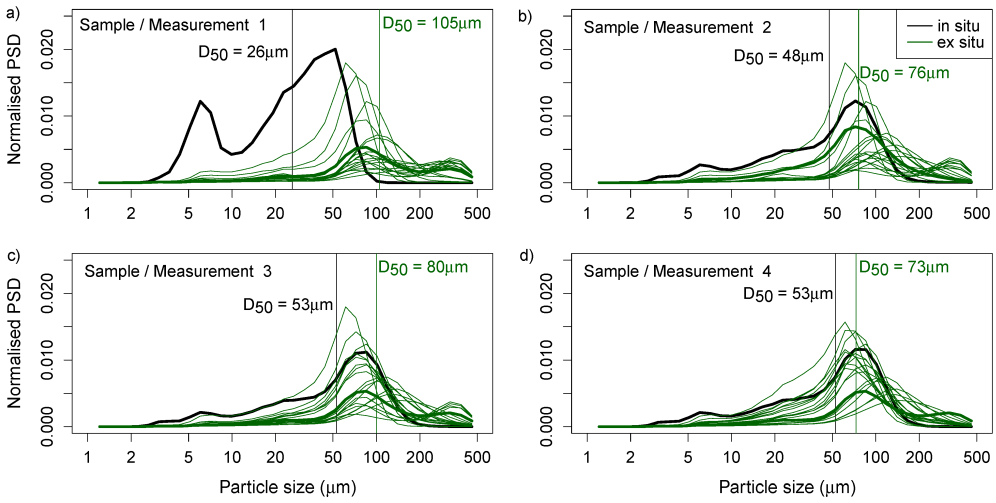


**Figure 2.3** | Average of in situ (black) and ex situ (green) normalised particle size distributions of 4 samples measured using a LISST-200X (ex situ: each thin line indicates a different storage condition, storage duration, and stirring speed). Mean in situ and ex situ $D_{50}$ are indicated with vertical lines in the corresponding colours. See Supplementary Figures S7-10 for the individual PSDs.

are still visible as plateaus in the PSDs of samples 2-4. The peaks and plateaus in the in situ PSDs are located at 3, 6, 22, 50-85, and 385 $\mu m$ (the largest plateau only in sample 2). These sizes correspond to the often made division between primary clay particles (3 $\mu m$), flocculi (15 $\mu m$), microflocs (50-200 $\mu m$) and macroflocs (200-500 $\mu m$) (Lee et al., 2012).

Finally, the discharge signature is also visible in the variability of in situ PSDs. This variability can be indicated by the coefficient of variation (standard deviation divided by mean) of the volumetric SPMC, which are 11, 9.7, 7.8, and 6.6 $\mu$L L$^{-1}$ for measurements 1-4 respectively (see also Supplementary Figure S11). The variability is the largest in the first sample. This could be related to the fact that flocs are often more irregularly shaped at low discharge, with a more open matrix (loosely bonded) in which macro-pores can develop (Williams et al., 2008), while they are more densely packed at high discharge (Droppo et al., 2005).

### 2.3.2 | Discrepancy between in and ex situ PSDs

Ex situ PSDs shown in Figure 2.3 include the PSDs from both storage conditions (hot and cold) measured after 1, 2, and 3 weeks of storage using different stirrer settings (100, 300, and 400 rpm; Table 2.1). The average $D_{50}$ of the samples measured ex situ (105 $\pm$ 34, 76 $\pm$ 26, 80 $\pm$ 26, and 73 $\pm$ 31 $\mu$m for samples 1-4 respectively, see Supplementary Table S1 for the $D_{50}$ corresponding to each measurement) is larger than those measured in situ, which is primarily caused by the presence of larger particles (Figure 2.3) - possibly flocs that form when particles settle at the bottom of the sample bottles during storage.

The presence of flocs in the samples is confirmed from microscopic images. They show that the particulate matter found in our samples range from PP (clay, silt, sand; Figure 2.4a-c) to flocs of different sizes (Figure 2.4d-f). The flocs found in our samples are rich in organic matter (Figure 2.4), and range up to 0.5 mm. Under low transport conditions, flocculated particles can be found in rivers, often in the presence of organic matter (Nicholas & Walling, 1996; Bungartz & Wanner, 2004) which is known to help in binding particles together in estuaries (Dyer, 1989; Winterwerp, 2002; Mietta et al., 2009). It is important to derive the effective PSD, including the flocculated particles, since flocs impact sediment transport by changing the settling velocity: flocs the size of medium sand have a settling velocity equivalent to fine silt (Lamb et al., 2020). Excluding flocs from the PSD would result in a shift in $D_{50}$ toward smaller sizes (Droppo, 2004). In the following sections, we explore the impact of flocs on ex situ PSD LISST measurements.

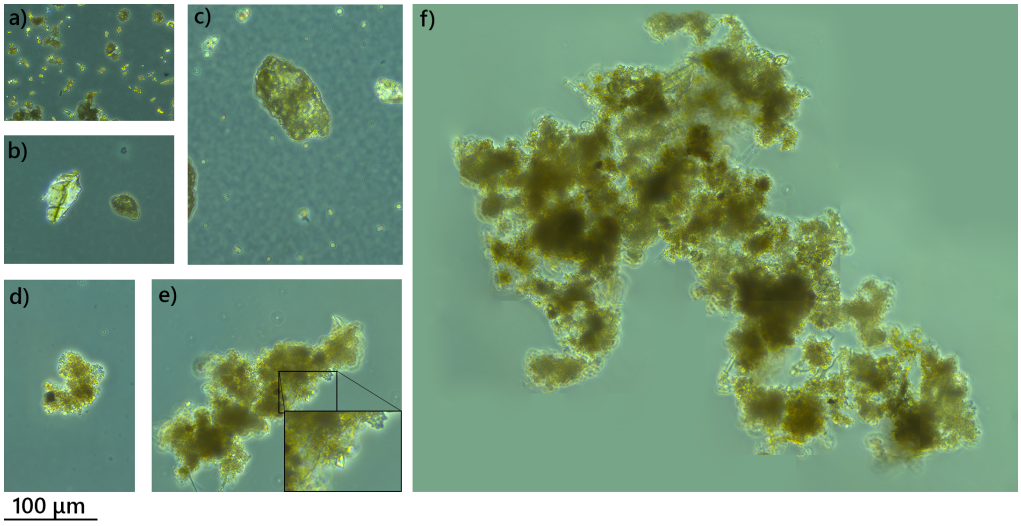


**Figure 2.4** | Examples of primary particles and flocs as seen under a microscope. a) clay. b) silt. c) sand. d) small floc. e) medium sized floc, insert showing the interaction between a primary particle and a floc. f) composite picture of a large floc. The scale is the same for all subfigures, except for the insert.

### 2.3.3 | Impact of stirring on ex situ measurements

The stirrer speed has a large impact on PSD ex situ measurements (Figure 2.5). For all samples, a decrease in $D_{50}$ values with an increase in stirrer speed was observed. This was on average 56% when stirrer speed changed from 100 to 300 rpm and 23% with a change from 300 to 400 rpm (Figure 2.5).

The stirrer speed is a measure for shear stress in the mixing jar, which is often several orders of magnitude higher than in natural rivers (Chakraborti et al., 2009). Since floc size is known to attain an equilibrium with the shear stress in the water column (Kranck, 1979), the stirrer speed will impact the floc size. The decrease in $D_{50}$ with

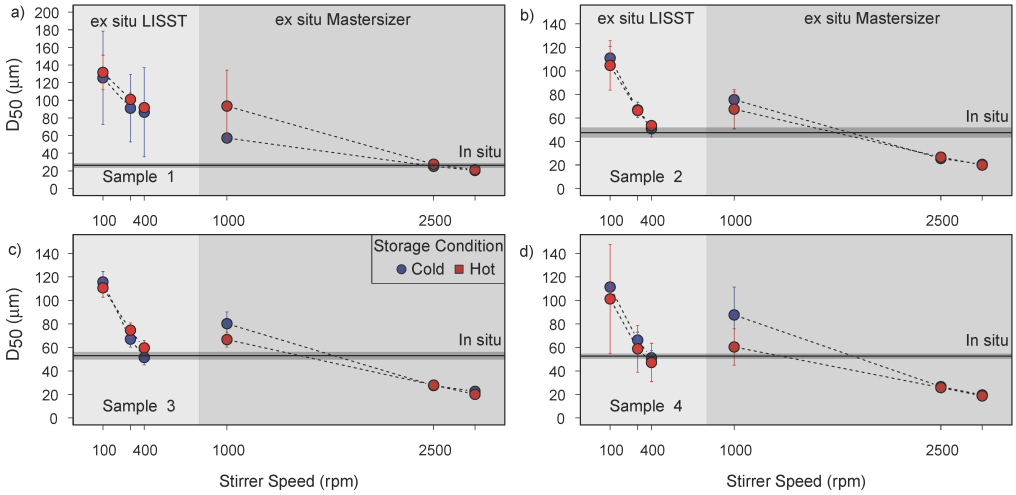


**Figure 2.5** | Impact of stirring speed on the $D_{50}$ values of the 4 samples (a-d) measured ex situ using a LISST and a Mastersizer. The $D_{50}$ values were calculated for the measurements taken for 3 consecutive weeks (week 1, 2 and 3) in both storage conditions (hot and cold) and applying different stirrer speeds using a LISST (100, 300, and 400 rpm) and a Mastersizer (1000, 2500 and 2500 rpm + US). The mean $D_{50}$ values are averaged over the storage duration; error bars indicate the standard deviation. The horizontal lines indicate the average in situ $D_{50}$, and the grey shading the variability within the 15-minute measurement period.

increasing stirrer speed, and therefore increased shear, is related to deformation (densification and coiling) (Chassagne et al., 2022), and/or breaking of flocs (Oles, 1992). Coiling is the restructuring of a floc into a more compact arrangement while maintaining its integrity, even after being subjected to external forces. This deformation often coincides with densification. Densification can also occur when flocs break and re-aggregate (Selomulya et al., 2003), but this results in flocs with weaker attachment strengths (Clark & Flora, 1991; Yeung & Pelton, 1996). It is unclear which process (deformation or breaking) leads to the decrease in $D_{50}$ of our samples. Yeung & al (1997) used turbidity as a proxy of the inverse of flocculation. Turbidity can be estimated by the transmission value of the LISST, and was found to be relatively constant (on average a decrease of 2% at the end of the measurement) in this study. Additionally, the total volume concentration remained constant. This implies that the number of particles remained the same, indicating that the deformation process dominated rather than the breaking process.

The $D_{50}$ values of the in situ LISST measurements of each individual sample are considered a reference for the ex situ LISST and Mastersizer measurements (Figure 2.5). The largest difference between the in situ and ex situ $D_{50}$ values using the LISST was observed at 100 rpm: the mean $D_{50}$ measured ex situ using LISST was on average 180% greater than the in situ value. 90% and 60% greater values were observed using 300 and 400 rpm.

The stirrer speed of the Mastersizer was larger than during the LISST measurements, resulting in smaller values of $D_{50}$ (Supplementary Figure S1 and S2). At the lowest stirrer speed of the Mastersizer (1000 rpm), the ex situ $D_{50}$ values are larger than the in situ values. At 2500 rpm (+US), the in situ values of $D_{50}$ are larger than the ex situ equivalents. Adding US slightly decreases the $D_{50}$, which could be due to breaking of the flocs, or because the vibrations caused by the high frequency sound waves lead to coiling of the flocs. The Mastersizer results suggest that there should be an intermediate stirring speed which breaks or deforms the flocs to such an extent that the conditions are equal to riverine conditions. Chakraborti et al. (2009) suggested that the choice of ex situ stirring speed can be adjusted to the in situ shear forces the researcher wants to mimic, to be able to compare in and ex situ measurements. This requires the assumption that field samples are taken in steady state, which could be true for the lake samples, but might not be the case for our riverine samples taken during the rising limb of a discharge event. As shown in this research, simulating natural conditions is very difficult, and simply measuring in situ might be the easiest and most reliable option.

Ex situ measurements are, however, valuable for determining the PSD of PPs. The difference between the effective PSD and PP PSD gives a measure of the degree of flocculation, and can also be useful to understand which size fractions in the PSD are influenced by organic matter (Lake et al., 2022). Our results suggest that the higher the stirring speed, the closer the data reflects the PSD of the PPs, which is specifically evident in the highest tested stirrer speed with the Mastersizer (Supplementary Figures S3-S6). To fully reduce the sample to PPs, hydrogen peroxide treatment is needed, which removes all the organic matter and the corresponding cohesive bonds (Gray et al., 2010; Walling et al., 2000). Lake et al. (2022) performed ex situ PSD analysis of samples taken close to our study area after removal of the organic matter. Their data indicated that the $D_{50}$ of PP is about 44-52% smaller than the ex situ measurements of the non-treated samples, both measured using a Mastersizer at 2500 rpm. This most certainly indicates that we have not reduced our samples to PPs by only increasing stirrer speed.

### 2.3.4 | Impact of storage on ex situ measurements

Samples showed flocculation during the first week of storage, as shown by the large increase in $D_{50}$ values between in situ and ex situ samples. After one week of storage, the ex situ mean $D_{50}$ was 258%, 59%, 46% and 57% larger than the in situ mean $D_{50}$ (Figure 2.6). Phillips & Walling (1995) explored the effects of storage on the sample in the first days after sampling. They found an increase in $D_{50}$ of 9-63% compared to in situ measurements after a relaxation time of up to three days and using the lowest stirrer speed possible to keep particles in suspension. After storing our samples for seven days, we found an increase in $D_{50}$ of 207-588% (average 293%) using the lowest

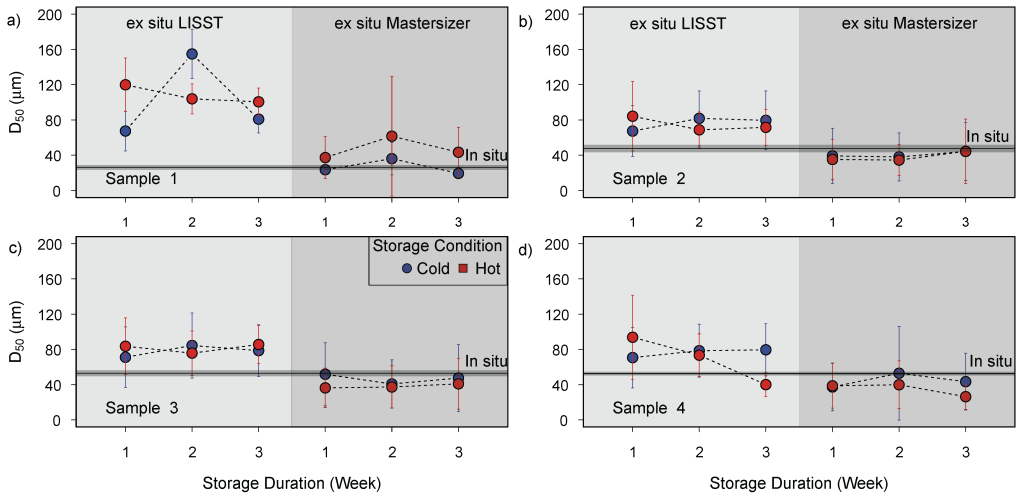


**Figure 2.6** | Impact of storage on the $D_{50}$ values of the 4 samples (a-d) measured ex situ using a LISST and a Mastersizer. The $D_{50}$ values were calculated for the measurements performed for 3 consecutive weeks (week 1, 2, and 3) in both storage conditions (hot and cold) and at different stirrer speeds using a LISST (100, 300, and 400 rpm) and a Mastersizer (1000, 2500, and 2500 rpm + US (ultrasonic vibrations)). The mean $D_{50}$ values are averaged over stirrer speeds; error bars indicate the standard deviation. The horizontal lines indicate the average in situ $D_{50}$, and the grey shading the variability within the 15-minute measurement period.

stirrer speed. This is much larger than the findings of Phillips & Walling (1995), suggesting that the process of floc formation increases beyond their study time. Neither in this study, nor in the study of Phillips & Walling (1995), it was possible to resemble the in situ reference state with ex situ measurements, once the sediment had settled in storage. However, they did report a good agreement between in and ex situ measurements when storage time was short enough to avoid particle settling in the sample containers, despite the fact that flocs can also break, deform, or grow during sampling (Gibbs, 1981; Eisma, 1986). However, the storage time until settling is so short that it is practically infeasible to transport the samples to a lab for ex situ measurements. This underlines the recommendation to measure in situ to obtain robust and representative PSDs, rather than to perform ex situ measurements.

Surprisingly, the influence of storage on flocculation beyond the first week was minimal (Figure 2.6), and stirrer speed turned out to be far more important for $D_{50}$ determination than storage time. The relatively constant $D_{50}$ over time indicates that flocculation did not continue, independent of storage condition. Stabilised conditions might inhibit any further floc formation. The slight increase (13% on average, compared to week 1) in $D_{50}$ for cold-stored samples, could potentially indicate that bonds had strengthened over time due to stabilisation. In contrast, the decrease (40% on average, compared to week 1) in $D_{50}$ for hot-stored samples could be related to the disintegration of the organic-rich flocs. Organic-rich flocs could be more susceptible

to decomposition and bio-degradation in warm conditions, leading to floc breakage rather than formation. Only the cold-stored samples in week 2 showed a large increase in $D_{50}$ compared to week one (201-292%, depending on stirrer speed), which could be caused by an unusually large microbiological presence in this specific sample.

### 2.3.5 | Required measurement time for a representative PSD

Figure 2.7 shows an example of the Monte Carlo bootstrap analysis for six samples. With an increasing number of measurements, the deviation of the minimum and maximum $D_{50}$ (and hence the possible range of outcomes) from the mean $D_{50}$ value obtained for the total population decreased exponentially. After a certain threshold, adding more measurements results in only a minor decrease in the statistical uncertainty (Figure 2.7b, d). This threshold defines the minimum amount of measurements (time) that are needed to obtain a statistically representative $D_{50}$. The threshold (threshold 1) measurement time is indicated with the vertical line, and is achieved when the smoothed slope of the minimum and maximum deviation from the actual mean reaches a slope lower than 0.005.

For all three thresholds, the required measurement time increases if the median particle size $D_{50}$ increases, and if the span value $SV$ increases (Figure 2.8). Samples which are characterised by a low $D_{50}$ but a high $SV$, or the other way around, require generally less measurement time to reach the threshold. The threshold of 5% deviation from the actual mean is the strictest threshold, which is mostly sensitive to $SV$ (Figure 2.8). The finding that larger grain sizes require longer measurement time, is also found by Topping et al. (2011). They compared point-measurements of SPMC to sequential SPMC measurements, and found that errors in suspended particulate sediment concentration measurements are induced by inadequate time-averaging (i.e., a too short measurement time). These errors were positively correlated with grain size, therefore they recommended to average over at least 60 seconds. To explore the robustness of the relation between sediment characteristics and required measurement time in our data, the required measurement times of all in situ and ex situ samples were calculated.

The impacts of the measurement method (in situ or ex situ), $D_{50}$, $SV$, and modality are summarised in Table 2.2. Regardless of the threshold, in situ, bi- or multi-modal samples with a large $D_{50}$ and $SV$ required longer sampling times. However, these PSD characteristics are interrelated. For example, the percentage of field samples that is classified as wide, large, and bimodal is 70, 68, and 60%, respectively. Similarly, only 18% of the samples are classified as wide and small, and 15% as wide and bimodal. We performed an ANOVA analysis (Supplementary Materials, Text S1 and Figures S12, S13) to determine the relative importance of PSD characteristics on the required measurement time. The required measurement time primarily depends on

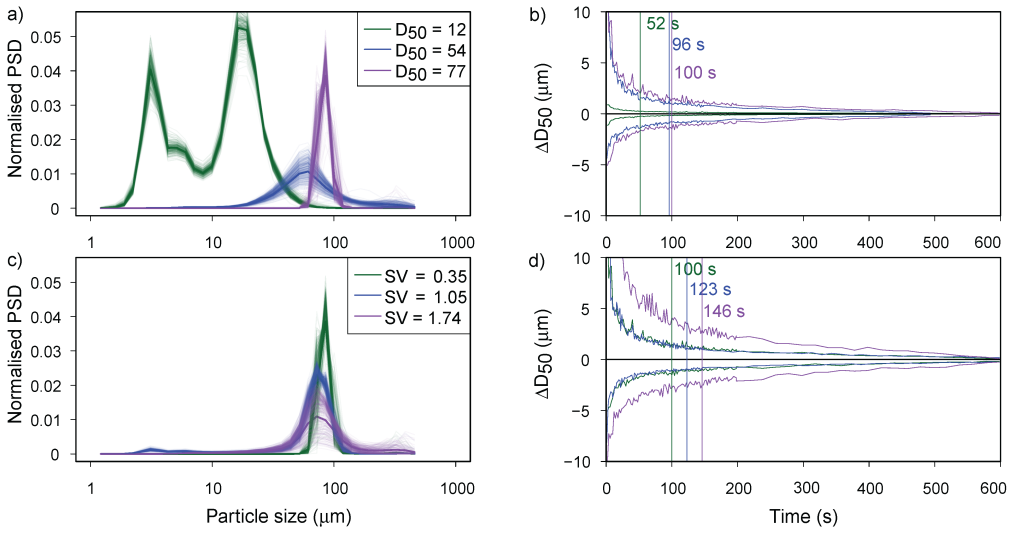


**Figure 2.7** | Example of the Monte Carlo bootstrap analysis to determine measurement time requirements. Panels a and c show examples of particle size distributions (PSDs) of individual measurements, with the average distribution indicated by the thicker line. The PSDs have different values of both $D_{50}$ (a) and *SV* span values (c). Panels b) and d) show the corresponding measurement time requirement (in seconds) calculated from the Monte Carlo bootstrap analysis, for the threshold slope = 0.005. The threshold is reached at the vertical line in the corresponding colour.

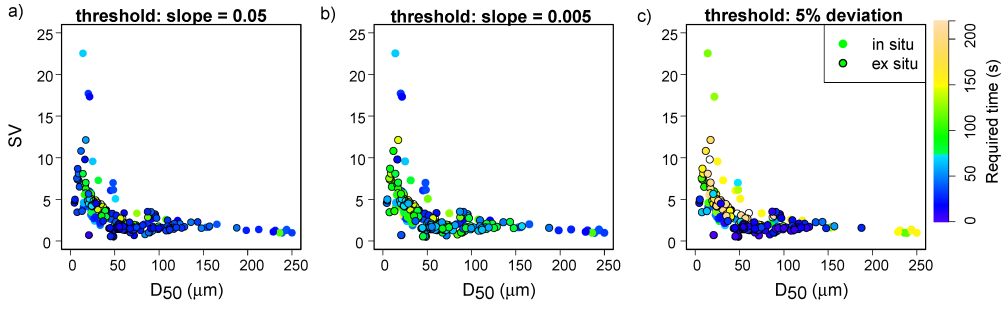


**Figure 2.8** | The relation between median particle size ($D_{50}$), span value (*SV*), and required measurement time (colours), for three different thresholds (a-c). Ex situ samples are indicated with a black circle. For the original data set source (Table 2.1), see Supplementary Figure S15.

measurement method (in/ex situ) for thresholds 1 and 3, and the interaction between the measurement method and $D_{50}$ for threshold 2. Other important variables were the interaction between $D_{50}$ and bimodality (threshold 1), the interaction between $SV$ and $D_{50}$ (threshold 2), the interaction between $SV$ and measurement method (in/ex situ) (threshold 2 and 3), and $SV$ (threshold 3).

The relation between measurement method, SV, bimodality, and measurement time can be understood intuitively. In situ samples show higher temporal variability than their ex situ equivalents, thereby increasing the required sampling time. Similarly, wide and bimodal distributions are more variable, and a longer sampling time is needed to remove the effect of this variability. By approximately knowing the character of the samples, the sampling time can be tailored to a research area. The fact that similar samples have similar characteristics (i.e. most field samples have a wide, bimodal distribution; Table 2.2), can be used in our favour, since only one of the characteristics has to be known to make an estimation of the required sample times. Samples with flocculated particles often have a wider, coarser, and more bimodal distribution compared to the non-flocculated equivalents. This means that the presence of flocs increases the sampling time required.

**Table 2.2** | Measurement time requirements (median, mean, and max) for different types of samples (including their number) and the three thresholds (slope = 0.05, slope = 0.005, and 5% deviation). Samples characterised as 'large', are samples with a $D_{50}$ that is larger than the population median. The opposite is true for samples characterised as 'small'. Samples with a 'narrow' PSD are characterised by an $SV$ that is smaller than the population median, the opposite is true for samples with a 'wide' PSD. # > th indicates the number of samples for which the threshold is not reached.

| Sample type (#) | Threshold (th) | | | | | | | | |
|---|---|---|---|---|---|---|---|---|---|
| | slope = 0.05 | | | slope = 0.005 | | | 5% deviation | | |
| | median (mean) (s) | max (s) | # > th | median (mean) (s) | max (s) | # > th | median (mean) (s) | max (s) | # > th |
| Ex situ (83) | 33 (45) | 158 | 2 | 59 (67) | 172 | 2 | 29 (66) | 186 | 6 |
| In situ (150) | 57 (61) | 154 | 3 | 64 (70) | 179 | 3 | 121 (117) | 217 | 6 |
| Small (116) | 32 (43) | 153 | 1 | 64 (67) | 179 | 1 | 30 (60) | 217 | 6 |
| Large (117) | 47 (58) | 158 | 4 | 80 (83) | 172 | 4 | 108 (108) | 212 | 6 |
| Narrow (117) | 31 (39) | 153 | 0 | 65 (67) | 172 | 0 | 20 (45) | 217 | 3 |
| Wide (116) | 52 (62) | 158 | 5 | 80 (83) | 179 | 5 | 135 (126) | 214 | 9 |
| Unimodal (139) | 33 (43) | 153 | 0 | 66 (69) | 160 | 0 | 29 (59) | 214 | 4 |
| Bi- and multimodal (94) | 50 (63) | 158 | 5 | 78 (83) | 179 | 5 | 130 (123) | 217 | 8 |

The recommended sampling time can serve as a baseline for the design of in situ monitoring protocols, or as an indication for the initial design of an ex situ measurement campaign. Especially for in situ measurements, resources (time, costs, battery duration) are limited, and sampling time should be minimised as much as possible. The obtained sampling times can help optimise time and resource allocation in data collection. Minimising sampling time means a higher spatial resolution can be obtained if time is no constraint.



When implementing this strategy in future research, one should be aware that the required measuring time is an indication, and may be system specific. Therefore, the same Monte Carlo bootstrap analysis method should be adopted in other systems independently. When a few samples with relatively long sampling times are taken, the bootstrap analysis can determine the sampling time needed in that specific system. Furthermore, the analysis can also be used to optimise the measurement time for other statistical parameters describing the PSD, such as $D_{10}$ or $D_{90}$. The procedure itself can be adjusted to the researcher's needs. The choice of threshold, which determines the time needed to obtain a representative number of measurements, is dependent on the required accuracy of the study. Additionally, if there is a need for higher spatio-temporal resolution, outlier reduction in post-processing can be considered. We tested this by excluding PSD outliers when calculating the $D_{50}$. An outlier is defined as the 95-percentile of the worst correlating individual samples, determined with cross-correlation. This decreased the averaged sampling time by 2 seconds. Care should be taken when filtering outliers, since 'outliers' on the large side of the PSD spectrum could be flocculated particles.

### 2.3.6 | Implications and recommendations

The effects of storage and stirring when doing ex situ measurement of suspended (flocculated) particles should be considered carefully. The formation of flocs during storage is not neutralised by the destruction/deformation of flocs during stirring, and the PSD as measured has very little resemblance to the original in situ PSD. Ex situ measurements give reliable data only about PPs, after the right sampling treatment. When interested in the effective PSD, in situ measurements should be preferred. The drawbacks of in situ measurements are the non-controlled environment in which they are performed and the impact of bubbles and debris on the measurements. To account for this variability the sampling time needed to obtain a robust mean is longer for in situ than ex situ measurements. Additionally, the presence of the device slightly alters the water flow, the effect of which can be minimised by optimising the positioning of the device. When in situ measurements are logistically infeasible, ex situ measurements should take place right away after sampling, without allowing the sediments to settle (Phillips & Walling, 1995), which comes with its own challenges.

This analysis reveals great variability among $D_{50}$ estimates that are often considered equivalent. Values of $D_{50}$ depend on the measurement instrument (LISST, Mastersizer), the measurement method (in situ and ex situ) and the sampling manipulation (storage, stirrer speed). The variability has several consequences. First, this means that "The" particle size distribution does not exist, which can have serious consequences. For example, implementing an erroneous $D_{50}$ of only 50 $\mu$m (300 instead of 250 $\mu$m - a realistic error as shown in this analysis) in the sediment transport predictor of Ribberink (1998), results in an underestimation of the non-dimensionalised sediment bed-load transport of 26% (Supplementary Figure S14). Second, particle size measurements reported in one study cannot be directly compared with other studies. This stresses the need for accurate reporting of PSD measurement and analysis protocols. Unfortunately, a standard protocol to measure PSDs is lacking. The constant change and improvements of measuring instruments (e.g., from the LISST-100X to the LISST-200X, and from the Mastersizer 2000 to the 3000 edition) leads to the development of new protocols based on different assumptions. Those changes hamper the direct comparison of PSD measurements that were taken over the course of time. Especially for multimodal PSDs, such as PSDs characterising flocculated particles (Lee et al., 2012, 2014), there is a need for a standard that allows for better comparison between measurements with alternative devices.

## 2.4 | Summary and conclusions

Experiments were performed to acquire in situ and ex situ particle size distribution (PSD) measurements with a LISST-200X. The probe was used to measure in situ during the rising limb of a runoff event, when water samples were simultaneously taken. Those samples were stored under hot and cold conditions for 1 – 3 weeks and subsequently measured with a LISST in the laboratory (ex situ) using a measurement chamber and magnetic stirrer. Additionally, a Mastersizer-3000 was used to study the impact of higher stirrer speeds. From these experiments, we can conclude that:

- There is a difference between the $D_{50}$ of in situ and ex situ PSD measurements. The $D_{50}$ of samples measured ex situ are larger, due to the formation and/or growth of flocs during the first week of storage.
- Values of $D_{50}$ do not significantly change during the subsequent weeks of storage. The process of flocculation does not continue after the first week. Stabilisation of the material on the bottom possibly prohibits further floc growth, but may strengthen the flocs. This process is more pronounced in cold-stored samples, resulting in slightly larger flocs than in hot-stored samples.

- During ex situ measurements, the magnetic stirrer causes the flocs to break and/or coil. This reduces the $D_{50}$ value of the samples significantly, and has a larger effect than storage duration after the first week. A higher stirrer speed results in a lower value for $D_{50}$. This was also visible in the measurements with the Mastersizer, where further stirrer speed increases results in even lower values of $D_{50}$. Adding ultrasonic vibrations disperses the flocs even more, thereby decreasing the $D_{50}$.

- It was impossible to return ex situ samples to their original, in situ, state, despite the fact that stirring effectively decreased floc size. Therefore, we recommend in situ measurements if the effective PSD is to be acquired. Ex situ measurements are only useful for obtaining the PSD of primary particles.

- The Monte Carlo bootstrap analysis shows that the PSD measurement time required to obtain a consistent and accurate value for $D_{50}$ primarily depends on the measurement methodology (in or ex situ). Furthermore, the median grain size, the span value, and the modality are important, confirming previous research.

- The variability during in situ measurements is higher than in controlled laboratory conditions, requiring a longer measuring time for a robust estimate of the median grain size. The average measurement time was 45 seconds for ex situ samples, and 61 seconds for in situ samples, for a threshold of slope = 0.05. The other tested thresholds were stricter, resulting in measurement times of up to 217 seconds.

*Dear bedforms,*
*I flooded the lab*
*Only to study*
*your spectacular shapes*
*It was worth it*

# 3

# Dunes in mixed sediment

This chapter is under review as:

de Lange, S.I., Niesten, I., van de Veen, S., Baas, J.H., Lammers, J., Waldschläger, K., Boelee, D., Hoitink, A.J.F. Fine sediment in mixed sand-silt environments impacts bedform geometry by altering sediment mobility. Under review by Water Resources Research.
DOI: 10.22541/essoar.170595144.49167925/v1

## Abstract

Geometric characteristics of subaqueous bedforms, such as height, length and leeside angle, are crucial for determining hydraulic form roughness and interpreting sedimentary records. Traditionally, bedform existence and geometry are predicted with phase diagrams and empirical equations, primarily based on uniform, cohesionless sediments. However, mixtures of sand, silt and clay are common in deltaic, estuarine, and lowland river environments, where bedforms are ubiquitous. The exact influence of these mixed sediments on bedform dimensions remains unknown. Here, we investigate the impact of fine sand and silt in sand-silt mixtures on bedform geometry, based on laboratory experiments conducted in a 14.4 m long tilting, recirculating flume. We systematically varied the content of sand and silt for different discharges, and we utilised a UB-Lab 2C (a type of acoustic Doppler velocimeter) to measure flow velocity profiles. The final bed geometry was captured using a line laser scanner. Our findings reveal that the response of bedforms to an altered fine sediment percentage is ambiguous, and depends on several factors, including bimodality-driven bed mobility and sediment cohesiveness. When fine, non-cohesive material (fine sand or coarse silt) is mixed with the base material (medium sand), the hiding-exposure effect comes into play, resulting in enhanced mobility of the coarser material and leading to an increase in dune height and length. However, the addition of weakly-cohesive fine silt reduces the mobility, suppressing dune height and length. Finally, in the transition from the dune regime to upper stage plane bed, the bed becomes unstable and bedform heights vary over time. The composition of the bed material does not significantly impact the hydraulic roughness, but mainly affects roughness via the geometry of the bedforms, especially the leeside angle.

## 3.1 | Introduction

River bedforms are ubiquitous in lowland rivers, and they are known to impact the river by altering its hydraulics, ecology, and sediment balance. The geometry of river bedforms, especially dunes, impacts the fairway depth (ASCE Task Force, 2002; Best, 2005), adds to the form roughness of the river bed (Warmink et al., 2013; Venditti & Bradley, 2022), and determines suitable foraging places for fish (Greene et al., 2020). It is therefore useful to predict the geometry of bedforms without having to perform regular field measurements. In non-supply limited conditions, river dunes may scale with flow depth (Allen, 1978). However, more recent studies have reinstated the observations by Yalin (1964), van Rijn (1984), and Karim (1995), indicating a relation between bedform geometry and some measure of transport stage (Bradley & Venditti, 2019; Venditti & Bradley, 2022), where transport stage represents the ratio between flow strength and the mobility of the bed material. Dune length increases with transport stage, while dune height increases with transport stage until a maximum is reached, whereafter the height decreases and the bedforms start to wash out (Baas & de Koning, 1995; Bradley & Venditti, 2019). This framework effectively predicts dune height and length, despite considerable variability, which can be up to two-orders of magnitude (Bradley & Venditti, 2017). This variability may in part be attributed to the influence of bed composition on bedform geometry.



The bed composition, i.e. the grain size distribution of the bed sediment, is one of the primary determinants for bedform existence and size. Measures of grain size appear in almost all existing phase diagrams (Southard & Boguchwal, 1990; van den Berg & van Gelder, 1993; Perillo et al., 2014), with the median grain size $D_{50}$ as general parameterisation. However, this simplification poses challenges when dealing with natural sediment mixtures characterised by complex, multimodal sediment size distributions, which are common in deltaic, estuarine and coastal environments featuring sediment mixtures of mud (i.e. clay and silt) and sand (Healy et al., 2002).

Recent research has focused on understanding how cohesive clay affects bedform geometry. It has been observed that even a small percentage of cohesive clay in sand-clay mixtures can effectively suppress bed mobility, resulting in a reduced bedform height (Schindler et al., 2015; Parsons et al., 2016) and limited bedform growth (Wu et al., 2022a). It is, however, unknown what the impact of non- and weakly cohesive fine materials (silts and fine sands) is on dune morphology, despite their abundance in downriver environments.

A few studies explored the influence of silt on erodibility of the sediment bed. For instance, Bartzke et al. (2013) examined the behaviour of sand (300 $\mu$m)-silt (50 $\mu$m) beds in an annular laboratory flume. They found that an increasing silt content, even at low percentages (as little as 0.18% silt), contributed to bed stabilisation through a

reduction in water inflow, attributed to pore-space plugging by silt. Yao et al. (2022) also reported increased stability (i.e., increased erosion threshold) with increasing silt content in their laboratory experiments, although stabilisation only occurred at a silt content of >35%, when a stable silt skeleton could be formed. Opposing Bartzke et al. (2013), a change in bed stability was not observed at lower silt contents. Additionally, Ma et al. (2017, 2020) studied a silt-rich sediment bed ($D_{50}$ = 15 - 150 $\mu$m) with low dunes in the Yellow River. Ma et al. (2020) showed that the presence of fine sediment (silt) led to a shift from a low-efficiency sediment transport regime (following the Engelund-Hansen equations (Engelund & Hansen, 1967)) to a high-efficiency regime. The high-efficiency regime prevailed for sediment beds with a medium grain size smaller than 88 $\mu$m, and, in the transitional range (88 $\mu$m < $D_{50}$ < 153 $\mu$m), the existence of this regime depended on sorting of the material ($\sqrt{D_{84}/D_{16}}$). They argued that the shift from a low- to a high-efficiency transport regime resulted from the transition from mixed load to suspended sediment transport, caused by the presence of silt.

Yet, none of these studies discussed the potential impact of silt content on bedforms. This is an important research gap, because an increase in bed stability, as observed by Bartzke et al. (2013) and Yao et al. (2022), could theoretically reduce bedform formation and growth due to a decrease in sediment transport, whilst Ma et al. (2020)'s suspension-load dominated high-efficiency regime would also mean suppression of bedform formation and growth, but then because bedload transport gets increasingly replaced by suspended load transport, which is incapable of forming bedforms. Clearly, the effect of silt in sand-silt mixtures on the resulting bedform geometry is largely unexplored. Therefore, our research seeks to address the following question: What is the influence of the fraction non-cohesive and weakly cohesive fine sediment in sand-silt mixtures on the dynamic equilibrium bedform geometry and the resulting hydraulic roughness?

To answer this question, we conducted 51 laboratory experiments in a recirculating flume, in which the influence of fine sand and silt percentage in sand-silt mixtures on bedform geometry was studied. For three flow velocities, 17 different sediment mixtures, largely falling within the studied range of Ma et al. (2020), were tested by systematically mixing various fractions of fine sand, coarse silt and fine silt with a coarser base material of medium sand. These experiments allowed us to assess how different sizes of fine sediment in a sand-silt mixture affect the transport stage and the resulting bedform geometry under different flow conditions. In the following sections, we provide a detailed description of the experimental setup, after which we discuss the different equilibrium bedform geometries that resulted from the experiments. We argue that the hiding-exposure effect enhances the mobility of the coarser fraction, whereas cohesion from fine silt decreases the bed mobility, leading to deviations from the expected relationship between transport stage and bedform dimensions.

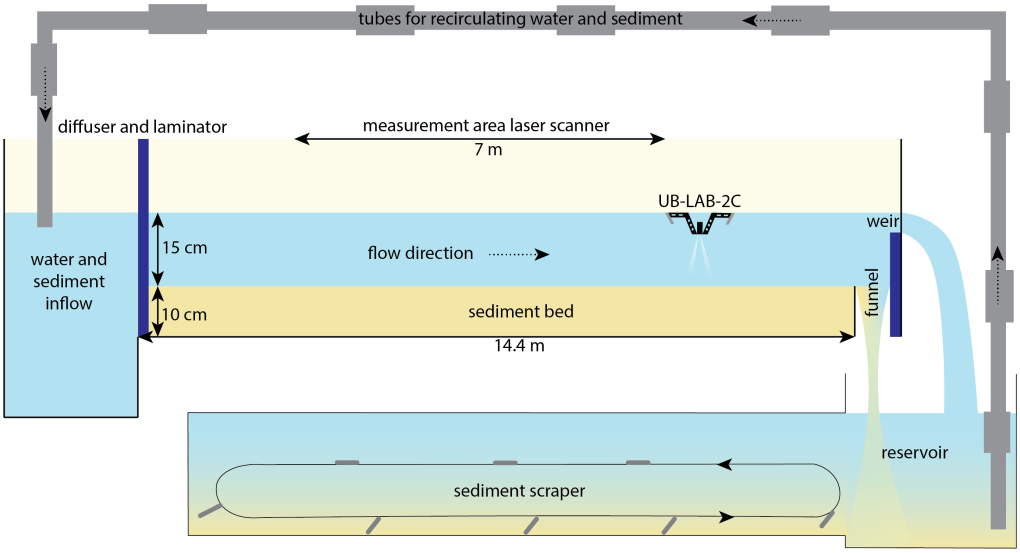


**Figure 3.1** | Schematic drawing of the experimental setup. The flume recirculates both water and sediment.

## 3.2 | Methods

### 3.2.1 | Experimental setup

The experiments were conducted in a tilting flume with recirculation facilities for both water and sediment in the Kraijenhoff van de Leur Laboratory for Water and Sediment Dynamics of Wageningen University and Research (Figure 3.1 and 3.2). The flume has an internal width of 1.20 m, a length of 14.4 m, and a height of 0.5 m. The water level is controlled by adjusting a downstream weir. A diffuser (Figure 3.2a) at the upstream part ensures that the inflow is distributed over the entire width of the flume. The diffuser is followed by a stacked pile of PVC tubes that serve as a laminator, suppressing turbulence at the inflow section. At the end of the flume, a funnel was installed to channel bedload material to a lower reservoir (Figure 1), and to prevent deposition in front of the weir. A continuously running sediment scraper ensures that the sediment stays in suspension in the lower reservoir, upon being pumped back to the inflow of the flume. At the end of one experiment (35% fine sand, medium discharge) the sediment funnel was clogged and the sediment was not fully recirculated. This run was excluded from the analysis.

The flow depth was set to 15 cm, measured from the initial flat sediment bed, and it was kept the same for all experimental runs by adjusting the weir height. The slope was set to 0.01 m $m^{-1}$. Experimental runs were performed for different discharges (low: 45 L $s^{-1}$; medium: 80 L $s^{-1}$; high: 100 L $s^{-1}$), to be able to distinguish

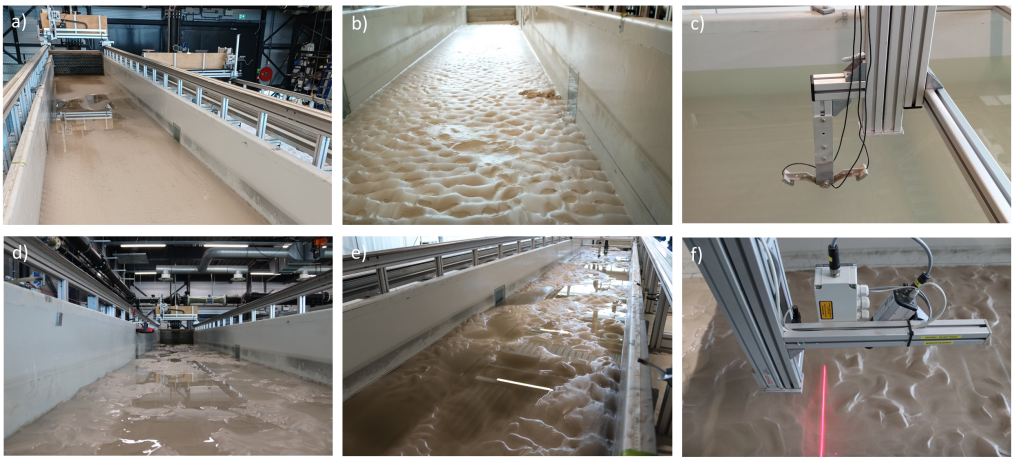


**Figure 3.2** | Pictures of the laboratory flume and the instrumentation. a) Flume with flatbed, facing upstream, including the upstream-located diffuser. b) Bed covered with small bedforms, facing downstream, including the downstream-located weir. c) UB-Lab 2C flow velocity profiler. d) Dune-covered bed, facing upstream. e) Dune-covered bed, facing downstream, with the UB-Lab 2C in background. f) Line laser scanner.

the effects of different transport stages on bedform morphology. The discharge was monitored and regulated with an electromagnetic flow meter. The corresponding calculated width- and depth-averaged flow velocities were 0.25, 0.44 and 0.56 m $s^{-1}$, the corresponding depth-averaged flow velocities in the middle of the flume (measured with an UB-Lab 2C, see Section 3.2.2) were slightly larger due to a side-wall effect (0.30, 0.45 and 0.58 m $s^{-1}$, respectively). The experiments were run for 12, 5 and 3 hours for the low, medium, and high discharges, respectively. Based on the ripple size predictor of Soulsby et al. (2012), the medium-sand ripples formed in the low-discharge experiments reached about 80% of their equilibrium height and length after 12 hours. Their planform at this development stage was linguoid, which agrees with the planform predicted by ripple development model of Baas (1999). Naqshband et al. (2016) studied the dune equilibrium time for medium sand (290 $\mu$m). Their equilibrium dimensions were reached after 3 hours for the experiments with a flow velocity of 0.64 m $s^{-1}$ and after 1.5 hours for 0.80 m $s^{-1}$. This suggests that the dunes formed at medium and high discharges in the present experiments reached equilibrium size.

The flow was sub-critical and turbulent during all experiments, determined by the Froude number, $Fr$ (-), being smaller than 1 (0.30, 0.54 and 0.69, respectively) and the Reynolds number, $Re$ (-), being larger than 4000 (38000, 67000, 83000, respectively), calculated with:

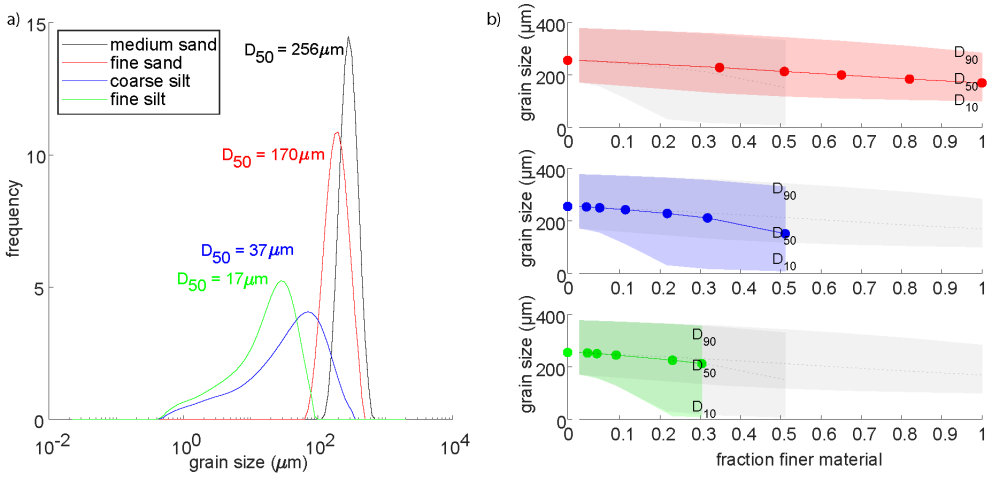


**Figure 3.3** | a) Grain-size distributions of the sediments used in the experiments. b) $D_{10}$, $D_{50}$ and $D_{90}$ of the tested mixtures, in which the finer material (fine sand, coarse silt or fine silt) is mixed with the base material (medium sand).

$$Fr = \frac{u}{\sqrt{gh}} \tag{3.1}$$

$$Re = \frac{hu}{\nu} \tag{3.2}$$

where $u$ is the time and depth-averaged flow velocity (m $s^{-1}$), $g$ is the gravitational acceleration (9.81 m $s^{-2}$), $h$ is the water depth (0.15 m), and $\nu$ is the kinematic viscosity ($m^2$ $s^{-1}$), which is weakly dependent on water temperature, $t$ (°C), as $\nu = 4 * 10^{-5}/(20 + t)$. Here, $\nu$ = 1.05 * $10^{-6}$ $m^2$ $s^{-1}$ for 18 °C is used.

A sediment bed with a thickness of 0.10 m was applied, which consisted of a mixture of two grain sizes: a base sediment of medium sand (median size, $D_{50}$ = 256 $\mu$m), mixed with fine sand ($D_{50}$ = 170 $\mu$m), coarse silt ($D_{50}$ = 37 $\mu$m) or fine silt ($D_{50}$ = 17 $\mu$m) (Figure 3.3a and Supplementary Figure S1 for images of the sediment). All sediments were composed of silica ($SiO_2$). The particle size distribution of the original sediments was measured with a Mastersizer 3000 (Figure 3.3). The fine sand and coarse silt are non-cohesive, whereas the fine silt could be classified as weakly-cohesive (Wolanski, 2007), confirmed by visual observation of the sticky fine silt slurry and a significantly higher submerged angle of repose (40° instead of 30° for sand). No visible flocculation of the silt fraction occurred during the experiments.

The weight percentage of finer material mixed with the base material ranged from 0 to 100 wt% for fine sand, to 51 wt% for coarse silt (with 49 wt% medium sand) and to 30 wt% for fine silt (with 70 wt% medium sand). In total, 17 different mixtures were tested, which were all exposed to the low, medium and high discharge. In Table 3.1,

**Table 3.1** | Overview of the performed experiments. Seventeen different sediment mixtures were tested, in which the type and percentage of fine material relative to the coarse material (base material) varied per experimental run. Each experiment with a distinct mixture was conducted for low, medium and high discharge, resulting in 51 experiments. * the experiment with medium discharge was excluded from analysis because of clogging of the pumps.

| **experiment number** | **% fine / % coarse** |
|---|---|
| *base experiment* | |
| 1 | 0/100 |
| *experiments with fine sand* | |
| 2-4 | 35/65* |
| 5-7 | 51/49 |
| 8-10 | 65/35 |
| 11-13 | 82/18 |
| 15-18 | 100/0 |
| *experiments with coarse silt* | |
| 19-21 | 2/98 |
| 22-24 | 5/95 |
| 25-27 | 11/89 |
| 28-30 | 22/78 |
| 31-33 | 32/68 |
| 34-36 | 51/49 |
| *experiments with fine silt* | |
| 37-39 | 2/98 |
| 40-42 | 4/96 |
| 43-45 | 9/91 |
| 46-48 | 23/77 |
| 49-51 | 30/70 |

an overview of the experimental mixtures is given. The $D_{50}$ and 90th percentile, $D_{90}$, values of the mixtures hardly changed when adding finer material, but the 10th percentile, $D_{10}$, values dropped significantly when adding coarse or fine silt (Figure 3.3b).

### 3.2.2 | Instrumentation

A line laser and 3D camera (Figure 3.2f), equipped with Gigabit Ethernet (SICK, 2012), was used to scan the bed topography. The devices were mounted on a measurement carriage that moved on fixed rails along the flume. After every experimental run, the flume was slowly drained, and an area of 7 x 1 m was recorded in three parallel, partially overlapping, swaths, with a resolution of 0.1 mm. See de Ruijsscher et al. (2018) for a detailed description of the line laser scanner.

During the first and last 30 minutes of an experimental run, an UB-Lab 2C (UBERTONE) (Figure 3.2c) was deployed to measure flow velocity profiles. The UB-Lab 2C is an ADVP (acoustic doppler velocity profiler, e.g. Hurther & Lemmin 2001; Mignot et al. 2009), which measures a two-component velocity profile at high spatial (1.5 mm) and temporal resolution, here 10 to 15 Hz. An acoustic signal is transmitted along a

single beam and received by two receivers under different observation angles. The resulting 2-component vector is than projected to yield the 2-dimensional velocity in the streamwise direction ($u$) and vertical direction ($w$) along the beam (1D-profile). The emission frequency was set to 1 MHz with a bin size of 1.5 mm. The pulse repetition frequency ranged from 1200 to 1800 Hz for low and high discharge, respectively.

### 3.2.3 | Data analysis

#### 3.2.3.1 | Sediment characterisation

The behaviour of the sediment in the experiments was estimated from the span value of the sediment-size distribution and the dominant way of sediment transport. This information was later used to interpret the observed bedform patterns.



The span value of the tested mixtures was used as a measure of distribution width, and was defined as:

$$SV = \frac{D_{90} - D_{10}}{D_{50}} \tag{3.3}$$

The sorting was determined as:

$$\sigma_g = \sqrt{\frac{D_{84}}{D_{16}}} \tag{3.4}$$

To determine the dominant way of transport, the ratio between the settling velocity of a particle, $w_s$, and the shear velocity, $u^*$, was calculated. If this ratio is larger than 3, the dominant transport mode is expected to be bedload, and if the ratio is smaller than 0.3, the dominant mode is expected to be suspended load (Dade & Friend, 1998). In between these values, the transport mode is mixed.

The settling velocity of a particle was approximated with (Ferguson & Church, 2004; Dietrich, 1982):

$$w_s = \frac{\rho_r g D_{50}^2}{C_1 \nu + \sqrt{0.75 C_2 R g D_{50}^3}} \tag{3.5}$$

where $\rho_r$ is the relative submerged density = $(\rho_s - \rho_w)/\rho_w$, and $C_1$ = 18 and $C_2$ = 1 for natural grains (Ferguson & Church, 2004). The $D_{50}$ of the original sediments was used rather than the $D_{50}$ of the mixture, giving a transport mode for the base sediment and the finer fraction separately. This approximation was verified by visual observation through a window in the side of the flume.

#### 3.2.3.2 | Bedform geometry

Final bed configurations were determined from the bed elevation data obtained with the line laser scanner. Five longitudinal transects were constructed across the width of the flume, with an interspacing of 200 mm. The resulting transects served as input for the bedform tracking tool of van der Mark & Blom (2007), which gives bedform geometry based on specific detrending lengths, used to differentiate between bedform scales. Two bedform length scales were identified: $150 \pm 100$ mm (hereafter referred to as small bedforms), and $1100 \pm 400$ mm (referred to as large bedforms). Small bedforms were observed in the low-discharge experiments, whilst larger bedforms were observed in the medium and high-discharge experiments, and the bedform tracking tool was applied accordingly. Only if the bedform occurred in at least two profiles of a bed scan, bedform statistics were calculated.

Bedform characteristics (Figure 3.4) in this study included bedform height, $\Delta$ (m), the vertical distance between crest and downstream trough; bedform length, $\lambda$ (m), the horizontal distance between two subsequent crests; leeside angle, *LSA* (°), the slope angle derived from a linear fit of the bedform's leeside, excluding the upper and lower 1/6th of the bedform height; stoss side angle, *SSA* (°), calculated similarly to the leeside angle; and the slip face angle, *SFA* (°), the steepest part of the leeside, calculated as the 95th percentile of the distribution of angles along the leeside. The bedform roundness index, *BRI*, of the small bedforms was defined as the ratio between the length from the dune crest to the stoss side at 0.5 times the dune height ($\lambda_{0.5stoss}$) and the length of the stoss side ($\lambda_{stoss}$) (Perillo et al., 2014; Prokocki et al., 2022). A bedform was classified as rounded if $BRI \geq 0.6$. Finally, the bedform width, $W$ (m), was derived by constructing six cross-sectional profiles transverse to the flow, with an interspacing of 1000 mm. Next, the same bedform tracking tool was applied using the same settings as for the longitudinal profiles. The bedform width was calculated only for the low-discharge experiments, where the width of the bedforms was considerably smaller than the width of the flume.

#### 3.2.3.3 | Bedform geometry predictors

Various bedform geometry predictors were tested based on our data. The selected predictors for dune height and length included a measure of flow strength (van Rijn, 1984; Venditti & Bradley, 2022), and the predictor of Soulsby et al. (2012) was used for the height and length of ripples.

van Rijn (1984) developed an empirical dune height and length predictor, the former being dependent on the transport stage, $T_{vRijn}$, as measure of flow strength.

$$\Delta_{vRijn} = 0.11h\left(\frac{D_{50}}{h}\right)^{0.3}(1 - e^{-0.5T_{vRijn}})(25 - T_{vRijn}) \tag{3.6}$$

$$\lambda_{vRijn} = 7.3h \tag{3.7}$$

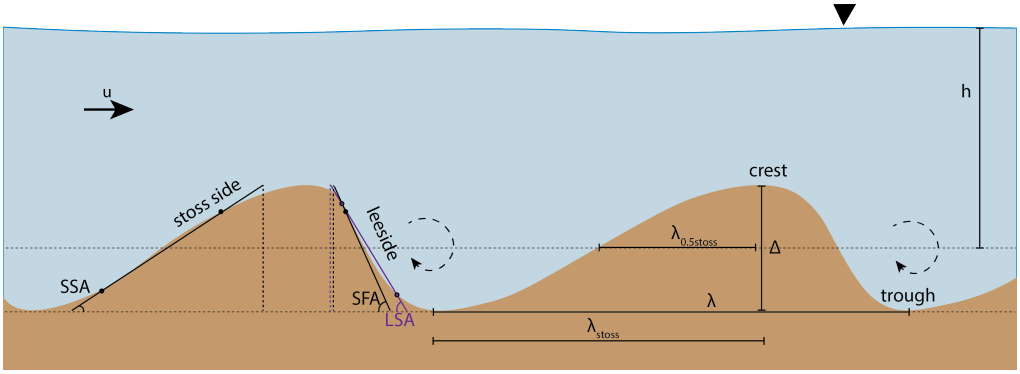


**Figure 3.4** | Definition of the bedform characteristics, showing the bedform height ($\Delta$), the length ($\lambda$), the total length of the stoss side ($\lambda_{stoss}$) and the length of the stoss side at 0.5*$\Delta$ ($\lambda_{0.5stoss}$), the leeside angle (*LSA*), in which the upper and lower 1/6th of the leeside is excluded, the stoss side angle (*SSA*), also excluding the upper and lower 1/6th of the stoss side, and the slip face angle (*SFA*), which is the steepest part (95th percentile) of the leeside. The steepest part of the leeside is indicated with a small purple marker, and the location of the upper and lower 1/6th of the lee and stoss side are indicated with a small black marker.



$T_{vRijn}$ depends on shear stress and critical shear stress. See Appendix 3A for a full explanation.

Venditti & Bradley (2022) developed an empirical equation based on a different transport stage, $T_{VB}$, defined as $\frac{\theta}{\theta_c}$, which is the ratio of the non-dimensionalised shear stress, $\theta$, and critical shear stress, $\theta_c$. The equations suitable for laboratory flows with a water depth less than 0.25 m are:

$$\Delta_{VB} = h\left(-0.00100(\frac{\theta}{\theta_c} - 17.7)^2 + 0.417\right) \tag{3.8}$$

$$\lambda_{VB} = h\left(0.0192(\frac{\theta}{\theta_c} - 8.46)^2 + 6.23\right) \tag{3.9}$$

The geometry of ripples is only dependent on a measure of grain size ($D^*$) and independent of transport stage (Baas, 1994, 1999). According to the equations of Soulsby et al. (2012), their geometry can be predicted with:

$$\Delta_{Souslby} = D_{50}202D^{*-0.554} \tag{3.10}$$

$$\lambda_{Soulsby} = D_{50}(500 + 1881D^{*-1.5}) \tag{3.11}$$

All definitions and symbols are given in Appendix 3A.

#### 3.2.3.4 | Roughness characterisation

Hydraulic roughness was estimated following two methods. Firstly, the measured velocity profiles were used, following the method of Hoitink et al. (2009). Secondly, an indirect hydraulic roughness predictor of van Rijn (1984) was used, based on bed geometry and sediment characteristics.

The first method is based on the Law of the Wall:

$$\frac{\overline{u}(z)}{u^*} = \frac{1}{\kappa} ln(\frac{z+h}{z_0}) \tag{3.12}$$

where $\overline{u}$ is the mean velocity (m $s^{-1}$), $\kappa$ = 0.4 is the Von Karman constant, $h$ is the mean water depth (m), $z$ is the height above the bed (m), and $z_0$ is roughness length (m).

For a water column that satisfies equation 3.12, i.e. where the velocity profiles are logarithmic (Supplementary Figure S3), the shear velocity can be determined from the slope of the velocity versus non-dimensionalised depth $\sigma_d$ (equation A3.10). This, in turn, can be used to derive roughness length and, ultimately, Manning's n, $n_{man}$ (s $m^{-1/3}$). See Appendix 3B for an elaborate definition. Experiments 13-18 were excluded from analysis, since erroneous mounting caused invalid profiles.

Roughness was also approximated indirectly based on the predictor of van Rijn (1984). The total predicted hydraulic roughness, expressed as friction factor, $\hat{f}$, results from form friction and grain friction (Einstein, 1950). The total hydraulic roughness was predicted as in van Rijn (1984):

$$\hat{f} = \frac{8g}{(18\log(\frac{12h}{k_s}))^2} \tag{3.13}$$

where $k_s$ is a measure of roughness both consisting of form roughness and grain roughness. See Appendix 3B for the corresponding equations.

Friction factor $\hat{f}$ can be converted to $n_{man}$ via (Manning, 1891; Silberman et al., 1963):

$$n_{man} = \frac{R_h^{1/6}}{\sqrt{\frac{8g}{\hat{f}}}} \tag{3.14}$$

where $R_h$ is the hydraulic radius, which is equal to the cross-sectional area $A$ divided by the wetted perimeter ($P$ = width + 2$h$).

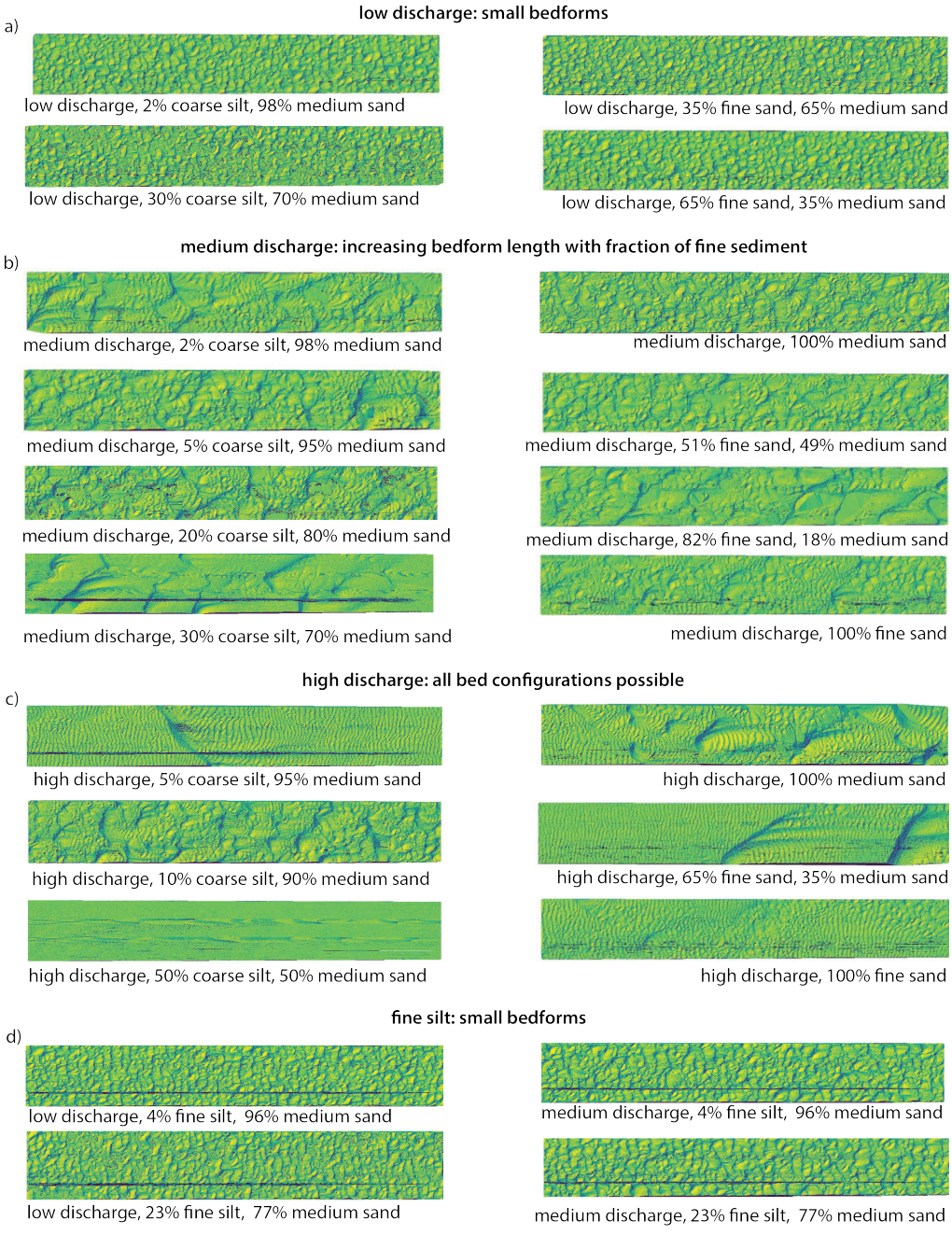


**Figure 3.5** | Dynamic equilibrium bed morphologies at the end of selected experiments. All images represent a 1 m wide and 7 m long section of flume. a) Bed morphologies at low discharge. b) Bed morphologies at medium discharge, showing increasing dune length with increasing finer material. c) Bed morphologies with large variability at high discharge. d) Impact of fine silt on bed morphology. Scans in (c) show small two-dimensional ripples superimposed on larger bedforms and flat beds. These ripples are artifacts caused by draining the flume over an almost flat bed (see Supplementary Figure S5 for verification).

## 3.3 | Results

### 3.3.1 | Observed bed geometries

The bed geometries in the experiments were dependent on discharge (Figure 3.5a-c, see Supplementary Figures S2-S4 for the bed geometry of all runs), and on the addition of fine material. Below, we show the results separately for low, medium and high discharge.

#### 3.3.1.1 | Low discharge bed geometries

At low discharge, only small bedforms appeared on the bed (Figure 3.5a). The small bedforms had an average height of 0.011 m, an average length of 0.12 m and a non-rounded shape with a slip face angle of 22°.

Bedform height and width both decreased with the addition of coarse silt and fine silt, which is especially pronounced at a silt percentage above 20% (Figure 3.6a). The bedform height decreased by 38% for coarse silt and 28% for fine silt compared to the experiment with pure medium sand. The corresponding decrease in length was considerably smaller (14% and 4%, respectively). This decrease in bedform height was not visible in the experiments with fine sand. Similarly, bedform width decreased by 11% and 23% for coarse and fine silt (Figure 3.6c), indicating that the bedforms became more three-dimensional in shape. The *LSA*, *SFA* and *BRI* of these bedforms were independent of the type and percentage of finer material added (Figure 3.6d-f) .

#### 3.3.1.2 | Medium discharge bed geometries

The bedforms generated during medium discharge were generally larger than those that emerged during low discharge, with an average height of 0.027 m, a length of 0.54 m, and a slightly lower slip face angle of 20°. Those bedforms followed two general trends. Firstly, the runs with an increasing amount of fine sand and coarse silt showed an increase in bedform height and length (Figure 3.5b). Especially for the coarse-silt runs, the increase in bedform length was considerable (Figure 3.7b). The bedform length in these runs was on average 0.59 m for the experiments with 20% coarse silt or less, and increased to 1.1 m for the experiments with a higher coarse-silt percentage in the bed. This increase in bedform length was accompanied by a smaller increase in bedform height from 0.032 m to 0.043 m (Figure 3.7a). Bedform heights and lengths for the experiments with fine sand were smaller than for the experiments with coarse silt (on average $\Delta$ = 0.026 m and $\lambda$ = 0.54 m for fine sand, and $\Delta$ = 0.035 m and $\lambda$ = 0.73 m for coarse silt). The lee-face angles varied per experiment, but the slip face angles remained relatively constant, lacking a consistent trend with increasing content of fine material (Figure 3.7c, d).

The experiments with fine silt revealed smaller bedforms that were larger than the bedforms in the low-discharge experiments, but comparable in planform (Figure 3.5d),

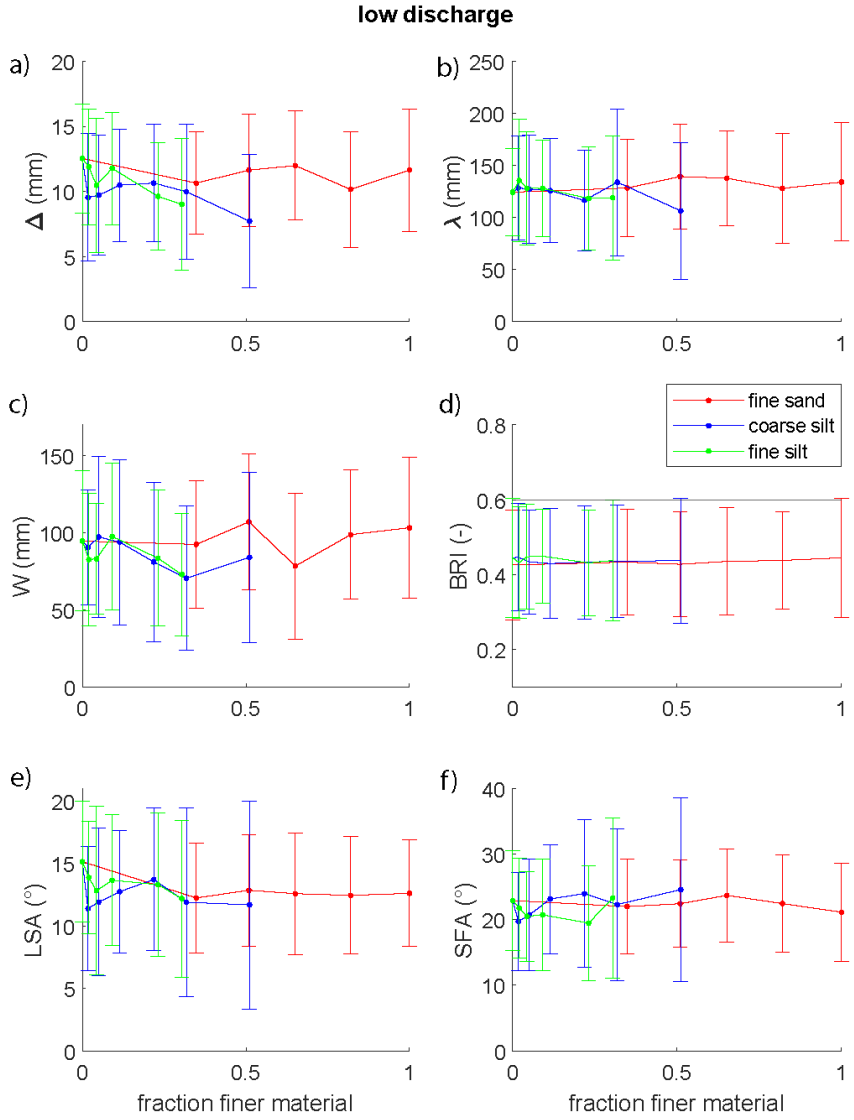


**Figure 3.6** | Bedform geometries at low discharge (45 L $s^{-1}$). a) Bedform height. $\Delta$. b) Bedform length, $\lambda$. c) Bedform width, *W*. d) Bedform roundness index, *BRI*, where $BRI < 0.6$ indicates non-rounded bedforms. e) Leeside angle, *LSA*. f) Slip face angle, *SFA*.

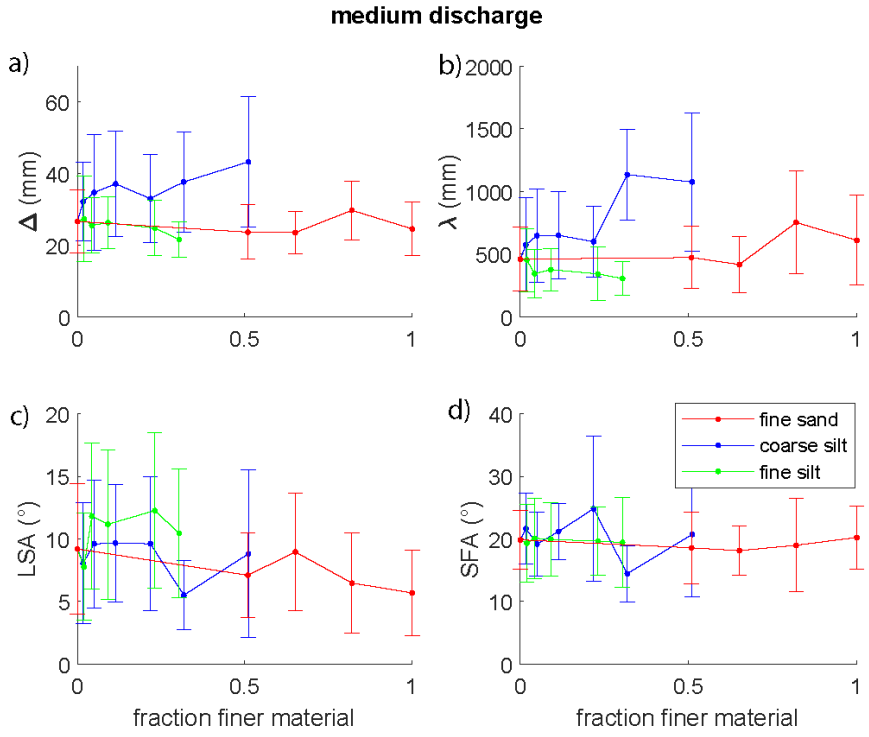


**Figure 3.7** | Bedform geometries at medium discharge (80 L $s^{-1}$). a) Bedform height, $\Delta$. b) Bedform length, $\lambda$. c) Leeside angle, *LSA*. d) Slip face angle, *SFA*.

despite the clear increase in depth-averaged flow velocity. The mean bedform length was 0.38 m, which is significantly smaller than for the experiments with fine sand and coarse silt. However, at 0.025 m, the mean bedform height is comparable to the runs with fine sand. A decrease in length and height was observed for the runs with 0 to 30% fine silt (23% decrease in bedform height, 51% decrease in bedform length). Leeside angles were 28% larger than in the experiments with fine sand and coarse silt, but the slip face angles were comparable.

#### 3.3.1.3 | High discharge bed geometries

The bedforms formed at high discharge were on average slightly larger than during medium discharge (Figure 3.8), with an average height of 0.029 m and length of 0.72 m. The slip face angle was 18°, which was slightly lower than at medium discharge. However, the geometrical parameters were highly variable, with a standard deviation of 1.6 cm, 39 cm, 4.6° for bedform height, length and slip face angle, respectively, and without a clear relationship with the amount of fine material. The experiments with fine silt resulted on average in shorter bedform lengths and higher leeside angles than the experiments with coarse silt and fine sand, which agrees with the observations at medium discharge.

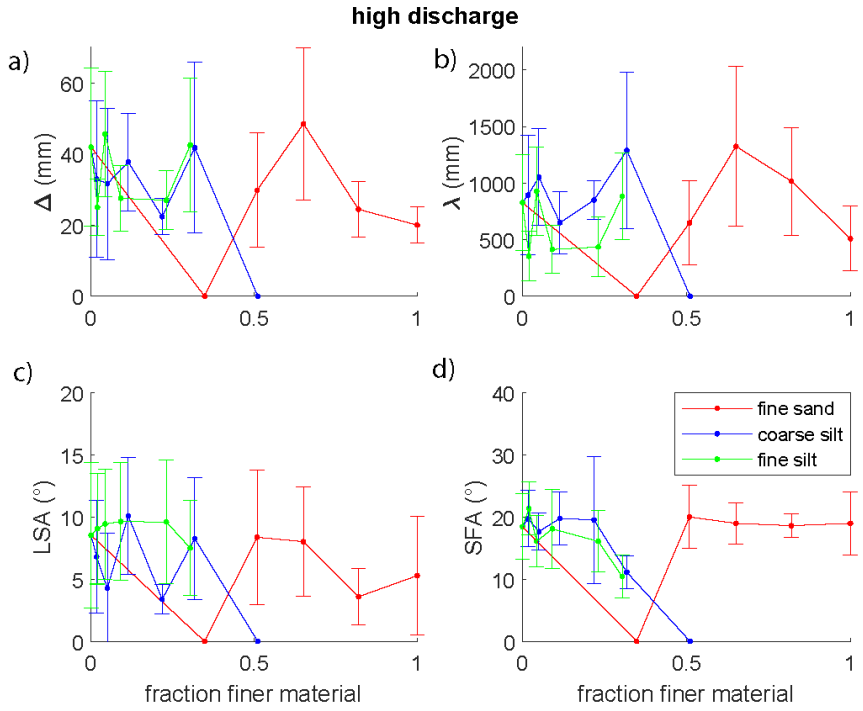


**Figure 3.8** | Bedform geometries at high discharge (100 L $s^{-1}$). a) Bedform height, $\Delta$. b) Bedform length, $\lambda$. c) Leeside angle, LSA. d) Slip face angle, SFA. Zero values indicate a flat bed.

The high discharge experiments were conducted close to the suspension threshold ($w_s$ / $u^* < 0.3$), and the bedforms started to wash out towards upper stage plane bed, when three alternating bed states were observed (Figure 3.5c): an almost flat bed with one or two large, steep bedforms; a bed covered with dunes; and a flat bed.

### 3.3.2 | Bedform variability

Relationships between bedform geometry and transport stage, $\theta/\theta_c$, are evident from the experimental data. Bedform length increased, and leeside and slip face angle decreased with increasing transport stage, whereas the relationship between bedform height and transport stage approached a parabola (Figure 3.9a-d). Additionally, the variability in bedform geometry increased with increasing transport stage, indicated by the grey shaded band in Figure 3.9a-d.

The near-bed velocity $U_{0.2}$, which is the time-averaged velocity at the non-dimensionalised height above the bed of $\sigma_d$ = 0.2 and directly measured with the UB-Lab 2C, is a representation of the near-bed conditions influencing and being influenced by the bed geometry. The near-bed velocity shows a strong relation with the dimensionless bedform length ($R^2$ = 0.66) (Figure 3.9e).

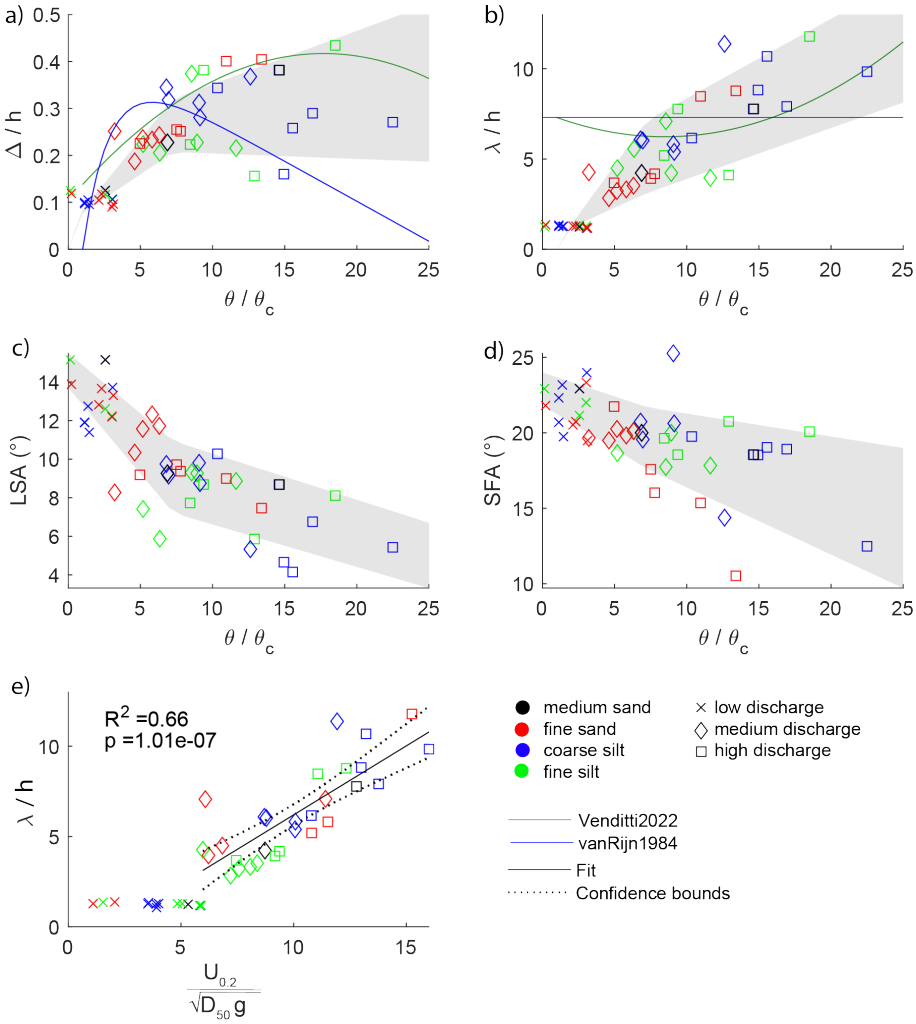


**Figure 3.9** | Increasing variability in bedform geometry with increasing flow strength, expressed as transport stage ($\theta/\theta_c$) in (a-d) and as non-dimensionalised velocity at 20% above the bed in (e). a) Bedform height divided by water depth. b) Bedform length divided by water depth. c) Leeside angle. d) Slip face angle. e) Bedform length divided by water depth. Grey shading indicates one standard deviation from the mean value, in which the standard deviation is calculated from all bedforms in either low, medium or high discharge experiments. The base runs are indicated with black markers (medium sand). In (a) and (b), the predicted values by Venditti & Bradley (2022) and van Rijn (1984) are shown.

The bedform height and length predictions for dunes based on van Rijn (1984) and Venditti & Bradley (2022) are shown in Figure 3.9a and b. For the low-discharge runs, these predictions overestimate the measured bedform dimensions significantly. However, the ripple predictor of Soulsby et al. (2012) performs relatively well, with root-mean-square errors of 0.001 m for height and 0.02 m for length. The bedforms can therefore be classified as ripples. For the medium and high discharge runs, the Soulsby et al. (2012) equation for ripples underpredicts the bedform size significantly. These bedforms are therefore classified as dunes. The predictor of van Rijn (1984) performs reasonably well for medium transport stages, but it mostly underpredicts bedform heights for high transport stages. The predictor of Venditti & Bradley (2022) slightly overpredicts bedform height, but the measured values are still within their margins of error. The bedform length predictor of van Rijn (1984), which is purely based on water depth, does not capture the trend of increasing dune length with increasing transport stage. The predictor of Venditti & Bradley (2022) largely overestimates bedform length for medium transport stages, but performs better for the high transport stages by capturing the observed increase in length.



### 3.3.3 | Hydraulic roughness

Hydraulic roughness, expressed as the depth-independent Manning's n and calculated via the Law of the Wall based on the velocity profiles (equation 3.12), averaged 0.038 s $m^{-1/3}$. Manning's n increased with increasing leeside angle ($R^2$ = 0.31) and decreasing bedform length ($R^2$ = 0.40) (Figure 3.10c, d). The relation with leeside angle stands out (Figure 3.10c), since the ripples and dunes are both part of the linear correlation, whereas no relation between ripple length and roughness was observed. Generally, the roughness was larger during the experiments with fine silt (Figure 3.10) and the experiments with a rippled bed (on average 0.039 s $m^{-1/3}$). The larger roughness is likely to be related to the relatively high leeside angle of the bedforms observed in those experiments.

Counter-intuitively, hydraulic roughness does not exhibit a statistically significant relationship with dune height and the fraction of added finer material (Figure 3.10a, b). The lack of a relationship with added fine material is consistent with the roughness predictor of van Rijn (1984), which differentiates between skin friction, related to grain size, and form friction, related to bedform size. According to this predictor, on average, 97% of the total amount of friction is attributed to form friction in the experiments, indicating that bed composition is less important for hydraulic roughness than bedform geometry. The roughness predictor of van Rijn (1984) yields on average a Manning's $n$ of 0.030 s $m^{-1/3}$, which is 11% lower than the measured friction based on the Law of the Wall.

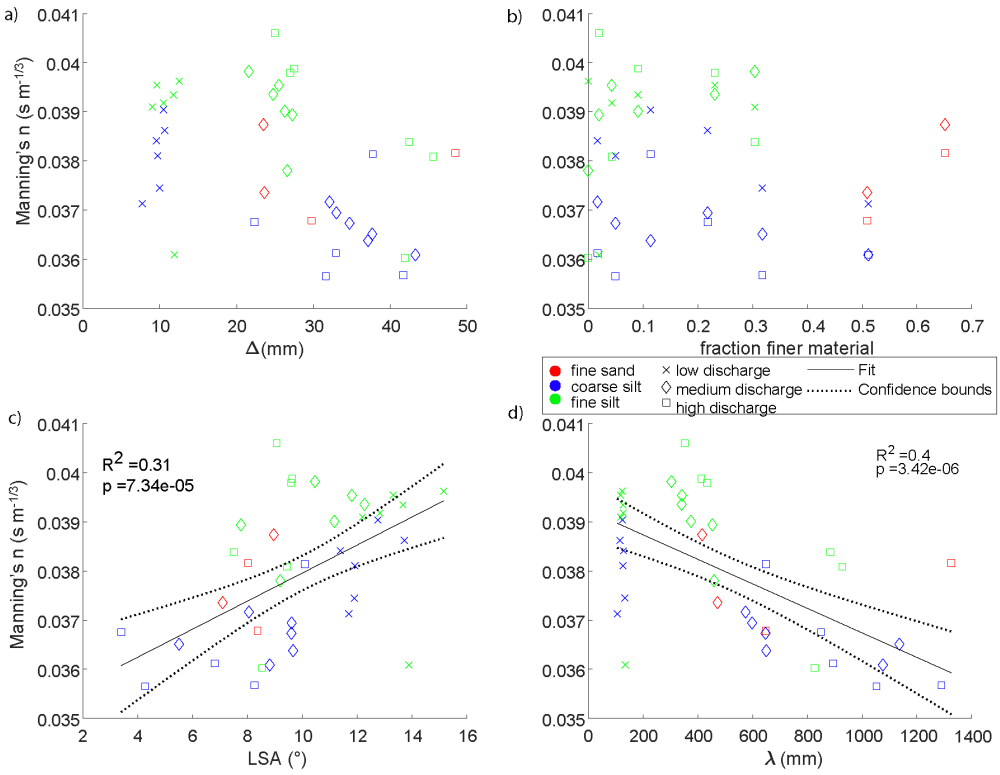


**Figure 3.10** | The relation between the hydraulic roughness $n_{man}$, calculated with the Law of the Wall, and a) Bedform height, $\Delta$. b) Fraction finer material within the base material. c) Leeside angle, *LSA*. d) Bedform length, $\lambda$. Significant linear relations are shown in c and d.

## 3.4 | Discussion

### 3.4.1 | A shift in transport stage due to addition of fines

The transport stage-based dune height predictor of Venditti & Bradley (2022) provides a way to visualise the experimental results and assess deviations from expected heights caused by the sediment mixtures (Figure 3.11). The predictor implies a parabolic relationship between bedform height and transport stage, as well as confidence levels for data variability (Bradley & Venditti, 2017). The parabolic relation can be interpreted as follows. As the transport stage increases, the transport mode changes from bed load to mixed load ($w_s$ / $u^*$ decreases), and dune height increases. This corresponds to our low and medium-discharge experiments. As the transport stage increases further, bedforms start to become washed-out, thus reducing the bedform height. This corresponds to our high-discharge experiments (Yalin, 1972; Naqshband et al., 2014a).

Although this framework is generally associated with a change in flow strength (Shields number, $\theta$), it can also be used to frame the experimental data using changes in sediment mobility (critical Shields number, $\theta_c$) caused by the addition of fine material to a coarser base sediment (Figure 3.11). During the medium-discharge experiments, adding non-cohesive fine sand and coarse silt led to an increase in dune height and length. When comparing this to the expected change based on the predictor of Venditti & Bradley (2022) due to a decrease in $D_{50}$ resulting from the addition of fine sediment, the change in bedform geometry was larger than expected. We attribute the increase in bedform size to an increase in mobility of the bed material (i.e. a decrease in $\theta_c$), leading to a larger change in transport stage (Section 3.4.2) than expected based on the change in $D_{50}$ (Supplementary Table S1). Therefore, adding fine, non-cohesive material leads to a shift to the right on the bedform height - transport stage diagram (Figure 3.11). In contrast, adding fine, weakly cohesive material to the bed decreases the mobility of the sediment (Section 3.4.3), and therefore decreases the transport stage, resulting in a decrease in bedform size, leading to a shift to the left on the diagram in Figure 3.11. Furthermore, the large variability in bedform geometry at the high transport stages is attributed to instabilities that occur when the system moves towards upper-stage plane bed (Section 3.4.4). Finally, the ripples formed at low discharge do not fit within the transport stage diagram, since ripple size is only dependent on grain size and not on flow velocity (Baas, 1994, 1999; Soulsby et al., 2012). Below, these changes are discussed in more detail.



### 3.4.2 | Impact of non-cohesive fine sediment (sand and coarse silt)

#### 3.4.2.1 | Hiding-exposure effect

During the medium-discharge experiments, we observed an increase in dune size with larger fractions of fine non-cohesive material (fine sand and coarse silt) mixed into the base material. This may be attributed to an increased mobility of the coarse sediment. In mixed sediments, differently sized grains interact with the flow and with each other in a different way than in equally sized sediments (McCarron et al., 2019), leading to selective entrainment. This is called the hiding-exposure effect, where small grains are hidden from the flow between the coarser grains. This does not only result in a more difficult mobilisation of the fines (hiding), but also in an increased mobility of the larger grains (exposure) (Einstein, 1950) (see Section 3.4.2.2).

The hiding-exposure effect is mostly dependent on the ratio between the fraction of interest $D_i$ (here, the coarse fraction) and the $D_{50}$. Hill et al. (2017) tested the influence of this ratio for gravel-sand mixtures. They found that if the two mixed sediments had similar grain sizes, ($D_{coarse} / D_{fines} < 2$), the bed aggregated without preferentially mobilising the coarser fraction, and the fines became part of the bed structure (Frings et al., 2008). For intermediate particle ratios ($2 < D_{coarse} / D_{fines} < 20$), the fine sediment filled or bridged the pores of the coarser base matrix, resulting in increased mobility

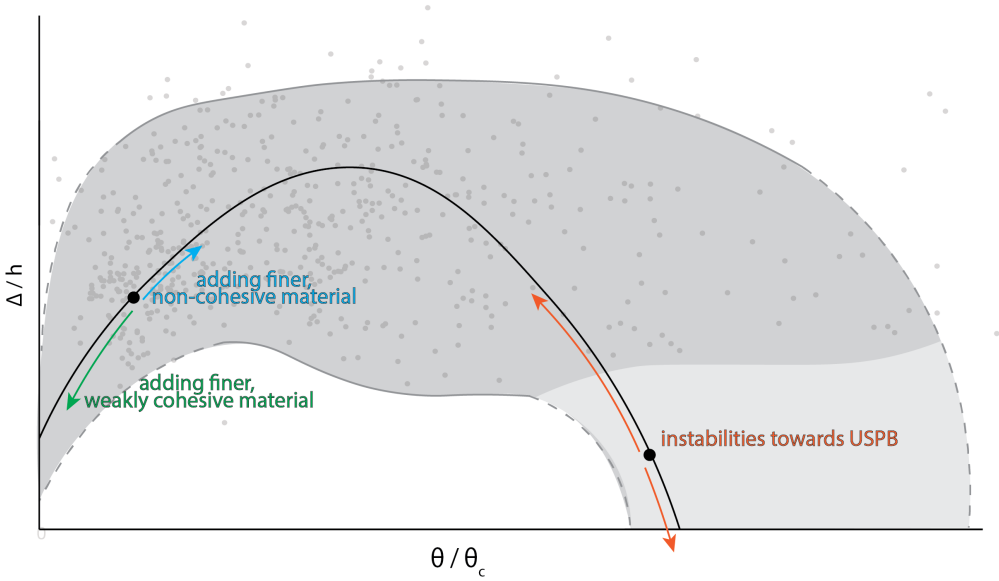


**Figure 3.11** | Conceptual diagram of non-dimensionalised dune height against transport stage, indicating the impact of adding non-cohesive and cohesive fine sediment to the bed material at relatively low transport stages, and the increased variability of bedform height due to flow instabilities at high transport stages. The dark grey shading indicates the 5 and 95th percentiles of data aggregated from Venditti et al. (2016) and Bradley & Venditti (2019). No data are available for the light grey shaded area. The dashed lines show the estimated course of the confidence intervals.

of the coarse fraction (Section 3.4.2.2). For large ratios ($D_{coarse}$ / $D_{fines}$ > 20), the fine sediment percolated through the base sediment. The subsurface became clogged, but the fines were not present in the surface layer, because all free fines were entrained and transported in suspension.

In the present experiments, the ratios between the coarse and fine fractions were 1.5, 6.9 and 15 for fine sand, coarse silt and fine silt, respectively. Following Hill et al. (2017), this implies that the fine sand aggregated the bed structure, whereas the coarse and fine silt bridged or filled the pores of the coarse fraction. For the silts, the hiding-exposure effect should have played a role, increasing the mobility of the coarse fraction, whereas, for the fine sand, the increased size distribution might have resulted in increased mobility of the entire sediment bed due to an increase in grain protrusion and a decreased friction angle (Kirchner et al., 1990; Buffington et al., 1992). However, this effect may have been smaller than the mobility increase caused by the hiding-exposure effect by coarse silt, which is indicated by the increased lengthening of dunes in a bed with coarse silt compared to fine sand. Increased mobility means an increased transport stage, hence an increased dune length (Section 3.4.1).

Various methods have been developed to correct the initiation of motion of sediments for the hiding-exposure effect (see McCarron et al. (2019) for a review). Generally, the correction factor lowers the critical Shields number, $\theta_c$, for the coarse fraction ($D_i > D_{50}$), and increases it for the fine fraction ($D_i < D_{50}$). The correction factor, $\zeta$, commonly takes this form (Einstein, 1950; Wilcock, 1993):

$$\zeta = \alpha \left( \frac{D_i}{D_{50}} \right)^{-\beta} \tag{3.15}$$

where $D_i$ is the grain size of the fraction of interest, $\beta$ controls the strength of the hiding-exposure effect (Buffington & Montgomery, 1997; McCarron et al., 2019), and $\alpha$ = 1 for sediments with the same density. Exponent $\beta$ has been approximated using $\sigma_g$, as a measure for sorting (Patel et al., 2013; McCarron et al., 2019): $\beta$ = 0.96 for $\sigma_g < 2.85$ and $\beta = 2.67e^{-0.37\sigma_g}$ for $\sigma_g \geq 2.85$, where $\sigma_g$ is determined with equation 3.4.



Applying this correction factor to the experimental data shows that adding a larger fraction of fine material results in a larger increase in mobility of the coarse material. For example, replacing 50% of the base material by fine sand causes $\theta_c$ of the base material to decrease from 0.021 to 0.019 (-11%) and to 0.016 for 50% coarse silt (-31%) (Supplementary Table S1). Applying this adjusted critical Shields number to our data reduces the root-mean-square error of the observed normalised dune height by 0.019 (-9%) and 0.032 (-15%) for fine sand and coarse silt, respectively, when evaluated against the predictor of Venditti & Bradley (2022). In contrast, the same adjustment increases the root-mean-square error for the experiments with fine silt by 0.011 (+6%) and causes the variability for the high discharge runs to remain high, with a root-mean-square error of 0.31. These results are discussed in Sections 3.4.3 and 3.4.4, respectively.

#### 3.4.2.2 | The hiding-exposure effect in mixed gravel-sand and sand-silt beds

The hiding-exposure effect is not commonly recognised in studies focused on sand-silt mixtures, and is mainly based on experiments in gravel-sand mixtures. McCarron et al. (2019) described an increase in mobility in gravel-sand experiments based on a decrease in $\theta_c$ by 64% compared to well-sorted sediment of a similar size (2.14 mm). Frings et al. (2008) speculated that hiding-exposure could result in a more mobile coarse fraction than a fine fraction in the downstream part of sand-bed rivers. Our observations with sand-silt mixtures show many parallels to gravel-sand mixtures, but on a smaller grain-size scale. We therefore infer from our experiments that the hiding-exposure effect also plays a role in sand-silt mixtures.

Mechanisms explaining the increased mobility of gravel in sand-gravel mixtures were suggested by Ikeda (1984) and subsequently built on in later studies (e.g. Li & Komar 1986; Whiting et al. 1988; Dietrich et al. 1989; Wilcock 1993; Venditti et al. 2010). Firstly,

by filling pores with fine grains, the pivoting angle of large grains is reduced, thus facilitating entrainment (Li & Komar, 1986). Secondly, there is a lower probability that particles in transport are caught in the wake of protruding particles and deposit, since particles protrude less far into the flow. Finally, filling pores with fine material results in a smoother bed, thus resulting in lower drag, which in turn increases the near-bed velocity. These suggestions were built upon by Venditti et al. (2010), who suggested that the infilling of the pores causes dampening of small wakes in the lee of particles, resulting in acceleration of the near-bed flow, which in turn mobilises the larger particles. Our experimental results suggest that this acceleration of near-bed velocity is reflected in an increase in dune length and height at medium discharge (Figure 3.9d).

The observation that the sediment mobility increases when adding coarse silt to the bed is in line with what can be expected from experiments with gravel-sand mixtures, but opposes previous observations in laboratory experiments with sand-silt mixtures. Bartzke et al. (2013) and Yao et al. (2022) observed that non-cohesive silt stabilises the sediment bed, but at different concentrations ($\sim$1.4% silt and >35%, respectively), whereas, in our experiments, even at 50% coarse silt the mobility of the sediment was increased. Interestingly, Bartzke et al. (2013), whose experiments fall in the range of pore bridging ($D_{coarse} / D_{fines}$ = 5.5), explained the filling of pore space as a reason for increased stability of the bed due to reduced hyporheic flow, rather than a reason for increased mobility of the coarse fraction as found in gravel-sand experiments (Section 3.4.2.1). The reason for these opposing effects could lie in the different experimental setups: the highest flow velocity tested in these experiments was 0.35 m $s^{-1}$, which is comparable to our lowest flow velocity. It is therefore likely that the supposed stabilising effect of silt is overruled by a large bed shear stress and the development of bedforms in our experiments.

Ma et al. (2020) studied the mobility of silt-sized sediment and the effects of sorting in laboratories and rivers world-wide, and found a high-mobility sediment transport regime related to the size and sorting of the bed sediment. Bed sediments of $D_{50} <$ 88 $\mu$m and poorly sorted sediments within a range of 88 $\mu$m $< D_{50} <$ 153 $\mu$m were found to be more mobile than expected from the sediment transport rate equations of Engelund & Hansen (1967), whereas sediments with $D_{50} >$ 153 $\mu$m confirmed these equations. In other words, poorly sorted sediments in the transitional range of very fine to fine sand are more easily mobilised than narrowly distributed sediments. This agrees with equation 3.15, where the strength of the hiding-exposure effect is related to the sorting of the material. Although Ma et al. (2020) did not explicitly mention the hiding-exposure effect, and related their observation to the change from mixed load to suspended-load dominated transport, the hiding-exposure effect may have played a role to achieve this change.

### 3.4.3 | Impact of weakly cohesive fine silt

Contrary to the increase in mobility observed when adding non-cohesive fine material, the mixing of fine silt into the bed reduced both the height and length of the bedforms. This can be attributed to the weakly cohesive character of the 17 $\mu$m-sized silt, because cohesive sediments such as clay are known to limit or suppress bedform growth (Schindler et al., 2015; Parsons et al., 2016) through London-van der Waals forces and by interparticle electrostatic bonding (Mehta, 2014), consequently increasing $\theta_c$.

The fine silt used in our experiments exhibited weakly cohesive properties, confirmed by visual stickiness of slurries of the fine silt and an increased angle of repose. Therefore, fine silt might have imparted similar attractive forces as clay, although to a lesser extent. Schindler et al. (2015) and Parsons et al. (2016) performed experiments with fine sand ($D_{50}$ = 239 $\mu$m) at a mean velocity $u$ = 0.8 m s$^{-1}$, and observed an inverse linear relationship between dune height and clay percentage, with a lack of dunes at a clay percentage of 15%. The sharp decline in bedform height with clay content as observed in their experiments, was not evident in the present experiments, and the bed remained mobile up to 30% fine silt. Nevertheless, in the medium-discharge experiments, the dune heights and lengths for fine silt were significantly reduced, as opposed to the increase for coarse silt and fine sand, likely due to decreased mobility of the entire bed. In the low-discharge experiments, the ripple size was reduced too, but, as shown below, this could be a result of decreased grain size rather than decreased mobility.

Wu et al. (2022a) recorded a decrease in ripple height with increasing clay percentage under wave-current conditions ($D_{coarse} / D_{fines} \sim 51$). Below 11% clay, the clay was winnowed out of the bed, allowing clean-sand ripples of similar size to develop. Above 11%, the cohesiveness of the bed was large enough to limit bed mobility, and only small ripples formed. In our experiments, this effect did not occur, as even at small percentages of fine silt ($\sim$ 2%) bedform height decreased, as in the current-ripple experiments with mixed clay-sand of Baas et al. (2013). During the medium-discharge experiments, cohesion impeded dune formation, and only small bedforms formed. In the high-discharge experiments, dunes did form, but their planform was more similar to the dunes formed in the medium-discharge experiments with fine sand and coarse silt than to those in the high-discharge runs (Supplementary Figure S2 and S3), indicating cohesion-induced hampered mobility.

In summary, the formation of relatively small bedforms in our experiments with fine silt can be attributed to reduced mobility, caused by the weakly cohesive properties of fine silt. This effect is less pronounced than in previous experiments with more strongly cohesive clay, in which the mobility was limited more strongly. The decreased mobility leads to an increase in the critical Shields number, and a shift to the left in the transport-stage diagram of Figure 3.11.

### 3.4.4 | Instabilities at high discharges

The present study shows that any impact of fine sediment on bed geometry at high transport stages is swamped by the inherent variability of dune geometry (Figure 3.11). This variability encompasses three bed configurations, without any apparent relationship with the type or fraction of fines: a dune-covered bed; a flat bed with one large dune (cf. Saunderson & Lockett (1983) and Naqshband et al. (2016)); and a completely flat bed.

The variability in bedform geometry and the presence of multiple bed configurations have been described before in literature. Saunderson & Lockett (1983) performed experiments around the transition from dunes to upper-stage plane bed and found four different bed states: asymmetrical dunes; convex dunes; humpback dunes (comparable to the single large dune configuration in this study); and a flat bed. These bedform states were seen to transform into one another. Saunderson & Lockett (1983) dedicated this behaviour to the close position of the bed to the phase boundary between dunes and upper-stage plane bed, but did not provide a physical explanation. Venditti et al. (2016) observed three phases in high-velocity experiments: a plane bed with washed-out dunes; a field of large dunes; and a field of small dunes. The water depth, shear stresses and water surface slope co-varied with the changes in bed configuration. During the plane-bed phase, intense localised erosion was followed by the formation of small or large bedforms, which then washed out to form a new flat bed. These cycles lasted from several minutes to more than half an hour, with transitions between individual bedform types happening in seconds or minutes. Similarly, Bradley & Venditti (2019) stated a 'tremendous variability' between bed states at a high transport stage, and reasoned that numerous observations of the bed are needed to get an average bed state that scales with the transport states described by equations 3.8 and 3.9.

However, none of these studies provided an explanation for the large variability in dune height at high transport stages. In Chapter 5, we reanalysed the data of Venditti et al. (2016) and Bradley & Venditti (2019), and found a bimodal dune height distribution at high transport stages. We attributed this to a critical transition, exhibiting flickering between a high and low alternative stable state. Our current observations support the idea of these alternative stable states. The large variability in bed con-

figurations explains the lack of a predictable succession of bed states with increasing amounts of fine sediment in the current study. This variability is so large that all bed states can occur at any moment, independent of the bed composition. However, the upper stage plane bed condition was not observed in the high-discharge experiments with fine silt, which once again shows a decreased mobility as a result of the cohesiveness of the sediment, leading to a shift to the left on the bedform-transport stage diagram, preventing flattening of the bed.

### 3.4.5 | Ripples at low discharges

Ripples formed in the low discharge experiments. Ripple height and length are a product of the size of the bed material, and are independent of flow velocity (Baas, 1994, 1999; Soulsby et al., 2012). Therefore, the transport stage framework as suggested above for dunes is not relevant for ripples. The height and width of the ripples, and to a lesser degree their length, decreased with an increasing amount of coarse and fine silt. The decrease in height is most apparent at silt concentrations above 20%, the same percentage at which the $D_{10}$ of the sediment distribution drops considerably (Figure 3.3).

Adding fine sand to the base material led to a decrease in height of about 15%, a similar decrease as expected based on Soulsby's ripple predictor (equation 3.10). This suggests that the change in grain size dominated the change in ripple height, and the hiding-exposure effect was small. However, adding coarse silt to the base material had a larger decreasing effect on height and length than fine sand. In the run with 50% coarse silt, both the height and the length were at, or close to the predicted values of 8 mm and 95 mm, respectively, suggesting that equilibrium was reached in this run. Hence, adding coarse silt increases the development rate of the ripples compared to fine sand. This may be caused by three processes; (a) a mobility increase induced by the hiding-exposure effect; (b) a shorter equilibrium time for coarse silt ripples at the same Shields stress; (c) a larger relative effect of coarse silt than fine sand, as a 50% increase in weight of the finer fraction involves a much larger number of coarse silt than fine sand particles (in the same volume, there are 331 times more coarse silt particles than medium sand particles, as opposed to 3 times for fine sand). Finally, adding fine silt to the base material shows the effect of cohesion by reducing the ripple height. However, the effect of particle size cannot be distinguished with confidence from that of cohesion. The decrease in ripple height with increasing fraction of fine silt is larger than for coarse sand, which might be at least partly caused by the cohesive properties of the fine silt.

It should be emphasised that the response of ripples to an increase of fine bed sediment is different from the response of dunes. Whereas dune geometry gets adjusted by the increased mobility of the non-cohesive bed sediment, ripple geometry mainly results directly from the particle size distribution of the material.

### 3.4.6 | The impact of bed sediment on hydraulic roughness

We confirm that for relatively steep dunes, roughness is related to the steepness of the leeside, consistent with findings of Kwoll et al. (2016) and Lefebvre & Winter (2016). At the leeside of the dune, flow separation generates turbulence, resulting in energy dissipation in the turbulent wake, which constitutes the main source of dune-related roughness (Lefebvre et al., 2014b; Venditti & Bennett, 2000). In our experiments, the bedforms had on average a leeside angle of $10^{\circ}$ with a relatively steep section (mean slip face angle $20^{\circ}$), resulting in intermittent flow separation (Lefebvre & Cisneros, 2023). The presence of flow separation can also be determined using the defect Reynolds number (Baas & Best, 2000), $Re_d$ ($Re_d = \frac{\Delta u^*}{\nu}$). In all our experiments, $Re_d$ is far larger than 4.5, which indicates the presence of flow separation (Williams & Kemp, 1971; Best & Bridge, 1992; Gyr & Müller, 1996).

Previous research suggested that the composition of the sediment bed has only a small influence on hydraulic roughness (Smith & McLean, 1977). This corresponds with our findings and equation 3.13 as far as skin friction is concerned; only 3% of the total roughness is attributed to skin friction in the present experiments. However, the bed composition strongly impacts the bed geometry, thereby influencing form roughness.

### 3.4.7 | Wider implications

Our results show that the presence of fines affects sediment mobility, even if the fines only slightly change the $D_{50}$ of the sediment. Therewith, fine material influences bedform properties and hydraulic roughness, which is worth accounting for in bedform size predictors. Moreover, the interaction of fine silt and sand with coarser sand is relevant for channel nourishment aimed at preventing incision (Czapiga et al., 2022).

To adequately determine bedform geometry, some measure of bimodality or sorting may be included in future predictors. This measure could focus on the fine fraction, such as the $D_{10}$. Additionally, the bed geometries for added fine and coarse silt differ notably, if the fine silt fraction is cohesive. Hence, assessing the cohesive properties of silt, such as yield stress and viscosity, is crucial, and lumping fines into one fraction, with a cut-off at 63 $\mu$m (e.g. van Rijn 2020) is to be avoided.

## 3.5 | Conclusions

We performed 51 laboratory experiments, in which the bed composition was varied using three different sediment mixtures (medium sand with fine sand, coarse silt and fine silt) in different ratios, for three different discharges (low, medium, high). We measured the bed morphology at the end of the experiments to assess the effect of bed composition on bedform geometry, and used this to indirectly assess sediment mobility and transport stage. The main conclusions of the research are:

- Bedform response to the addition of fine material depends, amongst others, on transport capacity, bimodality-impacted bed mobility, and cohesion.
- In the dune regime, adding fine sand or coarse silt to medium sand increases the mobility of coarser material. This leads to an increase in transport stage, $\theta/\theta_c$, an increase in dune length, and an increase or decrease in dune height, depending on the initial value of $\theta/\theta_c$.
- The increase in mobility of medium sand is inferred to be caused by the hiding-exposure effect, with the filling of pores by coarse silt leading to a larger near-bed flow velocity. Fine sand is too coarse to fit in the pores, which causes an increase in grain protrusion and a decrease in friction angle, and therefore increased sediment mobility.
- Adding weakly cohesive fine silt to medium sand has a similar effect to adding cohesive clay (Schindler et al., 2015), by causing a decrease in transport stage and inhibiting dune growth.
- In the ripple regime, adding fine material leads to a decrease in ripple height, which responds directly to the decreased particle size.
- In the transitional regime from dune to upper-stage plane bed, bed geometries may flicker between alternative stable bed states, complicating the relation between bedform height and length and fine sediment fraction.
- The composition of the sediment bed does not significantly influence hydraulic roughness from skin friction drag, but it alters the bed morphology, and thus indirectly changes the hydraulic roughness through form drag.

*I like mud.*
*I like it on my clothes.*
*I like it on my fingers.*
*I like it on my toes.*

# 4

# Floc capturing by dunes

This chapter is under review as:

de Lange, S.I., van der Wilk, A., Chassagne, C., Ali, W., Born, M.P., Brodersen, K., Hoitink, A.J.F., Waldschläger, K. Migrating subaqueous dunes capture clay flocs. Under review by Science Advances.

## Abstract

Recent research highlights the abundance of flocculated particles (flocs) in rivers, formed by the aggregation of clay particles with organic matter. These flocs affect the transport and eventual fate of clay. Flocs exhibit distinct behaviour from their unflocculated sedimentary counterparts: they can deform and break, and have larger settling velocities than the individual particles. The latter causes flocs to have the potential to deposit and possibly interact with the riverbed. Systematic experiments in an annular laboratory flume were conducted. Flocs showed a saltating (bouncing) behaviour, and were incorporated in the sediment bed as single flocs, clusters of flocs, or floc sheets, via deposition and burial in the lee of a dune, featuring clear diagonal layering. The dune geometry itself was negligibly impacted by the presence of flocs. This study is the first to highlight the potential active role of flocculated clay particles in riverine systems. Rather than the previously assumed passive behaviour of clay particles as wash load, the burial of flocculated clay particles can affect contaminant spreading, aquatic ecology, the interpretation of deposition patterns, and clay transport.

## 4.1 | Introduction

Flocculated particles (flocs), as found in coastal environments, are particles composed of mineral clay particles (so-called primary particles) aggregated to organic matter (Droppo, 2001; Dyer, 1989; Winterwerp, 2002; Mietta et al., 2009; Lasareva & Parfenova, 2023; Safar et al., 2022; Deng et al., 2019). Flocs are not only abundant in estuarine systems worldwide (van Leussen, 1999; Deng et al., 2022; Gratiot et al., 2017), but prevail in riverine systems as well (Nicholas & Walling, 1996; Bungartz & Wanner, 2004; Lamb et al., 2020; Fettweis, 2008). Understanding the fate of clay, in the form of primary or flocculated particles, is crucial in attempts to understand the global carbon cycle (Torres et al., 2017), to create resilience of coastal landscapes against sea level rise (Edmonds & Slingerland, 2010), to interpret river-floodplain morphodynamics (He & Walling, 1997; Aalto et al., 2008), and to setup sediment budgets (Ongley et al., 1992). The presence of flocs has a tremendous impact on total sediment transport rates in rivers (Fettweis, 2008; Guo & He, 2011).



Compared to the primary particles that make up the flocs, flocs have lower densities and are a few orders of magnitude larger (up to 1 mm, compared to clay particles of $10^{-3}$ mm). This causes their settling rates to be up to 100 times larger, and to have a higher critical shear stress for entrainment (Lamb et al., 2020). Consequently, unlike primary clay particles, flocs can interact with the sediment bed through settling and entrainment, instead of being transported solely as washload (Winterwerp et al., 2021; Lamb et al., 2020). Wysocki & Hajek (2021) found mud deposits in the sediment bed of their flume, but could not confirm whether flocs drive the deposition of muddy deposits in riverbeds. Additionally, Mooneyham & Strom (2018) observed clay aggregates moving as bedload, independent of flow conditions, albeit without interaction with an immobile gravel bed. Similarly, Schieber et al. (2007) observed deposition of clay flocs under transport conditions capable of moving sand, despite the low density of flocs.

Unlike primary particles, flocs can deform and break. Deformation alters the shape, size, and density of flocs (Yu et al., 2023; Shakeel et al., 2020), while breaking results in the creation of smaller flocs, having the capacity to re-aggregate. In open water, turbulence is the main driver for the aggregation, break-up, and deformation of flocs (van Leussen, 1988). Flocs grow with increasing collision frequency and thus with higher shear: mineral clay and organic matter interact to form clay-organic matter aggregates, which are in turn subjected to floc-floc aggregation. However, long exposure to shear, or a further increase in shear rate, can lead to a decrease in floc size over time (Shakeel et al., 2020), as flocs break apart or deform into denser aggregates (Chapter 2; Pérez et al. 2022). These cycles of breakage, regrowth, and restructuring, caused by local hydrodynamic conditions, shape the flocs into stable structures (Yu et al., 2023; Safar et al., 2022). If, in the process of settling, the floc is sufficiently strong

to withstand the near-bed shear stresses, it will deposit on the bed and attach itself to the bed by cohesive bonds (Debnath et al., 2007; Parchure & Mehta, 1985). Weaker flocs may break (Chassagne & Safar, 2020) and will be re-entrained. Alternatively, individual flocs might not remain intact during the cycles of settling and entertainment, but rapidly reform (Lamb et al., 2020).

In sand-bedded rivers, near-bed turbulence is primarily influenced by bedforms (ripples and dunes). Locally, the shear stress increases over a bedform crest, and decreases in a bedform trough (Kirca et al., 2020). This could alter the size (Grangeon et al., 2012) and density of the flocs, and therefore their settling velocity (Guo & He, 2011). The migration of river bedforms mainly determines the bedload sediment flux, via erosion from the stoss and deposition in the lee (Allen, 1982; Kennedy, 1963). As it has shown that flocs can deposit on the bed, the question arises if and how flocculated particles are affected by the migration of river bedforms. Vice versa, bedform geometry, primarily determined by the size of the bed material and the strength of the flow (Venditti & Bradley, 2022; van Rijn, 1984; Best, 2005), can be altered by biological processes (Parsons et al., 2016; Grant et al., 1986), pollutants in the water column such as plastics (Russell et al., 2023), the size distribution of the bed sediment (Chapter 3), and the suspended sediment concentration (Best, 2005; Wan, 1985), yet the impact of flocculated clay on the river bedforms remains unknown. Altogether, the interaction of flocs with bed sediment in a bedform-dominated environment is unclear.

The aim of this study is to deepen our understanding of floc transportation, incorporation, and release in bedform-covered systems, and to establish whether flocs can alter the bedform dynamics and vice versa. We seek to understand what flocs in a bedform-dominated system mean for the transport mode of clay particles. To this extent, we conducted systematic laboratory experiments in an annular flume, where continuous shear created bedforms in a mixed sand-clay bed (2 w% clay) and flocculation was induced with a synthetic flocculant. A synthetic flocculant was chosen rather than a bioflocculant, as the former has been well-studied and is well-characterised (Mehta & Partheniades, 1975; Hasan & Fatehi, 2018; Pérez et al., 2022; Droppo, 2009; Shakeel et al., 2020). Flocs created using polyacrylamide-based polymers have similar properties to flocs created by polysaccharides produced by microorganisms, and are therefore comparable to flocs found in nature (Zhang et al., 2024; Ali et al., 2022). Two shear stress values and six flocculant dosages were imposed, resulting in diverse bedform sizes and different degrees of clay flocculation. Dune and floc characteristics were measured and visual imaging provided insights into floc-sediment bed interactions.

## 4.2 | Methods

### 4.2.1 | Preparatory experiments to define the parameter space

A series of preliminary settling and rotating wheel experiments were carried out in the joint Deltares-TU Delft laboratory in Delft, the Netherlands. These tests aimed to determine the appropriate flocculant type and dosage, clay type and concentration, the response of the flocs to shear, and the mixing method of the flocculant. The tests are described in Supplementary Materials Text S1 and their results are summarised below.

Polyacrylamide flocculants, either cationic (positively charged) or anionic (negatively charged), are commonly used in wastewater treatment and therefore widely studied (Hasan & Fatehi, 2018; Pérez et al., 2022; Droppo, 2009; Pillai, 1997). A cationic flocculant ZETAG – 8125 (BASF, 2013) was selected, which is a copolymer of acrylamide and quaternised cationic monomer, of low cationic charge and high molecular weight. Using a cationic polyelectrolyte, in contrast to the use of an anionic polyelectrolytes, the polymer-clay flocculation is mainly driven by the electric interaction between the positively charged polymer and the negatively charged clay particles, irrespective of salinity. This prevented cumbersome water quality analysis and matching water properties, as tap water was used.



Flocculant dosage impacts floc size and their resistance (strength) to shear (Shakeel et al., 2020; Hasan & Fatehi, 2018). Its optimal dosage for the experiments was determined based on the preparatory tests. The test parameters were based on a lower limit inferred from the detection limit for the floc camera, being 20 $\mu$m, and an upper limit determined by the optimum flocculant concentration. An increasing amount of flocculant leads to the formation of flocs containing a large amount of flocculant, which have slower flocculation kinetics than flocs formed at smaller dosages. Well above the optimum flocculant concentration, unflocculated polyelectrolytes remain in suspension (Shakeel et al., 2020; Hasan & Fatehi, 2018). In our experiments, we remain below the optimum concentration to prevent an increase in water viscosity caused by an overdose of flocculant (Romero et al., 2018; Hasan & Fatehi, 2018). Kaolin clay with a $D_{50}$ of 1.3 $\mu$m was used as primary mineral clay particles. The clay concentration was decided to be 2 w% (relative to the sand; 0.5 v% relative to the water). This was sufficient to form substantial flocs, without the clay significantly impeding bedform growth (as seen in Wu et al. 2022a; Wan 1985; Wan & Wang 1994).

The appropriate shear stress was determined to fall within the dune regime (van den Berg & van Gelder, 1993), while preserving floc integrity (Krishnappan, 2006) (Table 4.1). This was tested in preliminary experiments, where we observed that flocs interacted with the bed by being buried and re-entrained. As anticipated, flocs were smaller when exposed to shear (Chapter 2; Shakeel et al. 2020), yet the determined

dosages remained accurate. Finally, the mixing method was tested, from which it was found that the final floc characteristics are insensitive to the mixing method.

### 4.2.2 | Experimental setup

The experiments took place in an annular flume in the hydraulic lab of the Institute of Hydraulic Engineering and Water Resources Management (IWW) at RWTH Aachen University, Germany. The flume, with a diameter of 350 cm, a width of 25 cm, and a height of 100 cm (Figure 4.1), was preferred over other types of flumes for its ability to recirculate water without necessitating pumps, which could break or deform the flocs (Gibbs, 1981; Partheniades et al., 1969). Water flow was generated through rotation of a lid, while the counter-rotation of the flume limited secondary currents (Baar et al., 2020; Petersen & Krishnappan, 1994). The ratio between lid and flume rotation was chosen such that the centrifugal forces balance each other (Spork, 1997), converting the annular flume into a representation of an infinite straight river.

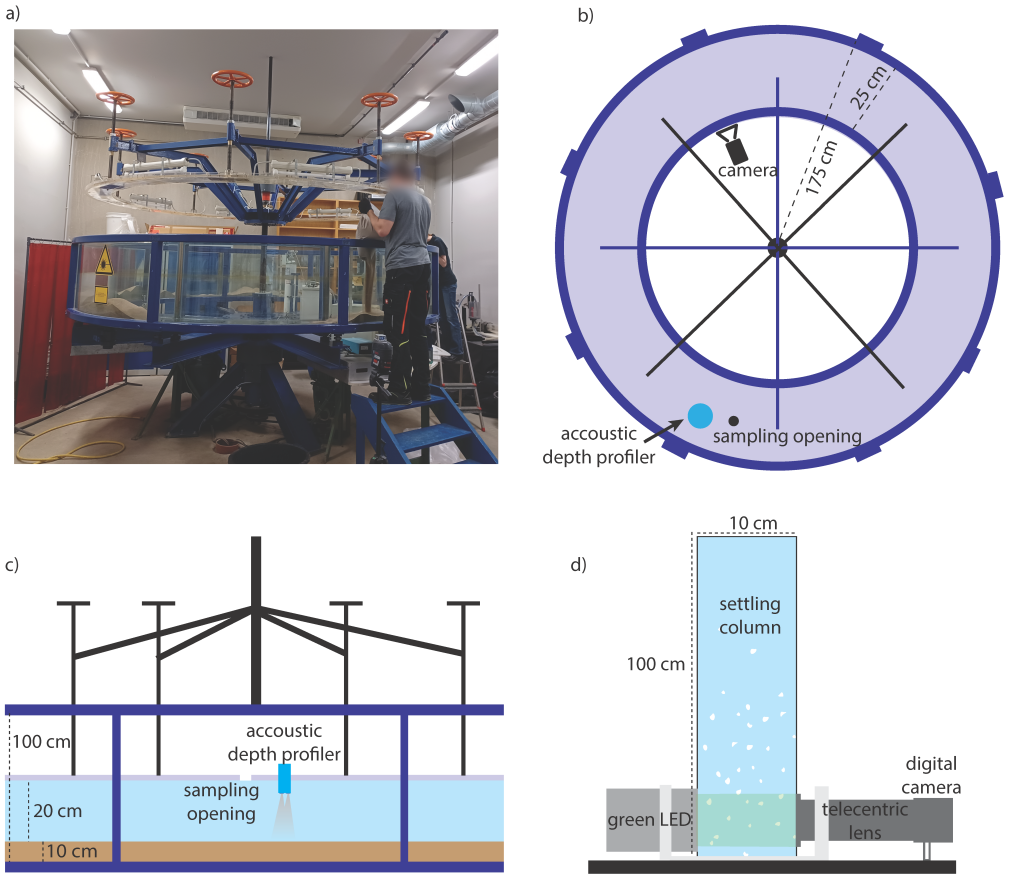


**Figure 4.1** | Experimental setup. A picture (a), schematised top-view (b) and schematised side view (c) of the annular flume. d) Side-view of the settling column setup. Subfigure b-d) are not to scale for visualisation purposes.

**Table 4.1** | Experiments (number #) and their corresponding test parameters. The amount of flocculant in the experiments is shown in grams, milligram per litre of water, and milligram per gram of clay.

| # | shear stress (N $m^{-2}$) | clay (w%) | flocculant | | |
|---|---|---|---|---|---|
| | | | $g$ | $mg\ L^{-1}$ | $mg\ g^{-1}$ |
| 1, 2 | 0.35, 0.5 | 0 | 0 | 0 | 0 |
| 3, 4 | 0.35, 0.5 | 2 | 0 | 0 | 0 |
| 5 | 0.35 | 2 | 1.5 | 5.9 | 0.18 |
| 6 | 0.35 | 2 | 1.9 | 7.4 | 0.23 |
| 7, 8 | 0.35, 0.5 | 2 | 2.3 | 9.0 | 0.28 |
| 9, 10 | 0.35, 0.5 | 2 | 3.7 | 15 | 0.46 |
| 11, 12 | 0.35, 0.5 | 2 | 4.7 | 18 | 0.58 |
| 13, 14 | 0.35, 0.5 | 2 | 5.7 | 22 | 0.70 |

The flume was filled with a 10 cm layer of mixed sediment, consisting of medium sand with a median grain size ($D_{50}$) of 350 $\mu$m, and 2 w% kaolin clay with a $D_{50}$ of 1.3 $\mu$m. Before each experiment, the sediment bed was levelled, and the flume was filled with 20 cm tap water. The cationic powdered flocculant was dissolved and mixed overnight before each experiment, to ensure a complete solution and a uniform distribution in the flume. Just before the experiment, the dissolved flocculant was added to the water in the flume.



Each experiment ran for 4 hours, with a total duration of 5.5 hours to accommodate bed level measurements (Section 4.2.3). The second bed level survey was taken 45 minutes after the first, after which the measurement frequency was increased to every 30 minutes for the last four surveys. Throughout the experiments, the water temperature was 22.6°C (standard deviation $\sigma$ = 0.8), with an electrical conductivity of 310 $\mu$S $m^{-1}$ ($\sigma$ = 22) and a pH of 7.4 ($\sigma$ = 0.4). After each experiment, the bed was levelled, and the shear stress and flocculant amount were adjusted to match the next experimental setting.

The parameter set tested was determined through the preparatory experiments (Section 4.2.1), and is described in Table 4.1. Six different flocculant amounts were used in the experiments, ranging from 0 to 22 mg $L^{-1}$ (corresponding to 0.7 mg $g^{-1}$ clay and 13 mg $kg^{-1}$ total sediment). Four base experiments were conducted for the two different shear stresses, including two with no clay and no flocculant, and two with only sand and clay, but no flocculant. This enabled us to observe deviations from conditions without flocs present. Two different shear stresses, 0.35 and 0.5 N $m^{-2}$, were tested, such that all experiments fall within the dune regime (van den Berg & van Gelder, 1993), while preserving floc integrity (Krishnappan, 2006). For the two lowest flocculant dosages, only the low shear stress conditions were tested, as flocs were very small during these experiments, and would not have been visible under higher shear conditions.

### 4.2.3 | Instrumentation

An acoustic depth profiler, the StreamPro Acoustic Doppler Current Profiler (hereafter StreamPro), manufactured by Teledyne, was used to measure bed elevation, from which bedform geometry was derived (Section 4.2.4.2). This acoustic device is capable of penetrating turbid water, which was necessary for this experimental setup. The StreamPro was attached to the moving lid of the flume, positioned 7 cm from the outer edge. By rotating the flume, four profiles corresponding to the four beams of the StreamPro could be measured, with a frequency of 1 Hz. To ensure a millimetre resolution, the rotational speed of the flume bottom was temporarily reduced to 0.11 rotations per minute for the measurements, after which the rotational speed was increased again to the experimental shear stress. Any temporarily deposited flocs were directly re-suspended by the accelerating flow.

A 10 x 10 x 100 cm settling column was used to determine floc characteristics (Figure 4.1d), following a setup similar to Ye et al. (2020) and Ali et al. (2022). First, after three hours of experimental run time, flocs were collected from 10 cm below the water surface and at the top of the sediment bed. A 25 mL pipette was used to carefully extract flocs from the flume, and by subsequently touching the water surface of the settling column the flocs could flow into the settling column with minor disturbance. The characteristics of the captured flocs were recorded using a UI-3160CP Rev. 2.1 floc camera from IDS with a TC23024 lens from opto engineering. A green light (LTCLHP024-G from Opto Engineering) was used to illuminate the flocs in the settling column. The floc camera was controlled using the uEye cockpit software developed by IDS, configured to produce monochrome images for improved contrast to visualise the flocs.

A GoPro 6 was positioned in the middle of the flume, facing outward, to record bed evolution during the experiment at a fixed location, covering approximately 45 cm in width, and the whole water depth. Pictures were taken every 5 seconds.

### 4.2.4 | Data analysis

#### 4.2.4.1 | Floc characterisation

The images from the floc camera were analysed using the SAFAS software (Sedimentation and Floc Analysis Software) (MacIver, 2019). Subsequently, the settling speed of the flocs, and the major and minor axis diameters of the flocs were determined. Throughout the experimental runs, there is a balance between breakage and aggregation of flocs, leading to the attainment of equilibrium in floc size (Yu et al., 2023). The floc diameter $D_f$ was then computed as (Ye et al., 2020):

$$D_f = \sqrt{\frac{D_{major}}{D_{minor}}} \tag{4.1}$$

The Kolmogorov length scale, $\eta$ (m), is known to correlate with the size of the flocs and can be approximated with Winterwerp et al. (2021):

$$\eta = \left( \frac{\kappa z \nu^3}{u^{*3}(1 - \frac{z}{h})} \right)^{\frac{1}{4}} \tag{4.2}$$

in which $\kappa$ is the Von Karman constant, $\nu$ the kinematic viscosity of water ($m^2\ s^{-1}$), $u^*$ the shear velocity ($m\ s^{-1}$), $z$ the height above the bed (m) and $h$ the water level (m).

The shear velocity $u^*$ was calculated by using the bed shear stress $\tau$ ($N\ m^{-2}$) and the density of the water $\rho_w$ ($kg\ m^{-3}$), via:

$$u^* = \sqrt{\frac{\tau}{\rho_w}} \tag{4.3}$$

#### 4.2.4.2 | Bedform geometry determination

The StreamPro data was processed using ADCPtools (Vermeulen, 2015; Vermeulen et al., 2014b), and bed elevation profiles from each of the four beams were determined. These profiles served as input for the bedform tracking tool from van der Mark & Blom (2007), which gives bedform geometry based on specific span values used to differentiate between different bedform scales. Two bedform lengths were identified: 0.2 m ± 0.1 m (hereafter referred to as ripples) and 2.2 m ± 0.8 m (referred to as dunes). In almost all experiments, ripples were superimposed on dunes.

Bedform characteristics were averaged over the four beams. The characteristics include: (1) bedform height $\Delta$ (m), the vertical distance between top and downstream trough, (2) bedform length, $\lambda$ (m), the horizontal distance between two subsequent crests, (3) leeside angle, *LSA* (°), the slope from a linear fit of the bedform's leeside, excluding the upper and lower 1/6th of the bedform height and, (4) the stoss side angle and *SSA* (°), calculated similarly to the leeside angle.

## 4.3 | Results and Discussion

### 4.3.1 | Response of flocs to shear

The diameter $D_f$ of the flocs responded to the imposed mean shear stress, resulting in slightly larger flocs (on average 75 $\mu$m) in the lower shear stress condition compared to the higher shear condition (59 $\mu$m) (Figure 4.2). The variability in floc size was more pronounced during low shear conditions ($\sigma(D_f)$ = 55 $\mu$m) than during high shear conditions ($\sigma(D_f)$ = 37 $\mu$m). Turbulence can transform flocs into compact, smaller and more stable flocs (Yu et al., 2023), as confirmed by the lower standard deviation at higher shear stress in our experiments. Beyond a flocculant concentration

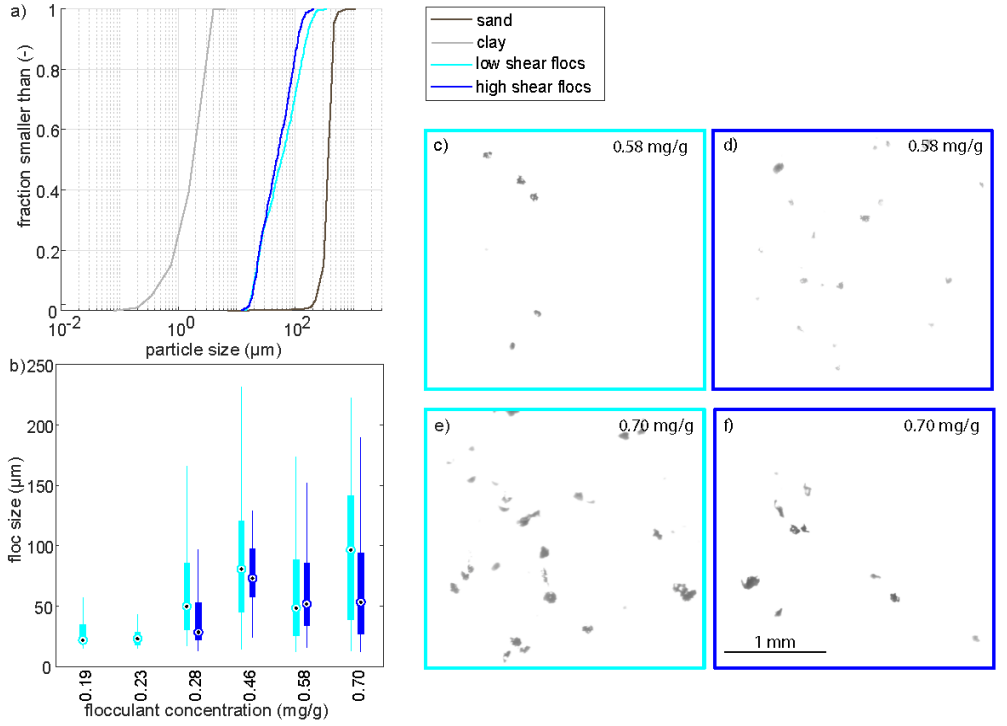


**Figure 4.2** | Floc characteristics subject to study. a) Cumulative size distribution of sand and clay used in the experiments, and flocs from high and low shear experiments combined. b) Floc size during the experiments. c-f) Example pictures of the flocs as taken by the floc cam.

of 0.46 mg $g^{-1}$, the increase in floc size due to the increased flocculant amount diminished, suggesting that turbulence became the primary factor influencing floc size.

The Kolmogorov length scale $\eta$, i.e. the smallest turbulence whirls, is often considered to be the upper limit of floc size. Assuming a uniform flow, $\eta$ can be estimated. At 10 cm below the surface, $\eta$ is 332 $\mu$m for low shear and 291 $\mu$m for high shear. This is considerably larger than the largest measured flocs (95th percentile of 183 $\mu$m and 129 $\mu$m). However, locally, the shear stress, and therefore $\eta$, varies depending on the position relative to the bedforms. Above the dune crest flow velocity is highest, while conditions are calmer in the dune trough (Kirca et al., 2020; Bennett & Best, 1995). High shear conditions on top of the dune set an upper limit for the floc size. Furthermore, $\eta$ decreases with decreasing distance from the bed, meaning that flocs that interact with the bed experience smaller turbulent whirls closer to the bed than higher in the water column. At a relative depth of 0.01 above an average dune crest (approximately 2 mm), $\eta$ measures 86 $\mu$m during the high shear experiments, and 103 $\mu$m during low shear experiments. Similarly, at a relative depth of 0.01 above an average dune trough (approximately 3 mm), assuming no flow separation, $\eta$ is estimated to amount to 97 and 107, respectively. This implies larger flocs can exist under low

shear conditions and in dune troughs, before they break or deform. Furthermore, this value corresponds well with the average floc sizes, indicating that the near-bed shear stress provides a proxy for floc size. However, above a bedform field, the local flow is nonuniform, and our estimation is based on a simplification of reality. Shear stresses are higher above the dune crest compared to the depth-averaged shear stress (Kirca et al., 2020), possibly resulting in a smaller average floc size than our estimate based on $\eta$. Additionally, for dunes with a large enough leeside angle (Kwoll et al., 2016; Lefebvre & Cisneros, 2023), flow separation occurs on the leeside, resulting in a recirculation zone that can trap flocs. This might mean that flocs could break or deform to denser aggregates on top of dune crests while being able to settle and aggregate in dune troughs.

### 4.3.2 | The interaction of flocs and the sediment bed

#### 4.3.2.1 | The transport of clay

Shortly after the start of the experiments, bedforms began to develop, resulting in the washing out of the clay from the active layer due to bedform migration (Figure 4.3a, b). This phenomenon, termed 'deep cleaning' by Wu et al. (2022a), has been observed in sand-clay mixtures with a clay percentage below 8%, where individual clay particles are washed out and subsequently transported in suspension.



However, with the presence of a flocculant, suspended clay particles can aggregate and form flocs. The 100-times larger size of the flocs increases their settling velocity to about 1 mm $s^{-1}$, allowing interaction with the sediment bed. In our experiment, the flocs are transported as mixed-load. They are partially transported in suspension, while also saltating over the bed (Figure 4.3b). Saltation refers to the bouncing motion of particles, where they are being lifted up and transported, before depositing. Flocs can saltate over the stoss side of the dune without breaking up (Figure 4.3b-1-5). At the crest of the dune, where the shear is the largest, the flocs can break and resuspend (Supplementary Figure S3), or saltate down the leeside of the dune (Figure 4.3b-6). In the recirculation zone of the leeside, the flocs can become trapped.

#### 4.3.2.2 | The incorporation of clay in the bed

We observed flocs being trapped in the leeside of the bedform and settling on the bed. There, they may attach to the bed through cohesive bonds (Mehta & Partheniades, 1975), increasing their resistance to erosion. The trapped flocs are subsequently incorporated in the bed by the migration of dunes. Dunes migrate by erosion of sediment particles from the stoss side and deposition at the leeside (Kennedy, 1963; Allen, 1982). The leeside deposition is responsible for the burial of the trapped flocs.

The incorporation of flocs within the dune (Figure 4.4) can occur at the scale of an individual floc, a cluster of flocs, or a floc sheet. An individual floc may stagnate on

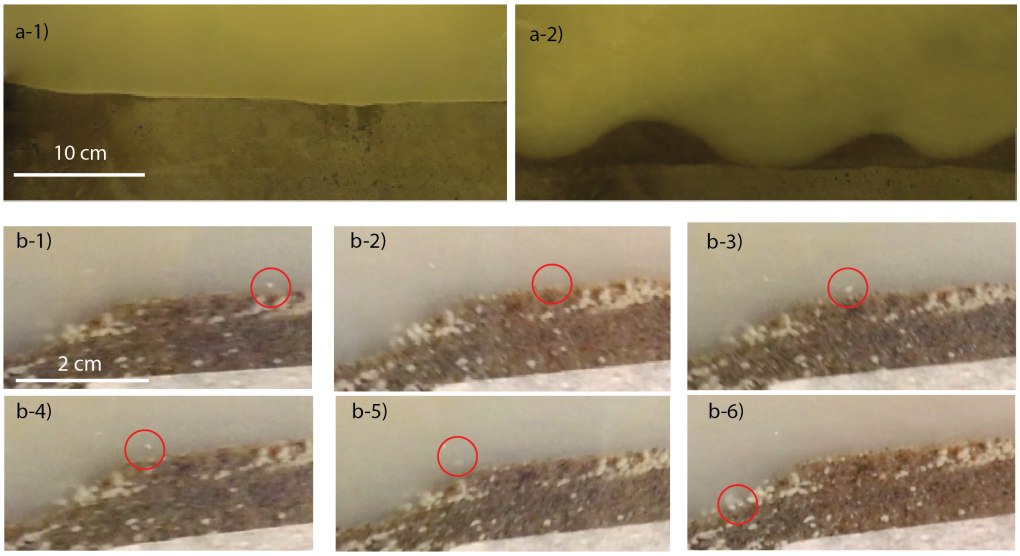


**Figure 4.3** | The transport of clay. a) Homogeneously mixed primary particles of clay (a-1) are washed out from the active layer into the water column (a-2). The image is slightly adjusted to remove reflections. b) Saltating behaviour of an individual floc (b-1-4), which is almost released into the water column (b-5), but ultimately becomes trapped in the leeside of the dune (b-6).

the leeside of the dune (Figure 4.4a-1, a-2), where the recirculating flow and the current balance each other out. Subsequently, denser grains avalanche down the leeside and bury the stagnant floc (Figure 4.4a-3). Depending on the timing and quantity of sand avalanching, more or fewer flocs have accumulated in the lee. Over time, a cluster of flocs may form on the leeside of the dune, which subsequently gets buried by a turbulent pulse causing avalanching of the grains (Figure 4.4b). With even more time, a sheet of flocs can cover almost the entire leeside of the dune (Figure 4.3c), with new flocs adhering to formerly deposited flocs, offering shelter from erosion. The classical erosion-deposition pattern within a dune exhibits diagonally-oriented sheet-like laminae at an angle similar to the leeside angle of the dune (Figure 4.3c). This pattern has also been observed in the incorporation of non-deformable objects such as plastics (Russell et al., 2023) and charcoal (Nichols et al., 2000).

Generally, a higher concentration of flocs resulting from an increased flocculant amount, led to more flocs being incorporated in the dunes. At higher shear stresses, smaller flocs were observed than at low shear stresses; however, the higher mobility of the dunes resulted in more visible incorporation of flocs in the dune. Similarly, Nichols et al. (2000) suggested that the amount of charcoal deposition is related to bedform migration rates.

Altogether, this means that while primary clay particles are lost from the bed via washing out, they can be incorporated into the bed through the migration of dunes, which bury the trapped flocs in the form of organised multilayered floc-clusters.

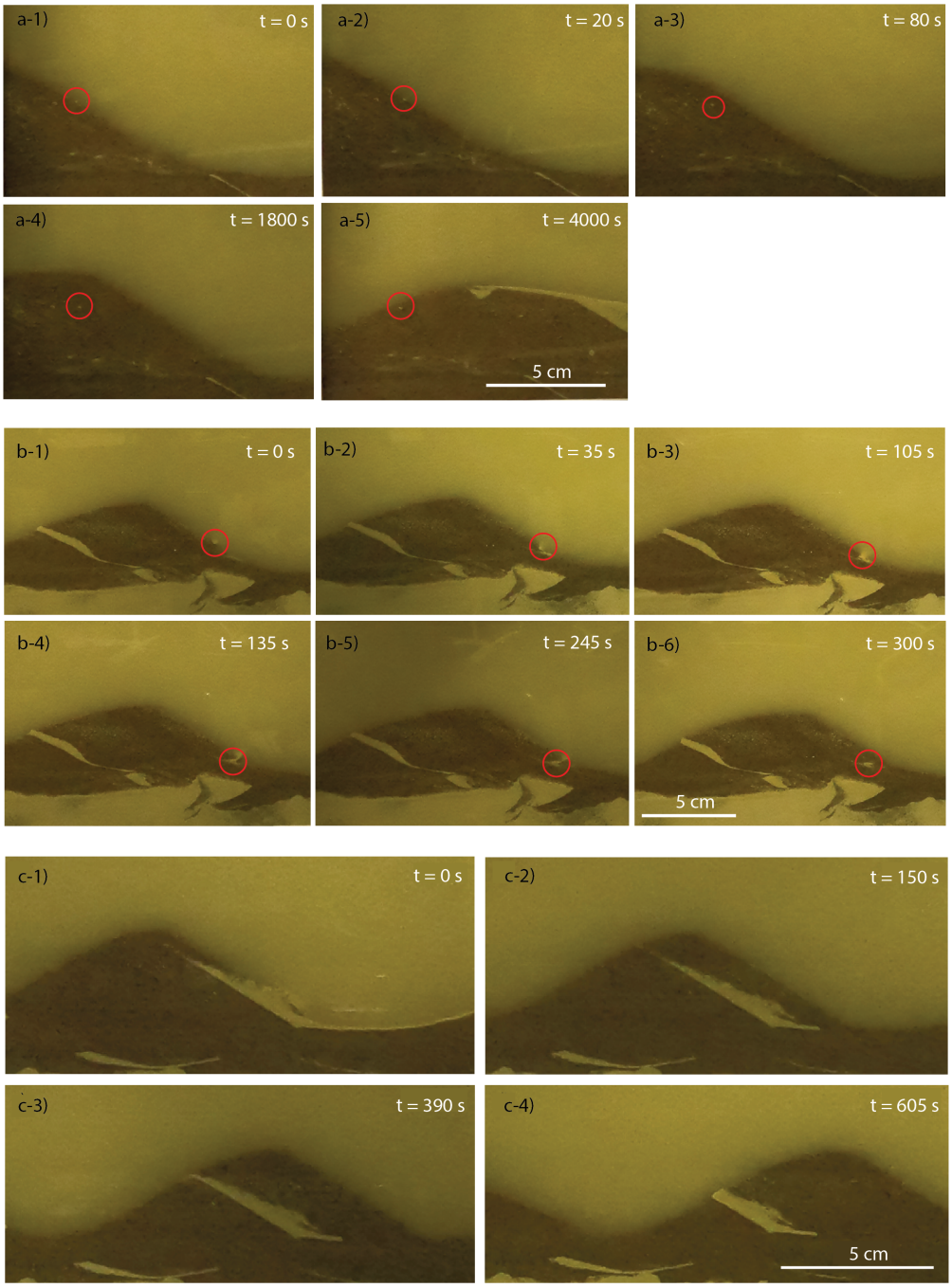


**Figure 4.4** | Transport of flocs and incorporation in the sediment bed. a) Incorporation of an individual floc into a dune (experiment 10). b) Incorporation of a cluster of flocs (experiment 13). c) Incorporation of a sheet of flocs in the bed (c-1, c-2) and the subsequent release into the water column (c-3, c-4) (experiment 13).

### 4.3.3 | The influence of flocs on dune geometry

Under continuous shear, the sediment bed developed into bedforms, often featuring dunes with superimposed ripples. The ripples had a relatively constant equilibrium height, length and leeside angle at both imposed shear stresses ($\Delta_r$ = 0.016 m, $\lambda_r$ = 0.24 m, $LSA_r$ = 9.8°). This behaviour was expected, since ripple geometry is related to the particle size of the bed material, and is independent of flow velocity (van Rijn, 1984; Baas, 1994, 1999; Soulsby et al., 2012). As expected, the equilibrium dune geometry shows a clear relation with shear stress (Allen, 1978; Yalin, 1964; Karim, 1995; van Rijn, 1984; Bradley & Venditti, 2019; Venditti & Bradley, 2022). Dunes in the higher shear stress regime are three times as high and twice as long ($\Delta_r$ = 0.093 m, $\lambda_r$ = 1.3 m) compared to dunes in the lower shear stress regime ($\Delta_d$ = 0.030 m, $\lambda_d$ = 0.63 m), although leeside angle remains constant ($LSA_d$ = 9.5°).

Equilibrium bedform geometry is not directly affected by flocculant amount or floc size (Table 4.2, Supplementary Figure S4). However, under low shear conditions, there is a slight, non-significant, increase in dune height and length with increasing flocculant amount. Contrarily, the incorporation of plastic particles (1 - 10 mm) in dunes (Russell et al., 2023), did lead to altering of the dune geometry. Pits or scours formed when plastic particles migrated towards the dune crest from the stoss side. Alternatively, they observed "bursts" of a cluster of plastic and sediment, being eroded rapidly from the stoss side, resulting in shorter dunes with steeper stoss sides.

In our experiments, a potential lengthening of the dunes with floc size appeared insignificant (Table 4.2). Erosion of flocculated particles from the stoss side (Figure 4.4a, c) did not create a pit as observed by Russell et al. (2023), nor were there observed bursts of flocs. The former could be explained by flocs being generally smaller than the sediment grains, while the plastic particles are larger than the grains. Hence, the erosion of an individual floc from the stoss will insignificantly impact the stoss side. The fact that no mass erosion of flocs occurred, contrary to the bursts of plastics, might relate to the organic nature of the flocs. According to Mehta & Partheniades (1975), upon settling, flocs form cohesive bonds with the bed and with each other, resulting in a higher erosion threshold than expected based on their density, potentially preventing simultaneous entrainment of entire floc sheets. Although flocs stick easily to other flocs, the strength of a floc-sand cohesion is unknown. Regardless of this, similar to a small percentage of primary clay particles in the bed (Wu et al., 2022a), cohesion seems to be insufficient to limit bedform growth. Instead, a slight increase in dune length with flocculant amount is observed, which can be related to their lower erosion threshold compared to sand particles (due to their lower densities), potentially increasing the average transport stage (the ratio of shear stress and critical shear stress). A higher transport stage generally results in longer dunes (Venditti & Bradley, 2022).

**Table 4.2** | The relation between dune geometry and floc characteristics. The strength of the relation is expressed in $R^2$. * Indicates a significance level of $0.05<p<0.1$. None of the relations has a significance level of $p<0.05$.

| | **dune height (m)** | | **dune length (m)** | |
|---|---|---|---|---|
| | low shear | high shear | low shear | high shear |
| **flocculant concentration (mg $g^{-1}$)** | 0.62* | 0.03 | 0.71* | 0.29 |
| **floc size ($\mu$m)** | 0.09 | 0.23 | 0.22 | 0.24 |

## 4.4 | Conclusion and Implications

The photo in Figure 4.5a visualises the key aspects of floc interaction with the bed. Clay in the water column is transported as suspended load, as individual or as flocculated particles (Figure 4.5a-I). These flocculated particles settle immediately if the flow is halted (Figure 4.5a-II), which may represent low river flow conditions in nature. During active sediment transport, the larger flocs are transported via saltation (Figure 4.3b). This leads to clay being captured in dunes in the form of flocs (Figure 4.5a-III), either as individual flocs, clusters, or as sheets. Continuous erosion and deposition processes of bedforms of various heights can result in floc drapes just below the currently active layer as a result of previous migration of larger bedforms (Figure 4.5a-IV), while clay particles remain mixed within the sand bed below the active layer (Figure 4.5a-V).

The interaction of clay with the bed is summarised in Figure 4.5b). Floc deposition is concentrated in areas with low shear and a higher Kolmogorov length scale (dune trough). Floc transport occurs over the dune stoss, where shear stresses are larger and the Kolmogorov length scale is smaller. The variability in shear stress due to the geometrical complexity of the bed allows for the trapping of flocs, even in conditions where the suspension of flocs is expected. Despite their deformability, flocs behave similar to plastic particles (Russell et al., 2023) and charcoal (Nichols et al., 2000) and do not break, likely because their size is already limited by the smallest turbulent whirls. At the top of the dune, where shear stresses are greatest, the fate of flocs is determined as flocs are either resuspended or trapped in the lee.

This study is the first to demonstrate that clay can be transported not only as washload, but also as bed and mixed load in the form of flocs. Flocs may not be passive components of river systems as was previously assumed, but interact with the sediment bed. The resulting incorporation of flocs in the sediment bed in a layered manner has significant impacts across a range of disciplines.

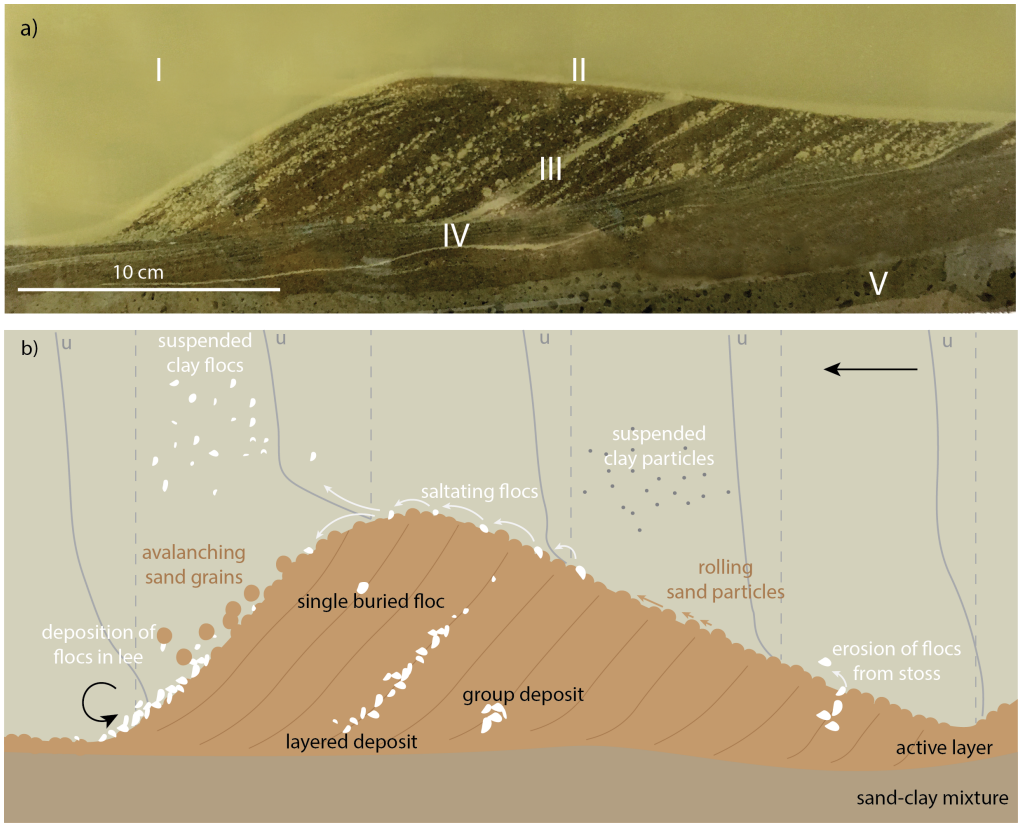


**Figure 4.5** | The possible fate of clay in rivers. a) Capturing of flocs in a bedform, in which five regimes are indicated, I: suspended, II: recently deposited, III: drapes in dune, IV: drapes below active surface (remnant), V: homogeneously mixed (initial experiment conditions). The image is slightly adjusted to reduce reflections. b) Schematic of the suspended and bed load transport of clay particles and flocs, and the subsequent trapping in the sediment bed. Velocity profiles (u indicates the flow velocity, dotted line indicates zero m $s^{-1}$) are schematised based on the measurements in Kirca et al. (2020).

Regarding environmental toxicology, the burial of flocs must be considered in contaminant studies. Flocs are key elements of contaminant transport, such as organic pesticides and heavy metals, due to the adsorption of the contaminant to the floc (Ongley et al., 1992; Milligan & Loring, 1997). Our study shows that the residence time of these clay-bound contaminants might be altered, by being easily incorporated in the bed sediment via flocs. These may then be released during higher discharge events (Crawford et al., 2022; Wölz et al., 2009) that feature larger dunes, with a deeper active layer. Additionally, microplastics could be entangled in flocs or could behave as flocculant (Laursen et al., 2022; Andersen et al., 2021; Yan et al., 2021). With the expected rise in plastic waste in the future (Geyer et al., 2017), the incorporation of microplastics in the bed via the process of floc burial might become a severe problem.

Ecologically, studies of riverine systems must consider the increased incorporation of clay flocs into the bed. Flocculation of clay removes clay from the water column, which alters the light climate (Avnimelech et al., 1982; Stross & Sokol, 1989). Additional incorporation of flocs within the bed could amplify this effect. Furthermore, an increased concentration of clay lenses in the bed could reduce hyporheic exchange, which may be problematic for biota living in the sediment that rely on gas exchange (Lu et al., 2018).

Sedimentologically, clay in deposits can serve as a proxy for fine sediment supply (Wysocki & Hajek, 2021) and ancient flow conditions (Schieber et al., 2007). Furthermore, the expected mud content in deposits is relevant for the compaction rate and subsequent subsidence, and the stability of river banks (Matsubara et al., 2015). From our study, it can be inferred that clay occurrence in deposits does not only indicate past flow conditions which are variable (Martinius & van den Berg, 2011) or calm (Potter et al., 1980, 2005), but also could indicate steady shear. This suggests that conclusions drawn from sediment deposits containing clay may need to be reconsidered (Schieber et al., 2007). When interpreting the rock record, layers of flocs would be detectable (Schieber et al., 2007). The incorporation of mud in the bed is significant (Wysocki & Hajek, 2021), and we now showed that this relates to flocculation, even in riverine systems that were, until recently, considered to have minimal floc formation.



Regarding sediment transport, floc capturing in the bed needs to be considered for mud transport modelling in various contexts (van Kessel et al., 2011; van Rijn & Grasmeijer, 2018). The smallest aggregate persisting in a particular flow field may easily contain hundreds of clay particles (Verney et al., 2011; Fugate & Friedrichs, 2003), and the burial of these flocs can significantly alter clay transport rates. The significance of the incorporation of flocs in the bed for clay transport needs to be studied, with a potential adjustment of clay transport models as a result.

In essence, this study calls for a renewed approach regarding the transport mechanisms of flocs and clay. It is critical to further investigate how flocs become incorporated in the sediment bed of rivers, and to quantify the effect of floc capturing, both in the lab and in the field.

*River, river, why do you run*
*You must be trying,*
*To catch-up with someone.*

*I'm on my way*
*To catch-up with the sea*
*But however fast I run*
*There is always more of me.*
*— Adapted from Grace Nichols*

# On the transition from dunes to upper stage flat bed

This chapter is under review as:

de Lange, S.I., van de Vijsel, R.C., Torfs, P.J.J.F., Hoitink, A.J.F. Bimodality in subaqueous dune height suggests critical transition at high flow. Under review by Nature Communications. DOI: 10.21203/rs.3.rs-3975821/v1

## Abstract

River bedforms influence fluvial hydraulics by altering bed roughness. With increasing flow velocity, subaqueous bedforms transition from flat beds to ripples, dunes, and an upper stage plane bed. Although prior research notes increased bedform height variation with flow strength and rapid shifts between bed configurations, the latter remains understudied. This study reanalyses data from earlier experiments, and reveals a bimodal distribution of dune heights emerges beyond a transport stage of 18. Dune heights flicker between a low and high alternative state, indicating critical transitions. Potentially triggered by local sediment outbursts, these shifts lead to dune formation before returning to an upper stage plane bed. This flickering behaviour challenges the adequacy of a single snapshot to capture the system's state, impacting field measurements and experimental designs, and questions the classical equilibrium equations. This study calls for further research to understand and quantify flickering behaviour in sediment beds at high transport stages.

# 5.1 | Introduction

Subaqueous river bedforms are ubiquitous in lowland rivers, and they are known to impact the river by altering its hydraulics, ecology, and sediment balance. In this way, the geometry of river bedforms impacts the fairway depth (ASCE Task Force, 2002; Best, 2005) and impacts dredging requirements, they add to the form roughness of the riverbed (Warmink et al., 2013; Venditti & Bradley, 2022) impacting the water level, and determine suitable foraging places for fish (Greene et al., 2020). In the lower flow regime (Froude number lower than one), and for a given grain size, various types of river bedforms can form, depending on the strength of the flow (e.g. Gilbert, 1914; Guy et al., 1966). Below the threshold of sediment motion, the riverbed can be flat, but as the flow increases, a continuum of bedforms evolves, consisting of ripples, followed by dunes, and eventually the dunes may wash out to an upper stage plane bed. This sequence is generally summarised in phase diagrams (van den Berg & van Gelder, 1993; Southard & Boguchwal, 1990) which correlate a measure of flow strength and a measure of grain size to various bedform planforms.

The height of the dunes, which increases with increasing flow strength and subsequently decays into upper stage plane bed, can be estimated using bedform predictors. For this purpose, Venditti & Bradley (2022) developed empirical equations for dune height prediction based on transport stage $T$, which is a measure of relative flow strength. $T$ is defined as the ratio of the Shields stress $\theta$ and the critical Shields stress $\theta_c$. The empirical equation for dune height $\Delta$ (m) as described below is obtained from laboratory studies (i.e. flows with a water depth $h$ less than 0.25 m), and yields a parabolic relation between dune height $\Delta$ and transport stage $T$:

$$\frac{\Delta}{h} = -0.00100 \left( \frac{\theta}{\theta_c} - 17.7 \right)^2 + 0.417 \tag{5.1}$$

Large scatter was observed when comparing the results from bedform height predictors to actual measurements (Bradley & Venditti, 2017), and various researchers describe an increased variability in bed geometry with increasing transport stage (Venditti et al. 2016; Bradley & Venditti 2019; Saunderson & Lockett 1983, Chapter 3) (Figure 5.1). The large variability at high transport stages might be the reason that not many measurements and lab experiments are done in the regime where dunes transition into a flat bed (Karim, 1995). Despite the importance of dune behaviour at high flow stages for, e.g., flood prediction (Julien & Klaassen, 1995) and infrastructure stability (Amsler & Schreider, 1999; Amsler & Garcia, 1997), not much attention has been given to this phenomenon.

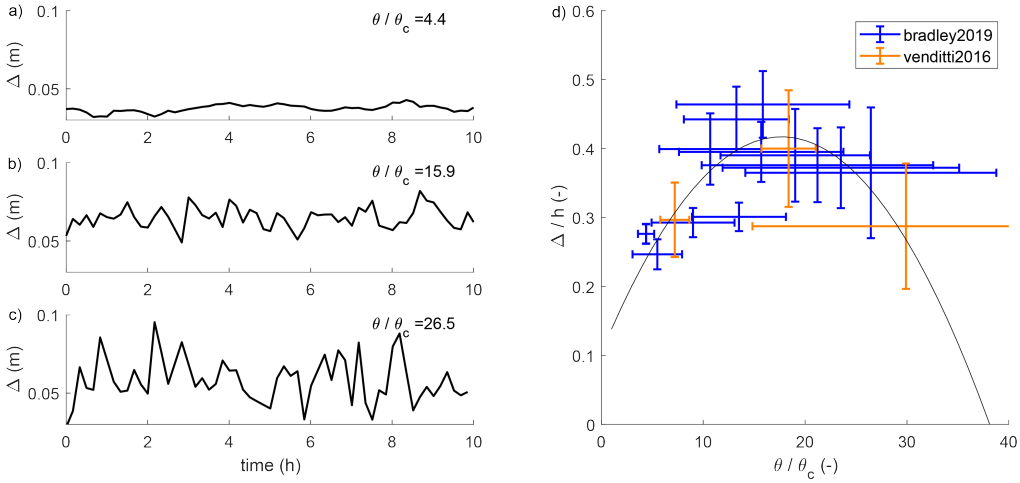


**Figure 5.1** | a-c) Dune height $\Delta$ over time for three experiments of Bradley & Venditti (2019), for three different transport stages $\theta/\theta_c$ (i.e., bed shear stress divided by critical shear stress). d) Variability in dimensionless dune height $\Delta/h$ increases with transport stage. Here, $h$ is time-averaged water depth. The predictive equation of Venditti & Bradley (2022) (equation 5.1) is shown in black. Coloured error bars indicate standard deviation for the experiments of Venditti et al. (2016) (red) and Bradley & Venditti (2019) (blue).

The increased variability in bedform height with increasing transport stage is visualised using the data of Venditti et al. (2016) and Bradley & Venditti (2019) in Figure 5.1. Bradley & Venditti (2019) stated a "tremendous variability" between bed states at a higher transport stage, and reasoned that numerous observations of the bed are needed to get an average bed state that actually scales with transport state. Saunderson & Lockett (1983) did experiments around the transition from dunes to plane bed. They found four different bed states (asymmetrical dunes, convex dunes, humpback dunes, and flat bed) that the bed alternated between. They attributed this behaviour to the close position of the system to a bed-phase boundary (from dunes to USPB). Also in Chapter 3, large variability at high transport stages was observed resulting in three different planforms, but no temporal data was acquired. Venditti et al. (2016) more thoroughly explored the variability at large transport stages, and they grouped the resulting geometries into three phases: a plane bed with washed-out dunes, a field of large dunes, and a field of small dunes. They observed that the transition between these phases was continuous, and that water depth, shear stress and water surface slope co-varied with bed state. During plane bed conditions, intense erosion on the flat areas lead to localised incision, followed by the formation of small or large bedforms, which in turn washed out into a flat bed. The time they observed between the phases varied between minutes to more than half an hour, with transitions between the phases happening in seconds or minutes.

Despite this phenomenon being observed for multiple decades, it has received little attention, and an explanation for the increase in variability in bedform geometry with increasing transport stage is lacking. In this study, we suggest a possible explanation for this behaviour, based on the theory of critical transitions (Scheffer et al., 2009, 2012; Lenton, 2013; Strogatz, 2018). This framework describes how sudden shifts to a qualitatively different (stable) regime can occur, once a system exceeds a critical bifurcation or tipping point. We hypothesise that in the transition from the dune regime towards upper stage plane bed, the bed exhibits flickering behaviour (Dakos et al., 2013), resulting from repeated state shifts between alternative stable states due to stochastic perturbations. To support this hypothesis, we reanalyse the data from Venditti et al. (2016) and Bradley & Venditti (2019) and show how the results seamlessly fit in the critical transition framework.

## 5.2 | Methods

### 5.2.1 | Temporal data of bed morphology

To test our hypothesis, we reanalyse the temporal bedform data obtained in Venditti et al. (2016) and Bradley & Venditti (2019), which are visualised in Figure 5.1. The experiments from both studies were executed in the River Dynamics Laboratory at Simon Fraser University, Canada. Their flume has an adjustable flow, recirculates water and sediment, and is 15 m long (12 m working section), 1 m wide and maximum 0.6 m deep. In both studies, the experiments were performed with unimodal sediment with a $D_{50}$ of 550 $\mu$m.



Venditti et al. (2016) conducted three experimental runs, under bed load, mixed load and suspended load-dominated conditions, resulting in mean flow velocities of 0.43, 0.59 and 0.87 m $s^{-1}$ with corresponding observed transport stages of 7.12, 18.3 and 29.7. These suspended load-dominated conditions were at the threshold of washing out. The bathymetry was measured every 10 minutes for the bed load and mixed load conditions, and every 5 minutes for the suspended load-dominated experiments. Measurements started after the bed already had fully adjusted to the flow.

Bradley & Venditti (2019) broadened the scope of these experiments by performing 15 experiments under five different transport conditions: threshold of motion, bed load, lower mixed load, upper mixed load, and suspended load-dominated conditions. Additionally, they varied the water depth in three steps between 15 and 25 cm, although for the highest water depth they only performed threshold and bed load-dominated experiments due to the capacity of the flume. These conditions resulted in a mean velocity of 0.43 and 1.1 m $s^{-1}$, and resulting mean transport stages between 4.4 and 26.45. They scanned the bed every 10 minutes, but only after the bed had fully adjusted to flow.

### 5.2.2 | Theoretical framework: critical transitions

The unstable behaviour close to the bed-phase boundary can be interpreted using the framework of critical transitions (Scheffer et al., 2009). A critical transition is a regime shift where a system shifts rapidly to a qualitatively different state or dynamical regime, once a critical threshold (a critical bifurcation or tipping point) is exceeded (Scheffer et al., 2009; Lenton, 2013). The framework of critical transitions has been successfully employed to interpret observations of large and rapid shifts, amongst others in ecology, climate dynamics, medicine and finance (Scheffer et al., 2012; Lenton, 2013), whereas it has found relatively little consideration in geomorphology (Hoitink et al., 2020). Many different types of tipping points exist, each described by different mathematical equations (Strogatz, 2018). Here, we focus on the so-called supercritical pitchfork bifurcation, as we hypothesise that this model system could explain the observed increase in bedform variability towards higher transport stages (Figure 5.1).

The simplest model that generates a supercritical pitchfork bifurcation is given by the following differential equation:

$$\frac{dy}{dt} = ry - y^3 \tag{5.2}$$

with state variable $y$, control parameter $r$ and time $t$. For $r < 0$, this differential equation has one equilibrium solution (i.e., where $dy/dt$=0), namely $\bar{y} = 0$. This equilibrium is stable to small perturbations (Strogatz, 2018), meaning that perturbations dampen out and the system returns to equilibrium. For $r > 0$, the solution $\bar{y} = 0$ becomes unstable, meaning that small perturbations amplify and the system moves away from its equilibrium when perturbed. For $r > 0$, two other stable solutions emerge, $\bar{y} = \pm\sqrt{r}$. When visualised in a stability diagram, which shows how equilibrium state $\bar{y}$ varies with $r$, this behaviour resembles a pitchfork; hence the name.

The increased variance with increasing transport stage (Figure 5.1d) can be explained by the emergence of a second equilibrium state, resembling the behaviour in a supercritical pitchfork bifurcation. However, instead of a "central" equilibrium solution that is independent of control parameter $r$, i.e. $\bar{y} = 0$, we expect this central equilibrium to be a parabola, similar to the dune height predictor (equation 5.1). We therefore substitute $y = -a + b\,r^2 + x$ in equation 5.2, with constants $a$ and $b$ and state variable $x$. Assuming that changes in $r$ are much slower than changes in $x$, we can write $dy/dt = dx/dt$, and equation 5.2 becomes:

$$\frac{dx}{dt} = r(-a + br^2 + x) - (-a + br^2 + x)^3 \tag{5.3}$$

Instead of the constant equilibrium $\bar{y} = 0$, the "central" solution of this modified pitchfork bifurcation now becomes a parabola, i.e. $\bar{x} = a - b\ r^2$, which again is stable for $r<0$ and unstable for $r>0$. For $r>0$, the two newly emerging solutions, $\bar{x} = a - b\ r^2 \pm \sqrt{r}$, are stable. These equilibria are shown in Figure 5.2, with stable equilibria indicated in solid black lines, the unstable equilibrium as a dashed black line, and the bifurcation point ($r$=0) as a black circle.

We hypothesise that the rapid shifts between high and low dune height observed at high transport stages (Figure 5.1c) are an expression of flickering. Flickering is a phenomenon described within the framework of critical transitions as a back-and-forth tipping between alternative stable states due to stochastic perturbations (Horsthemke & Lefever, 1984; Scheffer et al., 2012; Dakos et al., 2013). Indicators for flickering are multi-modality and a high variance (Scheffer et al., 2012; Dakos et al., 2012; Carpenter & Brock, 2006). As long as a system only has one stable equilibrium ($r<0$ in Figure 5.2a), observation time-series of system state will show a unimodal frequency distribution spread around the theoretical equilibrium solution (Figure 5.2b). However, once a second equilibrium solution emerges ($r>0$ in Figure 5.2a), the stochastic perturbations will occasionally cause the system to tip from one stable state into the other, which is reflected in a bimodally distributed system state (Figure 5.2d-f).

To illustrate flickering in the case of the modified pitchfork bifurcation, we generated a synthetic time series by numerically solving equation 5.3 while imposing continuous stochastic perturbations in $x$. We gradually vary control parameter $r$ over time, i.e. $r(t) = r(0) + \frac{dr}{dt}\ t$, with $\frac{dr}{dt}$ a fixed rate of change. We numerically discretise equation 5.3 over time using a 4th-order Runge-Kutta scheme (Strogatz, 2018):

$$\frac{dx}{dt} = f(x, t) \tag{5.4}$$

We then time-integrate the differential equation by calculating subsequent steps:

$$dx = f(x, t)dt + dW(0, \sigma_W) \tag{5.5}$$

where $dW(0, \sigma_W)$ is a white noise signal, i.e. a random number drawn at each time step $dt$ from a Gaussian distribution with mean 0 and standard deviation $\sigma_W$. In our case, $r(0)$ = -1, $dr/dt$ = 0.001, $dt$ = 0.01, $a$=1, $b$=1 and $\sigma_W$ = 0.05. This simple model demonstrates how flickering around the only existing equilibrium state $\bar{x} = a - b\ r^2$ for $r<0$ results in a unimodal frequency distribution of $x$, and a bimodal frequency distribution for $r>0$, with the modes corresponding to the two emerging stable solutions $\bar{x} = a - b\ r^2 \pm \sqrt{r}$.

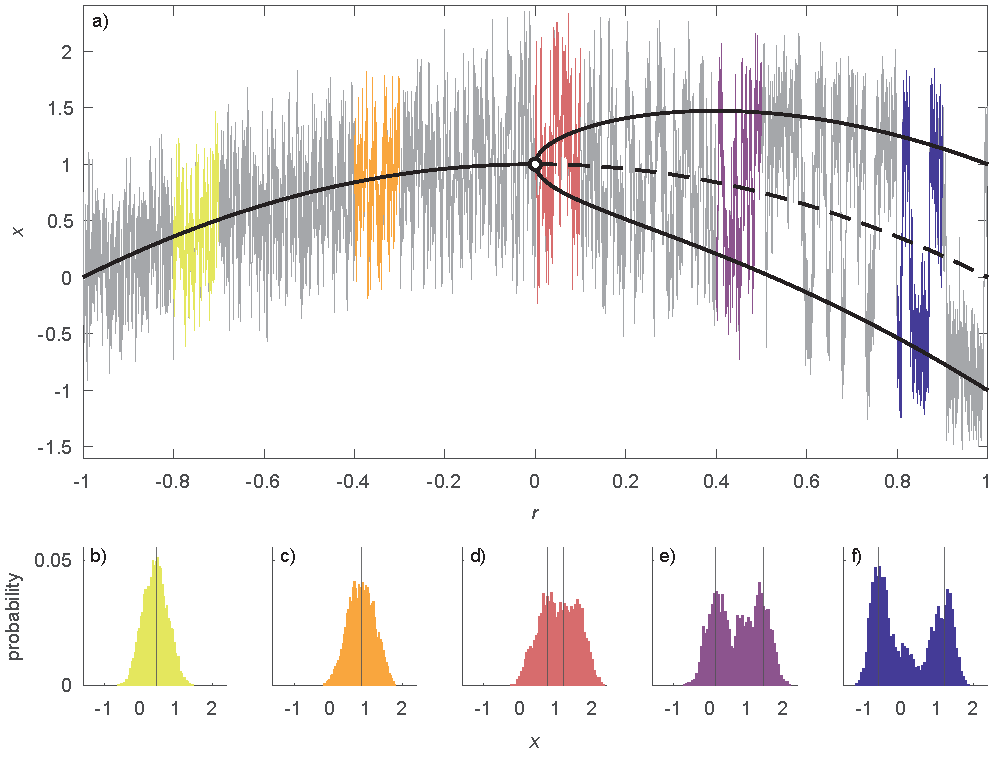


**Figure 5.2** | Model-generated flickering around a modified pitchfork bifurcation, i.e. the equilibrium solutions of equation 5.3. Solid black lines indicate stable equilibria, dashed black line indicates an unstable equilibrium, and the black circle indicates the pitchfork bifurcation point. Grey lines are simulated time series, i.e. the solution of the differential equation, with white noise added. Histograms of five time intervals are shown in corresponding colours below. Vertical black lines indicate the location of the stable equilibrium solution(s).

### 5.2.3 | Statistical analysis

To quantify variability in dune height, the standard deviation ($\sigma$) is determined as:

$$\sigma = \sqrt{\frac{\sum_{i=1}^{N} |x_i - \mu|^2}{N}} \tag{5.6}$$

in which $x_i$ are the observations, $\mu$ is the mean of the data set, and $N$ is the number of data points in the population.

To determine if a dune height distribution is bimodal, and to locate the modi of the distribution, a method based on Laplace's demon is used (Statisticat, 2021). This is a deterministic function that uses the kernel density of the dataset and reports a number of modes equal to half the number of changes in direction (i.e. where it switches from going up to going down). The function does not report modi that cover less than 10% of the distributional area.

If the distribution is indeed bimodal, the bimodality is considered significant if the distance between the two modi, $d_{modi}$, is larger than the coefficient of variation $CV$ (i.e. the normalised standard deviation):

$$CV = \frac{\sigma}{\mu} \tag{5.7}$$

## 5.3 | Results and Discussion

### 5.3.1 | Increasing variability of bedform height with transport stage

The raw data as shown in Figure 5.1 indirectly identify the increase of variability in dune height with transport stage. When this variability is expressed in the standard deviation $\sigma$ (equation 5.6), a significant linear relation ($R^2$ = 0.67) between transport stage and standard deviation in dimensionless dune height (Figure 5.3a) is revealed. Clearly, dune height becomes more variable with increasing flow strength.



From the 15 experiments analysed, nine of them were characterised by a bimodal distribution (Supplementary Materials Figure S1). The distance between the identified modi, $d_{modi}$, increases with an increasing transport stage (Figure 5.3b), featuring a significant linear relation ($R^2$ = 0.74). The modality of the distributions becomes significant if the distance between the modi is larger than the coefficient of variation, which is true for all experiments with a transport stage higher than 18. This behaviour is comparable to the increase in $d_{modi}$ as result of a pitchfork bifurcation (Figure 5.2).

### 5.3.2 | Emergence of a second bedform state

The observed increase in bed height variability with increasing transport stages can be interpreted as the emergence of a second equilibrium branch. This becomes apparent when visualising the raw data from Figure 5.1 in a two-dimensional histogram or density plot (Figure 5.4). For $\theta/\theta_c < 18$, the dune height observations are distributed in a relatively narrow zone around the theoretical dune height predictor (equation 5.1). The fitted modal distributions are either unimodal, or bimodal but with non-significant bimodality. For $\theta/\theta_c > 18$, the observations fan out towards higher and lower values of $\Delta/h$. For three different transport stages, the observed dune height distribution is significantly bimodal (Figure 5.3b).

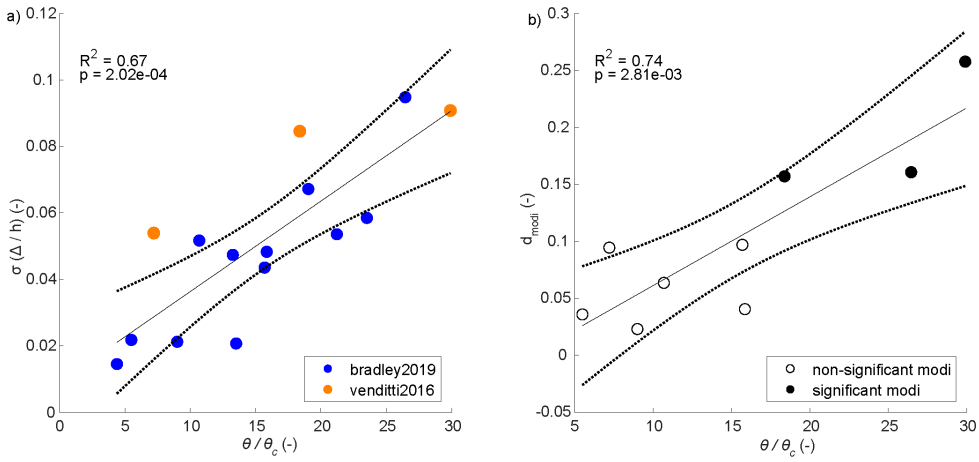


**Figure 5.3** | a) Standard deviation $\sigma$ of the dimensionless dune height $\Delta/h$ against transport stage $\theta/\theta_c$. b) The distributions of dimensionless dune height are often bimodal, and the distance between the modi ($d_{modi}$) increases with increasing transport stage. Significant bimodal distributions ($d_{modi} > CV$) are indicated with a filled marker; non-significant bimodality with an open marker.

For transport stages where dune heights are unimodally distributed, the parabolic dune height predictor (equation 5.1) is a good fit through these dune height modes. For transport stages where dune height is bimodally distributed (either with significant or non-significant bimodality), the dune height predictor is a good fit through the lowest modal value of of these bimodal distributions. For transport stages exceeding 18, the emergence of a statistically significant second mode at higher dune heights suggests a second equilibrium solution that branches off the parabolic dune height predictor, starting roughly at the top of the parabolic relation.

The pitchfork bifurcation (Figure 5.2) is no perfect model to fit to the observations. This bifurcation type shows a parabolic "central" solution that becomes unstable beyond the top of the parabola, and two diverging solutions branching off from there. Our observations, on the other hand, suggest that the parabolic solution itself remains stable for all transport stage values, but that a second solution branches off towards higher dune heights. Nonetheless, we consider the pitchfork bifurcation here, as it is the simplest mathematical model to illustrate how a second equilibrium can emerge beyond a tipping point (here: a critical transport stage), and how this may result in flickering between two states (Figure 5.1b, c) and bimodal dune height distributions with increasing spacing between modes (Figures 5.3 and 5.4).

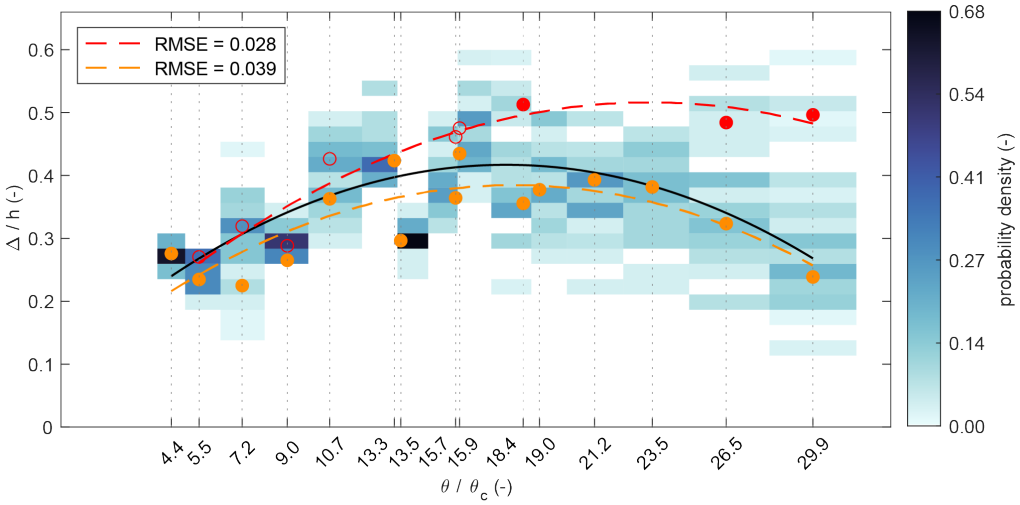


**Figure 5.4** | Density plot of the observations from Venditti et al. (2016) and Bradley & Venditti (2019), binned as a function of dune height $\Delta$ scaled by mean water depth $h$, and mean transport stage $\theta/\theta_c$. Mean values of transport stage are chosen since they are independent of the bed state. Orange bullets indicate the lower modal value found for that transport stage; red bullets indicate the higher modal value, if found for that transport stage. If the distribution for a specific transport stage is significantly bimodal, the red bullet marking the higher mode is filled; if non-significant, the red bullet is kept open. Quadratic relations were fitted through the orange bullets (orange dashed line) and through the red bullets (both filled and open; red dashed line). The black line indicates the dune height predictor (equation 5.1). Note that the vertical axis is divided into equidistant bins, while the transport stages along the horizontal axis are non-equidistant. Therefore, it was here assumed that, along the horizontal axis, each bin ranges until halfway between two subsequent transport stage values, which causes the bullets to not always be in the middle of the bins. For the left-most (right-most) transport stage value, the leftward (rightward) bin width is chosen the same as the rightward (leftward) bin width. Some tick labels along the horizontal axis are slightly displaced to avoid overlap, but ticks themselves are in the correct place.



### 5.3.3 | Physical explanation

We hypothesise that the changing states are a result of a temporary shift from suspended-dominated conditions to mixed- or bed load-dominated conditions. During bed load or mixed load conditions, there is a neutral or negative spatial lag between dune crest and maximum sediment transport rate, causing maintenance or growth of the dunes (Naqshband et al., 2017). During high flow conditions (suspended load dominated), a high concentration of sediment near the bed (Baas & de Koning, 1995; Naqshband et al., 2014a) causes the spatial lag to be positive, resulting in the washing out of dunes. Suspended load does not contribute to the migration of dunes (neither in subaqueous (Naqshband et al., 2017) or aeolian conditions (Courrech du Pont, 2015), but only to the deformation, causing a transition to plane bed (Naqshband et al., 2017; Naqshband & Hoitink, 2020). Washout conditions Best & Bridge (1992) found episodic short-lived outbursts of bed load sediment transport, that are also observed in aeolian transport (Livingstone et al., 2007; Butterfield, 1991; Baas &

Sherman, 2005). A local outburst of sediment (local erosion, or local disruptive pulses) can result into local bed- or mixed load conditions. This can temporarily result in dune formation, until suspended load conditions dominate and the bed flattens out.

The temporary formation of dunes and flattening out again could be the cause for the observed flickering. This flickering can be seen as noise-induced tipping. Noise-induced tipping means that a system is perturbed by a forcing whose time-scale is shorter than the system's intrinsic time scale (Ashwin et al., 2012; Scheffer et al., 2009). Local bed load conditions can cause the noise that tips the system. With an increase in transport stage, the likelihood of those outbursts to actually result into local bed load transport decreases, and local outbursts are more likely to be transported as suspended load. This means that the magnitude of the noise (i.e. the intensity of the local bed load conditions) decreases with increasing transport stage. Since a decrease in the lower modi of dune height is observed with an increasing transport stage (if the transport stage is larger than 18), it can be recognised that the magnitude of the noise scales with the state of the system (dune height), a phenomenon that is more generally observed in flickering processes (Dakos et al., 2013). Practically, this means that the system might eventually become 'trapped' in the stable state that is upper stage plane bed, while the alternative state becomes abandoned. This theory needs to be tested, as to date it is unclear if a fully stable USPB exists.

The observed flickering behaviour is not an artefact from the recirculating flume. Parker (2003) suggests that an artefact of recirculating flumes could be migrating lumps of sediment that persist for a long period of time until equilibrium is achieved. In the experiments of Venditti et al. (2016) and Bradley & Venditti (2019), a constant flow was applied until the bed reached equilibrium. Venditti et al. (2016) defined equilibrium conditions when no changes in the water depth and bed slope appeared anymore, which was after 72 hours for low transport stage runs, and after 30 hours for high transport stage runs. Bradley & Venditti (2019) allowed a constant flow of 10 to 25 hours depending on the transport stage until bedform height did not change anymore. Finally, Venditti et al. (2016) pointed out that one configuration is stable for a few minutes to half an hour. This indicates that there is no obvious regularity in the changes in bed configuration, which would be expected if this was due to migrating lumps in the recirculation system.

### 5.3.4 | Implications

Flickering alternative stable bed morphological states at high transport stages has several implications. At higher flow stages, the bed may not necessarily get flatter (by an increase in dune length), but rapidly switch between bed configurations. This means that one single snapshot is not enough to capture the state of the system. Field monitoring with multi-beam measurements at high flow stages only provide a

snapshot of the bed state, and accompanying logistical decisions (for e.g. high water protection, fairway depth, stability of buried pipes and cables) could not solely be based on this snapshot. At high flow conditions, many measurements in time are needed to get a complete appreciation of occurring bed states, and the large standard deviations here (Figure 5.1) indicate that mean values might be meaningless.

Laboratory experiments are known to be effective representations of the field, due to the natural scale independence of physical (geomorphological) processes (Paola et al., 2009). However, in scientific study designs, the repeatability of experiments should be considered. The presence of flickering behaviour results in serious dependence of the results to the timing of the measurements. This means that studies should not only focus on reproducibility (confirmation of the findings using different resources in an independent program), as suggested by Church et al. (2020), but also on repeatability (exact repetition of experiments to establish precision of results) of the experiments. When the temporal resolution of the measurements is less than the occurrence of flickering, there is a need for repetition of the experiments, because alternative bed states might not be detected. Geng et al. (2023) found that the development of a morphological system depends on the the initial bed conditions. The existence of multiple equilibria potentially increases the sensitivity to initial bed conditions, which once more stresses the need for repetition of experiments.



The classic equilibrium predictors might need to be revised to include this flickering behaviour. Although Bradley & Venditti (2019) already suggests the need for averaging many values, and Venditti & Bradley (2022) binned observations to obtain the equation relating dune height to transport stage, it is questionable if the average dune height is a relevant parameter when a bimodal distribution is featured with high transport stages. The equilibrium predictor is based on empirical relations fitted through averaged data, and may not grasp the right physical processes.

Future research about the flickering behaviour around the transition from dunes to USPB is critical, and longer high frequency time series of laboratory and field data should be acquired. A suggested next step could be detailed experimental observations of the critical transition over a longer (weeks) time scale. From this, the life time of the different phases could be determined (Arani et al., 2021), and a physical explanation for this phenomenon can be sought. This could be followed up by experiments using an increasing discharge over time, to observe the temporal changes in bed configuration and to confirm the type of tipping point.

## 5.4 | Conclusion

We reanalysed 15 laboratory experiments of bedform height over time from Venditti et al. (2016) and Bradley & Venditti (2019). The standard deviation and the bimodality of the datasets indicate flickering behaviour at high transport stages:

- The standard deviation of bedform height over time increases with an increasing transport stage. The bed can rapidly switch between bed configurations. The quantified distributions of bedform height show increasingly strong signs of bimodality. The distance between the two modi increases with increasing transport stage, and bimodality is significant for transport stages exceeding 18.
- The modi in the dune height distributions feature two branches. The lowest mode represents the branch that is also captured by the dune geometry predictor of Venditti & Bradley (2022). The other branch, that indicates the presence of large dunes at high transport stages, is not captured by the predictor.
- This behaviour is an indication that a second equilibrium state emerges for transport stages beyond approximately 18. Above this tipping point, repeated critical transitions triggered by stochastic perturbations (flickering) between the two alternative states results in the bimodal distribution as observed in the experiments.
- We hypothesise that this is the result of local outbursts of bedload sediment, resulting in a localised bedload transport, enabling dune growth. The likelihood that these outbursts actually result in local bedload conditions decreases with increasing transport stage, and decreasing averaged dune height. Therefore, the system eventually gets trapped in the upper stage plane bed-state, where perturbations are not strong enough to tip the system to the alternative state.
- The existence of flickering of a sediment bed has far-reaching consequences for field measurements, laboratory experimental design, and calls for reinterpretation of the classical equilibrium relations.

*Big whirls have little whirls,*
*That feed on their velocity.*
*And little whirls have lesser whirls,*
*And so on to viscosity.*
*— Lewis Fry Richardson*

# 6

# The contribution of dunes to hydraulic roughness

This chapter was originally published as:

de Lange, S.I., Naqshband, S., Hoitink, A.J.F. (2021). Quantifying hydraulic roughness from field data: can dune morphology tell the whole story? Water Resources Research 57(12). DOI:10.1029/2021WR030329

## Abstract

Hydraulic roughness is a fundamental property in river research, as it directly affects water levels, flow strength and the associated sediment transport rates. However, quantification of roughness is challenging, as it is not directly measurable in the field. In lowland rivers, bedforms are a major source of hydraulic roughness. Decades of research have focused on dunes to allow parameterization of roughness, with relatively little focus on field verification. This study aims to establish the predictive capacity of current roughness predictors, and to identify reasons for the unexplained part of the variance in roughness. We quantified hydraulic roughness based on the Darcy-Weisbach friction factor ($f$) calculated from hydraulic field data of a 78 km-long trajectory of the Rhine River and Waal River in the Netherlands. This is compared to predicted roughness values based on dune geometry, and to the spatial trends in the local topographic leeside angle, both inferred from bathymetric field data. Results from both approaches show the same general trend and magnitude of roughness values ($0.019 < f < 0.069$). Roughness inferred from dune geometry explains at best 31% of the variance. Efforts to explain the remaining variance from statistics of the local topographic leeside angles, which supposedly control flow separation, were unsuccessful. Unexpectedly, multi-kilometre depth oscillations explain 34% of the total roughness variations. We suggest that flow divergence associated with depth increase causes energy loss, which is reflected in an elevated hydraulic roughness. Multi-kilometre depth variations occur in many rivers worldwide, which implies a cause of flow resistance that needs further study.

## 6.1 | Introduction

Hydraulic roughness, which quantifies the resistance to flow by objects protruding into the water column (Chow, 1959), is a fundamental property in hydraulics. Due to its influence on water levels, flow structure and the associated sediment transport, understanding roughness is crucial to comprehend river dynamics. Quantification of hydraulic roughness is challenging, since it is not directly measurable in the field.

Hydraulic roughness at the bed of a main channel with abundant bedforms, consists of grain-friction drag and form drag. In lowland rivers, bedforms (bars, dunes, ripples) are typically the major cause of form roughness (Gates & Al-Zahrani, 1996; Julien et al., 2002). Form drag induced by dunes is estimated with predictors based on dune height and length (Bartholdy et al., 2010; Lefebvre & Winter, 2016; Soulsby, 1997; van Rijn, 1984). Many (semi-) empirical predictors are adjusted versions of the empirical roughness model of van Rijn (1984), and are mainly calibrated using flume data (Soulsby, 1997; Bartholdy et al., 2010). Unlike many others (Warmink, 2011; Engelund & Hansen, 1967), the predictor of van Rijn (1984) is also calibrated on field data, and the predictor by Lefebvre & Winter (2016) is based on numerical experiments. Unfortunately, the predictive value of those equations is often limited (Warmink et al., 2013), and there is a large variation in predicted roughness among alternative formulations (Warmink, 2011).

The limited predictive value can be attributed to two factors. First, hydraulic roughness is, just like bed shear stress, scale dependent (Vermeulen et al., 2013). In other words, roughness from a point measurement will be different from roughness integrated over a dune field, over a cross-section, or over a longitudinal transect (Buschman et al., 2009; Hoitink et al., 2009; Sassi et al., 2011; Hidayat et al., 2011). Roughness predictors are often empirical equations derived from laboratory flume studies and are based on an integration over 2D dunes in a dune field, with limited consideration of the scale-dependence. Secondly, relations drawn under laboratory conditions are translated to field situations by nondimensionalising the results. However, recent research has shown that dunes in laboratory settings have a steeper leeside angle than dunes observed in field conditions (Cisneros et al., 2020; Kostaschuk & Venditti, 2019; van der Mark et al., 2008). The slip face angle, the steepest part of the leeside, and the relative dune height determine the presence and strength of the flow separation zone (Best & Kostaschuk, 2002; Lefebvre & Winter, 2016; Lefebvre et al., 2016), and hence determine the total form roughness (Lefebvre et al., 2013). As a result, low-angle dunes produce less form roughness than angle-of-repose dunes (Lefebvre & Winter, 2016; Kwoll et al., 2016; Lefebvre et al., 2016). Relations drawn under laboratory conditions are therefore not directly applicable to field conditions and may lead to considerable uncertainties in model outcome (Warmink, 2011).

Roughness coefficients in numerical models are often calibrated based on measured water levels and discharges, instead of roughness predictors based on dune geometry. Unfortunately, those calibrated values are only valid for the conditions used for calibration (Klemes, 1986). To improve of operational models, it is essential to identify and quantify the spatiotemporal roughness variation, yet geographical insight into roughness is limited. Beyond using dune roughness predictors, bathymetric field data can be a potential source of knowledge about roughness induced by the river bed. In many lowland rivers, the bathymetry is measured regularly to control the navigation depth. Regular bathymetric measurements can identify spatiotemporal dynamics of bedforms, and disclose information about dune geometry. For example, recent research of de Ruijsscher et al. (2020) shows that geometrical properties of dunes change while they migrate over river banks, thereby exerting a different degree of resistance to the flow. The aim of this study is to establish the predictive capacity of well-established roughness predictors, and to identify reasons for the unexplained part of the variance in estimated roughness. We quantified the Darcy-Weisbach friction factor based on water surface slope measurements, over a trajectory of 78 kilometre of the main branch of the Rhine River in the Netherlands. We compare this to the predicted roughness value based on dune geometry, and to the spatial distribution of various measures of the leeside angle, both inferred from bathymetric field data. Ultimately, the insights could be used to improve roughness quantification in models, such as the state-of-the-art operational numerical flow model of the Rhine branches in the Netherlands. (RWS-WVL & Deltares, 2017).

## 6.2 | Field site

The study area is the lowland sand bedded part of the Rhine River with its main distributary, the Waal River. The Rhine River (also called Bovenrijn in Dutch) enters the Netherlands at Spijk at river kilometre (RK) 857, 5 km upstream of Lobith, and bifurcates into two branches (Waal and Pannerdensch Kanaal) at the Pannerdense Kop (RK 867). Our study area was the 78-km long reach (RK 857 - 935; Figure 6.1) of the Dutch part of the Rhine River, including its main branch, the Waal River. We focused on the reach between the Dutch border, and the location where the tidal motion starts to influence the water levels, near the city of Zaltbommel (RK 935).

The discharge entering the Netherlands at Lobith (RK 862) is on average 2300 $m^3\ s^{-1}$. It fluctuates significantly between 800 $m^3\ s^{-1}$ during low flow conditions, and reached up to 12,000 $m^3\ s^{-1}$ during a high discharge event in 1995 (Schielen et al., 2007). If the discharge exceeds 4000 $m^3\ s^{-1}$, floodplains convey part of the discharge. The main branch, the Waal River, receives about two thirds of the water discharge measured at Lobith (Schielen et al., 2007).

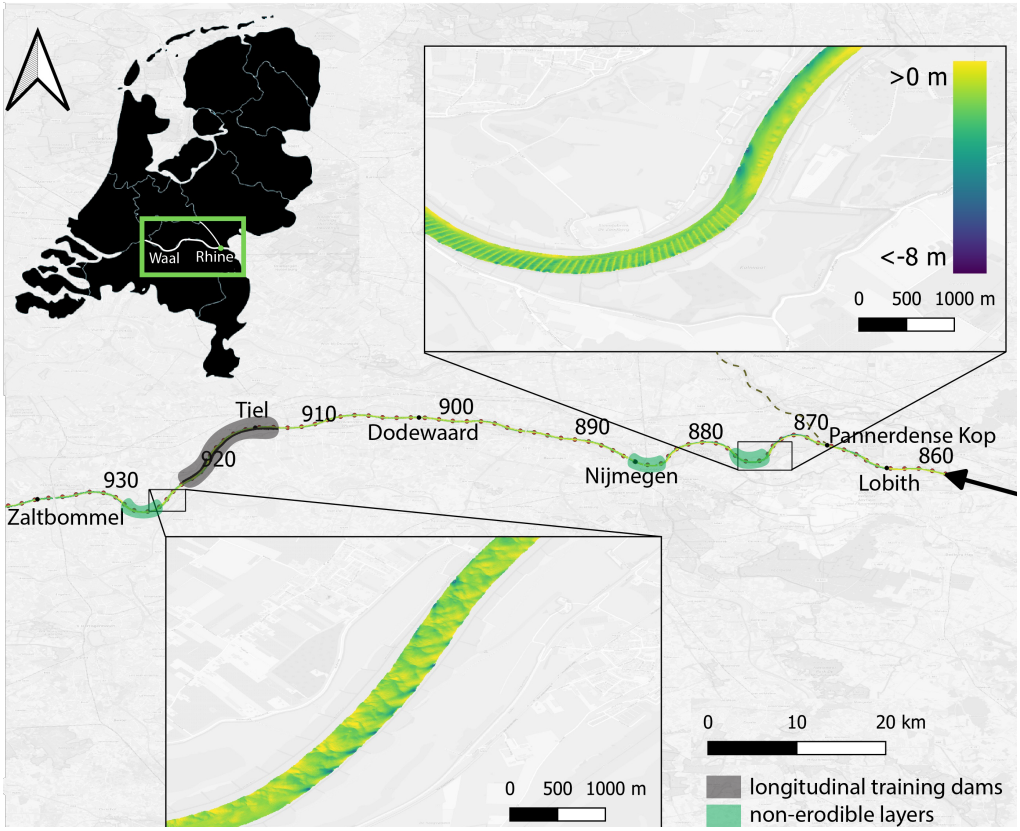


**Figure 6.1** | Overview of the study area (RK 857 to 935); consisting of the Rhine River and its main branch the Waal River in the Netherlands. The Rhine River bifurcates into the Waal River and the Pannerdensch Kanaal at the Pannerdense Kop (dashed line). The flow direction is from right to left. Non-erodible layers are located at RK 883-885 (Nijmegen), RK 925-928 (St. Andries) and RK 873-876 (Erlecom). Longitudinal training dams are located around Tiel. Each of the indicated sites has a gauging station. The inserts show local bathymetry (lower panel) and human interference by bendway weirs with a wavelength of 50 m, fixing the river bed (upper panel).



In this study area, the river changes from a river with relatively coarse sand and gravel to a fine sand bedded river. The width of the conducting section of the river channel varies between 220 m and 350 m, and generally increases in downstream direction. Bars and river dunes are ubiquitous in the river channel. They exist on multiple scales (de Ruijsscher et al., 2020; Zomer et al., 2021) and differences in dune dimensions are mainly caused by differences in grain size and discharge distribution (Wilbers & Ten Brinke, 2003). Just like dunes, the hydraulic roughness varies spatiotemporally (RWS-WVL & Deltares, 2017; Julien et al., 2002). The characteristics of the study area are summarised in Table 6.1.

The course of the Waal River is strongly influenced by artificial structures including groynes. Groynes are present on both river banks along the whole study area, extend 40 - 80 m into the main channel and are on average spaced 200 m apart (Yossef,

2004). Furthermore, three longitudinal training dams (LTDs) were constructed in 2014 and 2015 between river kilometres 912 and 921, (de Ruijsscher et al., 2020), replacing the groynes in the inner bends of the river. They split the river in a main channel and two bank-connected side channels of approximately 90 m width. Most field measurements were taken during the construction of the LTDs, and care should be taken when comparing data in this region from different months. Moreover, around Nijmegen (RK 883-885) and St. Andries (RK 925-928) fixed non-erodible layers in the outer bend (with a width of approximately 150 m) have been constructed (Sloff et al., 2006), and at Erlecom (RK 873-876) bendway weirs with a wavelength of 50 m fix the bed. Downstream of these layers, a long scour hole has developed, on average 3 m deep and 500 m long, and backwater raises water levels upstream. Therefore, the regions with a fixed bed were excluded from our current analysis.

**Table 6.1** | Overview of hydraulic conditions in the study area during the measurement period, derived from field data. Values are discretised per kilometre. *local variation is smoothed with an 8 km LOESS filter (Section 6.3.2.2). ** excluding bank connected side channels behind longitudinal training dams.

| | symbol | unit | mean | max | min | std |
|---|---|---|---|---|---|---|
| large-scale bed slope* | $S_0$ | - | $1.01\ 10^{-4}$ | $1.90\ 10^{-4}$ | $1.53\ 10^{-4}$ | $0.26\ 10^{-4}$ |
| large-scale pressure slope* | $S_p$ | - | $-0.19\ 10^{-4}$ | $0.42\ 10^{-4}$ | $-17.2\ 10^{-4}$ | $0.33\ 10^{-4}$ |
| width conducting section** | $W$ | m | 276 | 342 | 222 | 35 |
| water depth | $d$ | m | 4.5 | 5.6 | 3.5 | 0.4 |
| discharge at Lobith | $Q$ | $m^3\ s^{-1}$ | 1030 | 1664 | 772 | 83 |
| flow velocity | $u$ | $m\ s^{-1}$ | 0.84 | 1.06 | 0.44 | 0.12 |

## 6.3 | Methods

We describe the field data used for calculation of the Darcy-Weisbach friction factor, and for prediction of dune roughness. Then, we discuss a method to define local leeside angles. To assess how much of the variance in hydraulic roughness was explained by dune roughness predictors and leeside angle statistics, we introduce the coefficient of determination.

### 6.3.1 | Data availability and preprocessing

Field data were collected between 2014 and 2016 during periods of low river discharge, varying between 781 and 1353 $m^3\ s^{-1}$ at Tiel (RK 913; Table 6.2).

#### 6.3.1.1 | Water level and discharge

Gauging stations (at each indicated place name in Figure 6.1) continuously recorded 10-minute averages of the water level ($h$) with reference to the Amsterdam Ordnance Datum. The Dutch Ministry for Infrastructure and Environment, Rijkswaterstaat, calculated discharges at Lobith (RK 862), Pannerdense Kop (RK 867), and Tiel (RK 913) via a multistation rating curve. Water level and discharge data were made available

by RWS, and can be downloaded from their website (waterinfo.rws.nl). To correct for simplifications made in the rating curve and for recent changes in the system due to river training, we used 267 direct Acoustic Doppler Current Profiler measurement surveys from 2015 through 2017 to calculate a correction factor per location (see Section 6.3.2.2).

Three water surface slope profiles from Lobith (RK 862) until Zaltbommel (RK 935) were measured in July 2015, August 2015 and October 2016, corresponding with a river discharge at Tiel (RK 913) of 1270, 880 and 781 $m^3\ s^{-1}$, respectively (Table 6.2). The water surface surveys have yielded a high resolution profile (on average approximately 400 data points per km) of water level $h$ (m) and bed level $z$ (m) over the central axis. The water level was measured along the central axis by measuring the exact position of the vessel with a RTK GPS (Real-Time Kinematic Global Positioning System). The GPS measured with a frequency of 10 Hz and had an accuracy of 2 cm (Rijkswaterstaat, 2009). A virtual point on the vessel served as reference point, for which the pitch, roll and yaw (measured 50 times per second by a motion sensor) was used to correct the position. Subsequently, the measurements were related to the water level measured at gauging stations, which was used to correct the water surface slope profiles with a 95% confidence level. The average deviation between the measured water level with the sensor and the gauging stations during a survey was 0.11 m, 0.08 m and 0.02 m respectively. Fluctuations of water level during a measurement campaign due to slowly changing river discharge during the measurement period (about 24 hours), were in the order of a few centimeters, and were disregarded. Water surface slope profiles were measured during relatively low discharge conditions. This assured that only the main river channel was active, groynes were not flooded, and roughness imposed by the floodplains did not influence the water surface slope. Simultaneously with the water surface slope measurements, a singlebeam echosounder (SBES) scanned the underlying bathymetry along the same line. Corresponding multibeam echosounding (MBES) measurements in the same period were conducted separately on part of this transect, from the city of Dodewaard to Zaltbommel.



#### 6.3.1.2 | Multibeam echosounding

Data from a multibeam echosounder (MBES) were gridded onto a 1x1 $m^2$ grid by Rijkswaterstaat. Only grid cells with a minimum 10 hits per $m^2$ were analyzed, but in general a much larger number of data points were collected per cell. The resulting five MBES datasets contain $x$, $y$ and $z$ Cartasian coordinates. For two datasets an additional processing step was performed, where a surface was fitted through the individual points within the grid cell, resulting in an additional value for slope and orientation per grid cell. These two special campaigns contain data from the Dutch border (RK 857) until Zaltbommel (RK 935), measured in September 2014 and October and November 2014, over the whole river width. The average discharge at Tiel (RK 913) during the field measurements was 1249 $m^3\ s^{-1}$ and 1353 $m^3\ s^{-1}$ respectively

**Table 6.2** | Overview of field data in Cartesian coordinates. Water surface slope (WSS) measurements, with additional SBES bed-level measurements ($z$), were done at the same time as the three MBES campaigns. From these measurements, pressure slope ($S_p$) was derived. MBES campaigns measured $x$, $y$ and $z$, and two of the surveys measured an additional local topographic leeside angle $\gamma$.

| measurement type | field data | start date | duration (day) | discharge at Tiel ($m^3\ s^{-1}$) | survey range (RK) |
|---|---|---|---|---|---|
| WSS, SBES | $Sp$, $z$ | 6 July 2015 | 1 | 1271 | 857 - 952 |
| MBES | $x$, $y$, $z$ | 6 July 2015 | 12 | 1271 | 895 - 936 |
| WSS, SBES | $Sp$, $z$ | 5 Aug 2015 | 1 | 880 | 857 - 952 |
| MBES | $x$, $y$, $z$ | 5 Aug 2015 | 10 | 880 | 895 - 936 |
| WSS, SBES | $Sp$, $z$ | 12 Oct 2016 | 1 | 781 | 857 - 952 |
| MBES | $x$, $y$, $z$ | 12 Oct 2016 | 11 | 781 | 895 - 936 |
| MBES | $x$, $y$, $z$, $\gamma$ | 22 Sept 2014 | 12 | 1249 | 857 - 952 |
| MBES | $x$, $y$, $z$, $\gamma$ | 20 Okt 2014 | 7 | 1353 | 857 - 952 |

(Table 6.2). The surveys took approximately two weeks, wherein the river discharge was relatively constant. The discharge differences at the start and end of the surveys were 157 and 104 $m^3\ s^{-1}$, respectively.

The remaining three MBES datasets were taken around the same date as the water surface slope measurements (Section 6.3.1.1) and only comprise of $x$, $y$ and $z$ coordinates without the additional processing step for slope and orientation. They were limited to river kilometres 895 through 936 (Table 6.2).

Next, all bed-level data were converted from Cartesian ($x$, $y$) coordinates to curvilinear coordinates (s, n) maintaining the same spatial resolution (Vermeulen et al., 2014a). Herein, $s$ is the longitudinal direction, parallel to the river, and corresponds with river kilometres. $n$ is the cross-sectional direction, where $n$ = 0 m is defined as the river axis, which roughly coincides with the thalweg. Besides transformation of the $x$, $y$-coordinates, the vector rotation of the cells was calculated to transform the orientation of the fitted surface to the s-direction.

#### 6.3.1.3 | Grain size

Grain size samples were taken in 2020 with a Hamon Sampler, in which the upper 25 cm of the river bed was taken. The samples were taken at every 500 m at the centreline, and subsequently analysed with sieve sizes between 63 $\mu$m and 90 mm (Reneerkens, 2020). From this, the 50th and 90th percentile ($D_{50}$ and $D_{90}$) were determined.

### 6.3.2 | Parameters derived from field data

#### 6.3.2.1 | Determining river geometry from field data

The river geometry was parameterised by river width, cross-sectional area, curvature and transverse bed slope. Human-made structures fix the river width and curvature to near-constant values, however, cross-sectional area is dependent on water level.

River width $W$ (m) was determined from a polygon following a longitudinal river line through the groyne heads, and was taken constant over time. Under low discharge conditions, such as in this study, this measure was considered to be the discharge carrying section of the river. Assuming a trapezoidal shaped channel with a top width $W$, where the measured water depth represents the width averaged water level, and noting that the slope of the groynes equals $1/3$, the cross-sectional area $A$ ($m^2$) can be calculated. Curvature $r$ ($km^{-1}$) was defined as the inverse of bend radius, following the approach of de Ruijsscher et al. (2020). Finally, transverse bed slope $\xi$ (-) was defined as the slope between the two sides of the main river channel, longitudinally discretised in parts of 50m.

#### 6.3.2.2 | Determining hydraulic parameters from field data

The water depth $d$ (m) was calculated by subtracting the bed level $z$ from the water surface level $h$ obtained from the water surface surveys (Section 6.3.1.1). The bed level was derived from the corresponding bed-level measurements, which were taken simultaneously with the water-surface measurements. We chose to use bed-level measurements from the simultaneously taken SBES measurements, since the corresponding MBES measurements were not available over the full length of the study area. The validity of this procedure was checked by constructing a filtered width-averaged bed level from these three MBES surveys and comparing this with the filtered SBES profiles in the part of the study area where there was data available from both datasets. The datasets showed a very similar large-scale bed-level profile (correlation $> 95\%$), hence the use of the SBES dataset is acceptable.

River discharge $Q$ ($m^3\ s^{-1}$) at Lobith (RK 862), Pannerdense Kop (RK 867) and Tiel (RK 913) was calculated via a multi-station rating curve, and was subsequently corrected with a correction factor derived from Acoustic Doppler Current Profiler measurements (a fifth degree polynomial fit; see supplementary information Figure S1). Before correction, the discharge at Tiel was generally underestimated (up to 15%) while at Lobith, the rating relations could overestimate the discharge up to 10%. Discharge was set constant between Lobith and the Pannerdense Kop since no major confluences or bifurcations occur. From there until Tiel, discharge was assumed to vary linearly due to several small supply and drainage channels. From Tiel until Zaltbommel, discharge was considered to be constant. At the section of the LTDs, approximately 12 percent of the discharge was conveyed by the bank connected side channels (de Ruijsscher et al., 2019; Sieben, 2020). Width-averaged flow velocity $u$ ($m\ s^{-1}$) was determined by dividing the discharge in the main channel by the cross-sectional area between the groynes.

### 6.3.3 | Roughness inferred from water surface slopes

We estimated the Chézy coefficient directly from field measurements according to:

$$C = \frac{u}{\sqrt{d(S_0 - S_p - \frac{\partial Qu}{\partial s}\frac{1}{gA})}} \tag{6.1}$$

where $u$ = depth-width averaged flow velocity (m $s^{-1}$), $s$ = longitudinal river distance (m), $d$ = water depth (m), $S_0$ = bottom slope (= $\partial z/\partial s$, in which $z$ = bed level relative to Amsterdam Ordnance Datum, m), $S_p$ = pressure slope (= $\partial d/\partial s$), $Q$ is discharge ($m^3$ $s^{-1}$) and $A$ is cross-sectional area ($m^2$). Appendix 6 offers a derivation of equation 6.1. For uniform flow, the expression reduces to the Chézy equation.

All input parameters were discretised per kilometre, after smoothing with an 8 km LOESS filter (de Ruijsscher et al., 2018; Cleveland, 1979; Cleveland & Devlin, 1988). This span was considered to be the best trade-off between accuracy and resolution of the Chézy coefficient (see supplementary information Figure S2). From the Chézy coefficient, we calculated the dimensionless Darcy-Weisbach friction factor according to (Silberman et al., 1963):

$$f = \frac{8g}{C^2} \tag{6.2}$$

where $g$ = gravitational acceleration (m $s^{-2}$).

### 6.3.4 | Roughness predicted from dune characteristics

Existing roughness predictors based on primary dune characteristics including length ($\lambda$), height ($\Delta$) and leeside angle ($LSA$) were used to determine form roughness. Those characteristics were determined using a well-established Bedform Tracking Tool (BTT) (van der Mark & Blom, 2007), following the methodology described by de Ruijsscher et al. (2020).

The MBES bed-elevation data were initially detrended by subtracting a reference surface from the Dutch national water authority based on the minimum depth of the fairway, established for dredging. A longitudinal river profile was constructed at the central river axis, and from this, bedform characteristics were determined. A filter span constant c = 1/6 was chosen to filter out small features, which means that the length on which filtering takes place is 1/6 of the main bedform length. Two bedform lengths of interest were defined (Zomer et al., 2021): 5 m ±5 (hereafter referred to as superimposed bedforms) and 100m ±30 (hereafter referred to as dunes), and the corresponding span values ($P0$) were used as input for detrending the profile (Figure 6.2). Bedforms smaller than 5 m could not be detected due to the grid cell size of 1 x 1 $m^2$.

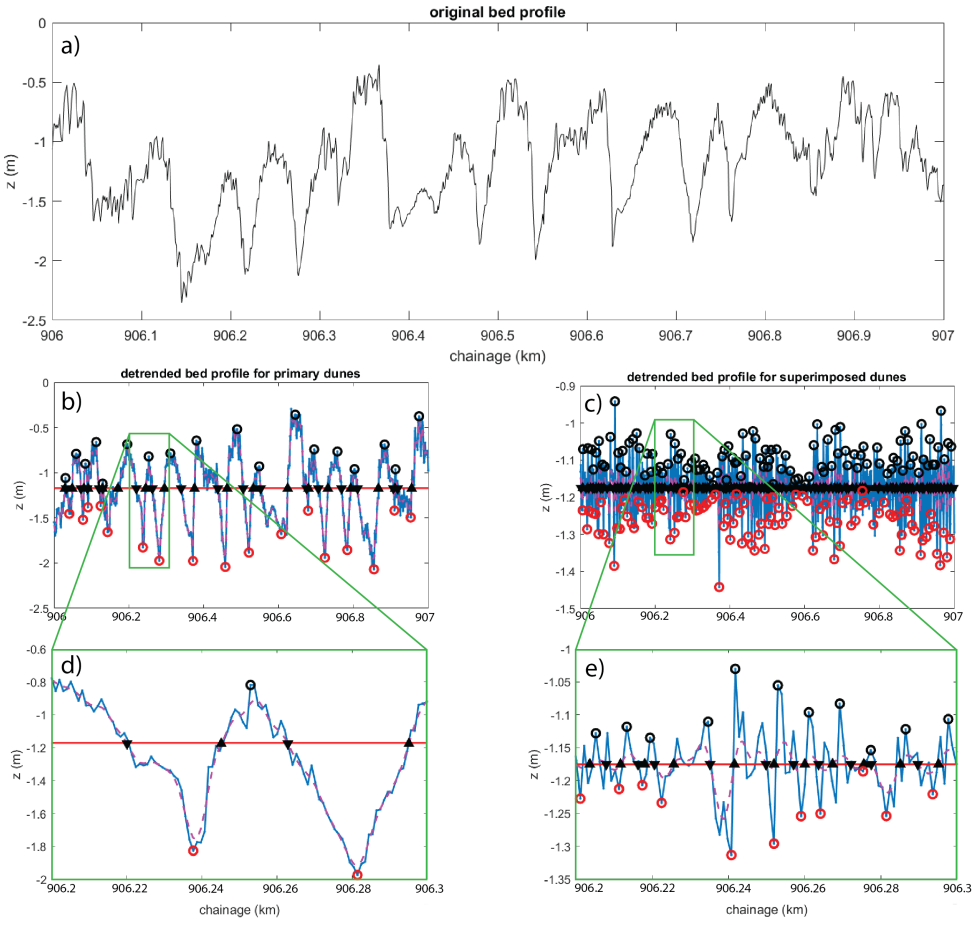


**Figure 6.2** | Dune characteristics were defined from the original bed profile (a) using the Bedform Tracking Tool by van der Mark & Blom (2007). Detrending and filtering was based on two span values (*P0*), one for primary dunes (b, d) and one for superimposed bedforms (c, e). Circles indicate crests (black) and throughs (red), triangles indicate crossings with the zero line.

The span values were based on a spectral analysis to determine the dominant wave lengths in each section. The bedform lengths of interest (estimated bedform length) was also an input parameter for the smoothing of the profile. Based on the zero-crossings profile (Figure 6.2), dune characteristics were described every kilometre. We only considered the three characteristics which are used in the roughness prediction equations: dune height $\Delta$ (m), i.e. the vertical distance between dune top and downstream trough, dune length $\lambda$ (m), i.e. the horizontal distance between two subsequent crests, and leeside angle $LSA$ (°), obtained from a linear fit of the leeside of the dune, excluding the upper and lower 1/6th of the dune height (van der Mark & Blom, 2007). Dune steepness $\Delta/\lambda$ can readily be inferred from this.

Form roughness ($f_f$) imposed by dunes can be predicted employing several previously developed equations, which commonly require primary dune height and length as input. The total predicted hydraulic roughness ($\hat{f}$) consists of form friction ($f_f$), and grain friction ($f_g$) (Einstein, 1950). Under the assumption that dunes are the fundamental structures causing form resistance, we calculated the total predicted hydraulic roughness using various approaches described below.

van Rijn (1984) developed an equation based on calibration of field and lab data.

$$\hat{f} = \frac{8g}{(18\log(\frac{12d}{k_s}))^2} \tag{6.3}$$

in which $k_s$ consists of roughness height $k_{sf}$ and grain roughness height $k_{sg}$:

$$k_s = k_{sg} + k_{sf} \tag{6.4}$$

$$k_{sg} = 3D_{90} \tag{6.5}$$

in which $D_{90}$ is the 90th percentile of the grain size distribution,

$$k_{sf} = 1.1\gamma_d\Delta(1 - e^{\frac{-25\Delta}{\lambda}}) \tag{6.6}$$

and $\gamma_d$ is taken as 0.7 in field conditions.

Soulsby (1997) used a different formulation for $k_{sf}$:

$$k_{sf} = 30(\Delta^2/\lambda) \tag{6.7}$$

Bartholdy et al. (2010) defined $k_{sf}$ as:

$$k_{sf} = 0.57\Delta \tag{6.8}$$

Lefebvre & Winter (2016) developed a new equation based on numerical experiments, including leeside angle, in which form friction is reduced for dunes with a low leeside angle.

$$f_{f,reduced} = f_f\theta_{red} \tag{6.9}$$

in which:

$$f_f = \frac{1}{19.75log(\frac{d\lambda}{\Delta^2}) - 20} \tag{6.10}$$

$$\theta_{red} = \frac{1}{1 + e^{-0.3LSA+5.9}} \tag{6.11}$$

To calculate the total hydraulic roughness, they summed grain roughness and form roughness as in $\hat{f} = f_f + f_g$. Herein, grain roughness was assumed to only depend on grain size distribution and water depth, and was calculated following the approach of van Rijn (1984).

$$f_g = \frac{8g}{(18\log(\frac{12d}{3D_{90}}))^2} \tag{6.12}$$

### 6.3.5 | Analysis of leeside angle statistics

We explored if hydraulic roughness variability was correlated to leeside angles, by inferring hydraulic roughness information from MBES data avoiding assumptions about bedforms. To do so, we calculated the local topographic leeside angle $\gamma$ (°) for each square metre in the fairway, based on the two MBES surveys that allow to do so. If the orientation of a slope in the 1 m x 1 m tile was directed downstream, defined as within $\pm$ 30° of the central axis -approximately parallel to the flow direction-, the slope was defined as the leeside.

The MBES data were influenced by side effects such as groynes. To purely focus on the fairway of the river, the groyne influenced part of the river bed was disregarded (Figure 6.3 and supplementary information Figure S3). To identify the part influenced by groynes, the river was subdivided in sections of 1 km in the stream-wise direction, and 1 m in the transverse direction. In these sections, the gradient of the adjacent mean leeside angles was taken and smoothed with a 20 point moving average filter. If the gradient at a certain river width was larger than an absolute value of 0.19, data at a larger width was removed from the analysis. This threshold of 0.19 coincides with 3 times the standard deviation of the gradient of the mean leeside angle in the central 100 m of the river, which was relatively undisturbed by side effects.

The mean local topographic leeside angle $\gamma$, calculated from 1 m x 1 m tiles of the river bed, was averaged over the river width and over 1 km along the river. It therefore includes the characteristics of 3D variations in bed geometry over the full width of the non-groyne influenced river bed.

### 6.3.6 | Coefficient of determination as a tool for explaining variance

The coefficient of determination ($R^2$) shows how much of the variance in hydraulic roughness $f$ is explained by the predictors.

$$R^2 = 1 - \frac{SS_{res}}{SS_{tot}} \tag{6.13}$$

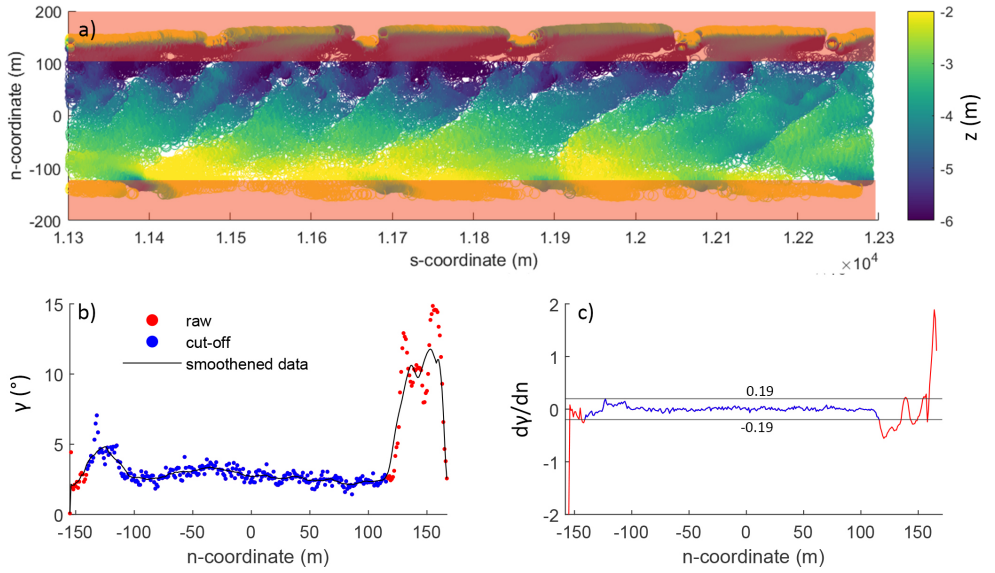


**Figure 6.3** | Method to remove the groyne influenced part of MBES data. a) example of a groyne-influenced bathymetry, in which the red shaded area is defined as the groyne-influenced part. b) mean leeside angle over the cross-section, averaged per kilometre. c) gradient of the mean local topographic leeside angle. When exceeding three times the standard deviation of the gradient of the mean leeside angle of the middle 100 m of the river (0.19), all data at a larger width is excluded from the analysis (red line).

$$SS_{tot} = \sum_i (f_i - \overline{f})^2 \tag{6.14}$$

$$SS_{res} = \sum_i (f_i - m_i)^2 \tag{6.15}$$

in which $SS_{tot}$ is the total sum of squares, $SS_{res}$ the residual sum of squares, $f_i$ the i$^{th}$ observation of $f$, $\overline{f}$ the mean of the observations $f$ and $m_i$ the i$^{th}$ model prediction output. $R^2$ will have a value below 1. A value between 0 and 1 explains how much of the variance of the observation is explained by the model, and values below 0 indicate that the model performs worse than simply taking the average of the observations. The coefficient of determination, $R^2$, is only equal to the square of the correlation, if a linear regression with an offset is applied. In this manuscript, we chose to use the coefficient of determination which shows the correlation also for non-linear relations. Uncertainty is quantified as the standard deviation of the residuals. The residuals were calculated as the difference between the modelled values (the predicted roughness, $\hat{f}$) and the observations (the roughness from water surface slope, $f$).

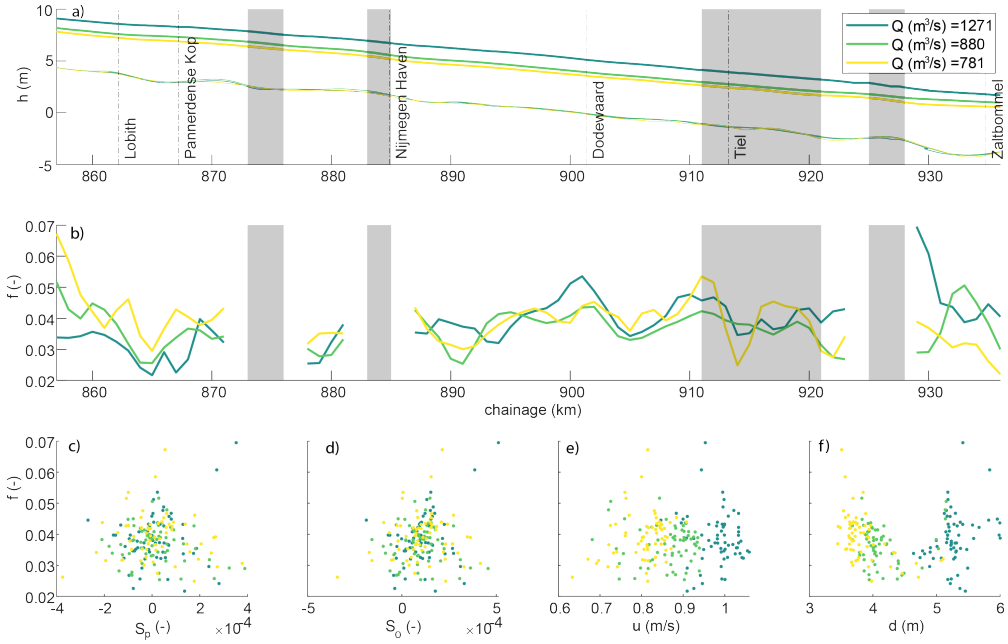


**Figure 6.4** | Water surface slope and the corresponding friction factor for three different discharges. Shaded grey bars indicate human-made structures in the main channel (fixed layers, bendway weirs and longitudinal training dams at Tiel). a) water surface (thick lines) and bed surface (thin lines) throughout the study area. b) friction factor $f$ calculated with equation 6.1. c-f) relation between friction factor and pressure slope, bed slope, flow velocity and water depth

# 6.4 | Results

## 6.4.1 | Roughness inferred from water surface slopes

Figure 6.4A shows the water surface profiles during the three surveys, indicating a relatively constant water surface slope over distance, for all three discharge conditions. Derived values of $f$ fluctuated between 0.019 and 0.069 (Figure 6.4c). With a mean of 0.035, the Waal River can be characterised as a natural, winding stream (Fetter, 2001). A low discharge, and correspondingly low flow velocities, generally resulted in a high roughness ($f$ averages 0.037, 0.034, 0.033 at a discharge of 1271, 880, 781 $m^3\ s^{-1}$ respectively). This is especially visible upstream of the Pannerdense Kop (RK 867), while downstream this apparent relation between roughness and discharge becomes less clear.

### 6.4.2 | Roughness predicted from dune geometry

#### 6.4.2.1 | Grain size and dune geometry observations

Grain size changed significantly over the study reach, with a $D_{50}$ ranging from 10 mm upstream to 0.7 mm downstream (Figure 6.5a). This decrease in grain size was reflected in a decrease in grain-related roughness.

Spatial variation in bedform geometry was substantial. Bedform height averaged per kilometre varied between 0.1 m and 1.5 m, with an average of 0.7 m (Figure 6.5c). Between Lobith and Pannerdense Kop (RK 857-867), an almost flat bed was observed. Dune height was almost zero in the first 8 kilometres, and increased downstream, but did not exceed 0.7 m (excluding the bendway weir at Erlecom (RK 873-876). Relatively constant dune heights, lengths and leeside angles were observed between river kilometres 885 and 915. Leeside and stoss side angles followed the same spatial trends as dune height and length. Throughout our whole research transect, smaller dunes were imposed on the primary dunes. Those superimposed dunes, or secondary dunes, were on average 0.1 m high and 10 m long, and were clearly distinguishable from the primary dunes being on average 0.7 m high and 55 m long. Additionally, in certain locations the bed geometry was imposed by the fixed layers. For example, in Erlecom (RK 873-876) the sine shaped fixed layer was clearly visible by a deviating "dune" length of 50 m and a height of 1.5 m (Figure 6.5d, e).

Temporal variation in dune geometry was smaller than spatial variation. A higher discharge generally resulted in higher dunes (on average 0.76 m, 0.82 m, 0.78 m, 0.67 m and 0.58 m between river kilometre 895-936 for $Q$ = 1353, 1271, 1249, 880 and 781 $m^3\ s^{-1}$, respectively; Figure 6.5). No obvious relation between dune height and water depth was found, neither in space nor for varying discharges.

#### 6.4.2.2 | Dune roughness prediction

Predicted values of the roughness coefficient ($\hat{f}$) followed the same pattern and were in the same order of magnitude as the values of $f$ inferred from the water surface slope (Figure 6.6). The general trend shown by all predictors reflected a relatively low roughness between Lobith and Pannerdense Kop (RK 857 - 867), and an increase in roughness between river km 885-925, followed by a slight decrease until the city of Zaltbommel (RK 935). Between Lobith and the Pannerdense Kop, almost all hydraulic roughness was caused by grain roughness (Figure 6.6), and grain size seemed to provide an upper limit for the predicted dune roughness values. More downstream, dunes increased in size (Figure 6.5) and the difference between total roughness and grain roughness also increased.

The alternative predictors performed differently, and not all variations in roughness inferred from the water surface slopes were captured (Figure 6.6). The differences between alternative predictors reached 0.021. At certain locations, the predicted dune

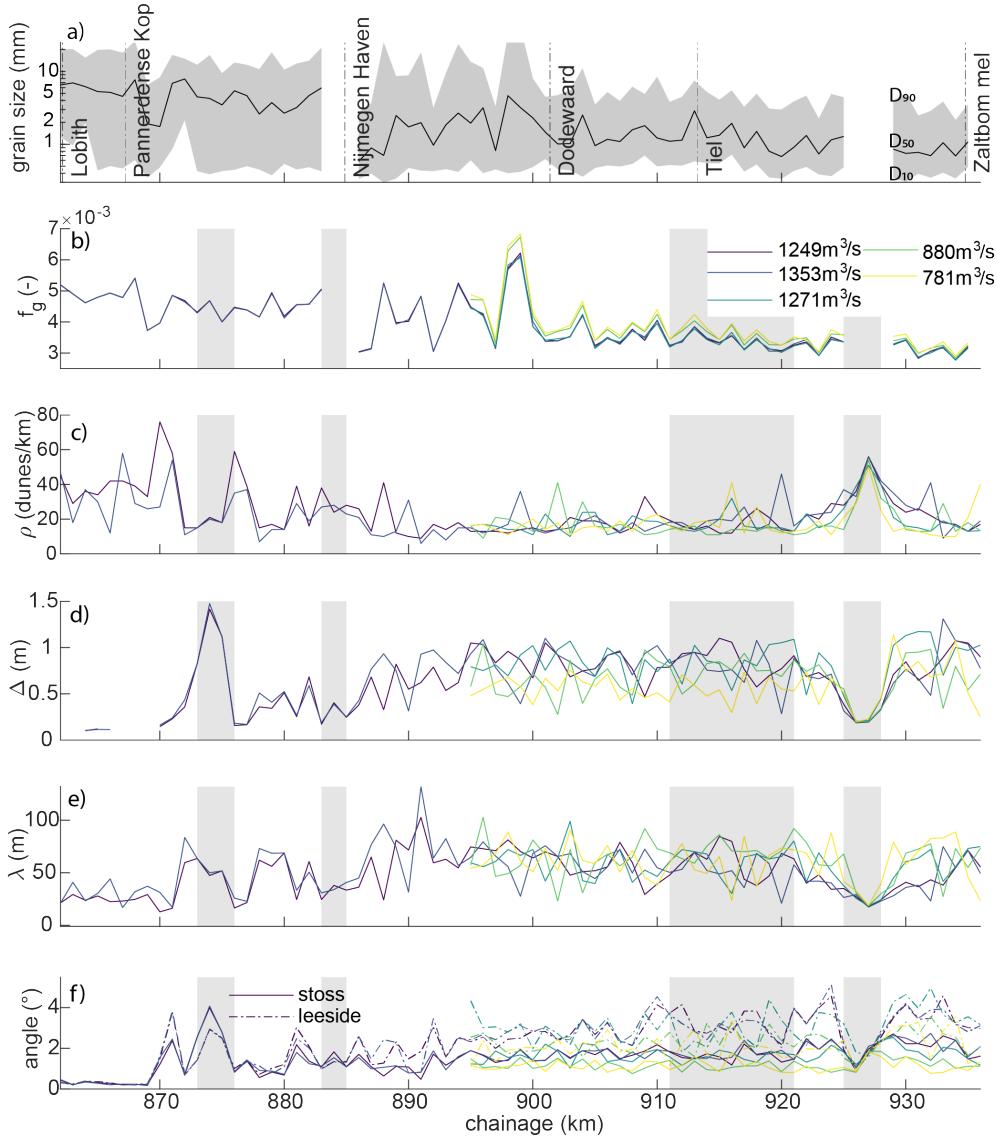


**Figure 6.5** | Dune geometry and grain size characteristics. a) Grain size. Solid line represents $D_{50}$, the shaded area $D_{10}$ (lower limit) and $D_{90}$ (upper limit). b) grain roughness, calculated with equation 6.12, for various discharges at Tiel. c) Bedform density (dunes/km). d) mean bedform height (for $\Delta > 0.2$ m). e) mean bedform length. f) stoss and leeside angles. Shaded grey bars indicate human-made structures in the main channel (fixed layers, bendway weirs and longitudinal training dams at Tiel).

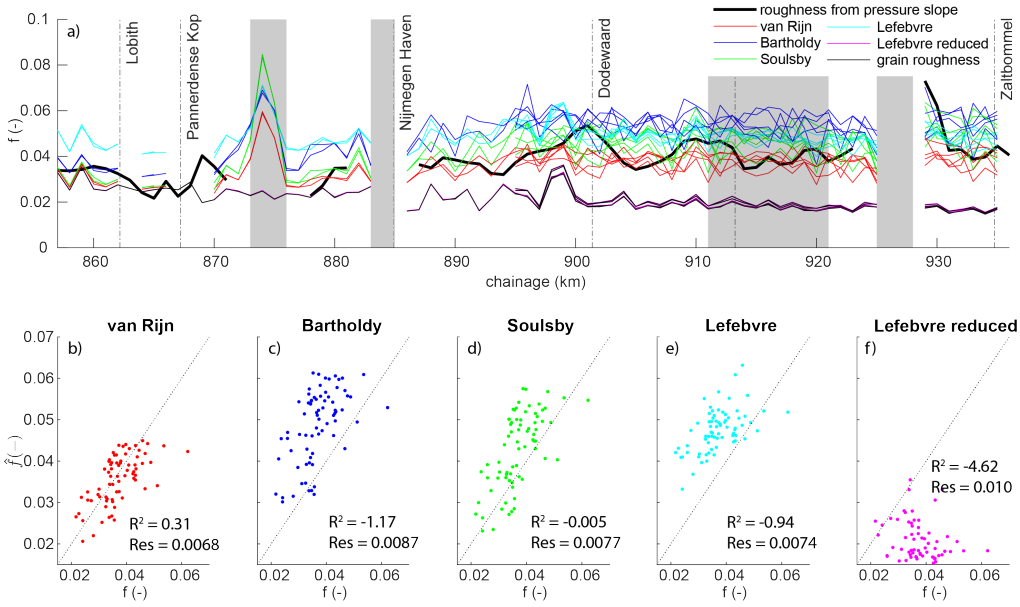


**Figure 6.6** | Dune roughness. a) estimates from various predictors (coloured lines) for various discharges (not differentiated) and roughness derived from the water surface slope, WSS. See Section 6.3.4 and 6.3.3 for corresponding equations. Shaded grey bars indicate human-made structures in the main channel (fixed layers, bendway weirs and longitudinal training dams at Tiel). b-e) relation between predicted roughness by various predictors and roughness calculated with the water surface slope. Values of the corresponding coefficient of determination ($R^2$), and standard deviation of the residuals (Res) are shown in the corresponding panels.

roughness by Bartholdy et al. (2010) was 1.6 times as high as the predicted roughness by van Rijn (1984). The equation by Lefebvre & Winter (2016), accounting for the low leeside angle, strongly under-predicts the roughness. Variations in roughness due to changing discharge conditions were strikingly smaller than differences related to the choice of predictor. The coefficient of determination ($R^2$) shows how much of the variance in $f$ is explained from $\hat{f}$ for various predictors. For example, $R^2$ for $\hat{f}$ predicted with van Rijn (1984) is 0.31, meaning that 31% of the variability of $f$ has been explained. The other predictors exhibit similar trends, yet they all have an $R^2$ value of less than 0. This means they perform worse than simply taking the average of the roughness inferred from water surface slope data.

### 6.4.3 | Relation between roughness and leeside angle statistics

The mean local topographic leeside angle was on average 3.5°, which is slightly higher than the mean dune leeside angle (being 2.3°). The distribution of the low topographic leeside angle was highly positively skewed, meaning low angles dominated and higher angles were less frequently occurring (see supplementary information Figure S4). A very low mean local topographic leeside angle was observed until the

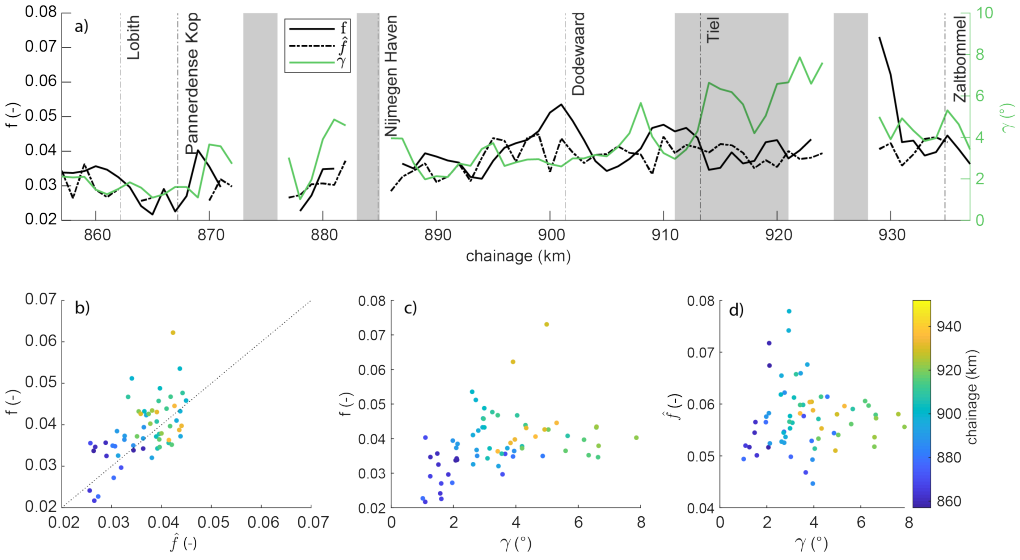


**Figure 6.7** | Relation between roughness from water surface slope ($f$), roughness predicted from dune geometry ($\hat{f}$) and local topographic leeside angle ($\gamma$), against chainage, and their relation. Dune roughness calculated with the predictor of van Rijn (1984). Compared data comes from different datasets with comparable discharge ($Q$ = 1271 and 1249 m$^3$ s$^{-1}$). Shaded grey bars indicate human-made structures in the main channel (fixed layers, bendway weirs and longitudinal training dams at Tiel).

.

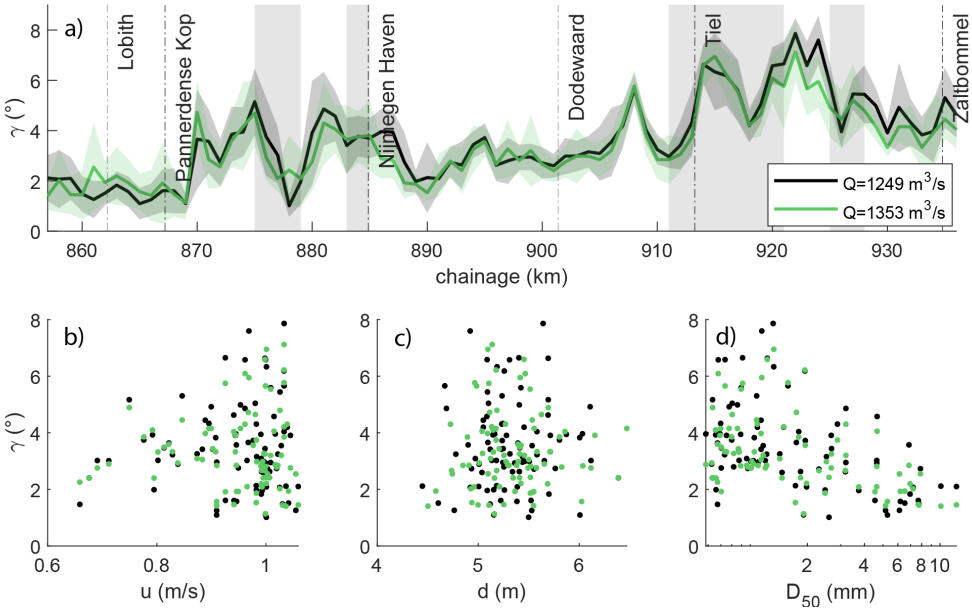


**Figure 6.8** | Local topographic leeside angle for two discharges, and its relation with flow velocity, river depth and median grain size. Shaded grey bars indicate human-made structures in the main channel (fixed layers, bendway weirs and longitudinal training dams at Tiel).

Pannerdense Kop (RK 867; mean 1.7°; Figure 6.8). Further downstream, the topographic leeside angle slowly increases until Tiel (RK 913). The trends were similar for both discharge conditions. Other statistical measures of the local topographic leeside angle follow the same pattern.

Mean local topographic leeside angle seems to be unrelated to flow velocity or water depth, and grain size sets an upper limit by limiting sediment mobility (Figure 6.8b-d). The coefficients of determination ($R^2$) between $\gamma$ and $f$ were negative, which contradicts our suspicion that mean leeside angles can better explain effective roughness than roughness predictors based on dune height and length (Figure 6.7).

### 6.4.4 | Influence of depth variation

Since dune predictors explain less than one third of the variance of $f$, it is likely that other roughness imposing elements cause a significant contribution to hydraulic roughness. Figure 6.9 shows variations in river geometry: the longitudinal river profiles of the detrended bed elevation, width, curvature, transverse bed slope ($\xi$), detrended stream-wise bed-elevation gradients ($dz_{det}/ds$) and the friction coefficient. For consistency, we show figures based on the two most comparable datasets ($Q$ = 1271 m$^3$ s$^{-1}$ and 1249 m$^3$ s$^{-1}$), and quantify dune roughness with equation 6.3 (van Rijn, 1984).

Two different areas can be distinguished in Figure 6.9d, up and downstream of RK 893. Downstream of RK 893, values of $f$ show a clear, persistent, out-of-phase relation with the gradient in bed elevation. To the authors' knowledge, such relation has never been established before. The downstream stretch is relatively straight, with persistent dune fields and relatively small fluctuations in the regional bed level. It is characterised by large dunes (mean $\Delta$ = 0.81m) with a relatively high leeside angle (mean $LSA$ = 3.0°, mean $\gamma$ = 4.4°), a comparatively small difference between hydraulic roughness and the roughness predicted based on dune geometry ($f$ - $\hat{f}$ = 0.005), small fluctuations in the smoothed detrended bed level (standard deviation of $z$ = 0.1) and a negative coefficient of correlation between $f$ and $dz/ds$ (corr = -0.67, see Figure 6.10). The negative coefficient of correlation indicates an inverse relation between smoothed detrended bed level and roughness. Upstream of RK 893, the out-of-phase relation between $dz_{det}/ds$ and $f$ is lost. This is a highly diverse reach, with coarse sediment, large fluctuations in grain size (Figure 6.5), impacts of fixed layers, and strong curvature (Figure 6.9). The reach is characterised by low dunes (mean $\Delta$ = 0.3m) with a low leeside angle (mean $LSA$ = 1.2°, mean $\gamma$ = 2.4°), a large difference between the hydraulic roughness and roughness predicted based on dune geometry ($f$ - $\hat{f}$ = 0.01), and large fluctuations in the smoothed, detrended bed level (standard deviation of $z$ = 0.2, Figure 6.10).

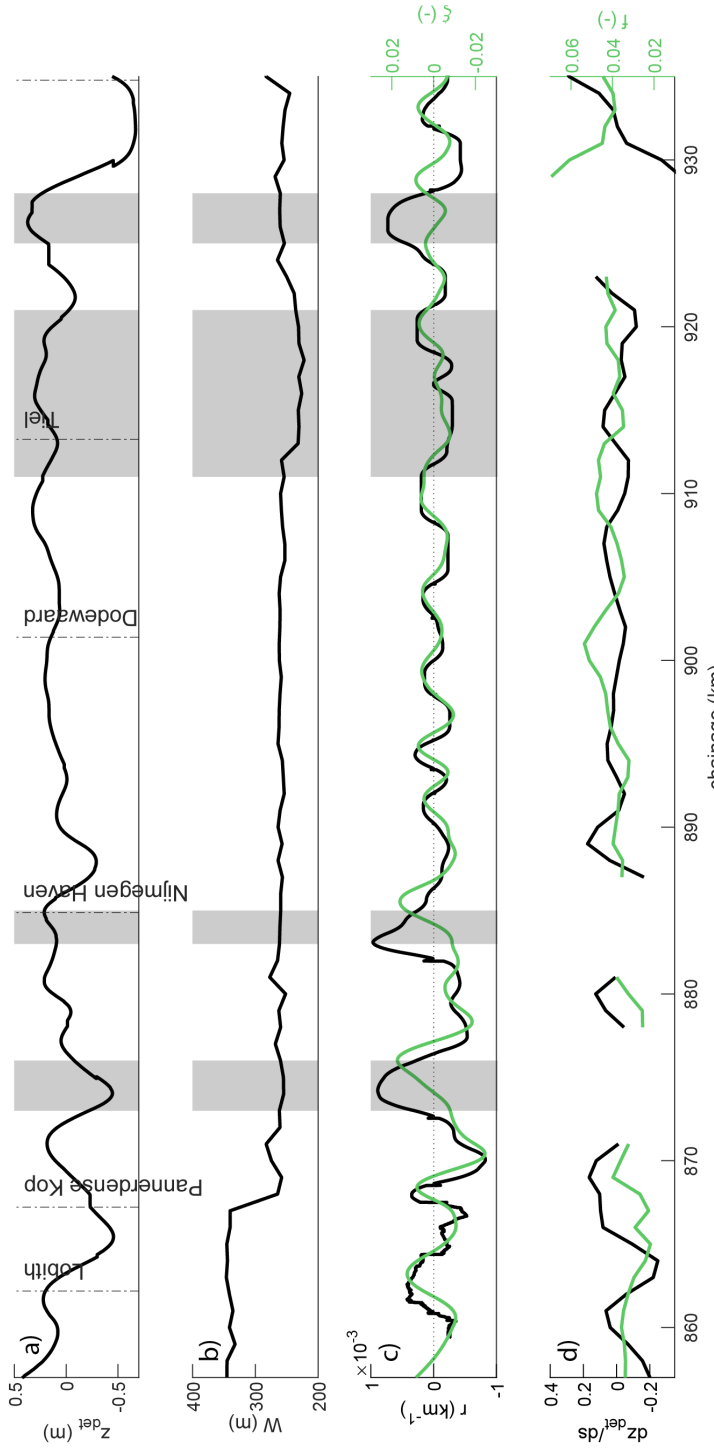


**Figure 6.9** | River geometry, curvature and hydraulic roughness, from datasets with comparable discharges ($Q$ = 1271 and 1249 m$^3$ s$^{-1}$). Shaded grey bars indicate human-made structures in the main channel (fixed layers, bendway weirs and longitudinal training dams at Tiel). a) bed level, detrended with a third degree polynomial and smoothed with a 8 km LOESS filter, b) river width, c) river curvature $r$ (black) and transverse bed slope $\xi$ (green), d) roughness calculated from the water surface slope (green) and gradient of detrended bed level ($z_{det}$; black).

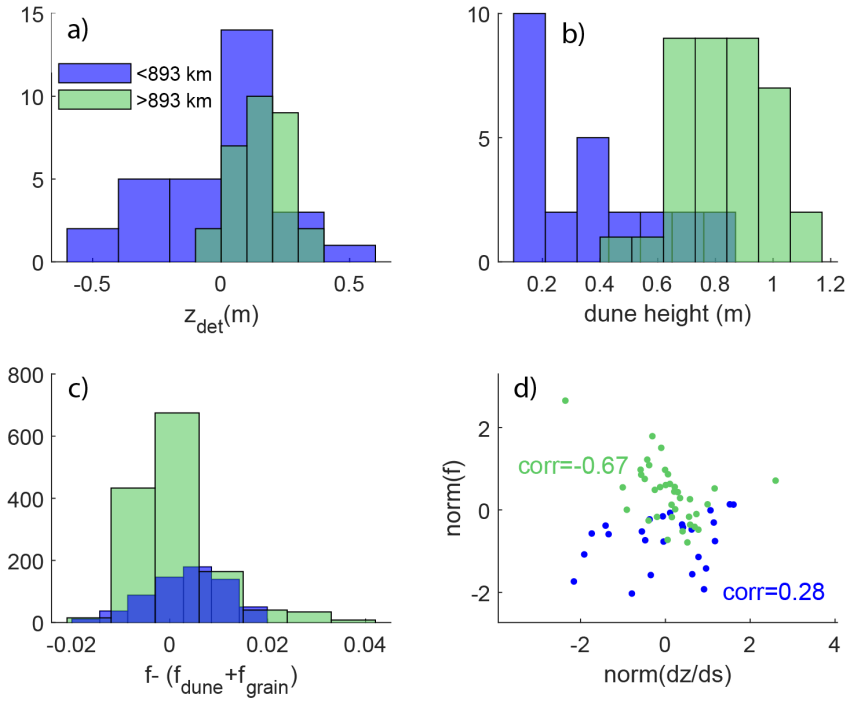


**Figure 6.10** | Histograms of various river characteristics upstream and downstream of river kilometre 893. a) Detrended bed level. b) dune height. c) the difference between roughness calculated with the water surface slope and with predictors based on dune geometry. d) normalised gradient of detrended bed level against normalised roughness, with a different Pearson's correlation coefficient (Pearson, 1909) (corr = 0.28 and -0.67, upstream and downstream of river kilometre 893, respectively).

## 6.5 | Discussion

We will discuss our findings related to the counter-phase fluctuation of bed-elevation gradient and friction factor, the choice of dune roughness predictor, and the impact of various measures of the (local topographic) leeside angle. Since the predictor of van Rijn (1984) captured the effect of bedforms on mean roughness relatively accurately, other sources of roughness hardly contributed to the mean roughness. However, the variance in roughness was not fully explained. Potential sources for the remaining variability in roughness will be discussed, including the presence superimposed dunes, lateral variation in river characteristics, and human-made structures.

### 6.5.1 | Counter-phase fluctuation of bed-elevation gradient and friction factor

The most remarkable outcome of our analysis focused on the factors controlling hydraulic roughness, is the counter-phase relation between bed-elevation gradient and the friction factor in the downstream reach of the study area (RK >893). The fluctuation in roughness $f$ seems to be imposed by the large scale bed elevation. They occur on a slightly larger spatial scale than alternating bars related to channel curvature, which are indicated by the alternating transverse bed slope in Figure 6.9c. Large-scale fluctuations of the river depth are found all around the world in studies demonstrating river geometrical variation (Trigg et al., 2009; Leuven et al., 2021; Gallo & Vinzon, 2005; Venditti et al., 2019), and are often related to stratigraphy or river-floodplain interaction.

The observed counter-phase relation between bed-elevation gradient and the friction factor suggests that when depth increases, and the accommodation space for the flow expands, flow energy is lost. We propose an explanation for the observed relation in Figure 6.11. When the flow runs into a deeper part of the river, the increase in water depth will cause the flow to diverge and decelerate. The resulting energy losses manifest as an increased value of $f$. This increase in roughness is not directly related to bed roughness from dunes or grains, but rather to internal energy loss where the flow diverges. The normalised values of the gradient in bed level and roughness have a coefficient of determination of 0.34, which means that the inverse gradient in bed elevation explains 34% of the variability in roughness.

Although the counter-phase relation between bed-elevation gradient and roughness can be considered a new finding at a scale of kilometres, it is known to occur at smaller scales. At smaller scales, flow divergence enhances turbulence, which leads to energy loss (Pope, 2000; Tennekes & Lumley, 1972). For example, at the stoss side of a river dune, the flow converges, turbulence is suppressed, and little energy loss takes place. The majority of the energy loss occurs at the leeside of the dune, where the depth increases and flow diverges, enhancing turbulence in the wake of the dune, and dissipating energy. Similarly, in a Venturi meter, the bulk of the energy loss occurs in the expanding section of the flow meter. Hydraulic roughness is closely related to energy loss, it is scale-dependent, and it has an intimate relation with the cascade of turbulent vortices that occur at multiple scales. Our finding suggests additional flow energy dissipates as a result of flow divergence at the scale of kilometres, which is typically viewed as a scale beyond what is relevant for hydraulic roughness.

The bed-elevation gradient depends on the level of data smoothing (Figure 6.12). In this study, the choice of filtering was motivated by a spectral gap between bed-level variations by bedforms, including dunes, and regional scale variations imposed by the geological setting, human-made constraints such as groynes, and alternating bars. We

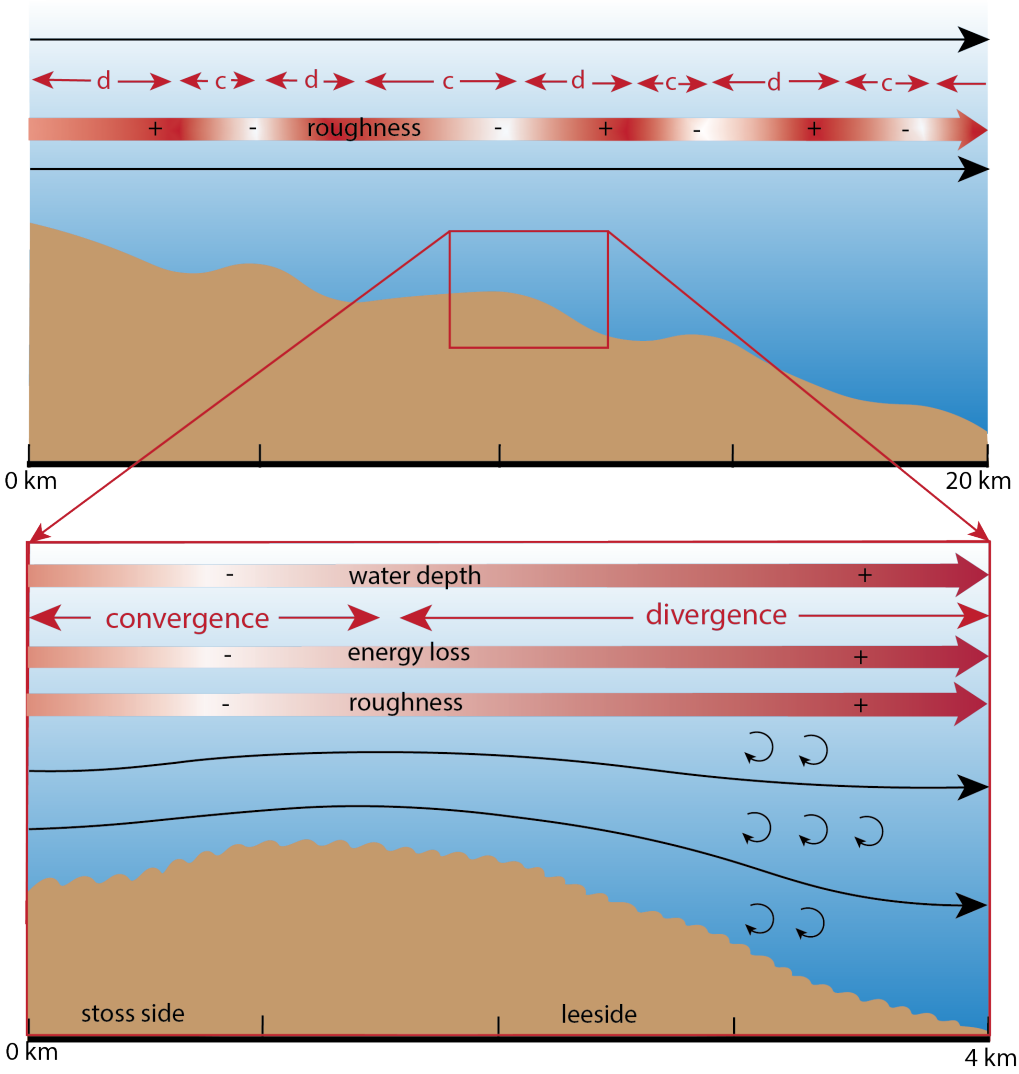


**Figure 6.11** | Graphical representation of the hypothesis how large-scale fluctuations of bed slope can influence hydraulic roughness. Low (-) and high (+) values of roughness, and convergence (c) and divergence (d) zones of the water flow are indicated.

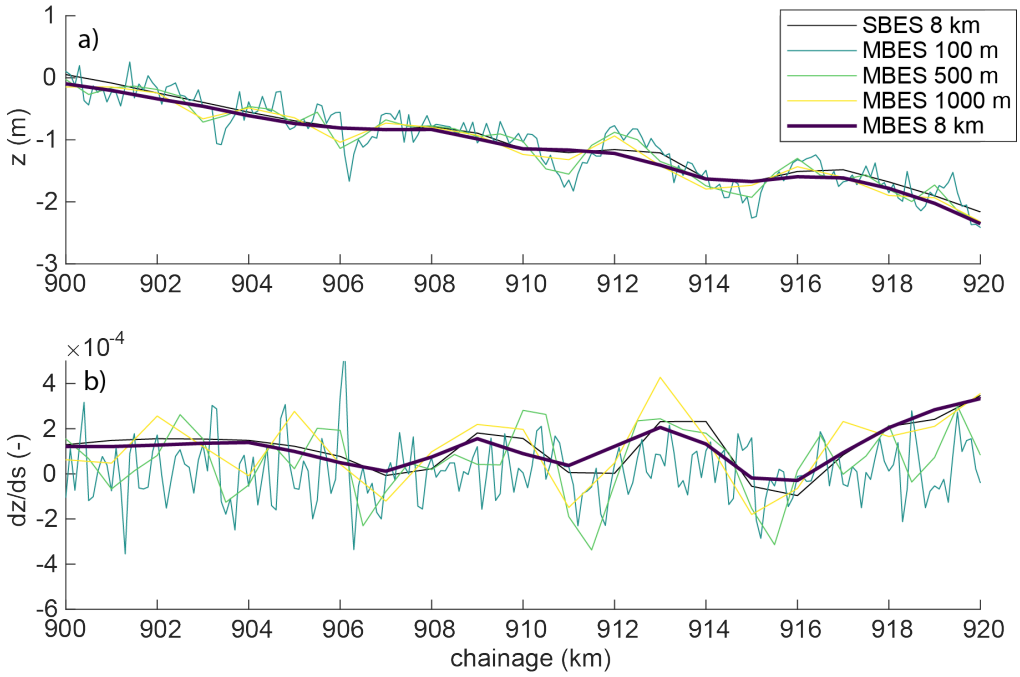


**Figure 6.12** | The influence of the choice of data input and the degree of smoothing on bed level and the corresponding bed-elevation gradient. Input data are either a single profile (SBES) or width-averaged (MBES) and smoothed with a LOESS filter of various degrees. When choosing a filtering of 8 km, both types of input data generate the same bed-elevation gradient.

expected that part of the variance of $f$ could be explained by each of the latter factors. The counter-phase fluctuation was only visible in the less disturbed middle reach of the study area. The absence of this relation in the more diverse upper reach indicates that the observed relation is not simply a result of bed level being an input parameter for the Chézy equation (equation 6.1), or depends on the choice of a smoothing filter.



### 6.5.2 | Roughness prediction

When simply looking at the explaining variance $R^2$, hydraulic roughness from bedforms and friction at the grain scale seemed to have limited predictive capacity. However, the estimation based on the equation by van Rijn (1984) did predict the mean roughness successfully, as it underestimated the total roughness only by 3.1%. It is not surprising that the predictor of van Rijn (1984) performs best, possibly because this predictor has been calibrated using data of Rhine River.

Grain size directly relates to grain roughness. The grain size distributions in the Rhine River and Waal River showed a clear pattern of downstream fining. Up until the Pannerdense Kop (RK 867), average roughness was almost fully explained by grain roughness. In that part of the river, the grain size distribution impacts the potential for

dune formation and dune growth (van den Berg & van Gelder, 1993), in such a way that in the Rhine dunes only form under high discharges (Wilbers & Ten Brinke, 2003). Dunes found under lower discharges can be remnants of former high flow conditions. Grain roughness decreased in downstream direction, where the contribution of grain roughness to the total roughness was lower.

### 6.5.3 | The impact of leeside angle on roughness prediction

The leeside angles observed in our study domain were low, which is common in large rivers (Galeazzi et al., 2018; Hendershot et al., 2016; Cisneros et al., 2020; de Ruijsscher et al., 2020). The mean leeside angle per kilometre did not exceed 5°. Mean dune leeside angles were slightly lower than local topographical leeside angles. This might indicate that the central axis of the river featured lower leeside angles than the sides, which were also included in the measure of local topographic leeside angle. Alternatively, the Bedform Tracking Tool (van der Mark & Blom, 2007) used herein can cause an underestimation in leeside angle, as it applies a linear fit of the middle 2/3th of the leeside of the dune (Zomer et al., 2021).

The slip face of low-angled dunes, i.e. the steepest part of the leeside angle, is considered to be important for flow separation (Paarlberg et al., 2007) and form roughness. Less strong and less frequent flow separation occurs at the leeside of low-angled dunes than at steeper dunes with permanent flow separation. Kornman (1995) found that form roughness is better quantified using the height of the slip face than using the bedform height. Lefebvre & Winter (2016) directly included the leeside angle in their predictive equations, introducing a correction factor for low leeside angles. In our study, the predictor by Lefebvre & Winter (2016) (equation 6.11) underestimated the total hydraulic roughness, which did not improve when the slip face angle instead of leeside angle was used. This does not necessarily prove the equation wrong, as a significant part of the discrepancy may be explained by alternative causes of roughness.

Against expectations, the various measures of leeside angle, including the mean local topographic leeside angles of low-angled dunes, explained little of the observed roughness variations. Attempts to explain the observed roughness variation from alternative statistics of local topographic leeside angles were unsuccessful (supplementary information Figure S4). Furthermore, implementing various measures of leeside angle (supplementary information Figure S5) in equation 6.11 does not improve roughness prediction. Contrary to the findings of Lefebvre et al. (2016), we found no hard evidence that the detailed shape of dunes matters, beyond properties that are included in classical roughness predictors such as the one from van Rijn (1984).

### 6.5.4 | Influence of superimposed bedforms on roughness prediction

Complexity in natural bed morphology at scales smaller than the primary dunes considered in this study may contribute substantially to roughness fluctuations. Secondary dunes are sometimes considered to be a separate roughness element (Julien et al., 2002; Yalin, 1992). In the approach of Julien et al. (2002), roughness heights are added as in $k_s = k_{sp} + kss + k_{sg}$ (roughness height from primary dunes, secondary dunes and grains, respectively), and subsequently the roughness predictor from van Rijn (1984) is used to quantify hydraulic roughness. Following the approach of Yalin (1992), the equation reads:

$$\frac{1}{C^2} = \frac{1}{C_g^2} + 0.5 \left[ \left( \frac{\Delta_p}{\lambda_p} \right)^2 \frac{\lambda_p}{h} + \left( \frac{\Delta_s}{\lambda_s} \right)^2 \frac{\lambda_s}{h} \right] \tag{6.16}$$

in which $C_g$ represents the grain roughness, and the subscripts p and s denote primary and secondary, respectively.

Neither of these approaches improve roughness predictions. Applying the equation of Yalin (1992) to our data resulted in an overestimation of the roughness by more than 100%. This overestimation may be caused the by interaction between primary and secondary dunes, which have a joint effect on the flow dynamics (Fernandez et al., 2006). Alternatively, the secondary dunes could be more important for roughness than the less steep primary dunes. We expect that the secondary dunes are an important cause of hydraulic roughness variation, but new tools are needed to quantify this effect.

### 6.5.5 | Influence of lateral variations on roughness prediction

Lateral variation in river geometry, dune geometry and grain size, can influence hydraulic roughness parameterisation and prediction. Regarding river geometry, the observed alternating bars in the Waal River can exert an indirect control on hydraulic roughness, which extends beyond the impact on dune properties (de Ruijsscher et al., 2020). Flow concentrates in the deepest part of the river, opposite to bars (Zomer et al., 2021). The resulting variation in flow velocity over the cross-section is significant, which means that for a uniform bedform field the effective roughness can vary over the cross-section. Consequently, considering the non-linearity of roughness relations, the 1D approach for quantification of bed geometry may not be entirely representative. Furthermore, width variations as visible in Figure 6.9b can further complicate the planimetric flow structure, causing the flow to converge or diverge. In our study area, width variations are small and gradual (except for the bifurcation at the Pannerdense Kop (RK 867) where the Rhine River bifurcates in the Waal River and Pannerdensch Kanaal) and are therefore not likely to strongly influence roughness.

Grain size can also show lateral variations. The passage of heavy ships induces erosion of the fine-grained beaches between the groynes, resulting in transport of fine-grained sand from the beaches to the river bed (Wilbers & Ten Brinke, 2003). Currents induced by ships are stronger during low discharge conditions (as present when measurements for this study were taken), and when ships are moving upstream (Bhowmik et al., 1995). Therefore, the southern side of the Waal River will be subject to more fine sand input than the northern side. The implications of variation in grain size over the cross-section on dune geometry remains to be explored. Roughness prediction may be improved by using a width-integrated approach, in which the spatial variability in both grain size and dune geometrical properties are both accounted for. A robust methodology for this is still to be developed.

### 6.5.6 | Influence of human influence on roughness prediction

Finally, human made structures and dredging can contribute to the total roughness and its variability. For this reason, the fixed layers, bendway weirs, and their region of influence are excluded from the analysis (Section 6.2). Resistance by groynes contributes to the total hydraulic roughness of the channel. Groynes are known to cause turbulence and scour behind the groyne heads. Locally, the river bed can show undulations with the same wave length as the groyne spacing (Wilbers & Ten Brinke, 2003). Those undulations are fixed and do not interact with bedforms (Wilbers, 1999; Ouillon & Dartus, 1997), but may statically influence bedform geometry (de Ruijsscher et al., 2020). The influence of groynes changes with high discharge conditions, especially when groynes are submerged and become part of the conducting section of the bed (Möws & Koll, 2019; Yossef, 2004). The low flow conditions studied minimise the impact of groynes, but the ubiquitous presence of groynes along the opposite banks complicates quantifying groyne roughness. The expected undulations in the water surface profile are too subtle to be observed based on ship positioning. High resolution measurements of the water surface topography, which cover the full width of the river instead of merely a single track along the centreline of river, may further elucidate the causes of hydraulic roughness variation. This will be to the benefit of models simulating flow, sediment transport and bed morphological change.

## 6.6 | Conclusions

We quantified hydraulic roughness based on the Darcy-Weisbach friction factor $f$ calculated from water surface slope measurements of a 78 km-long trajectory of the Rhine River and Waal River in the Netherlands. This was compared to predicted roughness values based on dune geometry, and to the spatial distribution of the local topographic leeside angle, both inferred from bathymetric field data.

In the upstream part of the study area (RK 857 - 867), where dunes are likely inactive under low flow conditions and human-made hard layers cause nonuniform flow, total hydraulic roughness cannot easily be predicted from bedform dimensions. In the downstream part (RK 867 - 935), predictions of the Darcy-Weisbach friction factor $f$ agree with estimates inferred from longitudinal surface level profiles. The best performing predictor explains 31% of the variance in $f$, which indicates that even in this part of the river, dune morphology is likely not the only factor explaining hydraulic roughness variation. We expected to explain part of the variance in $f$ from statistics of local topographic leeside angle, which control flow separation and energy loss, but did not find confirmation of this expectation.

Serendipitously, we found that the longitudinal gradient of the smoothed river bed level oscillates in counter phase with $f$. Towards a topographic high, the friction factor decreases, and towards a topographic low, the friction factor increases. A deepening of the river thus corresponds with a higher hydraulic roughness, which may relate to flow divergence in the decelerating flow, and the corresponding energy loss. The depth variations explain 34% of the variance in hydraulic roughness. This effect is clearly visible in the downstream region, where the grain size is relatively constant, dunes are comparatively large, and dune predictors explain a large part of the variance in $f$.

Unresolved influences on hydraulic roughness include the effect of human-made structures such as groynes, secondary dunes and topographical steering of the river flow. Future work to further elucidate the effect of various scales of complex bed geometry on hydraulic roughness is warranted, as primary dunes explain only a limited part of the flow resistance.

*De thee trekt*
*maar de zee nog meer*

# Hydraulic roughness in a tidal river

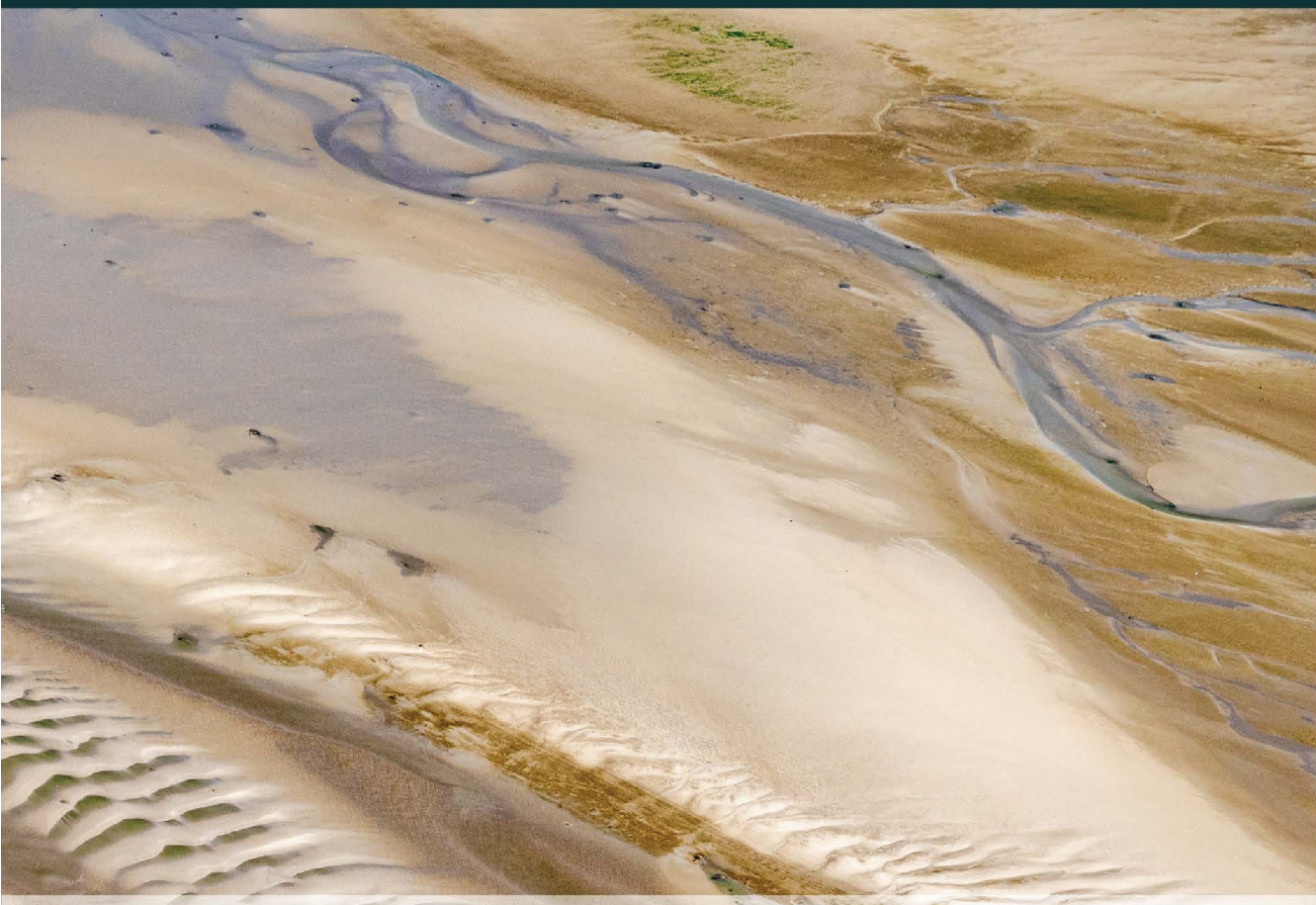

This chapter was originally published as:

de Lange, S.I., Bradley, R., Schrijvershof, R., Murphy, D., Waldschlager, K., Kostaschuk, R., Venditti, J.G., Hoitink, A.J.F. (2024). Dune geometry and the associated hydraulic roughness in the fluvial to tidal transition zone of the Fraser River at low river flow. JGR Earth Surface 129(2).
DOI: 10.1029/2023JF007340

## Abstract

In deltas and estuaries throughout the world, a fluvial-to-tidal transition zone (FTTZ) exists where both the river discharge and the tidal motion drive the flow. It is unclear how dune characteristics are impacted by changes in tidal flow strength, and how this is reflected in the hydraulic roughness. To understand dune geometry and variability in the FTTZ and possible impacts on hydraulic roughness, we assess dune variability from multibeam bathymetric surveys, and we use a calibrated 2D hydrodynamic model (Delft3D-FM) of a sand-bedded lowland river (Fraser River, Canada). We focus on a period of low river discharge during which tidal impact is strong. We find that the fluvial-tidal to tidal regime change is not directly reflected in dune height, but local patterns of increasing and decreasing dune height are present. The fluvial-to-tidal regime change is reflected in dune shape, where dunes have lower leeside angles and are more symmetrical in the tidal regime. The calibrated model allows to estimate local patterns of dune heights using tidally-averaged values of bed shear stress. However, the spatially variable dune morphology hampers local dune height estimation. Changes in dune shape do not significantly impact the reach-scale roughness, and estimated dune roughness using dune height and length is similar to the dune roughness inferred from model calibration. Hydraulic model performance with a calibrated, constant roughness is not improved by implementing dune-derived bed roughness. Instead, the data analysis revealed that large-scale river morphology may explain differences in model roughness and corresponding estimates from dune predictors.

## 7.1 | Introduction

Rivers debouching into a water body subject to tides have a fluvial-to-tidal transition zone (FTTZ). The FTTZ can be defined as the part of the river that is fully dominated by fluvial processes at its upstream end, and dominated by tidal and coastal processes at the downstream boundary (Phillips, 2022). The transition from fluvial to tidal can be gradual, but is often impacted by processes that modify the character of this transition by altering the channel bathymetry and adding friction (Godin, 1999; Horrevoets et al., 2004), such as an irregular underlying channel geology, bifurcations or confluences (Kästner et al., 2017), or dredging works (Gisen & Savenije, 2015). These changes can cause the gradual transition to become more abrupt, and a sudden change in tidal flow strength can lead to a change in hydraulic regime from a more fluvial to a more tidally dominated system. It is unclear how bedforms and their corresponding roughness respond to a change in hydraulic regime, even though dune geometry and roughness prediction are essential for river management (ASCE Task Force, 2002; Warmink et al., 2013; Best, 2005), interpreting sedimentary rock records (Das et al., 2022), and understanding sediment fluxes (Venditti & Bradley, 2022).

Dunes are rhythmic undulations of the river bed with heights of approximately $10^{-1}$ - $10^{0}$ m and lengths around $10^{1}$ - $10^{2}$ m, thereby being larger than ripples but smaller than bars. They adjust to changes in the hydraulic regime, but not in a consistent manner. Until recently, it was often assumed that any spatial variability in dune geometry was caused by dunes that are not in equilibrium (Carling et al., 2000; Bridge, 2003; Holmes & Garcia, 2008), and the primary geometry (dune height and length) of equilibrium dunes was assumed to scale with water depth (Yalin, 1964). However, recent research has shown significant local spatial variation in dune height (Bradley & Venditti, 2017; Murphy, 2023; Venditti & Bradley, 2022) in riverine systems, including the Fraser River (Murphy, 2023), independent of the water depth. In the FTTZ, this variability is expected to be even more pronounced, since tidally-influenced currents impose spatially-varying water level fluctuations (and therefore bed shear stress changes) on diurnal and semi-diurnal time scales (Sassi et al., 2011; Hoitink et al., 2003). The resulting spatial longitudinal variability of dune geometry in the FTTZ is understudied, but two key studies exist.

Prokocki et al. (2022) studied dunes in the lower 90 km of the Lower Columbia River (USA), and recognised differences in shape and 3D planform of dune geometry across the study reach. They related the changing dune morphology to downstream variations in grain size and spatiotemporal changes in tidal and fluvial flow. In the thalweg, they observed small upstream-oriented dunes downstream, and larger downstream-oriented dunes upstream. Unfortunately, they did not report on flow conditions in those distinct regions, or on the resulting hydraulic roughness differences. Lefebvre et al. (2021) studied 4-year long bathymetric data of the downstream

160 km of the Weser Estuary in Germany. They did not observe a clear trend in dune geometry in the longitudinal direction, but found dunes that are generally smaller than predicted based on the water depth (Allen, 1978). They did not provide information on the flow conditions or resulting roughness. Beyond these recent studies, the response of dune geometry to shear-stress variation at the change from a fluvial to tidal regime is unknown, and it is uncertain if dune geometry predictors apply here.

To date, it remains unclear to what extent variability in dune geometry is relevant for the large-scale roughness needed to model hydrodynamics in the FTTZ. Bedforms, especially dunes, are known to be a major source of roughness in lowland rivers (Gates & Al-Zahrani, 1996; Julien et al., 2002). Hydraulic roughness quantifies the resistance to flow by objects protruding into the water column (Chow, 1959). It consists of skin friction drag (grain resistance) and form drag, resulting from pressure variation (Einstein, 1950). Dune variability can impact roughness parameterisations via its impact on the form drag. When modelling the FTTZ hydraulically, a roughness value must be chosen, generally expressed as Manning's n, the Chézy coefficient, or the roughness height. We identify three options to adopt at a suitable roughness value. Firstly, the apparent hydraulic roughness can directly be inferred from calibration. The calibrated roughness is often represented by a single constant coefficient (Paarlberg et al., 2010); limited examples are available where a variable roughness coefficient is used. de Brye et al. (2011) used a linearly decreasing roughness coefficient in a model domain from a delta apex to the coast, to represent a gradual transition from the riverine to the marine environment. However, proof of the validity of this approach is lacking.

Secondly, a roughness predictor, such as that of van Rijn (1984), can be used to estimate hydraulic roughness, which have been developed mainly in alluvial conditions without tides. With an increasing amount of bathymetric data available from field surveys, measured dune geometry can be used as input for these predictors. Typically, even in this option for hydrodynamic modelling, a calibration constant is still implemented to adjust the estimated hydraulic roughness. Thirdly, when no field data is available, such as for inaccessible regions or during peak flow conditions, roughness predictors can be employed using dune characteristics estimated from predictors such as van Rijn (1984), Yalin (1964), Karim (1995) or Venditti & Bradley (2022). The latter approach needs iteration, since roughness impacts the water levels, which in turn impacts the dune geometry estimations. The reliability of these dune geometry predictors in the FTTZ is unknown, and needs testing. There is a need to improve hydraulic roughness parameterisation and dune geometry estimations in the FTTZ, since the output of hydrodynamic models strongly depends on an accurate specification of roughness (Lesser et al., 2004; Morvan et al., 2008; Wright & Crosato, 2011).

In this research, we aim to increase understanding of bedform variability and related roughness that occurs at the transition from a shallow mixed tidal-fluvial regime to

a tidal regime. To do so, we assess the bedform characteristics and the resulting hydraulic roughness of the FTTZ of the Lower Fraser River. The Lower Fraser River is a sand-bedded lowland river in British Columbia, Canada, with a significant decrease in tidal energy (amplitude) 40 kilometre landward of the river mouth (Wu et al., 2022b). We aim to answer three research questions. (1) How are bedform characteristics impacted by the sudden change in tidal flow strength? (2) How can dune variability in the fluvial-to-tidal transition zone be explained and estimated? (3) To what extent does dune geometry and variability affect reach-scale hydraulic roughness, and which other factors can play a role in determining this bed roughness? Bathymetric field data from base flow conditions were used, allowing us to focus on the impact of the tides, which penetrate further upstream during base flow. A 2D hydrodynamic model is created to assess hydraulic roughness, and to explore the impacts of spatial variation in river and tidal flow. The field data is analysed to assess bedform characteristics and its relation to hydraulics and river geometry, and model output is used to estimate dune geometry and assess its impact on hydraulic roughness.

## 7.2 | Field site

The Fraser River (Figure 7.1) is located in British Columbia, Canada, and drains 228,000 $km^2$ of mountainous terrain. The Fraser exits a series of bedrock canyons approximately 185 km upstream of the river mouth at river kilometre (RK) 0, where it enters the gently-sloping Fraser Valley, past the towns of Hope (RK 165) and Mission (RK 85). The Fraser River has an annual river discharge of 3,410 $m^3\ s^{-1}$ at Mission (Water Survey of Canada Station 08MH024), but flow rates vary between a mean low discharge of 1,000 $m^3\ s^{-1}$ in winter time (November - April) and a mean high discharge of 9,790 $m^3\ s^{-1}$ during the snow melt-dominated freshet in May, June and early July (Attard et al., 2014; McLean et al., 1999). At New Westminster, 34 km upstream from the river mouth, the river bifurcates, forming the Fraser Delta where the Main Channel splits into two tributaries: the North Arm and the Main Channel. The Main Channel carries 88% of the flow, until it bifurcates into Canoe Pass (RK 13), which conveys approximately 18% of the total flow (WCHL, 1977; NHC, 2008; Dashtgard et al., 2012). The fluvial-to-tidal transition zone of the river is influenced by a predominantly semi-diurnal tide (Wu et al., 2022b), with a mean tidal range at the mouth of approximately 3 m (Kostaschuk & Atwood, 1990). The tidal motion influences water levels up to Mission during high flow, but can penetrate up to Chilliwack (RK 120) during base flow conditions in August until April, creating a strong backwater effect (Kostaschuk & Atwood, 1990) (i.e. an increase in subtidal water level as response to the tidal forcing). The Fraser has an undammed, unregulated flow, which reflects climatic conditions. Human-made influences include dikes (90% of the reach), pipelines and bridge constructions, and dredging of the Main Channel occurs.

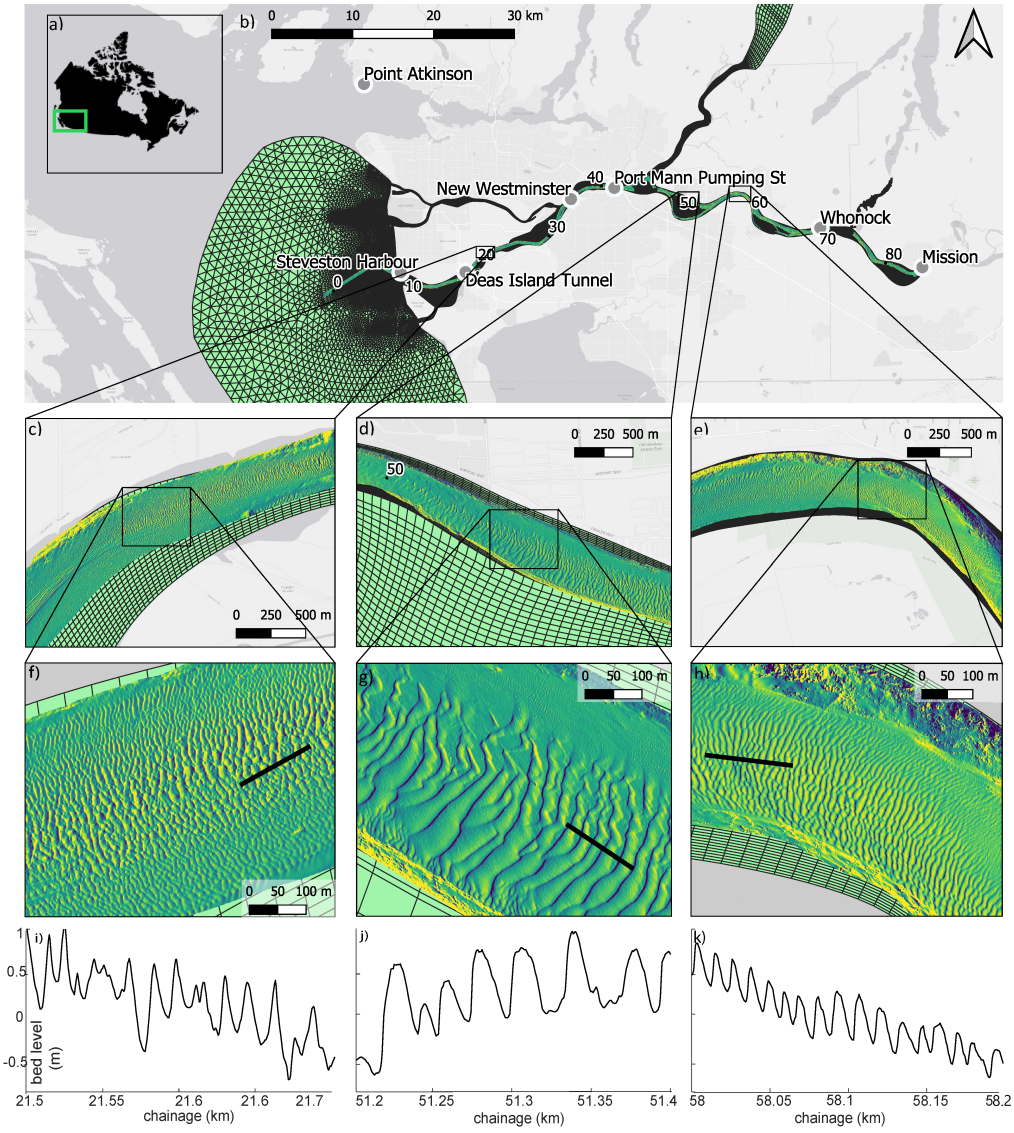


**Figure 7.1** | Study area of the Fraser River in British Columbia, Canada (a). b) The Fraser River from river kilometre 10 (Steveston Harbor) to 85 (Mission). Green shaded area indicates the model domain. Grey markers indicate gauging stations. c-e) Measured multibeam bathymetry in the three focus zones examined in this study, shown in hill shade, f-h) examples of hill shade depiction of the measured dune fields. i-k) example profiles of the dune fields along the corresponding black lines in subfigures f-h).

The Port of Vancouver dredges from the river mouth (RK 0) to the Port Mann Pumping Station (RK 42), with the most significant dredging in the deltaic reach from RK 35 to the river mouth (Nelson, 2017) to maintain a constant fairway depth (McLean & Tassone, 1989; Stewart & Tassone, 1989). The depth is larger in the tidal region, and has been made deeper by dredging. This results in a large decrease in momentum

flux (Wu et al., 2022b), defined as water mass times velocity in a unit area, at the upstream limit of the dredging works. Additionally, Wu et al. (2022b) related this decrease in momentum flux to the influence of the Pitt River. They identified the junction of the Pitt River as the transition from a tidally-dominated to a river-dominated regime, and they noted the importance of this system for tidal attenuation. Therefore, two different regimes can be identified in the study area. The first regime, hereafter called the tidally-dominated regime, occurs seaward of RK 40, and is characterised by a strong influence of tides and a large tidally-averaged water depth compared to the more landward-located region. The second regime is the mixed tidal-fluvial regime, in which tides are less strong and the water depth is shallower, which occurs landward of RK 40. This roughly coincides with the upstream end of the modern Fraser Delta at RK 35 (Venditti et al., 2015; Venditti & Church, 2014), where the Fraser River bifurcates into the North Arm and the Main Channel.

The difference in tidal strength in the two regions does not impact grain sizes of bed sediments in the thalweg. The main transition of grain size characteristics occurs around RK 100. Upstream of RK 100, the bed of the Fraser River consists of gravel, and downstream of a gravel-sand-transition near Mission, the main bed material is sand (Venditti & Church, 2014). The median grain size ($D_{50}$) is 351 $\mu$m and the mean is 415 $\mu$m (Figure 7.2). There is a minor trend of downstream fining in the thalweg of the lower 50 km of the river, (1.14 $\mu$m per kilometre, Figure 7.5c), resulting on average in a decrease in $D_{50}$ of approximately 100 $\mu$m over this reach, although there is considerable scatter due to gravel and mud deposits along the banks. The data underlying this figure is a compilation of multiple sources. The samples up until RK 48.5 were collected by McLaren & Ren (1995), who sampled bed material in the Main Channel and delta front at 0.5 km increments with a Shipek sampler. Although this grain size data is decades old, broad patterns are likely to be consistent with present conditions (Venditti & Church, 2014), and grain size shows little seasonal or year-to-year variation (Kostaschuk et al., 1989; McLean et al., 1999; Pretious, 1956). Venditti & Church (2014) measured 33 samples of RK 48.5 - 80, with a dredge sample in 2009, and Murphy (2023) collected 115 additional samples in this same reach using a pipe dredge. They did not perform analysis on the fraction smaller than 63 $\mu$m. The Pitt system does not impact the sediment composition of the Fraser, since the net bedload transport is directed upstream toward Pitt lake (Ashley, 1980). In the delta, the river deposits its sand load in the channel and its banks, and its silt load on the distal margins and tidal flats (Venditti & Church, 2014) (Figure 7.2a, c, d). Seaward of the river mouth, the grain size decreases dramatically to a $D_{50}$ of 22 $\mu$m. Locally, the river interacts with its bank and bed substrate. Gravel and clay patches are present at the outer banks on the north and south sides of the river. These patches are either modern deposits, such as gravel bars, or older Pleistocene glacial deposits seen as fine outwash deposits and coarse glacial till (Nelson (2017), Supplementary Figure S1), constraining the river's course.

This study focuses on the Main Channel of the Fraser River, from the confined part of delta mouth at Steveston Harbor at RK 10, to Mission at RK 85 (Figure 7.1). The area is located in the FTTZ, and low-angled dunes (Bradley et al., 2013; Kostaschuk & Best, 2005; Kostaschuk & Villard, 1996), with no or intermittent flow separation, cover the river bed. When assessing local scale processes, we focus on three zones in the FTTZ (Figure 7.2, and Supplementary Figure S7).The zones are located at RK 21.5-23 (zone 1; tidal regime), 50-52.5 (zone 2; fluvial-tidal regime) and 57-59.5 (zone 3; fluvial-tidal regime). The selection of zones is based on three criteria. Firstly, a decreasing amount of tidal energy (tidal amplitude) from zone 1 to 3. Secondly, a simple geometry, without bifurcations or confluences, to limit the influence of complex currents on dune geometry. Thirdly, a limited degree of human influence on the river bed. Zone 1 is 1 km shorter than the other zones due to dredging along the downstream side, and an engineering structure on the upstream side.

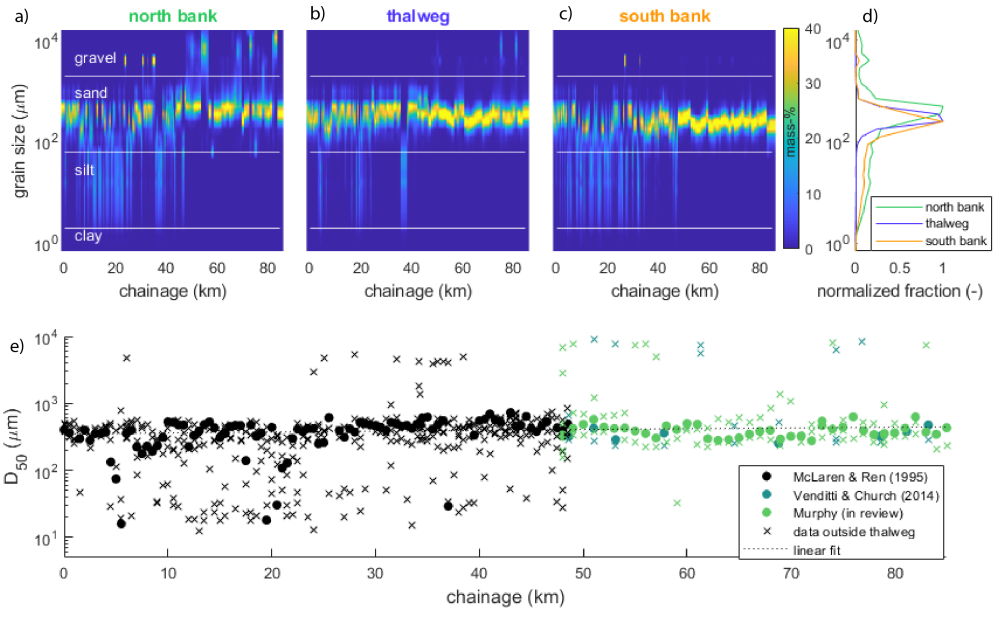


**Figure 7.2** | Grain size distributions of bed sediment in the Fraser River, shown in distance from the river mouth at RK 0 (chainage). a, b, c) grain size distribution along the north bank, thalweg and south bank. d) cumulative distribution at the north bank, thalweg and south bank. e) median grain size ($D_{50}$) in and outside of the thalweg. Markers differentiate between samples taken in the thalweg (solid marker) or outside along the river banks (indicated with 'x'). The data is from a data compilation by Venditti & Church (2014), which includes reanalysed observations from McLaren & Ren (1995), and recent observations by Murphy (2023).

## 7.3 | Methods

### 7.3.1 | Field data and preprocessing

Raw multibeam echosounder (MBES) riverbed data were provided by the Public Works and Government Services, Canada. The measured bathymetry comprises data of the Main Channel between river kilometre -1 to 85 and covers the navigation channel, but does not provide full bank-to-bank spatial coverage. Data were collected during base flow conditions in January, February and March of 2021. This period is characterised by relatively constant discharge and little change to the bed surface (Bradley & Venditti, 2021). During the survey period, the measured discharge (at an hourly interval) was relatively constant, with monthly mean values of 1416 $m^3\ s^{-1}$ (standard deviation ($\sigma$) 184 $m^3\ s^{-1}$), 1051 $m^3\ s^{-1}$ ($\sigma$ = 140 $m^3\ s^{-1}$) and 1074 $m^3\ s^{-1}$ ($\sigma$ = 35 $m^3\ s^{-1}$) at Hope (RK 165) for the three months, respectively (Water Survey of Canada, Station 08MF005).

The MBES data is gridded onto a 1 x 1 $m^2$ grid, and the resulting MBES datasets contain $x$, $y$ and $z$ coordinates. Next, all bed level data is converted from Cartesian coordinates ($x$, $y$) to curvilinear coordinates ($s$, $n$) with the same spatial resolution (Vermeulen et al., 2014a). Herein, $s$ is the streamwise direction, and corresponds with river kilometres (RK, i.e. chainage) and $n$ is the stream normal direction, wherein $n$ = 0 m is defined as the central river axis, which roughly coincides with the thalweg.

### 7.3.2 | Hydraulic model setup

A 2DH (two dimensional horizontal) hydraulic model was set up in the Delft3D Flexible Mesh (FM) model suite (Kernkamp et al., 2011). The model simulates depth-averaged flow quantities based on the two-dimensional shallow water equations. The numerical domain covers the Fraser River from river kilometre 85, to the offshore region of the Strait of Georgia reaches where depth exceeds 200 m. The bathymetry of the model of Wu et al. (2022b) was taken as a basis, and the higher resolution MBES data described above were used for the bathymetry of the channels in the estuary. The MBES data was smoothed with a LOESS filter (Cleveland, 1979; Cleveland & Devlin, 1988; de Ruijsscher et al., 2018), and interpolated on an unstructured curvilinear grid. The median cell size was 30 m, and varies between 5 m in the river and 1000 m offshore. Bars that do not get submerged during an average yearly freshet (flood) were not well-represented in the bathymetric data, so bar elevation in the model was manually increased to 10 m above mean sea level, to prevent flooding.

The upstream boundary condition is the discharge at Mission (RK 85) for the time period of November 2017 to October 2018. The discharge at Mission is estimated using a rating curve if the discharge exceeds 5,000 $m^3\,s^{-1}$. At lower discharge con-ditions, tidal influences make the rating curve at Mission inaccurate, and therefore 145

the discharge was calculated using the discharge at Hope (RK 165) and two smaller tributaries (Chilliwack River and Harrison River). Using this calculation method, discharges measured at Mission (larger than 5,000 $m^3\ s^{-1}$), were on average underestimated by 3%, and no significant temporal delay was observed. Additionally, at two downstream confluences, a constant discharge of 315 $m^3\ s^{-1}$ at Stave River (RK 74) and 130 $m^3\ s^{-1}$ from the Pitt River (RK 45) were added to the Fraser flow. Stave River is dammed at 3 km upstream, therefore having a controlled flow. The Pitt River drains a lake and has therefore a nearly constant outflow. At the downstream boundary (see Figure 7.1b), water levels influenced by tides are imposed. Eight primary tidal constituents, the most important overtide ($M_4$) and compound tides are determined via the Delft Dashboard toolbox (van Ormondt et al., 2020), using the TPXO8.0 database (Egbert & Erofeeva, 2002).

The tidal amplitudes and phases at the downstream boundary were corrected to minimise the error in the model-data comparison at the Point Atkinson tidal gauging station. This correction was on average 0.8% of the tidal amplitude and 20° for the tidal phases, for the 13 tidal components. The model was calibrated for low discharge (<1600 $m^3\ s^{-1}$; Figure 7.3b), to simulate flow conditions that correspond to the low-discharge bathymetry. The calibration was performed by varying the Manning's roughness coefficients and evaluating the resulting water levels and tidal amplitudes of the three most important tidal constituents at 7 gauging stations (RK 0, 9, 18.5, 35, 42, 70, 85) (Figure 7.2). The principal tidal constituent $M_2$ is used for calibration, together with $M_4$ and $K_1$. Relative phase differences between $M_2$ and $M_4$ (the first overtide of $M_2$) influence tidal duration asymmetry, the main mechanism for driving residual bed-load transport in estuaries (van de Kreeke & Robaczewska, 1993). The diurnal tide $K_1$ is relatively large at the west coast of North America, and interaction between diurnal and semi-diurnal frequencies can produce asymmetric tides as well (Hoitink et al., 2003).

The tidal amplitudes were derived from harmonic analysis using t_tide (Pawlowicz et al., 2002). The best performing model had a uniform Manning's roughness coefficient of 0.026 $s\ m^{-1/3}$ (Figure 7.3). Disconnecting the hydraulic roughness at the regime transition at RK 40, thereby allowing for two different roughness values, did not improve the calibration (Supplementary Figure S3a). The uniform Manning's coefficient (roughness) of 0.026 $s\ m^{-1/3}$ is slightly higher than the calibrated Manning's coefficient of Wu et al. (2022b), who used a uniform roughness of 0.015 $s\ m^{-1/3}$. The difference in roughness value is attributed to the difference in grid resolution. Our model grid in the river domain is overall coarser than the model of Wu et al. (2022b) who used a 10 m resolution, so that the schematisation of the bathymetric data on our grid results into slightly wider channels. Our value for roughness is considered to be more appropriate for natural sand-bedded rivers (Chow, 1959).

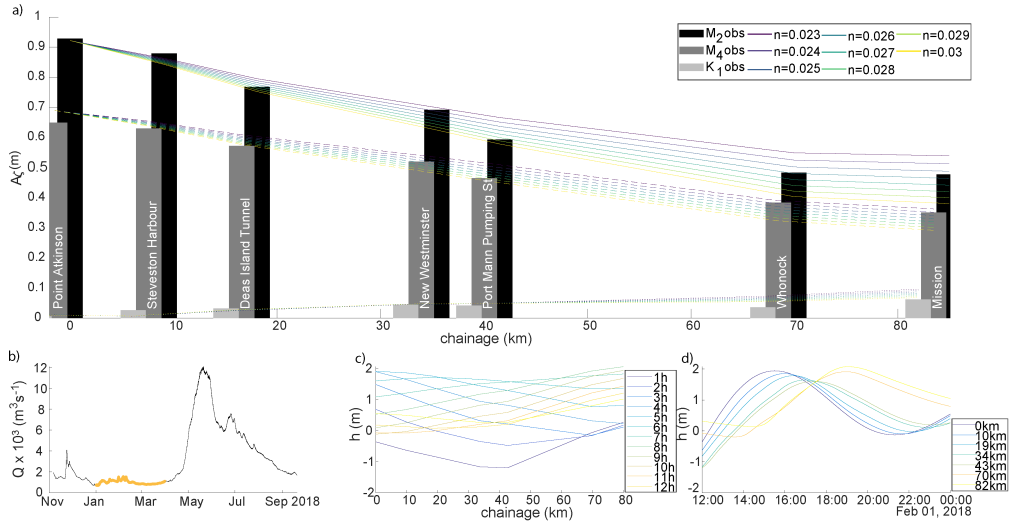


**Figure 7.3** | a) Calibration of the model with uniform roughness, shown along the river (chainage, where 0 indicates the river mouth). The observed tidal amplitude of the tidal constituents $M_2$ (black bars), $K_1$ (dark grey bars), and $M_4$ (light grey bars), and the corresponding modelled tidal amplitudes are indicated. b) Discharge at Mission. Highlighted part of the discharge curve indicates the timeframe of MBES data collection. c) Modelled water surface slope over time, simulated with the model with $n_{man}$ = 0.026 s $m^{-1/3}$. d) Modelled propagation of the tidal wave per station, simulated with the model with $n_{man}$ = 0.026 s $m^{-1/3}$.

## 7.3.3 | Data analysis

### 7.3.3.1 | Analysis of river bathymetry: dune detection

Bathymetry was analysed to derive dune characteristics. Three longitudinal profiles were taken, along the centreline and at approximately 80 m from the north and south bank, and their longitudinal location is expressed as chainage (km) i.e. along-river kilometre. In three focus areas (Figure 7.1), a longitudinal profile was taken every 10 meters, resulting in 27, 41 and 23 profiles for zones 1, 2 and 3 respectively, depending on the river width. To ensure that bedforms in all profiles were primarily caused by natural mobile bed conditions, we excluded bathymetry that showed extensive scour, human-made structures and dredging marks (Supplementary Figure S2).

From the filtered profiles, bedform characteristics were determined by using a standard bedform tracking tool (van der Mark & Blom, 2007). In the tool, the default filter span ($c$ = 1/6) was suitable to filter out small features such as measurement errors or outliers. Three span values ($P0$), corresponding with bedforms with a length of 20 m ±10, 50 m ±20 and 100 m ±30, were used as input to detrend and smooth the profile. The span values in the tool are based on a spectral analysis yielding the dominant bedform wave lengths in each section.

Based on the detrended and smoothed profile, a zero-crossings profile was defined, based on which individual dunes were identified, and dune characteristics were calculated (see van der Mark & Blom (2007) for more information). Dune characteristics include dune height $\Delta$ (m), the vertical distance between the crest and downstream trough, dune length $\lambda$ (m), the horizontal distance between two subsequent crests, the seaward-facing leeside angle *LSA* (°), the slope from a linear fit of the dune's leeside, excluding the upper and lower 1/6th of the dune height, and the landward-facing stoss side angle *SSA* (°) calculated in the same manner as the leeside angle. The bedform slip face angle *SFA* (°), the steepest part of the leeside, and is defined as the 95th percentile of the leeside angle. Finally, bedform asymmetry is calculated as the ratio between the length of the (seaward) leeside and the total bedform length (Lefebvre et al., 2021).

Bedforms with heights smaller than 0.1 m are not distinguishable from the error of the survey, and are excluded from the analysis. Bedform lengths smaller than 3 m are excluded as well, since the resolution of the bathymetric data (1 m) is too small to detect small bedform features. Features with a height greater than 2.5 m (2% of all detected bedforms) or a length greater than 200 m (0.08% of all detected bedforms) are classified as bed features unrelated to dunes such as scour holes or wake deposits downstream of human-made structures. These had a different geometry than mobile dunes, which was confirmed by visual inspection of the batymetric data. Large dunes (>2.5 m) as found in previous studies (Kostaschuk & Luternauer, 1989; Pretious & Blench, 1951; Venditti et al., 2019) were not observed in the low-discharge bathymetry used in this study.

#### 7.3.3.2 | Analysis of river geometry

To assess if and how river geometry impacts dune height and length, river geometry was parameterised by river width, curvature, transverse bed slope and excess depth. River width $W$ (m) was determined from a polygon following the longitudinal low water line, which is considered to be the discharge carrying section of the river under low discharge conditions. Cross-sectional area $A$ ($m^2$) was subsequently approximated from the tidally-averaged water depth and river width, assuming a trapezoidal shape of the cross-sectional area, where the river bank has a 60° slope. Curvature $r$ ($km^{-1}$) was defined as the inverse of bend radius following the approach of de Ruijsscher et al. (2020). Local transverse bed slope $\xi$ (-) was defined as the slope between the two sides of the main river channel, longitudinally discretised at intervals of 100 m. Finally, an excess depth parameter $D_e$ (-) was used as a measure to identify pools and scour holes (Vermeulen et al., 2014a), defined as:

$$D_e = \text{sign}(r) \left( \frac{D_{max}}{D_r} \text{-} 1 \right) \tag{7.1}$$

where $D_r$ is the regional mean depth of a discretised section of 500 m long, and $D_{max}$ the local maximum depth in this section. Sign indicates the signum function, which returns the sign of a real number.

#### 7.3.3.3 | Analysis of river hydrodynamics

To assess local flow conditions and tidal attenuation, the hydrodynamic model was evaluated during low flow conditions in March 2018 (Figure 7.3b). The flow magnitude and direction, water depth and bed shear stress magnitude and direction per grid cell were saved every ten minutes in the simulation. All output data were tidally-averaged using a Godin filter (Godin, 1972). The Godin filter removes the tidal and higher frequency variance to obtain a low-passed signal primarily caused by the river flow.

Besides transforming the data into along and across-channel coordinates ($s$,$n$) according to Vermeulen et al. (2014a), the flow and shear stress vectors were rotated, to transform their orientation to along-channel direction ($s$-direction). This allowed differentiation between the in- and outgoing currents, which are in $s$- and minus $s$-direction, respectively. The percentage of time that the flow reverses and flows upstream (reversal time, $t_{rev}$ (%)) was then calculated.

#### 7.3.3.4 | Dune geometry estimation

Flow data from the model was used to estimate dune height $\Delta$ (m), using several dune height predictors that include some measure of flow strength (van Rijn, 1984; Yalin, 1964; Karim, 1995; Venditti & Bradley, 2022). Multiple predictors were used to assess their applicability in the FTTZ, since none of the predictors was explicitly developed for the FTTZ. Simultaneously, this allows assessment of potential differences of dunes in the FTTZ and dunes in the river. Firstly, dune height was estimated using the widely applied dune geometry predictor of van Rijn (1984). This predictor is based on 84 laboratory experiments, with grain sizes ranging from 190 - 2300 $\mu$m, and 22 field data sets (490 - 3600 $\mu$m) of relatively wide rivers (width / depth $>$ 0.3) with unidirectional flow. This corresponds well with conditions found in the Fraser River, except that the Fraser experiences bidirectional currents. To account for this, values of water height and shear stress are tidally averaged, since bed-material sediment transport in the Lower Fraser River generally follows the pattern of mean velocity over the tidal cycle (Kostaschuk & Best, 2005). The tidal averaging is described in Section 7.3.3.3. Dune height is thus:

$$\Delta_{vRijn} = 0.11h\left(\frac{D_{50}}{h}\right)^{0.3}(1 - e^{-0.5T})(25 - T) \tag{7.2}$$

in which $D_{50}$ is median grain size (m), $h$ is the water depth (m) and transport stage $T$ is:

$$T = \frac{(u^*)^2 - (u_c^*)^2}{(u_c^*)^2} \tag{7.3}$$

where $u^*$ is the shear velocity (m $s^{-1}$), and $u_c^*$ is the critical shear velocity (m $s^{-1}$) for initiation of sediment movement. Shear stress $\tau$ (N $m^{-2}$) relates to shear velocity and is here expressed as the dimensionless Shields number $\theta$ as in:

$$\tau = u^{*2}\rho_w \tag{7.4}$$

$$\theta = \frac{\tau}{(\rho_s - \rho_w)gD_{50}} \tag{7.5}$$

in which $g$ is the gravitational acceleration (9.81 m $s^{-2}$), $\rho_s$ is the sediment density (2,650 kg $m^{-3}$ for quartz) and $\rho_w$ is the water density (1,000 kg $m^{-3}$ for fresh water). Therefore, equation 7.3 can be rewritten as:

$$T = \frac{\tau - \tau_c}{\tau_c} = \frac{\theta - \theta_c}{\theta_c} \tag{7.6}$$

When 50 $\mu$m $< D_{50} <$ 5,000 $\mu$m, the critical shields number $\theta_c$ (-) can be approximated with a simple expression (Zanke, 2003). The resulting values of $\theta_c$ are approximately 0.03 (medium sand):

$$\theta_c = 0.145 Re_p^{-0.333} + 0.04510^{-1100 Re_p^{-1.5}} \tag{7.7}$$

in which the particle Reynolds number $Re_p$ is:

$$Re_p = D_{50}^{3/2} \frac{\sqrt{Rg}}{\nu} \tag{7.8}$$

where the relative submerged density $R = (\rho_s - \rho_w)/\rho_w$ (-) and $\nu$ is the kinematic viscosity ($m^2$ $s^{-1}$), which is slightly dependent on water temperature as $\nu = 4 * 10^{-5}/(20 + t)$ in which $t$ = temperature (°C). Here, $\nu$ = 1.3 * $10^{-6}$ is used for 10 °C.

We also estimate dune height using the predictor of Yalin (1964):

$$\Delta_{Yalin} = \frac{h}{6}\left(1 - \frac{\tau_c}{\tau}\right) \tag{7.9}$$

The predictor of Karim (1995) builds on that of van Rijn (1984) and Allen (1978). The predictor of Allen (1978) is not included in this research, since it is mostly based on

laboratory experiments. The predictor of Karim (1995) is based on the suspension criterion which utilises the shear velocity and the particle fall velocity $w_s$:

$$\Delta_{Karim} = h\left(0.04 + 0.294(\frac{u^*}{w_s}) + 0.00316(\frac{u^*}{w_s})^2 - 0.0319(\frac{u^*}{w_s})^3 + 0.00272(\frac{u^*}{w_s})^4\right) \tag{7.10}$$

where $w_s$ follows from Ferguson & Church (2004) as:

$$w_s = \frac{RgD_{50}^2}{C_1\nu + (0.75C_2RgD_{50}^3)^{0.5}} \tag{7.11}$$

in which $C_1$ and $C_2$ are constants with values of 18 and 1.0, respectively, for slightly irregular particles.

Finally, we test the equation of Venditti & Bradley (2022):

$$\Delta_{VB} = h\left(10^{\left(-0.397(log\,\frac{\theta}{\theta_c} - 1.14)^2 - 0.503\right)}\right) \tag{7.12}$$

#### 7.3.3.5 | Hydraulic roughness estimation

To estimate the impact of dunes on the water levels in the study reach, the hydraulic roughness was determined. The hydraulic roughness estimates were then compared to the calibrated model roughness, and a simplified version was implemented in the model. The total hydraulic roughness, expressed as a friction factor $\hat{f}$, results from form friction and grain friction (Einstein, 1950). Assuming dunes are the dominant structures causing form resistance, the total hydraulic roughness was estimated as in van Rijn (1984):

$$\hat{f} = \frac{8g}{(18\log(\frac{12h}{k_s}))^2} \tag{7.13}$$

Herein, $k_s$ consists of form roughness height $k_{sf}$ and grain roughness height $k_{sg}$:

$$k_s = k_{sg} + k_{sf} \tag{7.14}$$

$$k_{sg} = 3D_{90} \tag{7.15}$$

where $D_{90}$ is the 90th percentile of the grain size distribution, and

$$k_{sf} = 1.1\gamma_d\Delta(1 - e^{\frac{-25\Delta}{\lambda}}) \tag{7.16}$$

where the calibration constant $\gamma_d$ is taken as 0.7 in field conditions (van Rijn, 1984). $\Delta$ and $\lambda$ are derived from field data.

In the modelling suite of Delft3D, roughness values of Manning's n, $n_{man}$ (s $m^{-1/3}$), are converted to a Chézy coefficient $C$ ($m^{1/2}s^{-1}$) via (Manning, 1891):

$$C = \frac{R_h^{1/6}}{n_{man}} \tag{7.17}$$

in which $R_h$ is the hydraulic radius, which can be simplified to the water depth $h$ (m) for rivers that satisfy $W \gg h$.

The Chézy coefficient is converted to the dimensionless Darcy-Weisbach friction factor $f_m$ according to Silberman et al. (1963):

$$f_m = \frac{8g}{C^2} \tag{7.18}$$

## 7.4 | Results

### 7.4.1 | Hydraulics and morphology of the fluvial-to-tidal transition zone

The tidally-averaged water depth in the study area fluctuates between 3 and 18 m (Figure 7.4a). In the mixed-fluvial tidal regime of the river (RK $>$ 40), it increases gradually in the seaward direction, and in the tidal regime (RK $<$ 40) it remains constant. The local increase in water depth is reflected in the tidally averaged and instantaneous shear stress profiles (Figure 7.4b). The downstream-directed maximum shear stress increases from 0.4 N $m^{-2}$ in the upstream area to 10 N $m^{-2}$ at the river mouth. Similarly, the upstream-directed maximum shear stress in relation to flow reversal (indicated by a minus sign in Figure 7.4b) increases to 6 N $m^{-2}$. In contrast, the tidally-averaged shear stresses remain relatively constant over distance (fitting a linear model gives a slope of $10^{-5}$ N $m^{-2}$ $km^{-1}$). The tidally averaged shear stress is on average 0.64 N $m^{-2}$ and fluctuates between -1.0 N $m^{-2}$ (indicating an upstream directed shear stress at the most downstream area, RK 0) and 2.2 N $m^{-2}$ (at RK 67).

The tidal effect on the water levels and flow direction weakens in the upstream direction, and the amplitude of the tidal constituents $M_2$ and $K_1$ decreases as the tides attenuate (Figure 7.4d). The $M_2$ tidal constituent shows a particularly strong decrease from RK 10 to 40, while landwards the tidal attenuation is minimal. In the most upstream reach, bidirectional currents can still be observed (Figure 7.4c). During low flow conditions, upstream (flood) flow occurs for 45% of the time at the river mouth (around RK 10), and decreases to 25% at the most upstream location of the study reach.

The morphology of the Fraser River does not show consistent trends in the streamwise direction. The river width fluctuates between 500 and 1100 m (Figure 7.5a). The cross-sectional area of the river remains relatively constant in the more upstream part of the river (RK > 40), since river depth varies inversely with river width. The more downstream part features larger fluctuations in cross-sectional area, since water depth remains relatively constant (Figure 7.5a). The bed level (Figure 7.5b) shows large variations, but remains relatively constant in the downstream part. River curvature, transverse bed slope and depth excess are strongly related ($R^2$ = 0.15 - 0.61, p < 0.005, Figure 7.5c), which reflects the low-sinuosity meandering morphology.

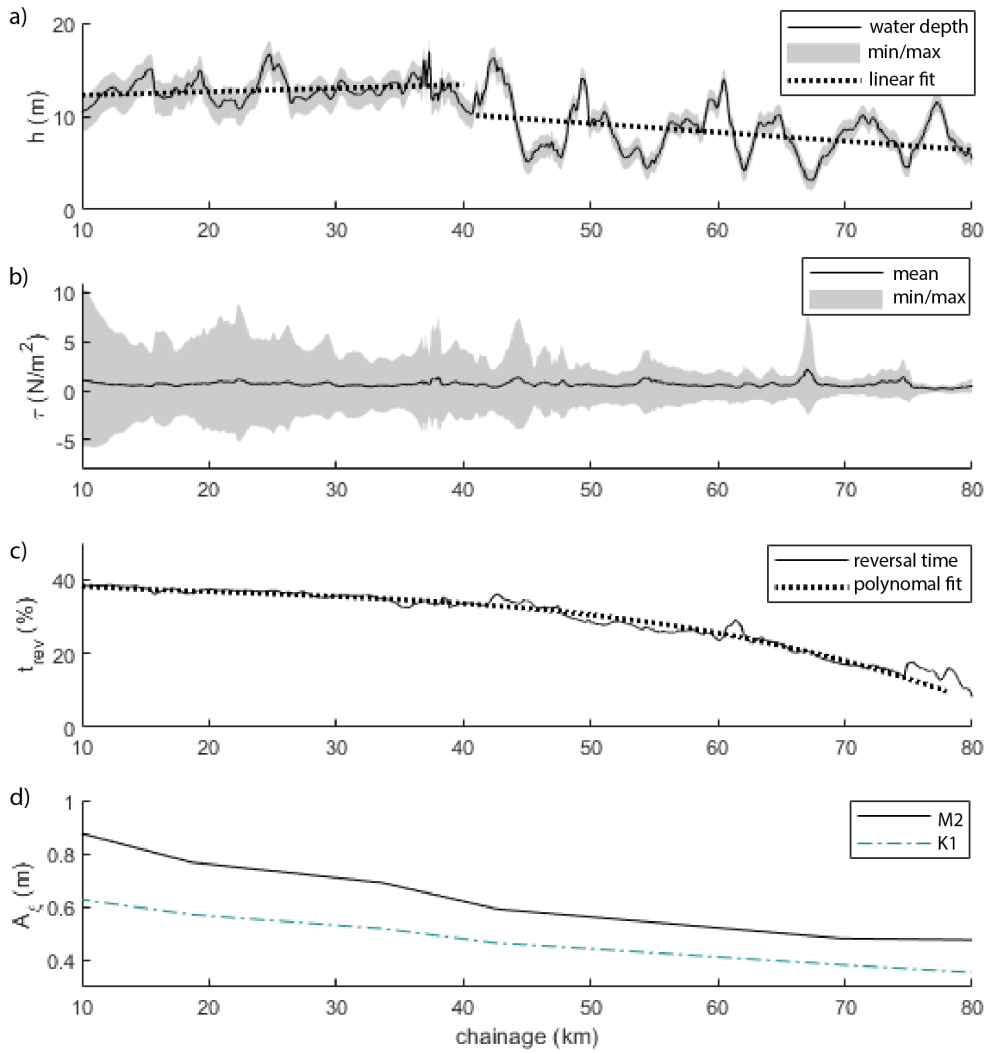


**Figure 7.4** | Hydraulic characteristics of the Lower Fraser River along chainage (river kilometre). a) water depth (h). b) tidally-averaged, maximum and minimum shear stress ($\tau$). c) reversal time ($t_{rev}$). d) tidal amplitude ($A_{\zeta}$) of the $M_2$ and $K_1$ tide.

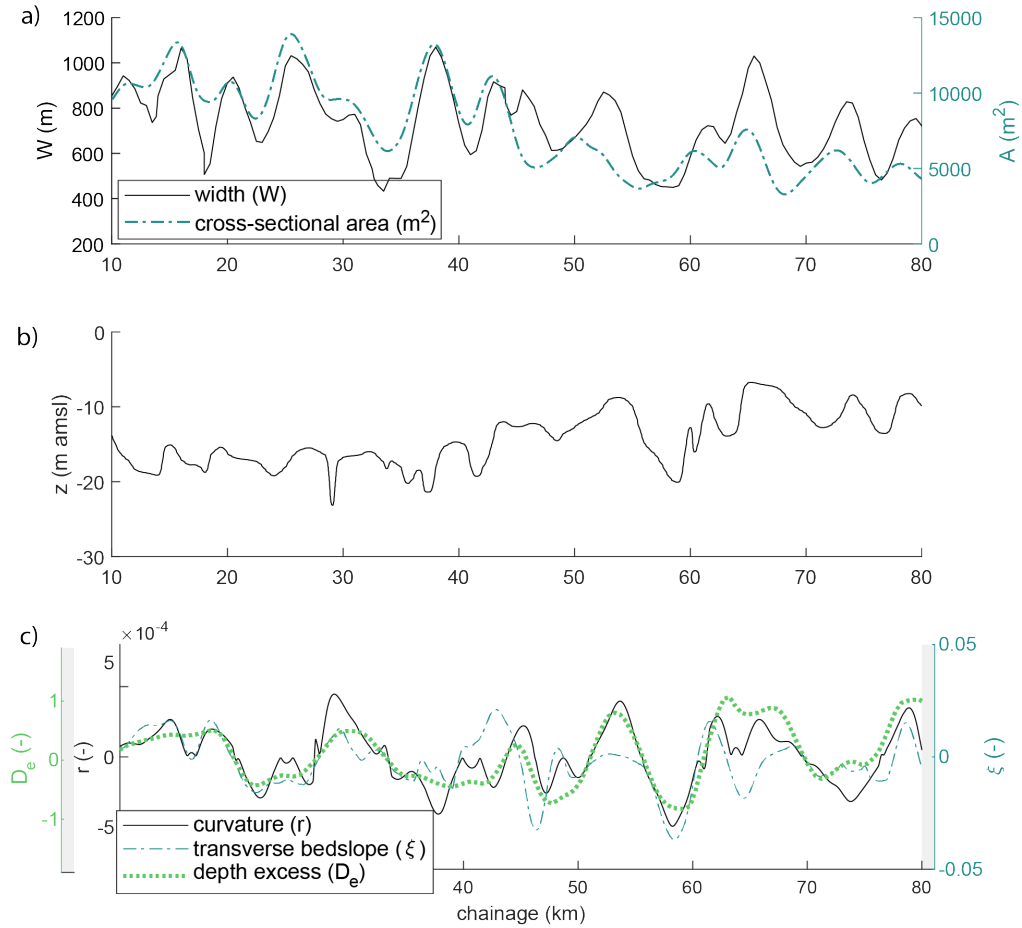


**Figure 7.5** | Morphological characteristics of the Lower Fraser River along chainage (river kilometre). a) smoothed channel width ($W$) and smoothed cross-sectional area ($A$). b) bed level $z_0$ in meters above sea level. c) channel shape, expressed as depth excess ($D_e$), transverse bed slope ($\xi$) and curvature ($r$)

### 7.4.2 | Response of dune geometry to tidal hydraulics

Dune geometry in the study reach varies considerably (Figure 7.6), with dune heights up to 2.4 m (mean: 0.46 m, median: 0.39 m, $\sigma$ = 0.28 m) and dune lengths up to 194 m (mean: 24 m, median: 16, $\sigma$ = 22 m). Multiple scales of superimposed bedforms co-exist, although most of the bed is covered only by primary dunes. Patterns in dune geometry are apparent, with some areas of relatively low and short dunes, and others with increasing or decreasing dune heights and lengths. For example, the thalweg has large dunes around RK 68, 77 and 85, with increasing and decreasing dune heights upstream and downstream of those local maxima. Such patterns are not consistent over the whole river width however, and where relatively large dunes prevail on one part of the river (e.g. north side), dunes may be small on the opposite side (see for example around RK 68). This variation in dune height and length, along the cross-

section and longitudinally, is expressed as the standard deviation of all dunes present in one unit of channel width. This allows for comparison between longitudinal and cross-sectional variability. The mean standard deviation in dune height and dune length in the cross-sectional direction (0.20 m and 13.0 m, respectively) is twice as high as the variation along the longitudinal direction (on average 0.11 m and 6.8 m, respectively) (Figure 7.6).

Local patterns in dune height and length are difficult to explain, and do not reflect the regime change around RK 40, trends in river geometry, or grain size in the thalweg. However, visual inspection reveals dune occurrence is primarily determined by grain size along the outer banks – when the grain size is too large (gravel) or too small (clay), dunes will be absent (Supplementary Figure S2e, f). When the river cuts into a clay or gravel layer on the north or south sides of the channel, abrupt changes in dune geometry can result.

The gradual increase in strength and duration of tidal currents in the seaward direction influences dune shape. Firstly, the dune crests become sharper (Figure 7.1i-k). Secondly, the leeside and slip face angle of the dunes decrease in downstream direction (Figure 7.7a, b). In particular the slip face angle decreases faster in the tidal regime than in the fluvial-tidal regime. Since the stoss side angle remains relatively constant (with a slight increase in the tidal regime), dunes become more symmetrical in the seaward direction (Figure 7.7c). When the asymmetry is equal to 0.5, dunes are perfectly symmetric. Dune symmetry occurs at nearly every location up to a distance of 75 km from the river mouth, but becomes consistent at around 40 km from the river mouth, indicating the impact of the regime change. Results from a two-paired student t-test shows that the leeside angle, slip face angle and asymmetry is significantly different (at a 95% confidence level) in the tidal and the fluvial-tidal regime, while stoss side angle is not. The leeside angle directly correlates with flow-reversal time (Figure 7.7d) and maximum shear stress (Figure 7.7e), showing lower leeside angles and more symmetric dunes in seaward direction, although large variation is observed.



### 7.4.3 | Dune geometry estimation from model output

Dune height predictors were applied to the FTTZ of the Fraser River at both reach scale and zone scale. The predictors were not specifically developed for tidal rivers with bidirectional currents, so input values were tidally-averaged.

The predictor of van Rijn (1984) works well when all data is reach-averaged (estimated $\Delta_{vRijn}$ = 0.52 m, compared to measured $\Delta$ = 0.50 m; Figure 7.8a). However, it underestimates dune height in the mixed fluvial-tidal regime (by about 20 cm at RK 80), and overestimates it in the tidally-dominated regime (by about 24 cm at RK 10). All other predictors are inaccurate and overestimate the dune height significantly, with an increasing error in the downstream direction (Figure 7.8b-d). For example, the reach-

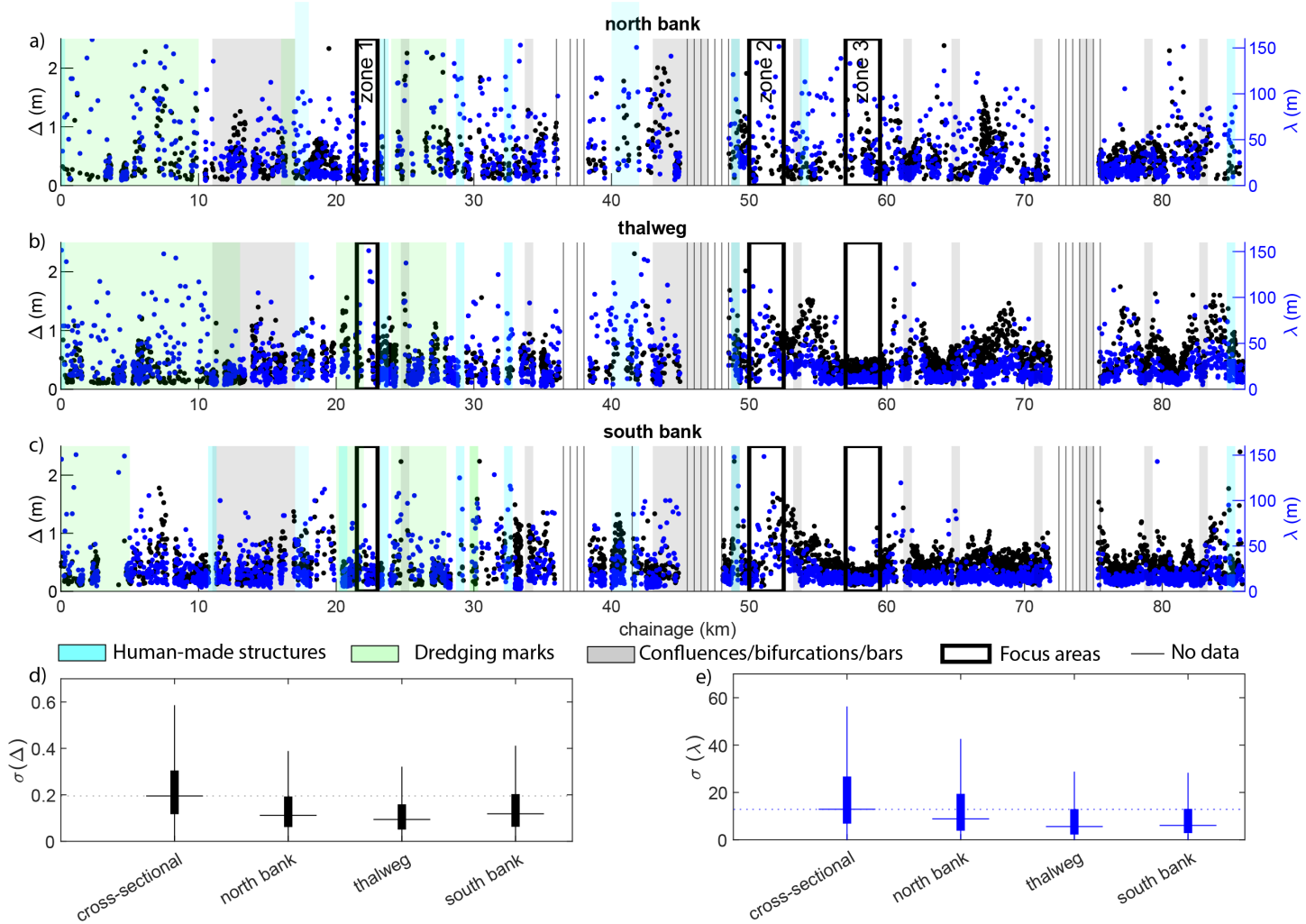


**Figure 7.6** | Dune geometry along chainage (river kilometre). a, b, c) Dune height ($\Delta$; black) and dune length ($\lambda$; blue) throughout the research area. Human-made structures, dredging marks, confluences, bifurcations and bars, focus areas, and zones with no data are indicated (see legend). d, e) Standard deviation ($\sigma$) within the mean multibeam echosounder coverage width (230 m) of dune height and dune length over the cross-section, north bank, thalweg and south bank. In each bar, the central mark indicates the median, and the bottom and top edges of the box indicate the 25th and 75th percentiles, respectively. The whiskers extend to the most extreme data points, and outliers are not shown.

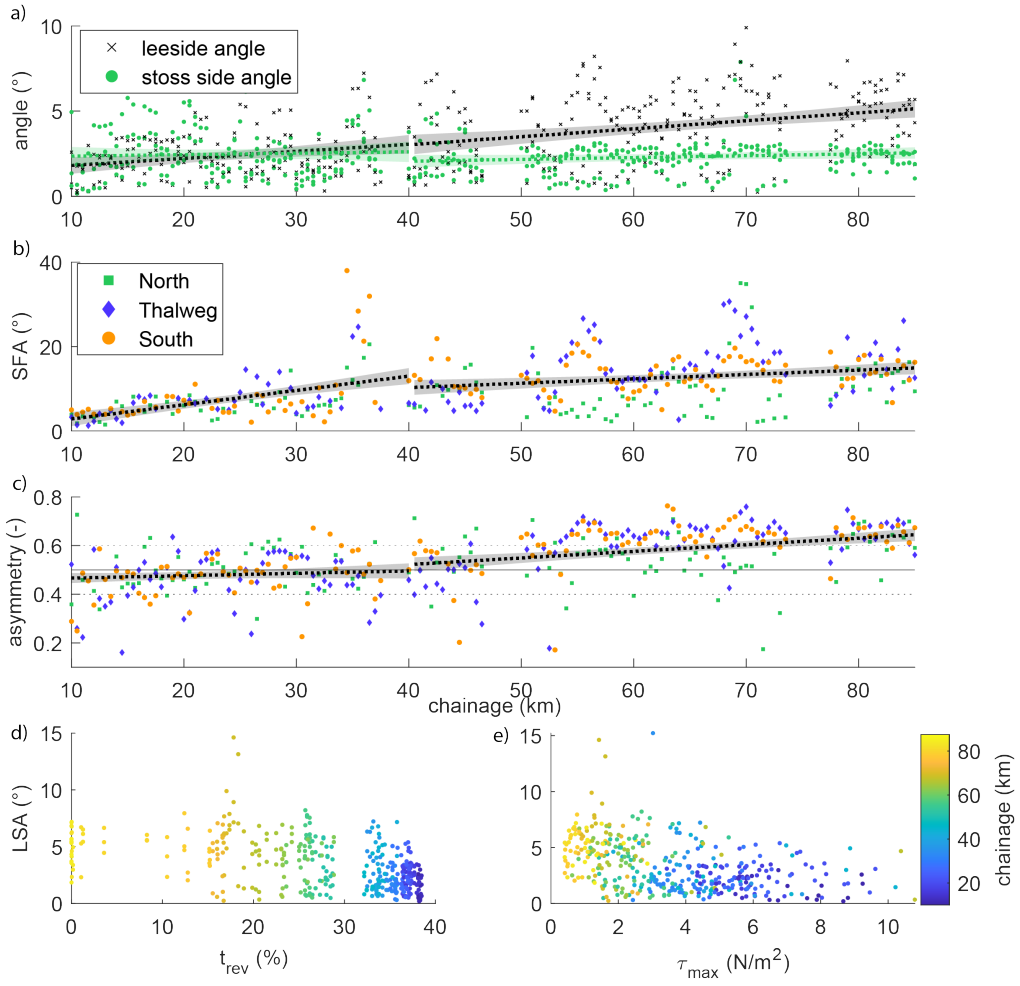


**Figure 7.7** | Dune shape in the study area along chainage (river kilometre). a) leeside angle (*LSA*) and stoss side angle (*SSA*). b) dune slip face angle (*SFA*). c) dune asymmetry, expressed as the ratio between the length of the (seaward) leeside and the total bedform length. A value of 0.5 indicates symmetric dunes, values of asymmetry smaller than 0.4 are defined as flood-asymmetric, while values larger than 0.6 are ebb-asymmetric. Confidence intervals of linear regressions are shown. Subfigure d) and e) show dune leeside angle against against reversal time ($t_{rev}$) and against maximum shear stress ($\tau_{max}$), respectively.



averaged estimated dune heights are 0.87 m, 1.27 m and 1.83 m for the predictors of Yalin (1964), Karim (1995) and Venditti & Bradley (2022), respectively.

Local variability in dune height in the study area is not captured in dune geometry predictors because of the considerable spatial variability in the measured dune geometry. To establish the degree to which local variability in dune properties relates to flow properties obtained with the 2DH hydraulic model assuming a constant roughness, we focus on three zones in the FTTZ (Figure 7.2). In those zones, flow characteristics are modelled (see Supplementary Figures S7-S11) and the dune height predictor of

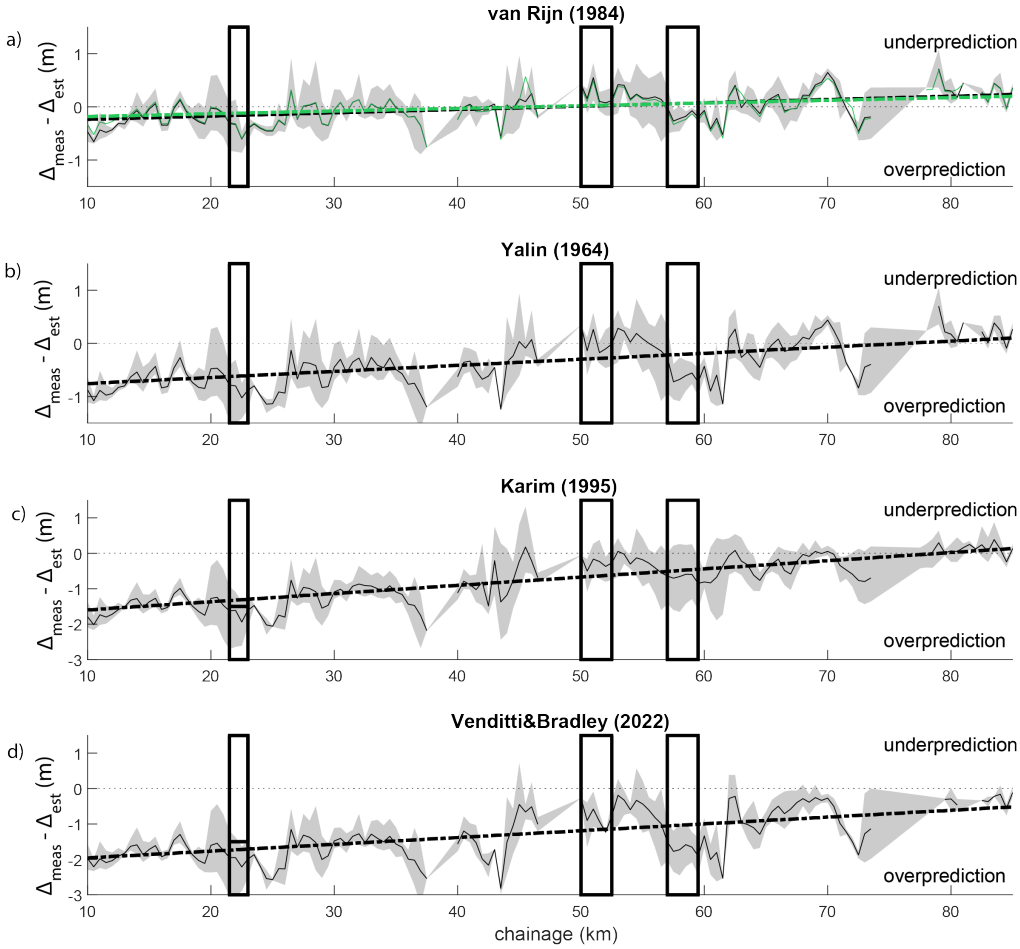


**Figure 7.8** | Residual dune height (measured dune height $\Delta_{meas}$ minus estimated dune height $\Delta_{est}$) along chainage (river kilometre), to assess dune height predictor performance of the predictor of a) van Rijn (1984). b) Yalin (1964). c) Karim (1995). d) Venditti & Bradley (2022). The measured data is based on the average of three longitudinal transects, and includes the minimum and maximum values in a grey shading. The modelled data is based on the model with a constant roughness of $n_{man}$ =0.026 s $m^{-1/3}$. In subfigure a) estimated dune height with dune-adjusted roughness (varying between 0.024 and 0.028 s $m^{-1/3}$) is displayed in green.

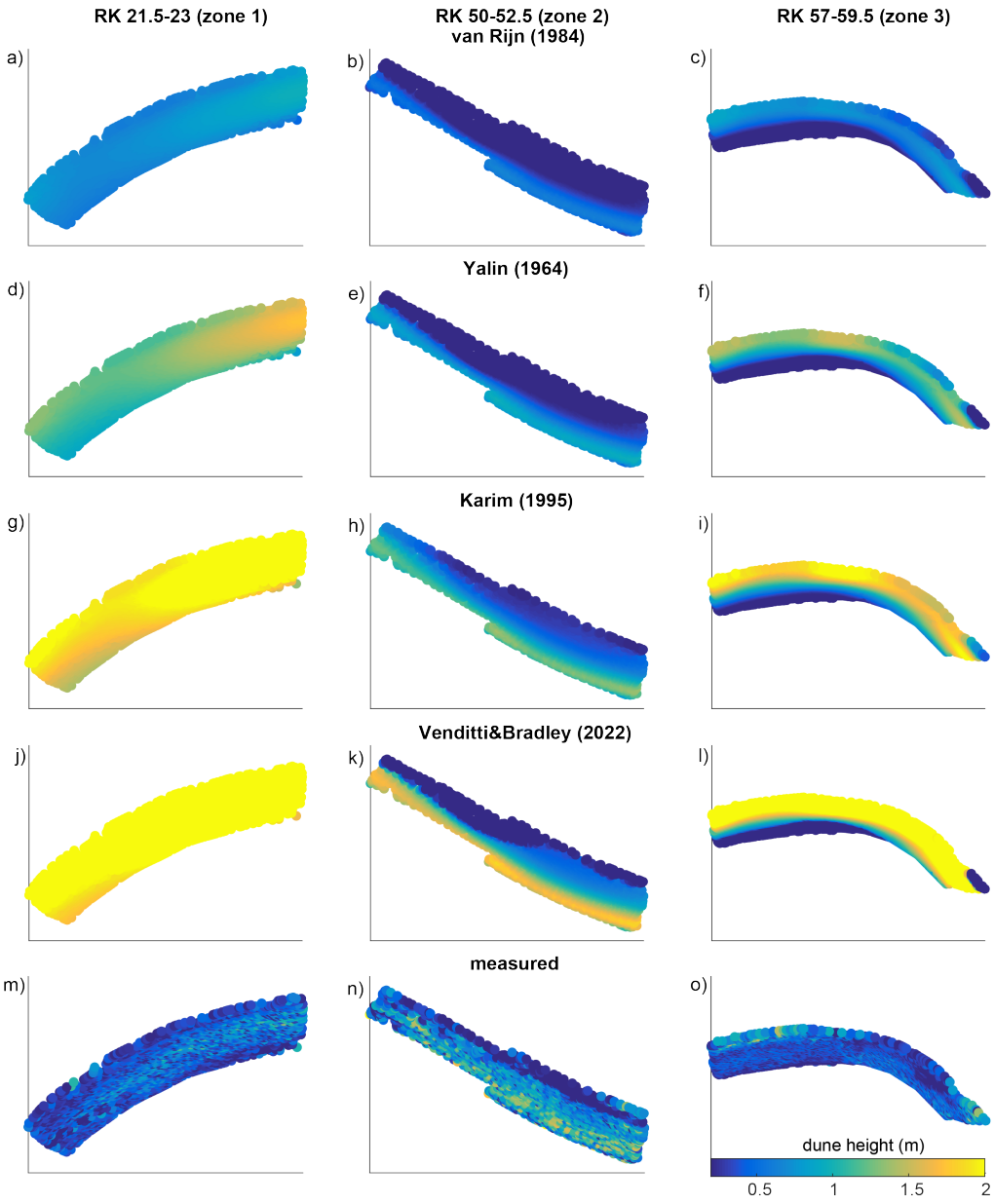


**Figure 7.9** | Dune height estimations from the predictors of van Rijn (1984) (a,b,c), Yalin (1964) (d,e,f), Karim (1995) (g,h,i) and Venditti & Bradley (2022) (j,k,l), compared to the measured dune height (m,n,o).

(van Rijn, 1984) (equation 7.2) is applied to each zone using model output per grid cell. The dune height predictor of van Rijn (1984) performs reasonably well in estimating the local spatial pattern of dune height in the three zones (Figure 7.9a-c), but the mean dune height is overestimated for zone 1 and 3, and underestimated for zone 2. To assess the performance of the van Rijn model in predicting dune patterns, a bias correction is performed. Numerical values were added to or subtracted from the predicted dune height in order to minimise the RMSE, and assess the overall patterns in the dune field rather than the actual value (Supplementary Figure S5). The bias-corrected RMSE values of dune height average 0.13 m, which indicates that the spatial pattern of dune heights is relatively well captured by the predictor. The dune height predictor of van Rijn (1984) captures the main processes that determine dune height in tidal environments, but does not reliably predict absolute values. The dune height predictors of Yalin (1964), Karim (1995) and Venditti & Bradley (2022) are even worse on the local scale (Figure 7.9d-l). Notably, the bias correction improves their performance, (Supplementary Figure S6), but they capture the pattern less than well than the predictor of van Rijn (1984).

### 7.4.4 | Comparison of observed dune roughness and model roughness

Hydraulic roughness generated by dunes was calculated using equation 7.13, which includes dune height and length, but does not include the leeside or stoss side angles. The estimated roughness decreases in the downstream direction (Figure 7.10), which is mainly caused by an increase in water depth. The main variability in roughness is due to variability in water depth, which is most pronounced in the upstream part (RK $>$ 40) of the river (Figure 7.4). Additionally, local fluctuations in roughness correspond to the local patches of higher dunes, for example at RK $\sim$54, 63 and 68. The decrease in grain roughness due to a subtle degree of downstream fining has a small impact on overall roughness, because grain roughness values are only around 3% of typical form roughness values. In the downstream reach (RK $<$ 40), smoothed roughness shows a persistent out-of-phase relation with the gradient in smoothed bed elevation (moving average filter of 8 km) (Figure 7.10a) that is absent in the upstream part of the river.

The calculated dune roughness differs slightly from the uniform roughness used in the model (Manning's roughness of $n_{man}$ = 0.026 s m$^{-1/3}$). The derived friction coefficient $f_m$ from the model's roughness (equation 7.17 and 7.18) displays the expected decrease in seaward direction, reflecting the increase in water depth. Dune roughness agrees reasonably well to the uniform model roughness (Figure 7.10b), but local fluctuations are not well-represented. In the upstream region (RK $>$ 40), the model roughness is slightly lower than the dune roughness, while they are similar in the downstream region.

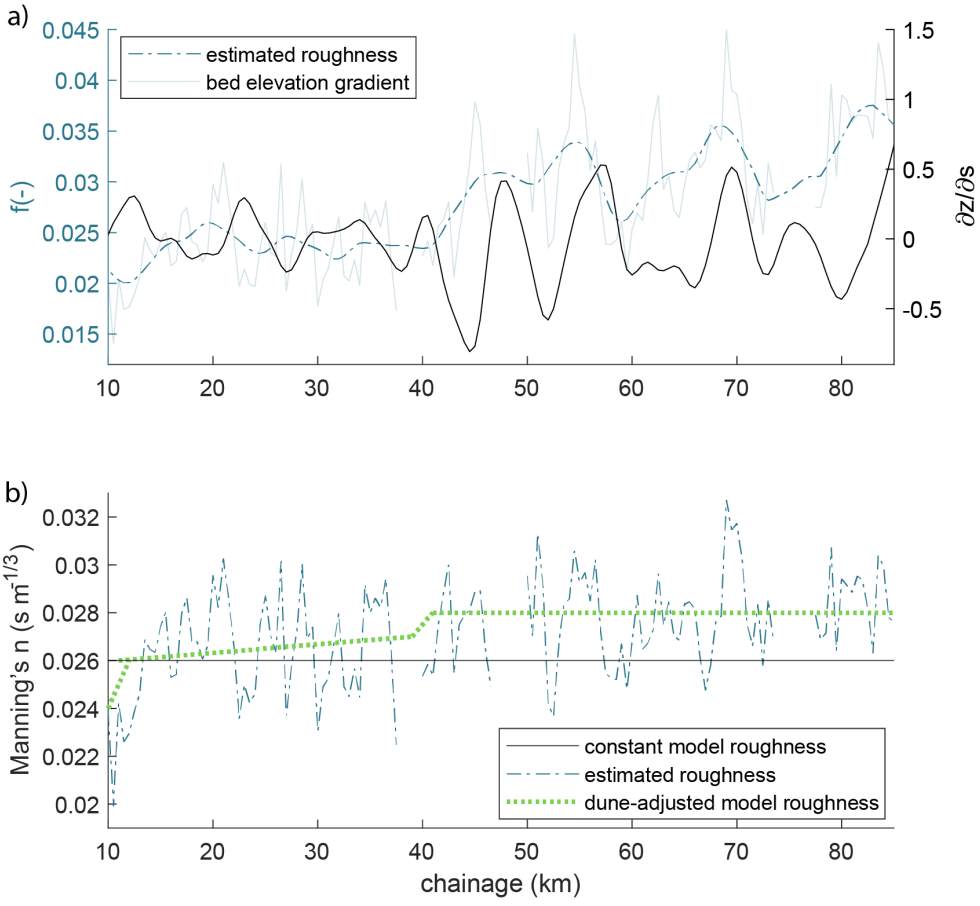


**Figure 7.10** | Hydraulic roughness along the river (chainage). a) smoothed roughness (*f*) (and original roughness in grey) calculated from dune geometry (equation 7.13) (blue) and the gradient of the smoothed bed level (∂z/∂s; black). b) roughness expressed in Manning's roughness coefficient $n_{man}$. Model roughness with a constant $n_{man}$ of 0.026 s $m^{-1/3}$ (black), roughness estimated from dune geometry (equation 7.13 and 7.17) (blue), and dune-adjusted model roughness (green).

To represent the effect of dune height variation on roughness in the hydrodynamic model, and to investigate if this can improve the calibration, the dune roughness as calculated by equation 7.13 is divided into three linear components: a uniform roughness of $n_{man}$ = 0.024 s $m^{-1/3}$ from RK 0 - 10, a linearly increasing roughness of $n_{man}$ = 0.026 to 0.027 s $m^{-1/3}$ in the tidally dominated regime (RK 10 - 40), and a uniform roughness of $n_{man}$ = 0.028 s $m^{-1/3}$ in the mixed fluvial-tidal regime (RK > 40). A small transition area between the breaks is implemented to ensure a smooth transition to the new roughness regime. These roughness transitions correspond with the transition from the fluvial regime to the deltaic regime around RK 40, and the downstream change from a confined to a less confined channel at around RK 10 (Figure 7.1).

The dune-derived roughness has little impact on the calibration of water levels and tidal amplitude of the $M_2$, $K_1$ and $M_4$ tidal components (Supplementary Figure S3b). On average, the RMSE value of the modelled water height decreases from 0.36 m to 0.35 m, and the difference between the modelled and observed $M_2$ amplitude increases from 3% to 4% and $K_1$ from 4% to 6%. Additionally, using the dune-derived roughness for dune height estimation with the Van Rijn predictor only slightly improves the estimated values (17 cm at RK 80 and RK 10) (Figure 7.8).

## 7.5 | Discussion

### 7.5.1 | How are bedform characteristics impacted by the sudden change in tidal flow strength during periods of low river discharge?

During the low river discharge conditions like studied in this research, the increase in water depth around RK 40 results into two different hydrodynamic regimes (Figure 7.11). The tidally-dominated regime is characterised by large maximum absolute shear stresses, a large tidally-averaged water depth, relatively symmetrical dunes, low leeside and slip face angles and low hydraulic roughness. The mixed tidal-fluvial regime is characterised by a weaker tidal influence, a shallower and more variable water depth, lower maximum absolute shear stresses, asymmetric dunes, higher leeside and slip face angles, and a rougher hydraulically regime. The increase in depth is the main reason that hydraulic roughness is lower in the tidal regime (equation 7.13), since the sources of roughness in the Main Channel, sediment composition and dune height, are relatively constant.

Contrasting flow conditions in the two regimes are not reflected in dune height or length. In other systems, dune height is sometimes found to decrease in tidally-influenced regions (Prokocki et al., 2022). Rapid local deposition of the sediment in the deltaic part of the Fraser might result in tidal dunes that are larger than expected (Villard & Church, 2005). The change in flow regime is reflected in the leeside angle, slip face angle, dune symmetry and dune crest shape. In particular slip face angles are

significantly larger in the fluvial-tidal regime, on average 13° compared to 7° in the tidal regime. Dunes are on average asymmetric upstream of the bifurcation at RK 40 (Figure 7.7), and symmetric downstream of RK 40. This agrees with the findings of Kostaschuk & Villard (1996), who relate the symmetric dunes to high sediment transport rates due to the tides, potentially flattening the leeside angles. Indeed, high maximum shear stresses (Figure 7.11b) are observed in the tidal regime, although tidally-averaged shear stresses remain relatively constant (Figure 7.4b).

The reversal of the current switches the leeside and stoss side every tidal cycle, steepening both sides in a similar manner (Lefebvre & Winter, 2016). This could be one of the reasons for the large observed variability in angles, since the MBES data is simply a snapshot of the riverbed. Bidirectional currents cause crest orientation to be time-dependent (Hendershot et al., 2016). Both the duration ($t_{rev}$) and the strength of the flow reversal ($\tau$ or $Q$) determine the dune shape. During low river discharge conditions, the maximum upstream-oriented discharge at RK 22 varies between 4000 and 6000 $m^3\ s^{-1}$, depending on the spring-neap tide cycle. Only 30 km further upstream this has decreased by 66-75%, although the reversal time has only dropped by 9%.

These observations partially agree with the findings of Lefebvre et al. (2021) and Prokocki et al. (2022). Prokocki et al. (2022) observed two different regimes in the Lower Columbia River, USA, based on dune geometry: (fluvial-)tidal dunes, and fluvial dunes. The former were restricted to the most downstream reach (RK $<$ 30 km), and were upstream oriented, predominately low-angled (based on maximum LSA), 2D dunes. Fluvial dunes were downstream oriented, and were higher and longer than the tidal dunes, with higher slip face angles. The division of the regimes in the Columbia is clearer than in the Fraser. One of the reasons for this could be that the division in the Columbia coincides with a change in grain size. The relatively minor downstream fining in the thalweg of the Fraser river (Figure 7.2e), which this is not uncommon in other large sand-bedded rivers (Frings, 2008), might be one of the contributors to the absence of a decrease in dune height in downstream direction as observed in the Lower Columbia.

Lefebvre et al. (2021) also found an increase in dune symmetry in the downstream direction in the Weser Estuary, Germany, but they did not distinguish between two different regimes. However, their data shows that around 60 km from the river mouth, upstream of the estuarine turbidity maximum, the leeside angle of dunes decreases, and dunes become more symmetric. The gradual transition is almost twice as far upstream as in the Fraser River, potentially attributable to the tidal effect in the Weser extending much further upstream than in the Fraser. In this study, and in those of Prokocki et al. (2022) and Lefebvre et al. (2021), the transition in dune morphology coincides with an increase in channel cross-sectional area, either by widening, deepening or both. The deeper regimes are more tidally-dominated, and the constriction

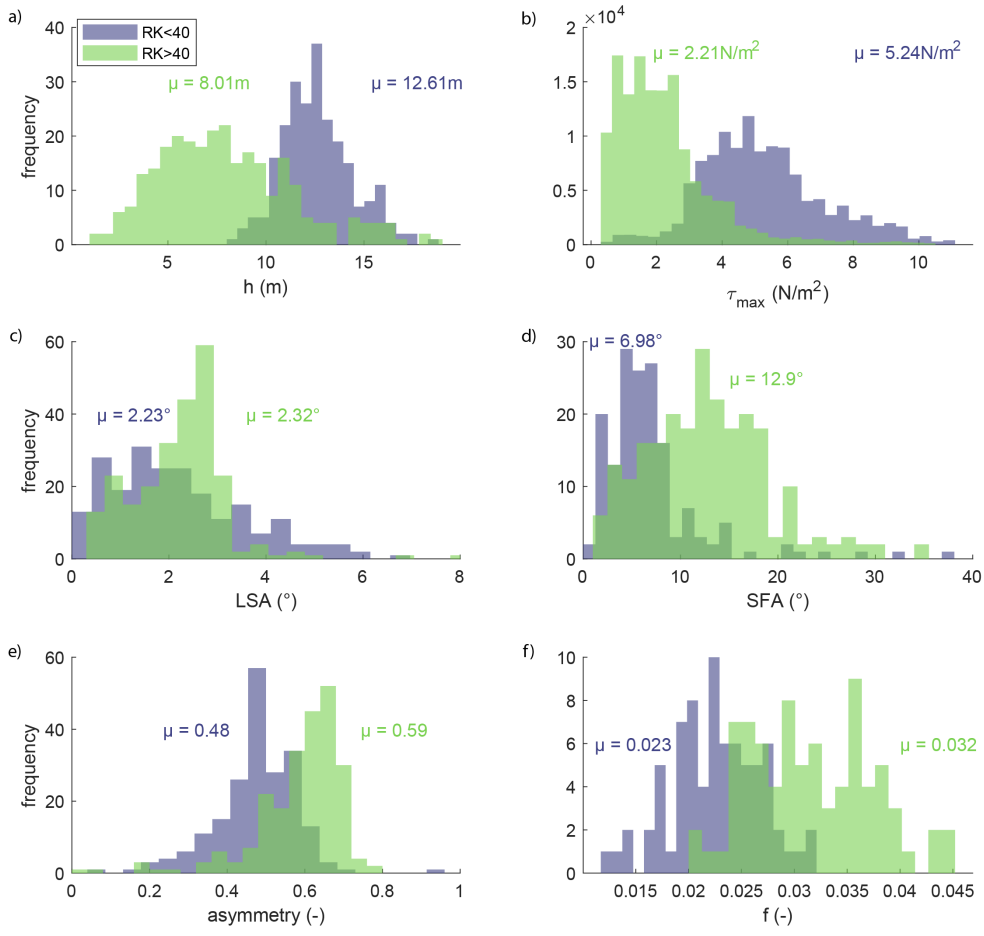


**Figure 7.11** | Characteristics of the tidally-dominated regime, seaward of river kilometre (RK) 40, and the mixed tidal-fluvial regime, landward of RK 40. a) water depth (*h*). b) maximum absolute shear stress ($\tau_{max}$). c) leeside angle (*LSA*). d) slip face angle (*SFA*). e) asymmetry. f) friction coefficient (*f*) derived from dune geometry with equation 7.13. Mean values are indicated in the figure.

upstream of the cross-sectional area leads to a rapid dissipation of tidal energy, that is reflected in the dune leeside angle and symmetry. Comparison between different river systems and disentangling the drivers behind the different patterns in dune geometry is worth future study.

### 7.5.2 | How can dune variability in the fluvial-to-tidal transition zone during low river discharge be estimated and explained?

Tidally-averaged bed shear stresses from the hydrodynamic model can be used to reliably estimate reach-averaged dune height using the predictor of van Rijn (1984). Furthermore, the shear stress distribution estimated by the hydrodynamic model with constant roughness can be used to estimate local dune patterns (Figure 7.8b-g), thereby capturing the cross-sectional variability in dune heights as observed in Figure 7.6. Shear stress, which varies over the cross-section, and is one of the input parameters of the dune predictor of van Rijn (1984), largely explains the observed patterns. For example, in zone 1, dune height decreases downstream, because river width increases and flow velocity decreases, resulting in lower shear stresses (Supplementary Figure S10). In zone 2, dunes are highest on the south side of the channel, where the river is deepest and the flow velocity and shear stresses are highest. Finally, in zone 3, centrifugal acceleration generates higher flow velocity and larger dunes on the outside of the bend, whereas upstream the dunes are the largest on the inner bend because, flow is accelerated by the momentum inherited from the bend upstream (Jackson, 1975).

van Rijn (1984) and other dune height predictors tested did not yield accurate estimates of absolute magnitude of local dune height using tidally-averaged bed shear stresses from the hydrodynamic model. Therefore, we did not use the predicted values in the roughness predictor, but used averaged values instead. The dune height predictors do reproduce the overall patterns of dune height, suggesting that the right processes are captured by the predictors. The van Rijn (1984) calibration factor may be adjusted to better represent the studied field conditions. The poor estimation of absolute values is likely related to a number of factors that are not included in the predictors, including self-organisation dunes in a shear stress field (Bradley & Venditti, 2019) (such as merging and splitting (Hendershot et al., 2018; Gabel, 1993) and crest line deformation (Venditti et al., 2005)), local sediment dynamics not captured by low resolution bed sediment sampling such as local scour (Leclair, 2002), discharge fluctuations and associated hysteresis (Bradley & Venditti, 2021; Julien et al., 2002) and the potential presence of remnant dunes from earlier high-flow conditions.

The influence of local factors can be seen in our three focus zones. The larger dunes observed in zone 2 may be related to the local sediment supply being higher here, so dunes develop to a maximum equilibrium size compared to zones 1 and 3. The dunes in zone 2 become longer in the downstream direction until they disappear, even though flow velocity and grain size do not change significantly. The disappearance of dunes in this area could be because the surface of the bed consists of a thin layer of medium sand overlying a deposit of Pleistocene or early Holocene sediment, such as cohesive clay (Clague et al., 1983) (see Supplementary Figure S1), that is not conducive

to dune formation. Similarly, in zones 1 and 3, dunes do not develop where the outer bank cuts into a clay layer (Supplementary Figure S9). Additionally, the dunes could be reworked remnants from the previous freshet (Bradley & Venditti, 2021), and their geometry could be related to the much stronger and predominantly downstream currents associated with high river discharge. However, Kostaschuk et al. (1989) found that dunes near Steveston (RK 10) adjusted to the post-freshet decline in discharge over a period of weeks, supporting our contention that the dunes observed herein (more than 6 months after the last freshet) are at least in quasi-equilibrium with low-flow conditions. Bradley & Venditti (2021) interpreted low-amplitude bed undulations at RK ~35 as relics from higher flow conditions with smaller dunes superimposed, the latter formed by the low-flow conditions. Kostaschuk et al. (1989) interpreted similar features as "washed-out" dunes that represented a transition from large, freshet bedforms to small dunes adjusted to low river discharge. In this study, we detrended the bed level prior to measuring dune geometry, thereby ensuring that the dunes that we analysed were representative of low flows.

The poor estimation of local dune geometry in the FTTZ and the observed variability in dune morphology has practical implications for scientists and engineers. Firstly, fairway depth cannot be maintained solely on the basis of an average dune height, because height varies unpredictably over the river bed. Secondly, models based on reach-averaged dune geometry may result in inaccurate estimates of form roughness and water levels and local values should be used instead. Thirdly, using estimated dune height to calculate hydraulic roughness would result in an inaccurate roughness prediction in the FTTZ. Finally, because the variability in dune height across the channel is twice that of dune height variation along the channel, the grid cell size in hydraulic models should be twice as large in the longitudinal direction than in the cross-river direction.

### 7.5.3 | To what extent does dune geometry and variability affect reach-scale hydraulic roughness?

Hydraulic roughness is traditionally predicted using dune height and length (Bartholdy et al., 2010; Lefebvre & Winter, 2016; Soulsby, 1997; van Rijn, 1984). However, recent research shows that the leeside angle of dunes might be important for roughness prediction (Lefebvre & Winter, 2016). Characteristics of the leeside angle determine the strength of the flow separation zone (Lefebvre et al., 2014a) in turn affects form roughness (Lefebvre et al., 2013). Large rivers are covered by low-angled dunes (LADs) with slip face angles (SFAs) $< 30^{\circ}$ (Cisneros et al., 2020; Kostaschuk & Venditti, 2019) that generate less flow separation than high-angled dunes that have steeper SFAs (Kwoll et al., 2016). However, weak or intermittent flow separation, with mean leeside angles (LSAs) of only $10^{\circ}$ still generates flow resistance (Kwoll et al., 2016). Lefebvre & Cisneros (2023) show that not only the leeside angle itself, but also

the shape of the leeside impacts flow properties and turbulence. Based on numerical experiments, they found that LADs with a mean LSA of $<10^{\circ}$ and a SFA of $<20^{\circ}$ are not capable of permanent flow separation. LADs do generate turbulence (Kostaschuk & Villard, 1996; McLean & Smith, 1979), however, because the decelerated downstream flow generates a shear layer that causes eddy generation (Kostaschuk & Villard, 1999; Best & Kostaschuk, 2002), sand resuspension and roughness.

In this study, the transition from a fluvial-tidal to a tidal regime and the corresponding change in dune LSAs and SFAs are not reflected in the reach-scale hydraulic roughness needed to attenuate the tidal motion in the model. Implementing a roughness change at the depth break at RK 40 could parameterise the change in dune leeside angle at the regime transition. Models with a higher roughness downstream than upstream performed slightly better than models with the highest roughness upstream (Supplementary Text S3). This is contrary to the expectations based on the leeside angle observations, and suggests a different source of roughness in the tidal regime (see below). Additionally, the dune roughness predictor (equation 7.2), based on dune height and dune length, yields very similar values to the calibrated model roughness (RMSE $f$ = 0.0053). This supports the application of the dune roughness predictor in a tidal environment, and also indicates that dune leeside angle might not be important in determining reach-scale model roughness. Finally, hydraulic model performance is not improved by using local dune geometry. This in turn suggests that variable dune roughness might not be needed to simulate large-scale (tidal) flow. Similar conclusions were drawn from a fluvial system where dune roughness calculated from dune geometry explained only 31% of the variance of the roughness inferred from the water surface slope (Chapter 6) and the remaining variance could not be explained by leeside angle statistics.

The limited impact of variation in local dune height, length and leeside angle on the hydraulic model could be due to several factors. Firstly, 3-dimensional dune fields such as those in our study area, generate less roughness than 2-dimensional dune fields (Venditti, 2007), which could explain the lack of model improvement when implementing dune-related roughness. Secondly, a complex leeside shape might have an effect on flow separation (Lefebvre & Cisneros, 2023) and form roughness. So, even though the SFAs are large enough to generate flow separation, the shape of the leeside might prevent it. Thirdly, we evaluated the hydraulic model by assessing tidal attenuation and water level fluctuations and found minimal impact from local dune geometry. This notwithstanding, incorporating dune roughness could be important for estimation of residual sediment transport (Herrling et al., 2021; Brakenhoff et al., 2020). Local values of shear stresses may be required for morphodynamic modelling, even if they are not needed for modelling tidal propagation in a hydrodynamic model.

We evaluated the model on the reach-scale where other components of roughness dominate (see below). These components are less relevant on the local scales, where dunes might be the main source of roughness. In addition, the estimation of hydraulic roughness generated by dunes deviates locally from the constant model roughness. As a result, in the mixed tidal-fluvial regime, the dune-induced roughness is larger than needed for attenuation based on the calibrated roughness. Davies & Robins (2017) found that the overall effective roughness of the bed is about half of the maximum local dune-induced roughness expressed in $k_s$. Halving the $k_s$ value in equation 7.13 results in a comparable dune roughness and calibrated roughness in the mixed fluvial-tidal regime (RMSE 0.0034 for RK $>$ 40; Supplementary Figure S4), but not in the tidally-dominated regime where dune roughness remains lower than calibrated roughness. This could be a result of lower LSAs in the tidal regime. Including the LSA in roughness estimation using the equation developed by Lefebvre & Winter (2016) results in unrealistically low values of roughness. In general, the available evidence indicates that the LSA does not have a significant impact on reach-scale model roughness.

In our research area there are several reach-scale sources of roughness. Firstly, large-scale river geometry, which is included in the hydraulic model by the bathymetry. We observed an out-of-phase relation between hydraulic roughness and the smoothed gradient of the bed level in the tidally-dominated regime (Figure 7.10). A similar relation was observed in the Rhine and Waal rivers in the Netherlands in Chapter 6, where it was hypothesised that multi-kilometre depth oscillations induce flow divergence associated with depth increase, which in turn causes energy loss. This is reflected in an elevated hydraulic roughness. Such an out-of-phase relation is again seen in the tide-dominated part of the lower Fraser, but not in the mixed tidal-fluvial regime. There, depth increases coincide with decreases in width, keeping the cross-sectional area relatively constant. As a result, changes in depth do not result in flow divergence or convergence and the out-of-phase relation does not develop. Secondly, intertidal areas affect reach-scale roughness. The calibrated friction in our model is an indication of the friction required to attenuate the tide. The model calibrated with a uniform Manning's roughness ($n_{man}$ = 0.026 s m$^{-1/3}$) performs reasonably well in modelling tidal propagation, but regions with a significant decrease in tidal energy (between RK 9-18.5 and 35-42) are not well-captured by the model (Figure 7.3). These regions include intertidal areas (Supplementary Figure S11), which flood during high tide and are not properly represented in the model, limiting tidal attenuation. Also, engineering works, such as the tunnel at RK 18 and the bridge at RK 36, could be an extra source of roughness.

It is worth noting that the results from this study may not be directly applicable to higher flows in the Fraser or other FTTZ-systems. During high discharge conditions in the Fraser (freshet), dunes generally increase in size compared to low flows (Bradley

& Venditti, 2021), and could be a larger source of roughness. However, slip face angle does not seem to increase significantly during freshet conditions (Bradley & Venditti, 2021), meaning that flow separation and the resulting elevated roughness will not occur more frequently than during low discharge. Additionally, during the freshet, more large-scale roughness elements will be included in the river corridor, including submerged intertidal areas and bars. We consider the effects of large-scale geometry changes on hydraulic roughness to be a key subject that has remained severely understudied to date.

## 7.6 | Conclusions

About 40 km from the mouth of the Fraser River, a local depth decrease separates a fluvial-tidal regime at the landward side from a tide-dominated regime crossing the Fraser Delta. Bathymetric data and a hydraulic model of the lowermost 85 km of the river were used to explore the spatial variability and controls of dune morphology in this fluvial-to-tidal transition zone (FTTZ). From our investigations, we conclude that:

- There are no significant spatial trends in dune height or length, even though the river deepens at RK 40. Local variability in dune height and length dominates regional trends, and variability in dune height and length in the cross-sectional direction is twice as large as in the longitudinal direction.
- In the tidal river, dune height predictors provide a good first approximation of regional dune height and local spatial patterns, but local shear stress predictions need to be improved to enable robust estimates of local dune heights. Using shear stresses from the hydraulic model calibrated with a constant Manning's $n$ roughness of 0.026 s $m^{-1/3}$, the dune height predictor of van Rijn (1984) reproduces local patterns of dune heights, using tidally-averaged values of bed shear stress. Other predictors of dune height perform worse.
- Mean leeside and stoss side angles of dunes are lower in the tidal regime compared to the fluvial-tidal regime, and dunes become symmetric under tidal influence. These changes in dune morphology do not affect reach-scale hydraulic roughness, because the calibrated model roughness is similar to the dune-derived roughness based on dune height and dune length. As a result, hydraulic model performance using a calibrated, constant, roughness is not improved by implementing dune-derived bed roughness.

- In the Fraser River, large-scale variations river geometry are more important than dune morphology in controlling variations in reach-scale roughness, a finding which is not unique to the Fraser River (Chapter 6). In the Fraser river, oscillations in river depth elevate hydraulic roughness in the tidal region, but this does not occur in the fluvial-tidal regime because changes in depth are compensated for by changes in width, keeping the cross-sectional area of the channel relatively constant. Intertidal areas in the Fraser are likely a significant source of flow resistance. Flow resistance by depth variation and intertidal areas needs further study.

*I could potter for hours on a lonely beach*
*Picking pebbles to roll in my hand*
*Wondering where will the next wave reach*
*Writing my name in the sand*
*— Eric Finney*

# Synthesis

## 8.1 | Introduction

In the previous chapters, I aimed to enhance understanding of the variability in bedform geometry, and its effect on the flow via hydraulic roughness. Therefore, an extensive analysis of factors influencing dune geometry was presented, and hydraulic roughness in fluvial and tidal systems was discussed. Doing so, I assessed the two main objectives as introduced in Chapter 1, namely:

- Establish and understand how environmental factors in the FTTZ alter bedform geometry.
- Determine how bedforms impact the hydraulic roughness in the FTTZ.

The first objective was reached by studying how mixed sediments can best be measured (Chapter 2), followed by an analysis of the impact of these mixed sediments (Chapter 3) and flocculation (Chapter 4) on dune geometry. Additionally, the impact of high flow velocities on dunes was explored (Chapter 5). For the second objective, the impact of dunes and their leeside angle on reach-scale roughness was explored, both in the fluvial realm (Chapter 6) and the fluvial-tidal realm (Chapter 7). The main conclusions are summarised in Figure 8.1.

I reached the objectives by combining multiple methods, including analysing field data, performing laboratory work, and building a computer model. The first main objective was achieved by performing various laboratory and field experiments, in which I studied the impact of mixed sediments, including flocculated sediment, and the impact of high flow conditions, on dune geometry. The second objective was fulfilled by analysing field data of the Waal River (the Netherlands) and the Fraser River (Canada), and a hydrodynamic model was made to assess the impact of dunes on roughness. In this final chapter, I will reflect on these two objectives by discussing my key findings. I examine the broader implications of these findings, and discuss future research directions which follow from my work.

## 8.2 | Main findings of this thesis

### 8.2.1 | Environmental factors altering dune geometry

In the FTTZ, different environmental factors impact dune geometry than in rivers, causing the geometry of the dunes to differ from values predicted with empirical equations developed for unidirectional flow and unimodal bed sediment. In this thesis, three of these environmental factors were discussed.

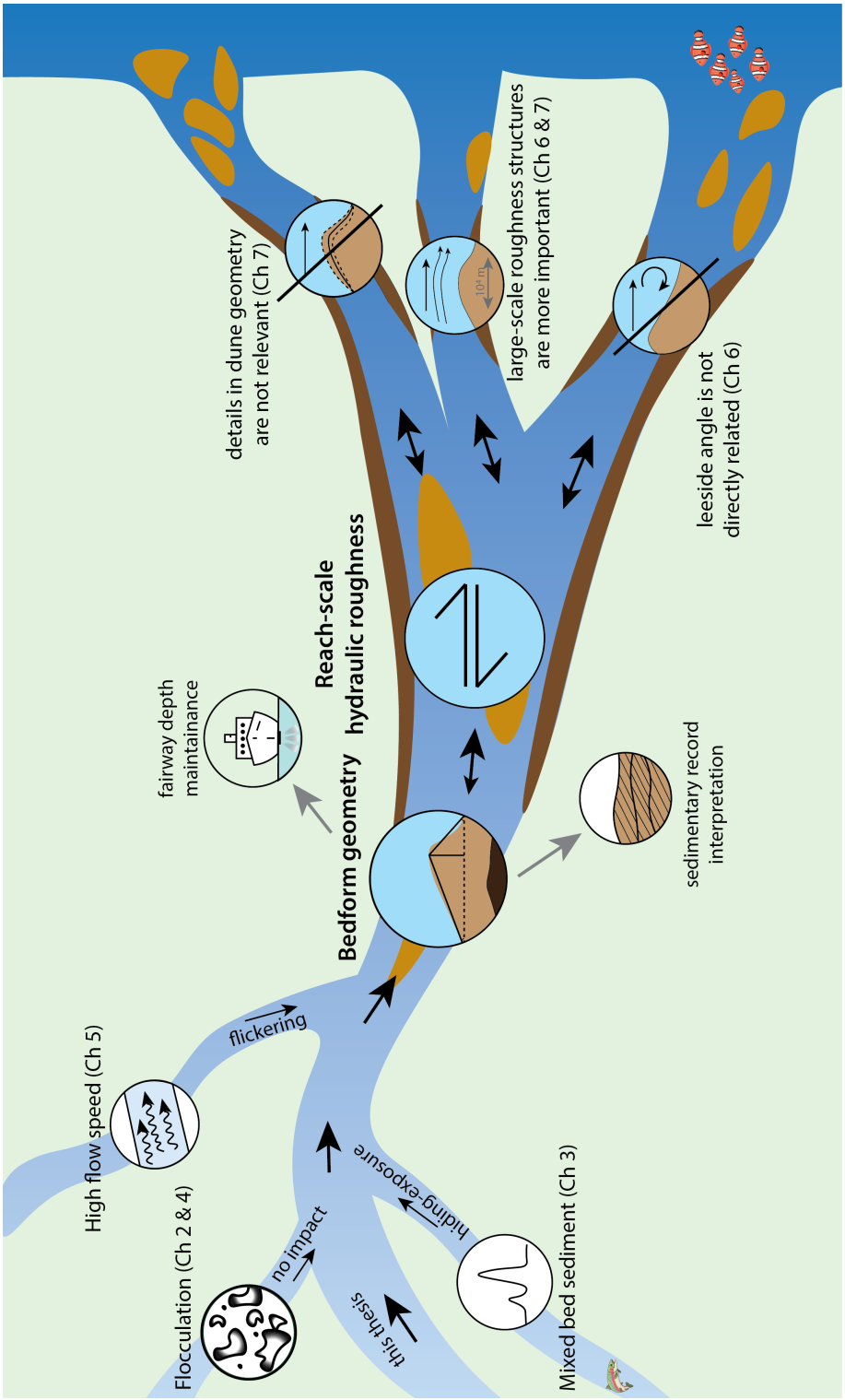


**Figure 8.1** | Graphical abstract of this thesis indicating the main conclusions of this thesis.

One of these factors is the particle size distribution (PSD) of mixed sediments. Accurate measurement of the PSD of mixed sediments is required, but this proved to be highly dependent on the measurement method. There is a large difference in PSD of mixed sediments measured in situ or ex situ, caused by ex situ deformation of the flocs which alters the (effective) particle size. When interested in the effective particle size, mixed sediments (containing flocs) can therefore best be measured in situ rather than ex situ, and careful time-averaging of the measurement data is required.

At low to medium transport stages, the PSD of the sediment bed impacts the geometry of the dunes. The impact of fine material in sandy sediment beds on dune geometry depends on the nature of the fine material. Non-cohesive fines in a base material of sand lead to an increase in mobility of the base material, caused by the hiding-exposure effect, which lengthens the dunes. However, cohesive fines result in a decrease in the mobility of the sandy base material, which hampers dune formation.

Flocculated sediments, either in the water column or incorporated in the river bed, do not impact the dune geometry significantly. However, the flocs interact with the bed by being buried in the leeside of the bedforms and released from the stoss.

At high transport stages, the dune geometry variation is not dominated by the sediment composition, but by bed instability. At high flow velocities, when dunes transition to upper stage plane bed, a bimodal distribution of dune heights emerges. This is attributed to flickering between two alternative states, indicating a critical transition. This critical transition is potentially triggered by local sediment outbursts, and could have considerable consequences for field measurements and experimental designs.

### 8.2.2 | Hydraulic roughness in the FTTZ

Reach-scale hydraulic roughness could be approximated using well-established roughness predictors using dune geometry, both in rivers and in the FTTZ. However, although dune geometry provides a base roughness, it does not fully explain the variance. Details in dune geometry, including various leeside angle statistics, do not seem to relate directly to the roughness. Instead, larger-scale roughness elements dominate the reach-scale roughness variance. These included energy losses due to kilometre-scale bed level undulations, and intertidal areas.

Using modelled local shear stresses in the FTTZ in empirical dune height predictors, poorly represent the actual dune height. However, they serve as a good predictor of local dune patterning, indicating that these equations could be in some form applicable to the FTTZ.

## 8.3 | Implications and broader context

### 8.3.1 | Implications for dune geometry prediction

This thesis once again demonstrates the high spatial variability of dune geometry. Even under conditions of unimodal, non-cohesive, sediment and a uniform and steady flow, dune geometry exhibits variations in both space and time (Venditti et al., 2016; Bradley & Venditti, 2019). The interaction between flow, sediment transport, and bed morphology, as well as the feedback mechanisms among them, result in an ever-changing bed and significant spatiotemporal variations in dune geometry, as observed in Chapters 3, 5, and 7. Consequently, predicting dune geometry cannot solely rely on reach-averaged values for flow and sediment characteristics (Chapter 7). Instead, if accurate dune geometry is required, local-scale variables should be used, either from a high resolution hydraulic model or detailed field measurements.

The spatial variability in dune geometry is not only complicating the prediction of the geometry, but also obscures back-predicting flow conditions from the sedimentary rock record (Reesink et al., 2015). Based on the expected preservation potential, dune geometry preserved in sedimentary rock is used to derive past flow conditions. However, due to the newly found large spatiotemporal variability in dune geometry both along and across the river (Chapter 7), preserved dune geometry only reflects local conditions, and is not representative of the general state of the river. Furthermore, spatial variability in flow and sediment transport alters the preservation potential (Reesink et al., 2015). Therefore, overlooking the substantial variability in dune geometry, particularly during high flow conditions (Chapter 5), leads to unreliable predictions of past flow conditions inferred from the sedimentary rock record.

On an operational level, variability in dune height that is not accounted for can impede shipping and dredging practises. Maintenance of a minimum depth of lowland rivers is crucial for shipping, and the water level must stay above the low navigable water level (LNWL) throughout the entire season. Large variations in dune height impact the fairway depth, and may jeopardise the enforcement of the LNWL. Therefore, unravelling the drivers behind this spatial variability is essential.

Spatial variability in bedform geometry may be partially intrinsic, but it can also be caused by spatially varying transport stages, stemming from variability in the sediment and flow characteristics (Chapters 2-5).

In a system with a sediment bed with a relatively constant grain size, local flow characteristics, such as bed shear stress, effectively capture the patterning of dunes (Chapter 7). However, especially in the FTTZ, significant grain size variations can occur on a local scale. There, an accurate determination of the bed particle size distribution (PSD) (and particle shape, see Deal et al. 2023) is essential, since the correspond-

ing sediment mobility is (implicitly) incorporated in dune geometry predictors. In the predictor of van Rijn (1984), an exponent of 0.3 dampens uncertainties in the PSD parameterisation, while in the predictor of Venditti & Bradley (2022), the critical shear stress is used, which is a direct product of the PSD. Failing to map spatial variation in PSD with sufficient resolution (Chapter 7), or inadequate measurement protocols (Chapter 2), leads to a poor representation of the local PSD and the corresponding sediment mobility, which hampers dune geometry prediction. Additionally, simplifying a complex particle size distribution into a single value of medium particle size can be problematic, particularly in the case of bimodal distributions where complex particle interactions and possibly cohesion (Schindler et al., 2015; Parsons et al., 2016) play a role (Chapters 2 and 3). Furthermore, the effective particle size, including flocs and all other natural components which interact with the bed (Chapter 4), differs from the primary particle size. The final particle size distribution depends on whether the selected measurement method includes these aggregated particles (Chapter 2). An accurate determination of the bed shear stress required for bed mobilisation, and a description of the interaction between the various particle classes within the PSD, are essential for deriving the effective mobility of the sediment bed, and predicting dune geometry.

This thesis has only briefly addressed the variability of flow, sediment, and dune characteristics over time (Chapter 5). However, this aspect cannot be overlooked. Due to the slower response of bed morphology compared to water in adapting to changing conditions, the geometry of the bed will naturally lag behind the fluctuations of an unsteady flow, a process called hysteresis. This makes the exact dune height prediction in unsteady flows challenging if not impossible. As suggested by Bradley & Venditti (2017), it is necessary to embrace average values with large error margins. A process not considered in this approach is the flickering of the bed between different states at high transport stages (Chapter 5). This phenomenon considerably increases the standard deviation in dune height and length. This poses challenges not only for fairway depth management, dike height, and the stability of buried pipes and bridges during high discharge conditions, but also questions the validity of relying on average values.

### 8.3.2 | Implications for hydraulic roughness determination

Many sources of roughness contribute to the total hydraulic roughness (Figure 8.2). Based on the findings in this thesis, dune geometry provides a base roughness, but does not manage to explain the observed variations in total roughness (Chapter 6 and 7). Instead, large-scale variations, such as kilometre-scale bed-level undulations (Chapter 6) and intertidal areas (Chapter 7) are an important source of energy dispersal as well. This suggests that, for accurate hydraulic modelling of the river system, the focus should be also on larger-scale roughness elements rather than only

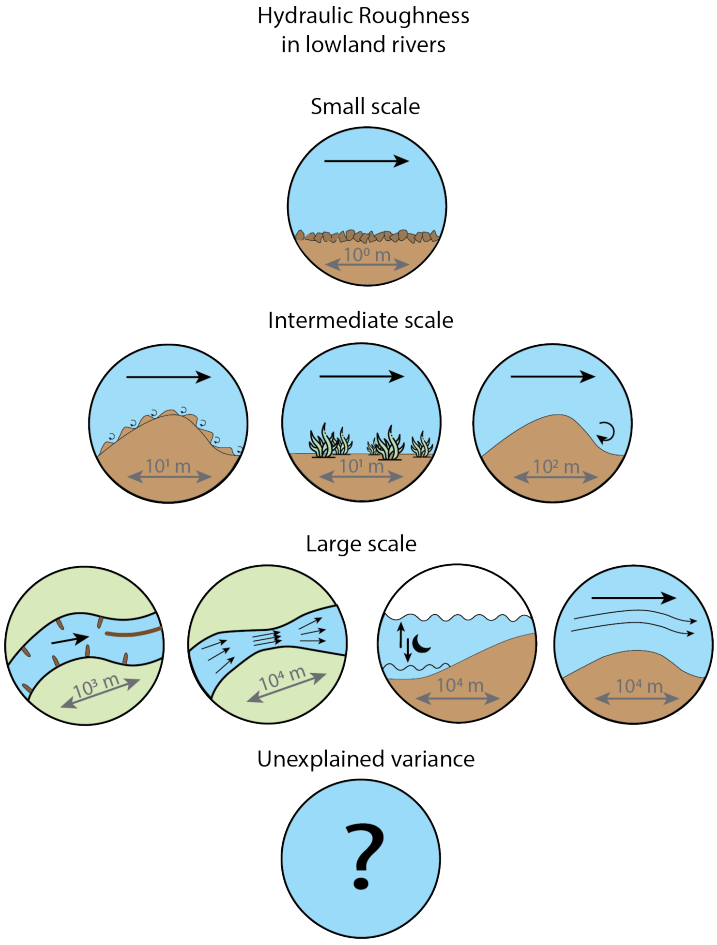


**Figure 8.2** | Sources of hydraulic roughness. Small scale (grain roughness), intermediate scale (superimposed dunes, vegetation, dunes), large scale (human-made structures, constrictions and widenings, intertidal areas, kilometre-scale bed-level undulations) and unexplained variance.

bedforms and equally- or smaller-sized roughness elements (e.g. vegetation, superimposed bedforms, or bed sediment). In lowland rivers, the larger-scale roughness elements that might significantly influence the friction include, in addition to the aforementioned suggestions, human-made structures such as groynes and variations in river width, such as constrictions and widenings (Figure 8.2). This finding might be not only relevant in lowland rivers, but also in mountain rivers, where Housageo et al. (2023) suggest that large-scale roughness elements (boulders, exposed bedrock, channel properties) impact the total hydraulic roughness more than abundant smaller-scale roughness elements (grain roughness).

Furthermore, in lowland rivers with low-angled dunes, we did not find evidence that details in dune geometry are relevant for the reach-scale roughness, although dunes themselves do provide a base roughness (Chapters 6 and 7). This contradicts the general notion that dune geometry, and especially a measure of the dune leeside angle, is a critical parameter for hydraulic roughness (Lefebvre & Cisneros, 2023; Kwoll et al., 2016). Arguably, the role of the dune's LSA might be relevant in the absence of larger roughness elements and in the presence of higher-angled dunes with obvious flow separation (Chapter 3; Lefebvre & Cisneros, 2023). Therefore, our findings need to be verified in other riverine systems.

In the fluvial-to-tidal transition zone, a presumed gradual transition from the fluvial to the tidal regime is often modelled to be reflected in the hydraulic roughness (e.g. de Brye et al. 2011; Schrijvershof et al. 2023; Bolle et al. 2010; Stark et al. 2017; Vroom et al. 2015). In the case of the Fraser River, the transition from a fluvial to tidal regime seems to be abrupt, but the hydraulic roughness in the river (up until the river mouth) could be considered constant (Chapter 7). If this finding can be extrapolated to other systems and various flow conditions, and the hydraulic roughness indeed can be deemed constant, this would greatly simplify modelling efforts. Then, models can simply adopt one Manning's $n$ value for the entire FTTZ, which would, after conversion to the Chézy coefficient, only vary with water level. However, the constant-roughness approach would necessitate an extremely accurate representation of the larger-scale bathymetry and river geometry, as variations in large-scale bathymetry primarily determine reach-scale roughness variations and consequently, tidal attenuation. It might be that this is already indirectly included in models (such as in Zijl & Groenenboom 2019) by adopting block-like roughness regions, derived from water level calibrations and without physical meaning.

## 8.4 | Future research directions

This thesis concentrates on how bedform geometry is impacted by sediment mobility and flow characteristics, and how this is reflected in reach-scale roughness. However, many more questions remain, and some of the most important scientific challenges are outlined below.

### 8.4.1 | Spatial variability in bedform geometry

Spatial variability in bedform geometry, and and its contributing factors, must be acknowledged and studied in more detail. To date, we are not able to predict spatial variability in dune geometry. Spatial variability does not only include variability in bedform geometry, but also the (2D or 3D) planform of an entire bedform field. Especially in the FTTZ, where variations in space and time are the norm rather than the exception, continued neglect of spatial variability could lead to inaccuracies in

predicting sediment transport patterns and fluxes. Using these inaccuracies for operational management of the rivers, can have severe impacts, including the instability of buried infrastructure, harming ecosystems, and inefficient maintenance of navigation channels.

Spatial variability in dune geometry is relevant on all spatial scales. In large, kilometre-wide systems, such as the Lower Meghna in Bangladesh, tremendous cross-sectional variability exists. For example, van den Berg (2021) found large variability in dune orientation depending on location within the channel, and three different scales of superimposed bedforms. Ebb and flood chutes exist, and sub-channels within these systems can be flooding while other channels are still ebbing. Additionally, numerous confluences and bifurcations influence the local flow. It is unknown how these local flow dynamics affect the resulting dune geometry.

On a smaller scale, the transition between dune fields and non-dune fields should be explored. A transition can be either abrupt or gradual. Examples of an abrupt transition could be caused by the emergence of a sticky clay deposit that the river has eroded into (Chapter 7). Alternatively, a gradual transition could occur when the sandy bed progressively becomes more clay-rich in downstream direction (downstream fining), as seen in the Pussur-Sibsa in Bangladesh (van den Berg, 2021). Local supply-limited conditions, as result of the underlying geology or due to the lack of mobile sediment input, impact dune geometry significantly (Tuijnder et al., 2009), but field research has primarily focused on well-developed dune fields (such as the well-studied Parana River (Parsons et al., 2005)). To address spatial variability in dune geometry caused by sediment variability (Chapters 3 and 4), more research should be done on the impact of mixed sediments on dune geometry, and efforts should be focused on determining the strength and importance of various effects (e.g. hiding-exposure, cohesion and flocculation). It is essential to find universal ways to parameterise mixed sediment distributions, considering their multimodality, and incorporating this into dune geometry predictors.

Finally, the effect of suspended sediment concentration on dunes should be explored further. Various suggestions have been made regarding how a high SSC could suppress dune growth and formation (Best, 2005). However, this effect is yet to be quantified, and focused laboratory studies are needed. If this effect proves to be significant at concentrations that are natural for lowland rivers, a high SSC in specific areas (e.g. the Estuarine Turbidity Maximum), could enhance the spatial variability of dune geometry.

### 8.4.2 | Scale dependence of roughness

One of the focus points of this thesis was determining reach-scale roughness (from dune geometry) with the purpose of model calibration. The use of the term "reach-scale" roughness implies the existence of multiple scales of hydraulic roughness. Roughness exists at various scales, ranging from individual grains to single dunes, dune fields, river cross-sections, river bends, multi-kilometre river sections, and entire river systems. This is summarised in Figure 8.2, and includes unexplained variance that warrants further exploration.

Based on this thesis, it becomes clear that the importance of large-scale bed undulations requires future investigation. The Waal and Fraser Rivers exhibit a counter-phase undulation of the bed level gradient with the friction factor (Chapters 6 and 7), and the general applicability of this finding needs to be explored. Furthermore, the hypothesis exploring a physical explanation for roughness from these undulations (Figure 6.11) necessitates verification, possibly with laboratory experiments providing detailed flow profiles.

Different scales of roughness can be relevant at different spatial scales. Which scale is studied, depends on the study aims and quantification methods. For example, roughness can be quantified via modelling (Warmink et al., 2013; de Brye et al., 2011; Paarlberg et al., 2010), turbulence (Biron et al., 2004; Pope, 2000; Williams et al., 1999; Vermeulen et al., 2013), velocity profiles (Buschman et al., 2009; Hoitink et al., 2009) or empirical equations including bed geometry (van Rijn, 1984; Lefebvre & Winter, 2016; Bartholdy et al., 2010). The scale of the study implicitly determines which processes are so small that they are all lumped in a term called roughness. For example, in hydraulic modelling, the grid size determines what is considered roughness, and what is explicitly solved (Smith, 2014). In the model of the Fraser (Chapter 7), dunes, which are smaller than the model grid scale, are not explicitly solved, and are parameterised as roughness. However, larger-scale roughness elements, such as the channel geometry and intertidal areas, are explicitly solved by the model, and therefore not included in the roughness parameterisation. All approaches to quantify roughness function at different spatial scales, and yield different absolute numbers (Vermeulen et al., 2013). In other words, the integration of grain-scale roughness does not necessarily yield the same value as the roughness over a cross-section. This means that although our findings suggest that the specifics of bedform geometry may not significantly affect reach-scale roughness, this may not hold for smaller-scale roughness.

Additionally, there might be an interplay between roughness elements, and between different scales of roughness. How one roughness element impacts another roughness element depends on the spatial arrangement of the roughness elements (Smith, 2014). For example, the spacing between river dunes could be large enough so that there is no interaction between their wakes. However, if the roughness elements are closely

spaced, the wakes can interact, creating a complex turbulent flow (Morris, 1955). Other examples include the sheltering effect, where larger roughness elements can shelter smaller elements from the flow (for example in the hiding-exposure effect, Chapter 3). Finally, there might be an interaction between different roughness scales. For example, a rougher sediment bed would create a larger turbulent boundary layer, which in turn would reduce the size of the wake at the leeside of the dunes (the 'golf ball effect'). This would mean that for a similar dune height, the hydraulic form roughness will be larger for a smooth sediment bed (i.e. fine or poorly sorted bed) than for a rough sediment bed. All together, the meaning of roughness is ambiguous, and the relation and interaction between roughness scales requires clarification.

Finally, to be able to fully and accurately parameterise hydraulic roughness in models, different sources of roughness and their relative contribution should be explored, both in rivers and in the FTTZ. Large-scale sources of roughness seem to dominate the total reach-scale hydraulic roughness (Chapters 6 and 7), but the amount contributed by different roughness elements under different circumstances remains unclear. Water surface slope measurements, either continuous (as used in Chapter 6), or discontinuous (with a dense network of water level gauges), could provide detailed insights into the roughness at small river sections. This methodology could be extended to the FTTZ, where roughness is anisotropic (Smith, 2014), and not only scale-dependent but also time-dependent (Lewis & Lewis, 1987; Herrling et al., 2021; Wallis & Knight, 1984). This means when using the St. Vernant equations based on field data, as in Chapter 6, the time derivative term cannot be ignored. The spatiotemporal variation in discharge and velocity can be estimated (Matte et al., 2018), after acquiring accurate bathymetric data of the bed slope and the wetted area for various water levels with MBES or SBES measurements (possibly in combination with LIDAR for obtaining the topography of the river banks). Additionally, this approach could facilitate the examination of roughness dependency on tides and current direction, considering factors such as dune crest and leeside reversal (Herrling et al., 2021), as well as larger-scale phenomena, such as differences in geometry of ebb and flood chutes, and differences in the inundated area (Wallis & Knight, 1984).

### 8.4.3 | (Critical) transitions

Based on this thesis, phase diagrams should include the unstable behaviour observed at the transition from the dune regime towards USPB (Chapter 5). However, prior to this, the theory should be tested with continued laboratory experiments in which the sediment bed is regularly scanned, and during which flow velocity and sediment concentration profiles are taken. These experiments could help in explaining the flickering behaviour, manifest the underlying feedback mechanisms, and establish the duration of the different bed phases (Arani et al., 2021).

This new phase diagram should also include the possible superposition of bedforms. Superimposed bedforms are ubiquitous in rivers (Zomer et al., 2021, 2023), but their existence is not generally implemented in phase diagrams and bedform identification tools. A new phase diagram that acknowledges abrupt, gradual and unstable transitions between phases, and that would implement superimposed bedforms, would present a more realistic view, and could be a start to encompass the natural complexity.

Finally, efforts should be made to incorporate more geomorphological concepts in the critical transition framework (Scheffer et al., 2009, 2012). Spatiotemporal dynamics of dunes can serve as an early warning indicator for tipping points (van de Vijsel et al., 2024), and might be easier to observe than complex changing channel conditions. For example, the abrupt disappearance of bedforms with increasing (physical and biological) cohesion of the sediment bed (Schindler et al., 2015; Parsons et al., 2016; Wu et al., 2022a) could indicate fining of the river bed. Similarly, reduced bedform dimensions can indicate an increase in turbidity (Baas et al., 2016; Best, 2005). In both scenarios, the bedform-generated roughness would be reduced. In the FTTZ, a reduction in bedform-generated roughness might increase the import of fine sediment from the sea (van Maren et al., 2015; Dijkstra et al., 2019), resulting in a positive feedback loop. Therefore, a decrease in bedform dimensions could be an indicator of a trend towards the fining of a system. Monitoring this with easily repeatable MBES surveys could give indirect evidence for (future) regime shifts.

*The River's a wanderer,*
*A nomad, a tramp,*
*She doesn't choose one place,*
*To set up her camp.*
*— Adapted from Valerie Bloom*

# 9

# Supplementary Information

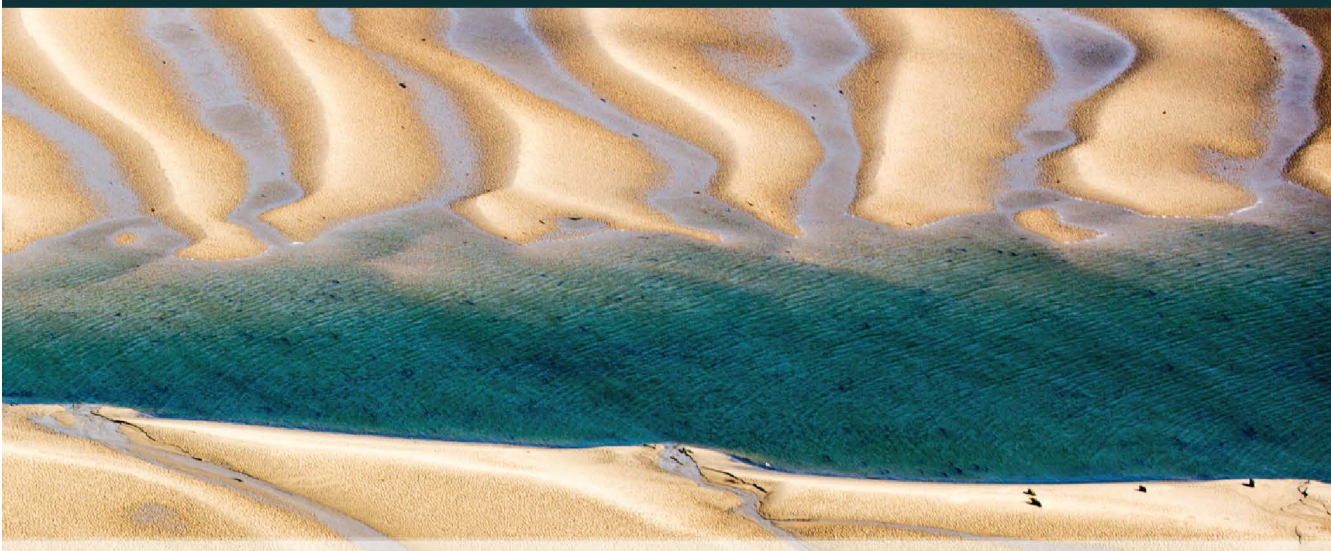

Appendices
Bibliography
Supplementary material
Nomenclature
Acknowledgements
Statement of authorship contribution
List of publications
Curriculum Vitae
Graduate school certificate

# Appendices

**Appendix of Chapter 3: A - Bedform geometry predictors**

The dune height and length predictions based on van Rijn (1984) follow equation 3.6 and 3.7 in which $T$ is van Rijn (1984)'s definition of the transport stage:

$$T_{vRijn} = \frac{(u^*)^2 - (u_c^*)^2}{(u_c^*)^2} \tag{A3.1}$$

where $u^*$ is the shear velocity (m $s^{-1}$), and $u_c^*$ is the critical shear velocity (m $s^{-1}$). Both the shear velocity and the critical shear velocity are unknown, but can be expressed in known parameters. The shear velocity can be expressed via:

$$u^* = u\frac{g^{0.5}}{C'} \tag{A3.2}$$

in which $u$ is the time and depth-averaged velocity (m $s^{-1}$) derived from the measurements with the UB-LAB 2C and $C'$ is the grain-related Chézy parameter ($m^{0.5}$ $s^{-1}$), which can be expressed as:

$$C' = 18log\frac{12R_h}{3D_{90}} \tag{A3.3}$$

Herein, $R_h$ is the hydraulic radius, which is equal to the cross-sectional area $A$ divided by the wetted perimeter ($P$ = width + $2h$) .

The critical shear velocity can be calculated as:

$$u_c^* = \sqrt{\frac{\tau_c}{\rho_w}} \tag{A3.4}$$

In turn, the critical shear stress can calculated using the critical Shields number $\theta_c$:

$$\tau_c = \theta_c(\rho_s - \rho_w)gD_{50} \tag{A3.5}$$

and $\theta_c$ is obtained from Parker et al. (2003):

$$\theta_c = 0.5\left(0.22Re_p^{-0.6} + 0.06 * 10^{(-7.7Re_p^{-0.6})}\right) \tag{A3.6}$$

In which the particle Reynolds number, $Re_p$ (-), is defined as:

$$Re_p = D_{50}^{3/2} \frac{\sqrt{\rho r g}}{\nu} \tag{A3.7}$$

Venditti & Bradley (2022)'s empirical equation for predicting dune height and length can be found in equation 3.8 and 3.9. The dimensionless shear stress $\theta$ is derived by calculating the shear stress $\tau$ from the shear velocity (via equation A3.4, replacing $\tau$ for $\tau_c$). The critical shear stress $\theta_c$ is calculated via equation A3.6.

The geometry of ripples is predicted based on Soulsby et al. (2012) via equation 3.10 and 3.11 in which $D^*$ (-) is given by:

$$D^* = D_{50} \left( \frac{g(\frac{\rho_s}{\rho_w} - 1)}{\nu^2} \right)^{1/3} \tag{A3.8}$$

**Appendix of Chapter 3: B - Hydraulic roughness determination**

For a water column that satisfies equation 3.12, the equation can be rewritten into:

$$\overline{u}(\sigma_d) = \frac{u^*}{\kappa}(ln(\sigma_d) + 1) + U \tag{A3.9}$$

in which $U$ is the depth-mean velocity, and $\sigma_d$ is the dimensionless depth using:

$$\sigma_d = \frac{z + h}{h} \tag{A3.10}$$

The value of $u^*$ can be derived from the slope of a linear regression line through the data points of $\overline{u}$ versus (ln($\sigma_d$)+1). The average velocity $\overline{u}(\sigma_d)$ was determined as the average streamwise velocity during a single measurement. The averaging time window of 30 minutes was narrowed down to cover an integer number of bedforms, defined from top to top. The $\sigma_d$-coordinate was defined such that $\sigma_d$=0 coincides with the top of the highest bedform during a measurement (the 95th percentile of the measured bed elevation was chosen, to exclude outliers as a result of backscatter spikes). The $\sigma_d$=1 coordinate is located at the top of the vertical measuring range, which corresponds to the elevation of the UB-Lab-2C transducer. The time-averaged relation between $\overline{u}$ and $ln(\sigma_d)$ was consistently linear at the middle half of the measured profile (between -0.175 < $\sigma_d$ < -0.625), so this part of the profile was used for determining $u^*$ (Supplementary Figure S6). The goodness of the linear fit of the log-profiles had on average a $R^2$-value of 0.96. Following Hoitink et al. (2009), the roughness length $z_0$ (m) can be calculated using:

$$z_0 = \frac{h}{e^{\left(\frac{\kappa U}{u^*}\right)} + 1} \tag{A3.11}$$

Finally, Manning's n, $n_{man}$ (s $m^{-1/3}$) can be calculated in the following steps (Pope, 2000; Chow, 1959):

$$k_b = 30 * z_0 \tag{A3.12}$$

$$n_{man} = \frac{k_b^{\frac{1}{6}}}{25} \tag{A3.13}$$

in which $k_b$ is the total roughness height (m).

Roughness height can also be approximated indirectly based on the predictor of van Rijn (1984) with equation 3.13, resulting in the dimensionless Darcy-Weisbach friction

factor, $\hat{f}$. Herein, $k_s$ consists of form roughness height $k_{sf}$ and grain roughness height $k_{sg}$:

$$k_s = k_{sg} + k_{sf} \tag{A3.14}$$

$$k_{sg} = 3D_{90} \tag{A3.15}$$

$$k_{sf} = 1.1\gamma_d \Delta (1 - e^{\frac{-25\Delta}{\lambda}}) \tag{A3.16}$$

where the calibration constant $\gamma_d$ is taken as 1 in laboratory conditions (van Rijn, 1984).

The friction factor, $\hat{f}$, can be converted to Manning's n ($n_{man}$) via the Chézy coefficient $C$ ($m^{1/2}s^{-1}$) (Manning, 1891; Silberman et al., 1963).

$$C = \frac{R_h^{1/6}}{n_{man}} \tag{A3.17}$$

$$\hat{f} = \frac{8g}{C^2} \tag{A3.18}$$

**Appendix of Chapter 6: Derivation of st. Venant equation**

The momentum balance of the St.-Venant equations expressed in water level and velocity reads:

$$\frac{\partial u}{\partial t} + u\frac{\partial u}{\partial s} + gS_p = g(S_0 - S_f) \tag{A6.1}$$

where $u$ = depth and cross-sectional averaged flow velocity (= $Q/A$ (m s$^{-1}$), where $Q$ = discharge (m$^3$ s$^{-1}$) and $A$ = wetted area (m$^2$)), $S_p$ = pressure slope (= $\frac{\partial d}{\partial s}$, where $d$ is hydraulic depth), $S_0$ = bottom slope (= $\frac{\partial z}{\partial s}$, where $z$ = bed level relative to Amsterdam Ordnance Datum, m), and

$$S_f = \frac{Q^2}{C^2 A^2 R} \tag{A6.2}$$

in which $C$ = Chézy coefficient (m$^{1/2}$ s$^{-1}$), and $R$ = hydraulic radius (m). Assuming $R \approx d$, which applies to lowland rivers for which $W \gg d$, equation A6.2 can be simplified as:

$$S_f = \frac{u^2}{C^2 d} \tag{A6.3}$$

For the lowland river subject to study the time derivative term is two orders of magnitude smaller than other terms in the momentum equation, so we set $\frac{\partial u}{\partial t} \approx 0$. After rewriting, Chézy coefficient can be obtained as:

$$C = \frac{u}{\sqrt{d(S_0 - S_p - \frac{\partial Qu}{\partial s}\frac{1}{gA})}} \tag{A6.4}$$

Although commonly the simplified form of the Chézy equation is used ($C = \sqrt{\frac{u}{S_0 d}}$), this assumption does not hold when there are significant variations in either time or space (non-uniform flow). The bed-level profile (Figure 6.4a) does not have a constant slope, which causes significant variations in pressure slope.

# Bibliography


Aalto, R., J. W. Lauer & W. E. Dietrich (2008). Spatial and temporal dynamics of sediment accumulation and exchange along Strickland River floodplains (Papua New Guinea) over decadal-to-centennial timescales. *Journal of Geophysical Research: Earth Surface*, 113(F1). doi: 10.1029/2006JF000627.

Agrawal, Y. C. & H. C. Pottsmith (2000). *Instruments for particle size and settling velocity observations in sediment transport*. Technical report.

Agrawal, Y. C., A. Whitmire, O. A. Mikkelsen & H. C. Pottsmith (2008). Light scattering by random shaped particles and consequences on measuring suspended sediments by laser diffraction. *Journal of Geophysical Research: Oceans*, 113(4). doi: 10.1029/2007JC004403.

Ali, W., D. Enthoven, A. Kirichek, C. Chassagne & R. Helmons (2022). Effect of flocculation on turbidity currents. *Frontiers in Earth Science*, 10. doi: 10.3389/feart.2022.1014170.

Allen, J. (1982). *Sedimentary structures: their character and physical basis*, volume 30. Developments in Sedimentology, Elsevier, 1st edition.

Allen, J. R. (1978). Computational models for dune time-lag: calculations using Stein's rule for dune height. *Sedimentary Geology*, 20(C), 165–216. doi: 10.1016/0037-0738(78)90054-4.

Allen, J. R. L. (1972). *Instability of an upper-phase plane bed: a test of Bagnold's criterion*. Technical report.

Amsler, M. & M. Garcia (1997). Sand-dune geometry of large rivers during floods. *Journal of Hydraulic Engineering*, 123(6).

Amsler, M. & M. Schreider (1999). Dune height prediction at floods in the Paraná River, Argentina. *River sedimentation: Theory and applications*, pages 615–620.

Andersen, T. J., S. Rominikan, I. S. Olsen, K. H. Skinnebach & M. Fruergaard (2021). Flocculation of PVC Microplastic and Fine-Grained Cohesive Sediment at Environmentally Realistic Concentrations. *The Biological Bulletin*, 240(1), 42–51. doi: 10.1086/712929.

Andrews, S., D. Nover & S. G. Schladow (2010). Using laser diffraction data to obtain accurate particle size distributions: The role of particle composition. *Limnology and Oceanography: Methods*, 8(OCT), 507–526. doi: 10.4319/lom.2010.8.507.

Arani, B. M., S. R. Carpenter, L. Lahti, E. H. Van Nes & M. Scheffer (2021). Exit time as a measure of ecological resilience. *Science*, 372(6547). doi: 10.1126/science.aay4895.

ASCE Task Force (2002). Flow and transport over dunes. *Journal of Hydraulic Engineering*, 127, 726–728.

Ashley, G. M. (1980). Channel morphology and sediment movement in a tidal river, Pitt River, British Columbia. *Earth Surface Processes*, 5(4), 347–368. doi: 10.1002/esp.3760050406.

Ashwin, P., S. Wieczorek, R. Vitolo & P. Cox (2012). Tipping points in open systems: bifurcation, noise-induced and rate-dependent examples in the climate system. *Philosophical Transactions of the Royal Society A: Mathematical, Physical and Engineering Sciences*, 370(1962), 1166–1184. doi: 10.1098/rsta.2011.0306.

Attard, M. E., J. G. Venditti & M. Church (2014). Suspended sediment transport in Fraser River at Mission, British Columbia: New observations and comparison to historical records. *Canadian Water Resources Journal*, 39(3), 356–371. doi: 10.1080/07011784.2014.942105.

Auerbach, L. W., S. L. Goodbred Jr, D. R. Mondal, C. A. Wilson, K. R. Ahmed, K. Roy, M. S. Steckler, C. Small, J. M. Gilligan & B. A. Ackerly (2015). Flood risk of natural and embanked landscapes on the Ganges–Brahmaputra tidal delta plain. *Nature Climate Change*, 5(2), 153–157. doi: 10.1038/nclimate2472.

Avnimelech, Y., B. W. Troeger & L. W. Reed (1982). Mutual Flocculation of Algae and Clay: Evidence and Implications. *Science*, 216(4541), 63–65. doi: 10.1126/science.216.4541.63.

Baar, A. W., S. A. Weisscher & M. G. Kleinhans (2020). Interaction between lateral sorting in river bends and vertical sorting in dunes. *Sedimentology*, 67(1), 606–626. doi: 10.1111/sed.12656.

Baas, A. C. W. & D. J. Sherman (2005). Formation and behavior of aeolian streamers. *Journal of Geophysical Research: Earth Surface*, 110(F3). doi: 10.1029/2004JF000270.

Baas, J. & H. de Koning (1995). Washed-Out Ripples: Their Equilibrium Dimensions, Migration Rate, and Relation to Suspended-Sediment Concentration in Very Fine Sand. *SEPM Journal of Sedimentary Research*, Vol. 65A. doi: 10.1306/D42680E5-2B26-11D7-8648000102C1865D.

Baas, J. H. (1994). A flume study on the development and equilibrium morphology of current ripples in very fine sand. *Sedimentology*, 41(2), 185–209. doi: 10.1111/j.1365-3091.1994.tb01400.x.

Baas, J. H. (1999). An empirical model for the development and equilibrium morphology of current ripples in fine sand. *Sedimentology*, 46(1), 123–138. doi: 10.1046/j.1365-3091.1999.00206.x.

Baas, J. H. & J. L. Best (2000). Ripple formation induced by biogenic mounds—comment. *Marine Geology*, 168(1-4), 145–151. doi: 10.1016/S0025-3227(00)00040-2.

Baas, J. H., J. L. Best & J. Peakall (2016). Predicting bedforms and primary current stratification in cohesive mixtures of mud and sand. *Journal of the Geological Society*, 173(1), 12–45. doi: 10.1144/jgs2015-024.

Baas, J. H., A. G. Davies & J. Malarkey (2013). Bedform development in mixed sand–mud: The contrasting role of cohesive forces in flow and bed. *Geomorphology*, 182, 19–32. doi: 10.1016/j.geomorph.2012.10.025.

Bartholdy, J., B. W. Flemming, V. B. Ernstsen, C. Winter & A. Bartholomä (2010). Hydraulic roughness over simple subaqueous dunes. *Geo-Marine Letters*, 30(1), 63–76. doi: 10.1007/s00367-009-0153-7.

Bartzke, G., K. R. Bryan, C. A. Pilditch & K. Huhn (2013). On the stabilizing influence of silt on sand beds. *Journal of Sedimentary Research*, 83(8), 691–703. doi: 10.2110/jsr.2013.57.

BASF (2013). *Zetag ® 8125 Solid Grade Cationic Polyelectrolyte*. Technical report.

Bennett, S. J. & J. L. Best (1995). Mean flow and turbulence structure over fixed, two-dimensional dunes: implications for sediment transport and bedform stability. *Sedimentology*, 42(3), 491–513. doi: 10.1111/j.1365-3091.1995.tb00386.x.

van den Berg, J. & A. van Gelder (1993). A new bedform stability diagram, with emphasis on the transiton of ripples to plane bed in flows over fine sand and silt. *Spec. Publs Int. Ass. Sediment*, 17, 11–21. doi: 10.1002/9781444303995.ch2.

van den Berg, K. (2021). Spatial variation of bedform dynamics in the fluvial to tidal transition zone of the Ganges-Brahmaputra-Meghna delta.

Berne, S., P. Castaing, E. Le Drezen & G. Lericolais (1993). Morphology, internal structure, and reversal of asymmetry of large subtidal dunes in the entrance to Gironde Estuary (France). *Journal of Sedimentary Petrology*, 63(5), 780–793. doi: 10.1306/d4267c03-2b26-11d7-8648000102c1865d.

Best, J. (2005). The fluid dynamics of river dunes: A review and some future research directions. *Journal of Geophysical Research: Earth Surface*, 110(4), 1–21. doi: 10.1029/2004JF000218.

Best, J. & J. Bridge (1992). The morphology and dynamics of low amplitude bedwaves upon upper stage plane beds and the preservation of planar laminae. *Sedimentology*, 39(5), 737–752. doi: 10.1111/j.1365-3091.1992.tb02150.x.

Best, J. & R. Kostaschuk (2002). An experimental study of turbulent flow over a low-angle dune. *Journal of Geophysical Research: Oceans*, 107(9), 18–1. doi: 10.1029/2000jc000294.

Bhowmik, B. N. G., R. Xia, A. Member, B. S. Mazumder & T. W. Soong (1995). Return flow in rivers due to navigation traffic. *Journal of Hydraulic Engineering*, 121(12), 914–918.

Bieganowski, A., M. Ryżak, A. Sochan, G. Barna, H. Hernádi, M. Beczek, C. Polakowski & A. Makó (2018). Laser Diffractometry in the Measurements of Soil and Sediment Particle Size Distribution. *Advances in Agronomy*, 151, 215–279. doi: 10.1016/bs.agron.2018.04.003.

Bilotta, G. S. & R. E. Brazier (2008). Understanding the influence of suspended solids on water quality and aquatic biota. doi: 10.1016/j.watres.2008.03.018.

Biron, P. M., C. Robson, M. F. Lapointe & S. J. Gaskin (2004). Comparing different methods of bed shear stress estimates in simple and complex flow fields. *Earth Surface Processes and Landforms*, 29(11), 1403–1415. doi: 10.1002/esp.1111.

Bolle, A., Z. Bing Wang, C. Amos & J. De Ronde (2010). The influence of changes in tidal asymmetry on residual sediment transport in the Western Scheldt. *Continental Shelf Research*, 30(8), 871–882. doi: 10.1016/j.csr.2010.03.001.

Boss, E., N. Haëntjens, T. K. Westberry, L. Karp-Boss & W. H. Slade (2018). Validation of the particle size distribution obtained with the laser in-situ scattering and transmission (LISST) meter in flow-through mode. *Optics Express*, 26(9), 11125. doi: 10.1364/oe.26.011125.

Bradley, R. W. & J. G. Venditti (2017). Reevaluating dune scaling relations. *Earth-Science Reviews*, 165, 356–376. doi: 10.1016/j.earscirev.2016.11.004.

Bradley, R. W. & J. G. Venditti (2019). Transport Scaling of Dune Dimensions in Shallow Flows. *Journal of Geophysical Research: Earth Surface*, 124(2), 526–547. doi: 10.1029/2018JF004832.

Bradley, R. W. & J. G. Venditti (2021). Mechanisms of Dune Growth and Decay in Rivers. *Geophysical Research Letters*, 48(20), 1–10. doi: 10.1029/2021GL094572.

Bradley, R. W., J. G. Venditti, R. A. Kostaschuk, M. Church, M. Hendershot & M. A. Allison (2013). Flow and sediment suspension events over low-angle dunes: Fraser Estuary, Canada. *Journal of Geophysical Research: Earth Surface*, 118(3), 1693–1709. doi: 10.1002/jgrf.20118.

Brakenhoff, L., R. Schrijvershof, J. van der Werf, B. Grasmeijer, G. Ruessink & M. van der Vegt (2020). From ripples to large-scale sand transport: The effects of bedform-related roughness on hydrodynamics and sediment transport patterns in delft3d. *Journal of Marine Science and Engineering*, 8(11), 1–25. doi: 10.3390/jmse8110892.

Bridge, J. (2003). *Rivers and Floodplains: Forms, Processes, and Sedimentary Record.* John Wiley & Sons, Malden, Massachusetts.

Brown, J. & A. Davies (2010). Flood/ebb tidal asymmetry in a shallow sandy estuary and the impact on net sand transport. *Geomorphology*, 114(3), 431–439. doi: 10.1016/j.geomorph.2009.08.006.

de Brye, B., S. Schellen, M. Sassi, B. Vermeulen, T. Kärnä, E. Deleersnijder & T. Hoitink (2011). Preliminary results of a finite-element, multi-scale model of the Mahakam Delta (Indonesia). *Ocean Dynamics*, 61(8), 1107–1120. doi: 10.1007/s10236-011-0410-y.

Buffington, J. M., W. E. Dietrich & J. W. Kirchner (1992). Friction angle measurements on a naturally formed gravel streambed: Implications for critical boundary shear stress. *Water Resources Research*, 28(2), 411–425. doi: 10.1029/91WR02529.

Buffington, J. M. & D. R. Montgomery (1997). A systematic analysis of eight decades of incipient motion studies, with special reference to gravel-bedded rivers. *Water Resources Research*, 33(8), 1993–2029. doi: 10.1029/96WR03190.

Bungartz, H. & S. C. Wanner (2004). Significance of particle interaction to the modelling of cohesive sediment transport in rivers. *Hydrological Processes*, 18(9), 1685–1702. doi: 10.1002/hyp.1412.

Buschman, F. A., A. J. Hoitink, M. Van Der Vegt & P. Hoekstra (2009). Subtidal water level variation controlled by river flow and tides. *Water Resources Research*, 45(10), 1–12. doi: 10.1029/2009WR008167.

Butterfield, G. R. (1991). Grain transport rates in steady and unsteady turbulent airflows. In *Aeolian Grain Transport 1: Mechanics*, pages 97–122. Springer Vienna. doi: 10.1007/978-3-7091-6706-9{_}6.

Carling, P. A., E. Gölz, H. G. Orr & A. Radecki-Pawlik (2000). The morphodynamics of fluvial sand dunes in the River Rhine, near Mainz, Germany. I. Sedimentology and morphology. *Sedimentology*, 47(1), 227–252. doi: 10.1046/j.1365-3091.2000.00290.x.

Carpenter, S. R. & W. A. Brock (2006). Rising variance: a leading indicator of ecological transition. *Ecology Letters*, 9(3), 311–318. doi: 10.1111/j.1461-0248.2005.00877.x.

Chakraborti, R. K., J. F. Atkinson & J. Kaur (2009). Effect of Mixing on Suspended Particle-Size Distribution. *Journal of Environmental Engineering*, 135(5), 306–316. doi: 10.1061/(asce)0733-9372(2009)135:5(306).

Chassagne, C. & Z. Safar (2020). Modelling flocculation: Towards an integration in large-scale sediment transport models. *Marine Geology*, 430. doi: 10.1016/j.margeo.2020.106361.

Chassagne, C., Z. Safar, Z. Deng, Q. He & A. J. Manning (2022). Flocculation in Estuaries: Modeling, Laboratory and In-situ Studies. In *Sediment Transport - Recent Advances*. IntechOpen. doi: 10.5772/intechopen.100404.

Chow, V. (1959). *Open-channel hydraulics*. McGraw-Hill Book Company, USA.

Church, M., A. Dudill, J. G. Venditti & P. Frey (2020). Are Results in Geomorphology Reproducible? *Journal of Geophysical Research: Earth Surface*, 125(8). doi: 10.1029/2020JF005553.

Cisneros, J., J. Best, T. van Dijk, R. P. de Almeida, M. Amsler, J. Boldt, B. Freitas, C. Galeazzi, R. Huizinga, M. Iannirubertо, H. Ma, J. A. Nittrouer, K. Oberg, O. Orfeo, D. Parsons, R. Szupiany, P. Wang & Y. Zhang (2020). Dunes in the world's big rivers are characterized by low-angle lee-side slopes and a complex shape. *Nature Geoscience*, 13(2), 156–162. doi: 10.1038/s41561-019-0511-7.

Clague, J. J., J. L. Luternauer & R. J. Hebda (1983). Sedimentary environments and postglacial history of the Fraser Delta and Lower Fraser Valley, British Columbia. *Canadian journal of earth sciences*, 20(8), 1314–1326. doi: 10.1139/e83-116.

Clark, M. M. & J. R. V. Flora (1991). *Floc Restructuring in Varied Turbulent Mixing*. Technical report.

Cleveland, W. (1979). Robust local weighted regression and smoothing scatterplots. *Journal of the American Statistical Association*, 74(368), 829–836.

Cleveland, W. & S. Devlin (1988). Weighted regression: an approach to regression analysis by local fitting. *Journal of the American Statistical Association*, 83(403), 596–610.

Crawford, S. E., M. Brinkmann, J. D. Ouellet, F. Lehmkuhl, K. Reicherter, J. Schwarzbauer, P. Bellanova, P. Letmathe, L. M. Blank, R. Weber, W. Brack, J. T. van Dongen, L. Menzel, M. Hecker, H. Schüttrumpf & H. Hollert (2022). Remobilization of pollutants during extreme flood events poses severe risks to human and environmental health. *Journal of Hazardous Materials*, 421, 126691. doi: 10.1016/j.jhazmat.2021.126691.

Czapiga, M. J., A. Blom & E. Viparelli (2022). Sediment Nourishments to Mitigate Channel Bed Incision in Engineered Rivers. *Journal of Hydraulic Engineering*, 148(6). doi: 10.1061/(ASCE)HY.1943-7900.0001977.

Czuba, J. A., T. D. Straub, C. A. Curran, M. N. Landers & M. M. Domanski (2015). Comparison of fluvial suspended-sediment concentrations and particle-size distributions measured with in-stream laser diffraction and in physical samples. *Water Resources Research*, 51(1), 320–340. doi: 10.1002/2014WR015697.

Dade, W. & P. Friend (1998). Grain-Size, Sediment-Transport Regime, and Channel Slope in Alluvial Rivers. *The Journal of Geology*, 106(6), 661–676. doi: 10.1086/516052.

Dakos, V., S. R. Carpenter, W. A. Brock, A. M. Ellison, V. Guttal, A. R. Ives, S. Kéfi, V. Livina, D. A. Seekell, E. H. van Nes & M. Scheffer (2012). Methods for detecting early warnings of critical transitions in time series illustrated using simulated ecological data. *PLoS ONE*, 7(7). doi: 10.1371/journal.pone.0041010.

Dakos, V., E. H. van Nes & M. Scheffer (2013). Flickering as an early warning signal. *Theoretical Ecology*, 6(3), 309–317. doi: 10.1007/s12080-013-0186-4.

Das, D., V. Ganti, R. Bradley, J. Venditti, A. Reesink & D. R. Parsons (2022). The Influence of Transport Stage on Preserved Fluvial Cross Strata. *Geophysical Research Letters*, 49(18). doi: 10.1029/2022GL099808.

Dashtgard, S. E., J. G. Venditti, P. R. Hill, C. F. Sisulak, S. M. Johnson & A. D. La Croix (2012). Sedimentation Across the Tidal-Fluvial Transition in the Lower Fraser River, Canada. *The Sedimentary Record*, 10(4), 4–9. doi: 10.2110/sedred.2012.4.4.

Davies, A. G. & P. E. Robins (2017). Residual flow, bedforms and sediment transport in a tidal channel modelled with variable bed roughness. *Geomorphology*, 295, 855–872. doi: 10.1016/j.geomorph.2017.08.029.

Deal, E., J. G. Venditti, S. J. Benavides, R. Bradley, Q. Zhang, K. Kamrin & J. T. Perron (2023). Grain shape effects in bed load sediment transport. *Nature*, 613(7943), 298–302. doi: 10.1038/s41586-022-05564-6.

Debnath, K., V. Nikora, J. Aberle, B. Westrich & M. Muste (2007). Erosion of Cohesive Sediments: Resuspension, Bed Load, and Erosion Patterns from Field Experiments. *Journal of Hydraulic Engineering*, 133(5), 508–520. doi: 10.1061/(ASCE)0733-9429(2007)133:5(508).

Deng, Z., Q. He, Z. Safar & C. Chassagne (2019). The role of algae in fine sediment flocculation: In-situ and laboratory measurements. *Marine Geology*, 413, 71–84. doi: 10.1016/j.margeo.2019.02.003.

Deng, Z., D. Huang, Q. He & C. Chassagne (2022). Review of the action of organic matter on mineral sediment flocculation. *Frontiers in Earth Science*, 10. doi: 10.3389/feart.2022.965919.

Dietrich, W. E. (1982). Settling velocity of natural particles. *Water Resources Research*, 18(6), 1615–1626. doi: 10.1029/WR018i006p01615.

Dietrich, W. E., J. W. Kirchner, H. Ikeda & F. Iseya (1989). Sediment supply and the development of the coarse surface layer in gravel-bedded rivers. *Nature*, 340(6230), 215–217. doi: 10.1038/340215a0.

Dijkstra, Y. M., H. M. Schuttelaars & G. P. Schramkowski (2019). A Regime Shift From Low to High Sediment Concentrations in a Tide-Dominated Estuary. *Geophysical Research Letters*, 46(8), 4338–4345. doi: 10.1029/2019GL082302.

Droppo, I. G. (2001). Rethinking what constitutes suspended sediment. *Hydrological Processes*, 15(9), 1551–1564. doi: 10.1002/hyp.228.

Droppo, I. G. (2004). Structural controls on floc strength and transport. *Canadian Journal of Civil Engineering*, 31(4), 569–578. doi: 10.1139/L04-015.

Droppo, I. G. (2009). Biofilm structure and bed stability of five contrasting freshwater sediments. *Marine and Freshwater Research*, 60(7), 690–699. doi: 10.1071/MF08019.

Droppo, I. G., K. Nackaerts, D. E. Walling & N. Williams (2005). Can flocs and water stable soil aggregates be differentiated within fluvial systems? *Catena*, 60(1), 1–18. doi: 10.1016/j.catena.2004.11.002.

Dyer, K. R. (1989). Sediment processes in estuaries: future research requirements. *Journal of Geophysical Research*, 94(C10). doi: 10.1029/jc094ic10p14327.

Edmonds, D. A. & R. L. Slingerland (2010). Significant effect of sediment cohesion on delta morphology. *Nature Geoscience*, 3(2), 105–109. doi: 10.1038/ngeo730.

Egbert, G. D. & S. Y. Erofeeva (2002). Efficient inverse modeling of barotropic ocean tides. *Journal of Atmospheric and Oceanic Technology*, 19(2), 183–204. doi: 10.1175/1520-0426(2002)019<0183:EIMOBO>2.0.CO;2.

Einstein, H. A. (1950). The bed-load function for sediment transportation in open channel flows. *Technical Bulletins 156389, United States Department of Agriculture, Economic Research Service.*

Eisma, D. (1986). *Flocculation and de-flocculation of suspended matter in estuaries*. Technical Report 3.

Engelund, F. & E. Hansen (1967). Monograph on Sediment Transport. *Technisk Forlag, Copenhagen, Denmark*.

Ernstsen, V. B., R. Noormets, C. Winter, D. Hebbeln, A. Bartholomä, B. W. Flemming & J. Bartholdy (2006). Quantification of dune dynamics during a tidal cycle in an inlet channel of the Danish Wadden Sea. *Geo-Marine Letters*, 26(3), 151–163. doi: 10.1007/s00367-006-0026-2.

Federal Interagency Sedimentation Project (1941). *Methods of analyzing sediment samples*. Technical report, University of Iowa Hydraulic Laboratory.

Ferguson, R. I. & M. Church (2004). *A simple universal equation for grain settling velocity*. Technical Report 6.

Fernandez, R., J. Best & F. López (2006). Mean flow, turbulence structure, and bed form superimposition across the ripple-dune transition. *Water Resources Research*, 42(5), 1–17. doi: 10.1029/2005WR004330.

Fetter, C. (2001). *Applied Hydrogeology*. New Jersey: Prentice Hall, 4th edition.

Fettweis, M. (2008). Uncertainty of excess density and settling velocity of mud flocs derived from in situ measurements. *Estuarine, Coastal and Shelf Science*, 78(2), 426–436. doi: 10.1016/j.ecss.2008.01.007.

Frings, R. M. (2008). Downstream fining in large sand-bed rivers. *Earth-Science Reviews*, 87(1-2), 39–60. doi: 10.1016/j.earscirev.2007.10.001.

Frings, R. M., M. G. Kleinhans & S. Vollmer (2008). Discriminating between pore-filling load and bed-structure load: A new porosity-based method, exemplified for the river Rhine. *Sedimentology*, 55(6), 1571–1593. doi: 10.1111/j.1365-3091.2008.00958.x.

Fugate, D. C. & C. T. Friedrichs (2003). Controls on suspended aggregate size in partially mixed estuaries. *Estuarine, Coastal and Shelf Science*, 58(2), 389–404. doi: 10.1016/S0272-7714(03)00107-0.

Gabel, S. L. (1993). Geometry and kinematics of dunes during steady and unsteady flows in the Calamus River, Nebraska, USA. *Sedimentology*, 40(2), 237–269. doi: 10.1111/j.1365-3091.1993.tb01763.x.

Galeazzi, C. P., R. P. Almeida, C. E. Mazoca, J. L. Best, B. T. Freitas, M. Iannirubertо, J. Cisneros & L. N. Tamura (2018). The significance of superimposed dunes in the Amazon River: Implications for how large rivers are identified in the rock record. *Sedimentology*, 65(7), 2388–2403. doi: 10.1111/sed.12471.

Gallo, M. N. & S. B. Vinzon (2005). Generation of overtides and compound tides in Amazon estuary. *Ocean Dynamics*, 55(5-6), 441–448. doi: 10.1007/s10236-005-0003-8.

Garcia, M. & G. Parker (1993). Experiments on the entrainment of sediment into suspension by a dense bottom current. *Journal of Geophysical Research: Oceans*, 98(C3), 4793–4807. doi: 10.1029/92JC02404.

Gartner, J. W., R. T. Cheng, P. F. Wang & K. Richter (2001). *Laboratory and field evaluations of the LISST-100 instrument for suspended particle size determinations*. Technical report.

Gates, T. & M. Al-Zahrani (1996). Spatiotemporal stochastic open-channel flow. II: simulation experiments. *Journal of Hydraulic Engineering*, 122(11), 652–611. doi: 10.1061/(ASCE)0733âĂŞ9429(1996)122:11(652).

Geng, L., S. Lanzoni, A. D'Alpaos, A. Sgarabotto & Z. Gong (2023). The Sensitivity of Tidal Channel Systems to Initial Bed Conditions, Vegetation, and Tidal Asymmetry. *Journal of Geophysical Research: Earth Surface*, 128(3). doi: 10.1029/2022JF006929.

Geyer, R., J. R. Jambeck & K. L. Law (2017). Production, use, and fate of all plastics ever made. *Science Advances*, 3(7). doi: 10.1126/sciadv.1700782.

Gibbs, R. J. (1981). Floc breakage by pumps. *Journal of Sedimentary Research*, 51(2), 670–672. doi: 10.1306/212F7D56-2B24-11D7-8648000102C1865D.

Gilbert, G. (1914). The transport of debris by running water. *USGS Professional Paper*, 86, 1–263.

Giosan, L., S. Constantinescu, F. Filip & B. Deng (2013). Maintenance of large deltas through channelization: Nature vs. humans in the Danube delta. *Anthropocene*, 1, 35–45. doi: 10.1016/j.ancene.2013.09.001.

Gisen, J. I. A. & H. H. Savenije (2015). Estimating bankfull discharge and depth in ungauged estuaries. *Water Resources Research*, 51(4), 2298–2316. doi: 10.1002/2014WR016227.

Glangeaud, L. (1938). Transport et sedimentation dans l'estuaire et a l'embouchure de la gironde caracteres petrographiques des formations fluviatiles, saumatres, littorales, et neritiques. *Bulletin of Geological Society of France*, 8, 599–630.

Godin, G. (1972). *The analysis of tides*. University of Toronto Press.

Godin, G. (1999). The Propagation of Tides up Rivers With Special Considerations on the Upper Saint Lawrence River. *Estuarine, Coastal and Shelf Science*, 48(3), 307–324. doi: 10.1006/ecss.1998.0422.

Gomez, B. (1978). Sedimentology. In *Encyclopedia of Sediments and Sedimentary Rocks*, pages 487–489.

Graham, G. W., E. J. Davies, W. A. M. Nimmo-Smith, D. G. Bowers & K. M. Braithwaite (2012). Interpreting LISST-100X measurements of particles with complex shape using digital in-line holography. *Journal of Geophysical Research: Oceans*, 117(C5). doi: 10.1029/2011JC007613.

Grangeon, T., C. Legout, M. Esteves, N. Gratiot & O. Navratil (2012). Variability of the particle size of suspended sediment during highly concentrated flood events in a small mountainous catchment. *Journal of Soils and Sediments*, 12(10), 1549–1558. doi: 10.1007/s11368-012-0562-5.

Grant, J., U. Bathmann & E. Mills (1986). The interaction between benthic diatom films and sediment transport. *Estuarine, Coastal and Shelf Science*, 23(2), 225–238. doi: 10.1016/0272-7714(86)90056-9.

Gratiot, N., A. Bildstein, T. T. Anh, H. Thoss, H. Denis, H. Michallet & H. Apel (2017). Sediment flocculation in the Mekong River estuary, Vietnam, an important driver of geomorphological changes. *Comptes Rendus Geoscience*, 349(6-7), 260–268. doi: 10.1016/j.crte.2017.09.012.

Gray, A. B., G. B. Pasternack & E. B. Watson (2010). Hydrogen peroxide treatment effects on the particle size distribution of alluvial and marsh sediments. *Holocene*, 20(2), 293–301. doi: 10.1177/0959683609350390.

Greene, H. G., M. Baker & J. Aschoff (2020). A dynamic bedforms habitat for the forage fish Pacific sand lance, San Juan Islands, WA, United States. In P. T. Harris & E. Baker (editors), *Seafloor Geomorphology as Benthic Habitat*, pages 267–279. Elsevier, 2nd edition. doi: 10.1016/B978-0-12-814960-7.00014-2.

Gugliotta, M., Y. Saito, V. L. Nguyen, T. K. O. Ta, R. Nakashima, T. Tamura, K. Uehara, K. Katsuki & S. Yamamoto (2017). Process regime, salinity, morphological, and sedimentary trends along the fluvial to marine transition zone of the mixed-energy Mekong River delta, Vietnam. *Continental Shelf Research*, 147, 7–26. doi: 10.1016/j.csr.2017.03.001.

Guo, L. & Q. He (2011). Freshwater flocculation of suspended sediments in the Yangtze River, China. In *Ocean Dynamics*, volume 61, pages 371–386. doi: 10.1007/s10236-011-0391-x.

Guy, H. (1969). Techniques of Water-resources investigations of the USGS. pages 1–56.

Guy, H., D. Simons & E. Richardson (1966). Summary of alluvial channel data from flume experiments, 1956–1961. *USGS Professional Paper 462-I, 1–96.*, pages 1–96.

Gyr, A. & A. Müller (1996). The role of coherent structures in developing bedforms during sediment transport. *Coherent flow structures in open channels*, pages 227–235.

Hacking, I. (1984). *Representing and intervening*. Cambridge University Press, Cambridge, UK.

Hasan, A. & P. Fatehi (2018). Cationic kraft lignin-acrylamide as a flocculant for clay suspensions: 1. Molecular weight effect. *Separation and Purification Technology*, 207, 213–221. doi: 10.1016/j.seppur.2018.06.047.

He, Q. & D. E. Walling (1997). Spatial variability of the particle size composition of overbank floodplain deposits. *Water, Air, & Soil Pollution*, 99(1-4), 71–80. doi: 10.1007/BF02406846.

Healy, T., Y. Wang & J. Healy (2002). *Muddy Coasts of the World: Processes, Deposits and Function*. Elsevier, Amsterdam, 1st edition.

Heller, V. (2011). Scale effects in physical hydraulic engineering models. *Journal of Hydraulic Research*, 49(3), 293–306. doi: 10.1080/00221686.2011.578914.

Hendershot, M. L., J. G. Venditti, R. W. Bradley, R. A. Kostaschuk, M. Church & M. A. Allison (2016). Response of low-angle dunes to variable flow. *Sedimentology*, 63(3), 743–760. doi: 10.1111/sed.12236.

Hendershot, M. L., J. G. Venditti, M. Church, R. Bradley, R. A. Kostaschuk & M. A. Allison (2018). Crestline bifurcation and dynamics in fluvially-dominated, tidally-influenced flow. *Sedimentology*, 65(7), 2621–2636. doi: 10.1111/sed.12480.

Herrling, G., M. Becker, A. Lefebvre, A. Zorndt, K. Krämer & C. Winter (2021). The effect of asymmetric dune roughness on tidal asymmetry in the Weser estuary. *Earth Surface Processes and Landforms*,

46(11), 2211–2228. DOI: 10.1002/esp.5170.

Hidayat, H., B. Vermeulen, M. G. Sassi, P. J. F. Torfs & A. J. Hoitink (2011). Discharge estimation in a backwater affected meandering river. *Hydrology and Earth System Sciences*, 15(8), 2717–2728. DOI: 10.5194/hess-15-2717-2011.

Hill, K. M., J. Gaffney, S. Baumgardner, P. Wilcock & C. Paola (2017). Experimental study of the effect of grain sizes in a bimodal mixture on bed slope, bed texture, and the transition to washload. *Water Resources Research*, 53(1), 923–941. DOI: 10.1002/2016WR019172.

Hoitink, A. J., F. A. Buschman & B. Vermeulen (2009). Continuous measurements of discharge from a horizontal acoustic Doppler current profiler in a tidal river. *Water Resources Research*, 45(11), 1–13. DOI: 10.1029/2009WR007791.

Hoitink, A. J., P. Hoekstra & D. S. Van Maren (2003). Flow asymmetry associated with astronomical tides: Implications for the residual transport of sediment. *Journal of Geophysical Research: Oceans*, 108(10). DOI: 10.1029/2002jc001539.

Hoitink, A. J., Z. B. Wang, B. Vermeulen, Y. Huismans & K. Kästner (2017). Tidal controls on river delta morphology. DOI: 10.1038/ngeo3000.

Hoitink, A. J. F. & D. A. Jay (2016). Tidal river dynamics: Implications for deltas. *Reviews of Geophysics*, 54(1), 240–272. DOI: 10.1002/2015RG000507.

Hoitink, A. J. F., J. A. Nittrouer, P. Passalacqua, J. B. Shaw, E. J. Langendoen, Y. Huismans & D. S. van Maren (2020). Resilience of River Deltas in the Anthropocene. *Journal of Geophysical Research: Earth Surface*, 125(3). DOI: 10.1029/2019JF005201.

Holmes, M. H. & M. H. Garcia (2008). Flow over bedforms in a large sand-bed river: A field investigation. *Journal of Hydraulic Research*, 46(3), 322–333. DOI: 10.3826/jhr.2008.3040.

Horrevoets, A., H. Savenije, J. Schuurman & S. Graas (2004). The influence of river discharge on tidal damping in alluvial estuaries. *Journal of Hydrology*, 294(4), 213–228. DOI: 10.1016/j.jhydrol.2004.02.012.

Horsthemke, W. & R. Lefever (1984). *Noise-induced transitions: Theory and applications in physics, chemistry and biology*. 1. Springer. DOI: 10.1007/BF00047115.

Housageo, R., R. Hodgje, R. Ferguson, C. Hackney, R. Hardy, S. Rice, J. Joel, E. Yager, T. Hoey & T. (2023). Relating spatial scales of rough-bed river surface roughness to channel characteristics. In *AGU Fall Meeting 2023*.

Hughes, Z. J. (2012). Tidal Channels on Tidal Flats and Marshes. In *Principles of Tidal Sedimentology*, pages 269–300. Springer Netherlands, Dordrecht. DOI: 10.1007/978-94-007-0123-6{_}11.

Hunt, J. (1968). *On the turbulent transport of a hetrogeneous sediment*. Technical report.

Hurther, D. & U. Lemmin (2001). A Correction Method for Turbulence Measurements with a 3D Acoustic Doppler Velocity Profiler. *Journal of Atmospheric and Oceanic Technology*, pages 446–458. DOI: 10.1175/1520-0426(2001)018<0446:ACMFTM>2.0.CO;2.

Ikeda, H. (1984). Flume experiments on the superior mobility of sediment mixtures. In *Ann. Rep. Inst. Geosci. 10*, pages 53–56. Univ. of Tsukuba, Tsukuba, Japan.

Jackson, R. G. (1975). Velocity-bed-form-texture patterns of meander bends in the lower Wabash River of Illinois and Indiana. *Bulletin of the Geological Society of America*, 86(11), 1511–1522. DOI: 10.1130/0016-7606(1975)86<1511:VPOMBI>2.0.CO;2.

Jones, A. E., A. K. Hardison, B. R. Hodges, J. W. McClelland & K. B. Moffett (2020). Defining a Riverine Tidal Freshwater Zone and Its Spatiotemporal Dynamics. *Water Resources Research*, 56(4), 1–17. DOI: 10.1029/2019WR026619.

Julien, P. & G. Klaassen (1995). Sand-dune geometry of large rivers during floods. 121(9), 657–663.

Julien, P. Y., G. J. Klaassen, W. B. Ten Brinke & A. W. Wilbers (2002). Case study: Bed resistance of

Rhine River during 1998 flood. *Journal of Hydraulic Engineering*, 128(12), 1042–1050. DOI: 10.1061/(ASCE)0733-9429(2002)128:12(1042).

Karim, F. (1995). Bed configuration and hydraulic resistance in alluvial-channel flows. *Journal of Hydraulic Engineering*, 121(1), 15–25. DOI: 10.1061/(ASCE)0733-9429(1995)121:1(15).

Kästner, K., A. J. Hoitink, B. Vermeulen, T. J. Geertsema & N. S. Ningsih (2017). Distributary channels in the fluvial to tidal transition zone. *Journal of Geophysical Research: Earth Surface*, 122(3), 696–710. DOI: 10.1002/2016JF004075.

Kennedy, J. F. (1963). The mechanics of dunes and antidunes in erodible-bed channels. *Journal of Fluid Mechanics*, 16(4), 521–544. DOI: 10.1017/S0022112063000975.

Kernkamp, H. W., A. Van Dam, G. S. Stelling & E. D. De Goede (2011). Efficient scheme for the shallow water equations on unstructured grids with application to the Continental Shelf. *Ocean Dynamics*, 61(8), 1175–1188. DOI: 10.1007/s10236-011-0423-6.

van Kessel, T., J. Vanlede & J. de Kok (2011). Development of a mud transport model for the Scheldt estuary. *Continental Shelf Research*, 31(10), S165–S181. DOI: 10.1016/j.csr.2010.12.006.

Kirca, V. S. O., S. M. Saghebian, K. Roushangar & O. Yagci (2020). Influence of surface roughness of dune bedforms on flow and turbulence characteristics. *International Journal of Sediment Research*, 35(6), 666–678. DOI: 10.1016/j.ijsrc.2020.06.003.

Kirchner, J. W., W. E. Dietrich, F. Iseya & H. Ikeda (1990). The variability of critical shear stress, friction angle, and grain protrusion in water-worked sediments. *Sedimentology*, 37(4), 647–672. DOI: 10.1111/j.1365-3091.1990.tb00627.x.

Kleinhans, M., M. Bierkens & M. van der Perk (2009). Hydrologists, bring out shovels and garden hoses and hit the dirt. *Hydrology and Earth System Sciences Discussions*, 6, 6581–6610.

Klemes, V. (1986). Operational testing of hydrological simulation models. *Hydrological Sciences Journal*, 31(1), 13–24. DOI: 10.1080/02626668609491024.

Kornman, B. (1995). *The effect of changes in the lee shape of dunes on the flow field, turbulence, and hydraulic roughness*. Technical report, University of Utrecht, Utrecht.

Kostaschuk, R. & L. Atwood (1990). River discharge and tidal controls on salt-wedge position and implications for channel shoaling: Fraser River, British Columbia. *Canadian Journal of Civil Engineering*, 17(3), 452–459. DOI: 10.1139/190-049.

Kostaschuk, R. & J. Best (2005). Response of sand dunes to variations in tidal flow: Fraser Estuary, Canada. *Journal of Geophysical Research: Earth Surface*, 110(4). DOI: 10.1029/2004JF000176.

Kostaschuk, R., M. Church & J. Luternauer (1989). Bedforms, bed material, and bedload transport in a salt-wedge estuary: Fraser River, British Columbia. *Canadian Journal of Earth Sciences*, 26(7), 1440–1452. DOI: 10.1139/e89-122.

Kostaschuk, R. & J. Luternauer (1989). The role of the salt wedge in sediment resuspension and deposition: Fraser River Estuary, Canada. *Journal of Coastal Research*, 5, 93–101.

Kostaschuk, R. & P. Villard (1996). Flow and sediment transport over large subaqueous dunes: Fraser River, Canada. *Sedimentology*, 45(1), 849–863. DOI: 10.1111/j.1365-3091.1996.tb01506.x.

Kostaschuk, R. & P. Villard (1999). Turbulent sand suspension over dunes. In N. Smith & Rogers. J. (editors), *Proceedings of the 6th International Conference on Fluvial Sedimentology*. Blackwell Sci., Malden, Mass.

Kostaschuk, R. A. & J. G. Venditti (2019). Why do large, deep rivers have low-angle dune beds? *Geology*, 47(10), 919–922. DOI: 10.1130/G46460.1.

Kosters, A., A. Spruyt & I. Niesten (2022). *Ontwikkeling zesde-generatie Rijntakken model Modelbouw, kalibratie en validatie*. Technical report.

Kranck, K. (1979). Dynamics and distribution of suspended particulate matter in the St. Lawrence estuary.

*Le Naturaliste canadien*, 106, 163–173.

van de Kreeke, J. & K. Robaczewska (1993). *Tide-induced residual transport of coarse sediment: application to the Ems estuary*. Technical Report 3.

Krishnappan, B. G. (2006). Cohesive sediment transport studies using a rotating circular flume. In *The 7th Int. Conf. on Hydroscience and Engineering*.

Kwoll, E., J. G. Venditti, R. W. Bradley & C. Winter (2016). Flow structure and resistance over subaqueous high- and low-angle dunes. *Journal of Geophysical Research: Earth Surface*, 121(3), 545–564. doi: 10.1002/2015JF003637.

Lake, N. F., N. Martínez-Carreras, P. J. Shaw & A. L. Collins (2022). High frequency un-mixing of soil samples using a submerged spectrophotometer in a laboratory setting—implications for sediment fingerprinting. *Journal of Soils and Sediments*, 22(1), 348–364. doi: 10.1007/s11368-021-03107-6.

Lamb, M. P., J. de Leeuw, W. W. Fischer, A. J. Moodie, J. G. Venditti, J. A. Nittrouer, D. Haught & G. Parker (2020). Mud in rivers transported as flocculated and suspended bed material. *Nature Geoscience*, 13(8), 566–570. doi: 10.1038/s41561-020-0602-5.

Lasareva, E. V. & A. M. Parfenova (2023). Influence of Organic Matter on the Transport of Mineral Colloids in the River-Sea Transition Zone. In *Oceanography - Relationships of the Oceans With the Continents, Their Biodiversity and the Atmosphere*. IntechOpen. doi: 10.5772/intechopen.110247.

Laursen, S., M. Fruergaard & T. Andersen (2022). Rapid flocculation and settling of positively buoyant microplastic and fine-grained sediment in natural seawater. *Marine Pollution Bulletin*, 178, 113619. doi: 10.1016/j.marpolbul.2022.113619.

Leclair, S. F. (2002). Preservation of cross-strata due to the migration of subaqueous dunes: An experimental investigation. *Sedimentology*, 49(6), 1157–1180. doi: 10.1046/j.1365-3091.2002.00482.x.

Lee, B., J. Kim, J. Hur, I. H. Choi, E. A. Toorman, M. Fettweis & J. W. Choi (2019). Seasonal Dynamics of Organic Matter Composition and Its Effects on Suspended Sediment Flocculation in River Water. *Water Resources Research*, 55(8), 6968–6985. doi: 10.1029/2018WR024486.

Lee, B. J., M. Fettweis, E. Toorman & F. J. Molz (2012). Multimodality of a particle size distribution of cohesive suspended particulate matters in a coastal zone. *Journal of Geophysical Research: Oceans*, 117(3). doi: 10.1029/2011JC007552.

Lee, B. J., E. Toorman & M. Fettweis (2014). Multimodal particle size distributions of fine-grained sediments: Mathematical modeling and field investigation. *Ocean Dynamics*, 64(3), 429–441. doi: 10.1007/s10236-014-0692-y.

Lefebvre, A. (2019). Three-Dimensional Flow Above River Bedforms: Insights From Numerical Modeling of a Natural Dune Field (Río Paraná, Argentina). *Journal of Geophysical Research: Earth Surface*, 124(8), 2241–2264. doi: 10.1029/2018jf004928.

Lefebvre, A. & J. Cisneros (2023). The influence of dune lee side shape on time-averaged velocities and turbulence. *Earth Surface Dynamics*, 11(4), 575–591. doi: 10.5194/esurf-11-575-2023.

Lefebvre, A., V. B. Ernstsen & C. Winter (2011). Influence of compound bedforms on hydraulic roughness in a tidal environment. *Ocean Dynamics*, 61(12), 2201–2210. doi: 10.1007/s10236-011-0476-6.

Lefebvre, A., V. B. Ernstsen & C. Winter (2013). Estimation of roughness lengths and flow separation over compound bedforms in a natural-tidal inlet. *Continental Shelf Research*, 61-62, 98–111. doi: 10.1016/j.csr.2013.04.030.

Lefebvre, A., G. Herrling, M. Becker, A. Zorndt, K. Krämer & C. Winter (2021). Morphology of estuarine bedforms, Weser Estuary, Germany. *Earth Surface Processes and Landforms*, 47(1), 242–256. doi: 10.1002/esp.5243.

Lefebvre, A., A. J. Paarlberg, V. B. Ernstsen & C. Winter (2014a). Flow separation and roughness lengths over large bedforms in a tidal environment: A numerical investigation. *Continental Shelf Research*, 91, 57–69. doi: 10.1016/j.csr.2014.09.001.

Lefebvre, A., A. J. Paarlberg & C. Winter (2014b). Flow separation and shear stress over angle-of-repose bed forms: A numerical investigation. *Water Resources Research*, 50(2), 986–1005. doi: 10.1002/2013WR014587.

Lefebvre, A., A. J. Paarlberg & C. Winter (2016). Characterising natural bedform morphology and its influence on flow. *Geo-Marine Letters*, 36(5), 379–393. doi: 10.1007/s00367-016-0455-5.

Lefebvre, A. & C. Winter (2016). Predicting bed form roughness: the influence of lee side angle. *Geo-Marine Letters*, 36(2), 121–133. doi: 10.1007/s00367-016-0436-8.

Lenton, T. M. (2013). Environmental Tipping Points. *Annual Review of Environment and Resources*, 38(1), 1–29. doi: 10.1146/annurev-environ-102511-084654.

Lesser, G. R., J. A. Roelvink, J. A. van Kester & G. S. Stelling (2004). Development and validation of a three-dimensional morphological model. *Coastal Engineering*, 51(8-9), 883–915. doi: 10.1016/j.coastaleng.2004.07.014.

van Leussen, W. (1988). Aggregation of Particles, Settling Velocity of Mud Flocs A Review. *Physical Processes in Estuaries*, pages 347–403. doi: 10.1007/978-3-642-73691-9{_}19.

van Leussen, W. (1999). The variability of settling velocities of suspended fine-grained sediment in the Ems estuary. *Journal of Sea Research*, 41(1-2), 109–118. doi: 10.1016/S1385-1101(98)00046-X.

Leuven, J., D. van Keulen, J. Nienhuis, A. Canestrelli & A. Hoitink (2021). Large-scale scour in response to tidal dominance in estuaries. *Journal of Geophysical research: Earth surface*, 126(5). doi: 10.1029/2020JF006048.

Leuven, J. R. F. W., H. J. Pierik, M. v. d. Vegt, T. J. Bouma & M. G. Kleinhans (2019). Sea-level-rise-induced threats depend on the size of tide-influenced estuaries worldwide. *Nature Climate Change*, 9(12), 986–992. doi: 10.1038/s41558-019-0608-4.

Lewis, R. & J. Lewis (1987). Shear stress variations in an estuary. *Estuarine, Coastal and Shelf Science*, 25(6), 621–635. doi: 10.1016/0272-7714(87)90011-4.

Li, Z. & D. Komar, Paul (1986). Laboratory measurements of pivoting angles for applications to selective entrainment of gravel in a current. *Sedimentology*, 33(3), 413–423. doi: 10.1111/j.1365-3091.1986.tb00545.x.

Livingstone, I., G. F. Wiggs & C. M. Weaver (2007). Geomorphology of desert sand dunes: A review of recent progress. *Earth-Science Reviews*, 80(3-4), 239–257. doi: 10.1016/j.earscirev.2006.09.004.

Livsey, D. N., J. R. Crosswell, R. D. Turner, A. D. Steven & P. R. Grace (2022). Flocculation of Riverine Sediment Draining to the Great Barrier Reef, Implications for Monitoring and Modeling of Sediment Dispersal Across Continental Shelves. *Journal of Geophysical Research: Oceans*, 127(7). doi: 10.1029/2021JC017988.

Lu, C., C. Yao, X. Su, Y. Jiang, F. Yuan & M. Wang (2018). The Influences of a Clay Lens on the Hyporheic Exchange in a Sand Dune. *Water*, 10(7), 826. doi: 10.3390/w10070826.

Ma, H., J. A. Nittrouer, K. Naito, X. Fu, Y. Zhang, A. J. Moodie, Y. Wang, B. Wu & G. Parker (2017). The exceptional sediment load of fine-grained dispersal systems: Example of the Yellow River, China. *Science Advances*, 3(5), 1–8. doi: 10.1126/sciadv.1603114.

Ma, H., J. A. Nittrouer, B. Wu, M. P. Lamb, Y. Zhang, D. Mohrig, X. Fu, K. Naito, Y. Wang, A. J. Moodie, G. Wang, C. Hu & G. Parker (2020). Universal relation with regime transition for sediment transport in fine-grained rivers. *Proceedings of the National Academy of Sciences of the United States of America*, 117(1), 171–176. doi: 10.1073/pnas.1911225116.

MacIver, M. (2019). Safas: Sedimentation and floc analysis software.

Manning, R. (1891). On the flow of water in open channels and pipes. *Transactions of the Institution of Civil engineers of Ireland*.

van Maren, D. S., J. C. Winterwerp & J. Vroom (2015). Fine sediment transport into the hyper-turbid

lower Ems River: the role of channel deepening and sediment-induced drag reduction. *Ocean Dynamics*, 65(4), 589–605. DOI: 10.1007/s10236-015-0821-2.

VAN DER MARK, C. F. & A. BLOM (2007). *A new and widely applicable tool for determining the geometric properties of bedforms*. Technical report, University of Twente.

VAN DER MARK, C. F., A. BLOM & S. M. HULSCHER (2008). Quantification of variability in bedform geometry. *Journal of Geophysical Research: Earth Surface*, 113(3), 1–11. DOI: 10.1029/2007JF000940.

MARTÍNEZ-CARRERAS, N., A. KREIN, F. GALLART, J. F. IFFLY, C. HISSLER, L. PFISTER, L. HOFFMANN & P. N. OWENS (2012). The Influence of Sediment Sources and Hydrologic Events on the Nutrient and Metal Content of Fine-Grained Sediments (Attert River Basin, Luxembourg). *Water, Air, & Soil Pollution*, 223(9), 5685–5705. DOI: 10.1007/s11270-012-1307-1.

MARTINIUS, A. & J. VAN DEN BERG (2011). *Atlas of sedimentary structures in estuarine and tidally-influenced river deposits of the Holocene Rhine-Meuse-Scheldt system: Their application to the interpretation of analogous outcrop and subsurface depositional systems*. EAGE Publications bv.

MATSUBARA, Y., A. D. HOWARD, D. M. BURR, R. M. WILLIAMS, W. E. DIETRICH & J. M. MOORE (2015). River meandering on Earth and Mars: A comparative study of Aeolis Dorsa meanders, Mars and possible terrestrial analogs of the Usuktuk River, AK, and the Quinn River, NV. *Geomorphology*, 240, 102–120. DOI: 10.1016/j.geomorph.2014.08.031.

MATTE, P., Y. SECRETAN & J. MORIN (2018). Reconstruction of Tidal Discharges in the St. Lawrence Fluvial Estuary: The Method of Cubature Revisited. *Journal of Geophysical Research: Oceans*, 123(8), 5500–5524. DOI: 10.1029/2018JC013834.

MCCARRON, C. J., K. J. VAN LANDEGHEM, J. H. BAAS, L. O. AMOUDRY & J. MALARKEY (2019). The hiding-exposure effect revisited: A method to calculate the mobility of bimodal sediment mixtures. *Marine Geology*, 410, 22–31. DOI: 10.1016/j.margeo.2018.12.001.

MCLAREN, P. & P. REN (1995). *Sediment transport patterns in the lower fraser river and fraser delta*. Technical report.

MCLEAN, D. & B. TASSONE (1989). *Effects of Dredging on Fraser River Channel Regime*. Technical report, Public Works Canada and Environment Canada, Vancouver. Unpublished report 883-578.

MCLEAN, D. G., M. CHURCH & B. TASSONE (1999). Sediment transport along lower Fraser River 1. Measurements and hydraulic computations. *Water Resources Research*, 35(8), 2533–2548. DOI: 10.1029/1999WR900101.

MCLEAN, S. R. (1992). On the calculation of suspended load for noncohesive sediments. *Journal of Geophysical Research: Oceans*, 97(C4), 5759–5770. DOI: 10.1029/91JC02933.

MCLEAN, S. R. & J. D. SMITH (1979). Turbulence measurements in the boundary layer over a sand wave field. *Journal of Geophysical Research*, 84(C12), 7791. DOI: 10.1029/JC084iC12p07791.

MEHTA, A. (2014). *An Introduction to Hydraulics of Fine Sediment Transport*. World Scientific.

MEHTA, A. J. & F. PARTHENIADES (1975). An investigation of the depositional properties of flocculated fine sediments. *Journal of Hydraulic Research*, 13(4), 1975. DOI: 10.1080/00221687509499694.

MIETTA, F., C. CHASSAGNE, A. J. MANNING & J. C. WINTERWERP (2009). Influence of shear rate, organic matter content, pH and salinity on mud flocculation. *Ocean Dynamics*, 59(5), 751–763. DOI: 10.1007/s10236-009-0231-4.

MIGNOT, E., D. HURTHER & E. BARTELEMY (2009). On the structure of shear stress and turbulent kinetic energy flux across the roughness layer of a gravel-bed channel flow. *Journal of Fluid Mechanics*, 638, 423–452. DOI: 10.1017/S0022112009990772.

MIKKELSEN, O. A. & M. PEJRUP (2001). The use of a LISST-100 laser particle sizer for in-situ estimates of floc size, density and settling velocity. *Geo-Marine Letters*, 20(4), 187–195. DOI: 10.1007/s003670100064.

MILLIGAN, T. & D. LORING (1997). The Effect of Flocculation on the Size Distributions of Bottom Sediment

in Coastal Inlets: Implications for Contaminant Transport. *Water, Air, and Soil Pollution*, 99(1/4), 33–42. DOI: 10.1023/A:1018307710140.

Mooneyham, C. & K. Strom (2018). Deposition of Suspended Clay to Open and Sand-Filled Framework Gravel Beds in a Laboratory Flume. *Water Resources Research*, 54(1), 323–344. DOI: 10.1002/2017WR020748.

Morris, H.M. (1955). Flow in Rough Conduits. *Transactions of the American Society of Civil Engineers*, 120(1), 373–398. DOI: 10.1061/TACEAT.0007206.

Morvan, H., D. Knight, N. Wright, X. Tang & A. Crossley (2008). The concept of roughness in fluvial hydraulics and its formulation in 1D, 2D and 3D numerical simulation models. *Journal of Hydraulic Research*, 46(2), 191–208. DOI: 10.1080/00221686.2008.9521855.

Möws, R. & K. Koll (2019). Roughness E ect of Submerged Groyne Fields with Varying Length, Groyne Distance, and Groyne Types. *Water*, 11(1253). DOI: 10.3390/w11061253.

Murphy, D. (2023). Sediment Delivery and Bedform Variability of the Lower Fraser River and Delta.

Naqshband, S., O. van Duin, J. Ribberink & S. Hulscher (2016). Modeling river dune development and dune transition to upper stage plane bed. *Earth Surface Processes and Landforms*, 41(3), 323–335. DOI: 10.1002/esp.3789.

Naqshband, S. & A. Hoitink (2020). Scale-Dependent Evanescence of River Dunes During Discharge Extremes. *Geophysical Research Letters*, 47(6). DOI: 10.1029/2019GL085902.

Naqshband, S., A.J. Hoitink, B. McElroy, D. Hurther & S.J. Hulscher (2017). A Sharp View on River Dune Transition to Upper Stage Plane Bed. *Geophysical Research Letters*, 44(22), 437–11. DOI: 10.1002/2017GL075906.

Naqshband, S., J. Ribberink & S. Hulscher (2014a). Using both free surface effect and sediment transport mode parameters in defining the morphology of river dunes and their evolution to upper stage plane beds. *Journal of Hydraulic Engineering*, 140(6), 1–6. DOI: 10.1061/(ASCE)HY.1943-7900.0000873.

Naqshband, S., J.S. Ribberink, D. Hurther, P.A. Barraud & S.J. Hulscher (2014b). Experimental evidence for turbulent sediment flux constituting a large portion of the total sediment flux along migrating sand dunes. *Geophysical Research Letters*, 41(24), 8870–8878. DOI: 10.1002/2014GL062322.

Nelson, A. (2017). *Effect of Longterm Navigation Channel Lowering on Scour and Degradation Processes on Lower Fraser River*. Technical report.

Nelson, J.M., S.R. McLean & S.R. Wolfe (1993). Mean flow and turbulence fields over two-dimensional bed forms. *Water Resources Research*, 29(12), 3935–3953. DOI: 10.1029/93WR01932.

Nelson, J.M. & J.D. Smith (1989). Flow in meandering channels with natural topography. pages 69–102. DOI: 10.1029/WM012p0069.

NHC (2008). *Fraser River hydraulic model update final report*. Technical report.

Nicholas, A. & D. Walling (1996). *The significance of particle aggregation in the overbank deposition of suspended sediment on fiver floodplains*. Technical report. DOI: 10.1016/S0022-1694(96)03023-5.

Nichols, G.J., J.A. Cripps, M.E. Collinson & A.C. Scott (2000). Experiments in waterlogging and sedimentology of charcoal: results and implications. *Palaeogeography, Palaeoclimatology, Palaeoecology*, 164(1-4), 43–56. DOI: 10.1016/S0031-0182(00)00174-7.

Oles, V. (1992). *Shear-Induced Aggregation and Breakup of Polystyrene Latex Particles*. Technical report.

Ongley, E.D., B.G. Krishnappan, G. Droppo, S.S. Rao & R.J. Maguire (1992). Cohesive sediment transport: emerging issues for toxic chemical management. *Hydrobiologia*, 235-236(1), 177–187. DOI: 10.1007/BF00026210.

van Ormondt, M., K. Nederhoff & A. van Dongeren (2020). Delft Dashboard: A quick set-up tool for hydrodynamic models. *Journal of Hydroinformatics*, 22(3), 510–527. DOI: 10.2166/hydro.2020.092.

Ouillon, S. & D. Dartus (1997). Three-dimensional computation of flow around groyne. *Journal of Hydraulic*

*Engineering*, 123(11). DOI: 10.1061/(ASCE)0733-9429(1997)123:11(962).

Paarlberg, A. J., C. M. Dohmen-Janssen, S. J. Hulscher & P. Termes (2007). A parameterization of flow separation over subaqueous dunes. *Water Resources Research*, 43(12), 1–10. DOI: 10.1029/2006WR005425.

Paarlberg, A. J., C. M. Dohmen-Janssen, S. J. Hulscher, P. Termes & R. Schielen (2010). Modelling the effect of time-dependent river dune evolution on bed roughness and stage. *Earth Surface Processes and Landforms*, 35(15), 1854–1866. DOI: 10.1002/esp.2074.

Paola, C., K. Straub, D. Mohrig & L. Reinhardt (2009). The "unreasonable effectiveness" of stratigraphic and geomorphic experiments. *Earth-Science Reviews*, 97(1-4), 1–43. DOI: 10.1016/j.earscirev.2009.05.003.

Paola, C., R. R. Twilley, D. A. Edmonds, W. Kim, D. Mohrig, G. Parker, E. Viparelli & V. R. Voller (2011). Natural Processes in Delta Restoration: Application to the Mississippi Delta. *Annual Review of Marine Science*, 3(1), 67–91. DOI: 10.1146/annurev-marine-120709-142856.

Parchure, T. M. & A. J. Mehta (1985). Erosion of Soft Cohesive Sediment Deposits. *Journal of Hydraulic Engineering*, 111(10), 1308–1326. DOI: 10.1061/(ASCE)0733-9429(1985)111:10(1308).

Parker, G. (2003). Persistence of sediment lumps in approach to equilibrium in sediment-recirculating flumes. In *Proceedings, International Association of Hydraulic Research Congress*.

Parker, G., T. Muto, Y. Akamatsu, W. E. Dietrich & J. Wesley Lauer (2008). Unravelling the conundrum of river response to rising sea-level from laboratory to field. Part II. The Fly–Strickland River system, Papua New Guinea. *Sedimentology*, 55(6), 1657–1686. DOI: 10.1111/j.1365-3091.2008.00962.x.

Parker, G., C. M. Toro-Escobar, M. Ramey & S. Beck (2003). Effect of Floodwater Extraction on Mountain Stream Morphology. *Journal of Hydraulic Engineering*, 129(11), 885–895. DOI: 10.1061/(asce)0733-9429(2003)129:11(885).

Parsons, D. R., J. L. Best, O. Orfeo, R. J. Hardy, R. Kostaschuk & S. N. Lane (2005). Morphology and flow fields of three-dimensional dunes, Rio Paraná, Argentina: Results from simultaneous multibeam echo sounding and acoustic Doppler current profiling. *Journal of Geophysical Research: Earth Surface*, 110(F4). DOI: 10.1029/2004JF000231.

Parsons, D. R., R. J. Schindler, J. A. Hope, J. Malarkey, J. H. Baas, J. Peakall, A. J. Manning, L. Ye, S. Simmons, D. M. Paterson, R. J. Aspden, S. J. Bass, A. G. Davies, I. D. Lichtman & P. D. Thorne (2016). The role of biophysical cohesion on subaqueous bed form size. *Geophysical Research Letters*, 43(4), 1566–1573. DOI: 10.1002/2016GL067667.

Partheniades, E., R. H. Cross & A. Ayora (1969). Further Results on the Deposition of Cohesive Sediments. In *Coastal Engineering 1968*, pages 723–742. American Society of Civil Engineers, New York, NY. DOI: 10.1061/9780872620131.047.

Patel, S. B., P. Lal Patel & P. Devidas (2013). *Threshold for initiation of motion of unimodal and bimodal sediments*. Technical Report 1.

Pawlowicz, R., B. Beardsley & S. Lentz (2002). Classical tidal harmonic analysis including error estimates in MATLAB using TDE. *Computers and Geosciences*, 28(8), 929–937. DOI: 10.1016/S0098-3004(02)00013-4.

Pearson, E. S. (1909). Determination of the Coefficient of Correlation. *Science*, 30(757), 23–25.

Pedocchi, F. & M. H. García (2006). Evaluation of the LISST-ST instrument for suspended particle size distribution and settling velocity measurements. *Continental Shelf Research*, 26(8), 943–958. DOI: 10.1016/j.csr.2006.03.006.

Pérez, K., N. Toro, M. Jeldres, E. Gálvez, P. Robles, O. Alvarado, P. G. Toledo & R. I. Jeldres (2022). Estimating the Shear Resistance of Flocculated Kaolin Aggregates: Effect of Flocculation Time, Flocculant Dose, and Water Quality. *Polymers*, 14(7). DOI: 10.3390/polym14071381.

Perillo, M. M., J. L. Best & M. H. Garcia (2014). A new phase diagram for combined-flow bedforms. *Journal of Sedimentary Research*, 84(4), 301–313. DOI: 10.2110/jsr.2014.25.

Petersen, O. & B.G. Krishnappan (1994). Measurement and analysis of flow characteristics in a rotating circular flume. *Journal of Hydraulic Research*, 32(4), 483–494. doi: 10.1080/00221686.1994.9728351.

Pfister, L., N. Martínez-Carreras, C. Hissler, J. Klaus, G. E. Carrer, M. K. Stewart & J. J. McDonnell (2017). Bedrock geology controls on catchment storage, mixing, and release: A comparative analysis of 16 nested catchments. *Hydrological Processes*, 31(10), 1828–1845. doi: 10.1002/hyp.11134.

Phillips, J. D. (2022). Geomorphology of the fluvial–estuarine transition zone, lower Neuse River, North Carolina. *Earth Surface Processes and Landforms*, 47(8), 2044–2061. doi: 10.1002/esp.5362.

Phillips, J. M. & D. E. Walling (1995). *An assessment of the effects of sample collection, storage and resuspension on the representativeness of measurements of the effective particle size distribution of fluvial suspended sediment*. Technical Report 11.

Pillai, J. (1997). *Flocculants and Coagulants: The Keys to Water and Waste Management in Aggregate Production Reprint R-680*. Technical report, NALCO, Reprint R-680.

Courrech du Pont, S. (2015). Dune morphodynamics. *Comptes Rendus Physique*, 16(1), 118–138. doi: 10.1016/j.crhy.2015.02.002.

Pope, N. D., J. Widdows & M. D. Brinsley (2006). Estimation of bed shear stress using the turbulent kinetic energy approach-A comparison of annular flume and field data. *Continental Shelf Research*, 26(8), 959–970. doi: 10.1016/j.csr.2006.02.010.

Pope, S. B. (2000). *Turbulent Flows*. Cambridge University Press.

Postma, H. (1967). Sediment transport and sedimentation in the estuarine environment. *American Association of Advanced Sciences*, 83, 158–179.

Potter, P. E., J. B. Maynard & P. J. Depetris (2005). *Mud and mudstones: Introduction and overview*. Springer Science & Business Media.

Potter, P. E., J. B. Maynard & W. A. Pryor (1980). *Sedimentology of Shale*. Springer New York, New York, NY. doi: 10.1007/978-1-4612-9981-3.

Pretious, E. (1956). *Bed-load Measurement in the Main Arm Fraser River Estuary*. Technical report.

Pretious, E. & T. Blench (1951). *Final Report on Special Observations of Bed Movement in the Lower Fraser River at Ladner Reach during 1950 Freshet*. Technical report, Natl. Res. Counc. Can, Vancouver.

Prokocki, E. W., J. L. Best, M. M. Perillo, P. J. Ashworth, D. R. Parsons, G. H. Sambrook Smith, A. P. Nicholas & C. J. Simpson (2022). The morphology of fluvial-tidal dunes: Lower Columbia River, Oregon/Washington, USA. *Earth Surface Processes and Landforms*, 47(8), 2079–2106. doi: 10.1002/esp.5364.

Reesink, A., J. Van den Berg, D. Parsons, M. Amsler, J. Best, R. Hardy, O. Orfeo & R. Szupiany (2015). Extremes in dune preservation: Controls on the completeness of fluvial deposits. *Earth-Science Reviews*, 150, 652–665. doi: 10.1016/j.earscirev.2015.09.008.

Renaud, F. G., J. P. Syvitski, Z. Sebesvari, S. E. Werners, H. Kremer, C. Kuenzer, R. Ramesh, A. Jeuken & J. Friedrich (2013). Tipping from the Holocene to the Anthropocene: How threatened are major world deltas? *Current Opinion in Environmental Sustainability*, 5(6), 644–654. doi: 10.1016/j.cosust.2013.11.007.

Reneerkens, M. (2020). *De bodemsamenstelling van de Rijntakken in de jaren 1995 en 2020*. Technical report, RWS ON rapport.

Ribberink, J. S. (1998). *Bed-load transport for steady flows and unsteady oscillatory flows*. Technical report.

Rijkswaterstaat (2009). *Dutch standards for hydrographic surveys*. Technical report, Data-ICT-Dienst, Rijkswaterstaat.

van Rijn, L. (1984). Sediment transport, part III: Bedforms and Alluvial Roughness. *Journal of Hydraulic Engineering*, 110(12), 1733–1754. doi: 10.1061/(ASCE)0733-9429(1984)110:12(1733).

van Rijn, L. C. (2020). Erodibility of Mud–Sand Bed Mixtures. *Journal of Hydraulic Engineering*, 146(1). doi: 10.1061/(asce)hy.1943-7900.0001677.

van Rijn, L. C. & B. Grasmeijer (2018). Effect of channel deepening on tidal flow and sediment transport—part II: muddy channels. *Ocean Dynamics*, 68(11), 1481–1501. doi: 10.1007/s10236-018-1205-1.

River, M. & C. J. Richardson (2019). Suspended Sediment Mineralogy and the Nature of Suspended Sediment Particles in Stormflow of the Southern Piedmont of the USA. *Water Resources Research*, 55(7), 5665–5678. doi: 10.1029/2018WR024613.

Romero, C. P., R. I. Jeldres, G. R. Quezada, F. Concha & P. G. Toledo (2018). Zeta potential and viscosity of colloidal silica suspensions: Effect of seawater salts, pH, flocculant, and shear rate. *Colloids and Surfaces A: Physicochemical and Engineering Aspects*, 538, 210–218. doi: 10.1016/j.colsurfa.2017.10.080.

Rügner, H., M. Schwientek, R. Milačič, T. Zuliani, J. Vidmar, M. Paunović, S. Laschou, E. Kalogianni, N. T. Skoulikidis, E. Diamantini, B. Majone, A. Bellin, G. Chiogna, E. Martinez, M. López de Alda, M. S. Díaz-Cruz & P. Grathwohl (2019). Particle bound pollutants in rivers: Results from suspended sediment sampling in Globaqua River Basins. *Science of The Total Environment*, 647, 645–652. doi: 10.1016/j.scitotenv.2018.08.027.

de Ruijsscher, T., A. Hoitink, S. Dinnissen, B. Vermeulen & P. Hazenberg (2018). Application of a Line Laser Scanner for Bed Form Tracking in a Laboratory Flume. *Water Resources Research*, 54(3), 2078–2094. doi: 10.1002/2017WR021646.

de Ruijsscher, T., S. Naqshband & A. Hoitink (2020). Effect of non-migrating bars on dune dynamics in a lowland river. *Earth Surface Processes and Landforms*.

de Ruijsscher, T. V., A. J. F. Hoitink, S. Naqshband & A. J. Paarlberg (2019). Bed morphodynamics at the intake of a side channel controlled by sill geometry. *Advances in Water Resources*, 134. doi: 10.1016/j.advwatres.2019.103452.

Russell, C. E., R. Fernández, D. R. Parsons & S. E. Gabbott (2023). Plastic pollution in riverbeds fundamentally affects natural sand transport processes. *Communications Earth and Environment*, 4(1). doi: 10.1038/s43247-023-00820-7.

RWS-WVL & Deltares (2017). *Beschrijving Modelschematisatie Rijn 5e-generatie Baseline, WAQUA en SOBEK3*. Technical report.

Safar, Z., C. Chassagne, S. Rijnsburger, M. I. Sanz, A. J. Manning, A. Souza, T. van Kessel, A. Horner-Devine, R. Flores, M. McKeon & J. Pietrzak (2022). Characterization and classification of estuarine suspended particles based on their inorganic/organic matter composition. *Frontiers in Marine Science*, 9. doi: 10.3389/fmars.2022.896163.

Sassi, M. G., A. J. Hoitink, B. De Brye, B. Vermeulen & E. Deleersnijder (2011). Tidal impact on the division of river discharge over distributary channels in the Mahakam Delta. *Ocean Dynamics*, 61(12), 2211–2228. doi: 10.1007/s10236-011-0473-9.

Saunderson, H. C. & F. P. J. Lockett (1983). Flume experiments on bedforms and structures at the dune-plane bed transition. *Spec Publs. int. Ass Sediment*, 6, 49–58.

Scheffer, M., J. Bascompte, W. A. Brock, V. Brovkin, S. R. Carpenter, V. Dakos, H. Held, E. H. Van Nes, M. Rietkerk & G. Sugihara (2009). Early-warning signals for critical transitions. doi: 10.1038/nature08227.

Scheffer, M., S. R. Carpenter, T. M. Lenton, J. Bascompte, W. Brock, V. Dakos, J. Van De Koppel, I. A. Van De Leemput, S. A. Levin, E. H. Van Nes, M. Pascual & J. Vandermeer (2012). Anticipating Critical Transitions. doi: 10.1126/science.1225244.

Schieber, J., J. Southard & K. Thaisen (2007). Accretion of Mudstone Beds from Migrating Floccule Ripples. *Science*, 318(5857), 1760–1763. doi: 10.1126/science.1147001.

Schielen, R. M., P. Jesse & L. J. Bolwidt (2007). On the use of flexible spillways to control the discharge ratio of the Rhine in the Netherlands. *Geologie en Mijnbouw/Netherlands Journal of Geosciences*, 86(1), 159. doi: 10.1017/S0016774600023155.

Schindler, R. J., D. R. Parsons, L. Ye, J. A. Hope, J. H. Baas, J. Peakall, A. J. Manning, R. J. Aspden,

J. Malarkey, S. Simmons, D.M. Paterson, I.D. Lichtman, A.G. Davies, P.D. Thorne & S.J. Bass (2015). Sticky stuff: Redefining bedform prediction in modern and ancient environments. *Geology*, 43(5), 399–402. doi: 10.1130/G36262.1.

Schrijvershof, R.A., D.S. van Maren, P.J.J.F. Torfs & A.J.F. Hoitink (2023). A Synthetic Spring-Neap Tidal Cycle for Long-Term Morphodynamic Models. *Journal of Geophysical Research: Earth Surface*, 128(3). doi: 10.1029/2022JF006799.

Sehgal., D., N. Martinez-Carreras & C. Hissler (2022). Data to reproduce the results presented in Sehgal et al. 2022. Journal of Geophysical Research Earth Surface, 10.1029/2022JF006838 ("A Generic Relation Between Turbidity, Suspended Particulate Matter Concentration, and Sediment Characteristics"). *Zenodo (dataset)*.

Sehgal, D., N. Martinez-Carreras & C. Hissler (2022a). Data to reproduce the results presented in Sehgal et al. 2022. Water Resources Research, 10.1029/2021WR030624 ("Inferring suspended sediment carbon content and particle size at high-frequency from the optical response of a submerged spectr...'). *Zenodo (dataset)*. doi: 10.5281/zenodo.6509837.

Sehgal, D., N. Martínez-Carreras, C. Hissler, V.F. Bense & A.J.F.T. Hoitink (2022b). A Generic Relation Between Turbidity, Suspended Particulate Matter Concentration, and Sediment Characteristics. *Journal of Geophysical Research: Earth Surface*, 127(12). doi: 10.1029/2022JF006838.

Sehgal, D., N. Martínez-Carreras, C. Hissler, V.F. Bense & A.J.F.T. Hoitink (2022c). Inferring Suspended Sediment Carbon Content and Particle Size at High Frequency From the Optical Response of a Submerged Spectrometer. *Water Resources Research*, 58(5). doi: 10.1029/2021WR030624.

Selomulya, C., G. Bushell, R. Amal & T.D. Waite (2003). *Understanding the role of restructuring in nocculation: The application of a population balance model*. Technical report.

Seminara, G., M. Bolla Pittaluga & N. Tambroni (2012). Long term morphodynamic equilibrium of tidal channels. In *Shallow Flows*, pages 207–216. Taylor & Francis. doi: 10.1201/9780203027325.ch26.

Shakeel, A., Z. Safar, M. Ibanez, L. van Paassen & C. Chassagne (2020). Flocculation of Clay Suspensions by Anionic and Cationic Polyelectrolytes: A Systematic Analysis. *Minerals*, 10(11), 999. doi: 10.3390/min10110999.

SICK (2012). *Ranger E/D reference manual – MultiScan 3D camera with Gigabit Ethernet (E), 3D camera with Gigabit Ethernet (D)*. Technical report, SICK Sensor Intelligence, Waldkirch, Germany.

Sieben, A. (2020). *Overzicht afvoermetingen 2016-2019 project monitoring langsdammen*. Technical report.

Silberman, E., R. Carter, H. Einstein, J. Hinds & R. Powell (1963). Friction factors in open channels. *Journal of Hydraulic Engineering*, 89(HY2), 97–143. doi: 10.1061/JYCEAJ.0000865.

Sloff, C.J., E. Mosselman & J. Sieben (2006). Effective use of non-erodible layers for improving navigability. *Proceedings of the International Conference on Fluvial Hydraulics - River Flow 2006*, 2, 1211–1220. doi: 10.1201/9781439833865.ch127.

Smith, J.D. & S.R. McLean (1977). Spatially averaged flow over a wavy surface. *Journal of Geophysical Research*, 82(12), 1735–1746. doi: 10.1029/JC082i012p01735.

Smith, M.W. (2014). Roughness in the Earth Sciences. doi: 10.1016/j.earscirev.2014.05.016.

Soulsby, R. (1997). *Dynamics of marine sands*. London, Thomas Telford, 249p.

Soulsby, R.L., R.J. Whitehouse & K.V. Marten (2012). Prediction of time-evolving sand ripples in shelf seas. *Continental Shelf Research*, 38, 47–62. doi: 10.1016/j.csr.2012.02.016.

Southard, J.B. & L.A. Boguchwal (1990). Bed configurations in steady unidirectional water flows, part 2. Synthsis of flume data. 60(5), 658–679.

Spencer, K.L., J.A. Wheatland, A.J. Bushby, S.J. Carr, I.G. Droppo & A.J. Manning (2021). A structure–function based approach to floc hierarchy and evidence for the non-fractal nature of natural sediment flocs. *Scientific Reports*, 11(1). doi: 10.1038/s41598-021-93302-9.

Spork, V. (1997). *Erosionsverhalten feiner Sedimente und ihre biogene Stabilisierung*. Ph.D. thesis, Wasserbau und Wasserwirtschaft, Aachen.

Stark, J., S. Smolders, P. Meire & S. Temmerman (2017). Impact of intertidal area characteristics on estuarine tidal hydrodynamics: A modelling study for the Scheldt Estuary. *Estuarine, Coastal and Shelf Science*, 198, 138–155. doi: 10.1016/j.ecss.2017.09.004.

Statisticat, L. (2021). LaplacesDemon: Complete Environment for Bayesian Inference.

Stewart, I. & B. Tassone (1989). *The Fraser River delta: a Review of Historic Sounding Charts*. Technical report, Environment Canada, Conservation and Protection, Vancouver, B.C.

Strogatz, S. H. (2018). *Nonlinear Dynamics and Chaos with Student Solutions Manual*. CRC Press. doi: 10.1201/9780429399640.

Stross, R. & R. Sokol (1989). Runoff and flocculation modify underwater light environment of the Hudson River Estuary. *Estuarine, Coastal and Shelf Science*, 29(4), 305–316. doi: 10.1016/0272-7714(89)90030-9.

Tennekes, H. & J. Lumley (1972). *A First Course In Turbulence*. The MIT Press.

Topping, D. J., D. M. Rubin, S. A. Wright & T. S. Melis (2011). *Field Evaluation of the Error Arising from Inadequate Time Averaging in the Standard Use of Depth-Integrating Suspended-Sediment Samplers*. Technical report, USGS.

Torres, M. A., A. B. Limaye, V. Ganti, M. P. Lamb, A. J. West & W. W. Fischer (2017). Model predictions of long-lived storage of organic carbon in river deposits. *Earth Surface Dynamics*, 5(4), 711–730. doi: 10.5194/esurf-5-711-2017.

Trigg, M. A., M. D. Wilson, P. D. Bates, M. S. Horritt, D. E. Alsdorf, B. R. Forsberg & M. C. Vega (2009). Amazon flood wave hydraulics. *Journal of Hydrology*, 374(1-2), 92–105. doi: 10.1016/j.jhydrol.2009.06.004.

Tuijnder, A. P., J. S. Ribberink & S. J. M. H. Hulscher (2009). An experimental study into the geometry of supply-limited dunes. *Sedimentology*, 56(6), 1713–1727. doi: 10.1111/j.1365-3091.2009.01054.x.

Vellinga, N., A. Hoitink, M. van der Vegt, W. Zhang & P. Hoekstra (2014). Human impacts on tides overwhelm the effect of sea level rise on extreme water levels in the Rhine–Meuse delta. *Coastal Engineering*, 90, 40–50. doi: 10.1016/j.coastaleng.2014.04.005.

Venditti, J. G. (2007). Turbulent flow and drag over fixed two- and three-dimensional dunes. *Journal of Geophysical Research*, 112(F4), F04008. doi: 10.1029/2006JF000650.

Venditti, J. G. (2013). *Bedforms in Sand-Bedded Rivers*, volume 9. Elsevier Ltd. doi: 10.1016/B978-0-12-374739-6.00235-9.

Venditti, J. G. & S. J. Bennett (2000). Spectral analysis of turbulent flow and suspended sediment transport over fixed dunes. *Journal of Geophysical Research: Oceans*, 105(C9), 22035–22047. doi: 10.1029/2000JC900094.

Venditti, J. G. & R. W. Bradley (2022). Bedforms in Sand Bed Rivers. In John (Jack) F. Schroder (editor), *Treatise on Geomorphology*, volume 6.1, chapter 6.13, pages 222–254. Elsevier, 2nd edition. doi: 10.1016/B978-0-12-409548-9.12519-9.

Venditti, J. G. & M. Church (2014). Morphology and controls on the position of a gravel- sand transition: Fraser River, British Columbia. pages 300–316. doi: 10.1002/2014JF003147.

Venditti, J. G., M. Church & S. J. Bennett (2005). On the transition between 2D and 3D dunes. *Sedimentology*, 52(6), 1343–1359. doi: 10.1111/j.1365-3091.2005.00748.x.

Venditti, J. G., W. E. Dietrich, P. A. Nelson, M. A. Wydzga, J. Fadde & L. Sklar (2010). Mobilization of coarse surface layers in gravel-bedded rivers by finer gravel bed load. *Water Resources Research*, 46(7). doi: 10.1029/2009WR008329.

Venditti, J. G., N. Domarad, M. Church & C. D. Rennie (2015). The gravel-sand transition: Sediment dynamics in a diffuse extension. *Journal of Geophysical Research: Earth Surface*, pages 300–316. doi: 10.

1002/2014JF003328.

Venditti, J. G., C. Y. M. Lin & M. Kazemi (2016). Variability in bedform morphology and kinematics with transport stage. *Sedimentology*, 63(4), 1017–1040. doi: 10.1111/sed.12247.

Venditti, J. G., J. A. Nittrouer, M. A. Allison, R. P. Humphries & M. Church (2019). Supply-limited bedform patterns and scaling downstream of a gravel–sand transition. *Sedimentology*, 66(6), 2538–2556. doi: 10.1111/sed.12604.

Vermeulen, B. (2015). Adcptools: Set of functions to process acoustic Doppler current profiler data.

Vermeulen, B., A. Hoitink & M. Sassi (2013). On the use of horizontal acoustic Doppler profilers for continuous bed shear stress monitoring. *International Journal of Sediment Research*, 28(2), 260–268. doi: 10.1016/S1001-6279(13)60037-2.

Vermeulen, B., A. J. Hoitink, S. W. van Berkum & H. Hidayat (2014a). Sharp bends associated with deep scours in a tropical river: The river Mahakam (East Kalimantan, Indonesia). *Journal of Geophysical Research: Earth Surface*, 119(7), 1441–1454. doi: 10.1002/2013JF002923.

Vermeulen, B., M. Sassi & A. Hoitink (2014b). Improved flow velocity estimates from moving-boat ADCP measurements. *Journal of the American Water Resources Association*, 50, 4186–4196. doi: 10.1111/j.1752-1688.1969.tb04897.x.

Verney, R., R. Lafite, J. Claude Brun-Cottan & P. Le Hir (2011). Behaviour of a floc population during a tidal cycle: Laboratory experiments and numerical modelling. *Continental Shelf Research*, 31(10), S64–S83. doi: 10.1016/j.csr.2010.02.005.

van de Vijsel, R., M. Scheffer & T. Hoitink (2024). Tipping points in river deltas. *in preparation*.

Villard, P. V. & M. Church (2005). Bar and dune development during a freshet: Fraser River Estuary, British Columbia, Canada. *Sedimentology*, 52(4), 737–756. doi: 10.1111/j.1365-3091.2005.00721.x.

Vroom, J., P. de Vet & J. van der Werf (2015). *Validatie waterbeweging Delft3D-NeVla model Westerscheldemonding*. Technical report, Deltares.

Walling, D. E., P. N. Owens, B. D. Waterfall, G. J. L. Leeks & P. D. Wass (2000). The particle size characteristics of fluvial suspended sediment in the Humber and Tweed catchments, UK. In *The Science of the Total Environment*, volume 251/252, pages 205–222.

Wallis, S. G. & D. W. Knight (1984). Calibration studies concerning a one-dimensional numerical tidal model with particular reference to resistance coefficients. *Estuarine, Coastal and Shelf Science*, 19(5), 541–562. doi: 10.1016/0272-7714(84)90015-5.

Wan, Z. (1985). Bed Material Movement in Hyperconcentrated Flow. *Journal of Hydraulic Engineering*, 111(6), 987–1002. doi: 10.1061/(ASCE)0733-9429(1985)111:6(987).

Wan, Z. & Z. Wang (1994). *Hyperconcentrated Flow*. Taylor and Francis, New York.

Warmink, J. J. (2011). *Unraveling uncertainties. The effect of hydraulic roughness on design water levels in river models*. Ph.D. thesis. doi: 10.3990/1.9789036532273.

Warmink, J. J., M. J. Booij, H. van der Klis & S. J. Hulscher (2013). Quantification of uncertainty in design water levels due to uncertain bed form roughness in the Dutch river Waal. *Hydrological Processes*, 27(11), 1646–1663. doi: 10.1002/hyp.9319.

WCHL (1977). *Feasibility Study, Development of a Forty-Foot Draft Navigation Channel, New Westminster to Sandheads: Vancouver, Western Canada*. Technical report.

Wells, J. T. (1995). Chapter 6 Tide-Dominated Estuaries and Tidal Rivers. pages 179–205. doi: 10.1016/S0070-4571(05)80026-3.

Whiting, P., W. Dietrich, L. Leopold, T. Drake & R. Shreve (1988). Bedload sheets in hetrogeneous sediment. *Geology*, 16(2), 105–108. doi: 10.1130/0091-7613(1988)016{%}3C0105:BSIHS{%}3E2.3.CO;2.

Wilbers, A. (1999). Bed Load Transport and Dune Development during discharge waves in the Rhine: Echo branches-soundings from the Flood November 1998 (in Dutch). *ICG Report 99/10. ICG, Utrecht University,*

*Utrecht*.

Wilbers, A. & W. Ten Brinke (2003). The response of subaqueous dunes to floods in sand and gravel bed reaches of the Dutch Rhine. *Sedimentology*, 50(6), 1013–1034. doi: 10.1046/j.1365-3091.2003.00585.x.

Wilcock, P. R. (1993). Critical Shear Stress of Natural Sediments. *Journal of Hydraulic Engineering*, 119(4), 491–505. doi: 10.1061/(ASCE)0733-9429(1993)119:4(491).

Williams, J. J., C. P. Rose, P. D. Thorne, B. A. O'connor, J. D. Humphery, P. J. Hardcastle, S. P. Moores, J. A. Cooke & D. J. Wilson (1999). *Field observations and predictions of bed shear stresses and vertical suspended sediment concentration profiles in wave-current conditions*. Technical report.

Williams, N. D., D. E. Walling & G. J. L. Leeks (2008). An analysis of the factors contributing to the settling potential of fine fluvial sediment. *Hydrological Processes*, 22(20), 4153–4162. doi: 10.1002/hyp.7015.

Williams, P. B. & P. H. Kemp (1971). Initiation of Ripples on Flat Sediment Beds. *Journal of the Hydraulics Division*, 97(4), 505–522. doi: 10.1061/JYCEAJ.0002932.

Winterwerp, J. (2002). On the flocculation and settling velocity of estuarine mud. *Continental Shelf Research*, 22(9), 1339–1360. doi: 10.1016/S0278-4343(02)00010-9.

Winterwerp, J. C., T. van Kessel, D. S. van Maren & B. C. van Prooijen (2021). *Fine Sediment in Open Water. From Fundamentals to Modeling*. Advanced Series on Open Engineering - volume 55. World Scientific. doi: 10.1142/12473.

Wolanski, E. (2007). *Estuarine Ecohydrology*. Elsevier Science. doi: 10.1016/B978-0-444-53066-0.X5001-6.

Wölz, J., C. Cofalla, S. Hudjetz, S. Roger, M. Brinkmann, B. Schmidt, A. Schäffer, U. Kammann, G. Lennartz, M. Hecker, H. Schüttrumpf & H. Hollert (2009). In search for the ecological and toxicological relevance of sediment re-mobilisation and transport during flood events. *Journal of Soils and Sediments*, 9(1), 1–5. doi: 10.1007/s11368-008-0050-0.

Wright, N. & A. Crosato (2011). The Hydrodynamics and Morphodynamics of Rivers. In *Treatise on Water Science*, volume 2, pages 135–156. doi: 10.1016/B978-0-444-53199-5.00033-6.

Wright, S. & G. Parker (2004). Flow Resistance and Suspended Load in Sand-Bed Rivers: Simplified Stratification Model. *Journal of Hydraulic Engineering*, 130(8), 796–805. doi: 10.1061/(ASCE)0733-9429(2004)130:8(796).

Wu, X., R. Fernandez, J. H. Baas, J. Malarkey & D. R. Parsons (2022a). Discontinuity in Equilibrium Wave-Current Ripple Size and Shape and Deep Cleaning Associated With Cohesive Sand-Clay Beds. *Journal of Geophysical Research: Earth Surface*, 127(9). doi: 10.1029/2022JF006771.

Wu, Y., C. Hannah, P. Matte, M. O'Flaherty-Sproul, R. Mo, X. Wang & P. MacAulay (2022b). Tidal propagation in the Lower Fraser River, British Columbia, Canada. *Estuarine, Coastal and Shelf Science*, 264(November 2021), 107695. doi: 10.1016/j.ecss.2021.107695.

Wysocki, N. & E. Hajek (2021). Mud in sandy riverbed deposits as a proxy for ancient fine-sediment supply. *Geology*, pages 1–5. doi: 10.1130/g48251.1.

Yalin, M. (1964). Geometrical Properties of Sand Wave. *Journal of Hydraulic Engineering*, 90, 105–119.

Yalin, M. (1972). *Mechanics of Sediment Transport*. Pergamon Press, Oxford. doi: 10.1061/JYCEAJ.0001097.

Yalin, M. (1992). *River Mechanics*. Pergamon Press Ltd., Oxord.

Yan, M., L. Wang, Y. Dai, H. Sun & C. Liu (2021). Behavior of Microplastics in Inland Waters: Aggregation, Settlement, and Transport. *Bulletin of Environmental Contamination and Toxicology*, 107(4), 700–709. doi: 10.1007/s00128-020-03087-2.

Yao, P., M. Su, Z. Wang, L. C. van Rijn, M. J. Stive, C. Xu & Y. Chen (2022). Erosion Behavior of Sand-Silt Mixtures: Revisiting the Erosion Threshold. *Water Resources Research*, 58(9). doi: 10.1029/2021WR031788.

Ye, L., A. J. Manning & T. J. Hsu (2020). Oil-mineral flocculation and settling velocity in saline water. *Water Research*, 173, 115569. doi: 10.1016/j.watres.2020.115569.

Yeung & al (1997). *Effect of Shear on the Strength of Polymer-Induced Flocs*. Technical report.

Yeung, A. K. C. & R. Pelton (1996). *Micromechanics: A New Approach to Studying the Strength and Breakup of Flocs*. Technical report.

Yossef, M. (2004). The effect of the submergence level on the resistance of groynes - an experimental investigation. In *The 6th Int. Conf. on Hydroscience and Engineering (ICHE-2004)*.

Yu, M., X. Yu, A. J. Mehta, A. J. Manning, F. Khan & S. Balachandar (2023). Persistent reshaping of cohesive sediment towards stable flocs by turbulence. *Scientific Reports*, 13(1), 1760. doi: 10.1038/s41598-023-28960-y.

Zanke, U. (2003). On the influence of turbulence on the initiation of sediment motion. *International Journal of Sediment Research*, 18(1), 17–31. doi: 10.1016/0029-8018(79)90021-0.

Zhang, F., X. Chen, J. Liu & Y. Zhang (2024). A new countermeasure to deep-sea mining sediment plumes: Using flocculant to enhance particles settling. *Applied Ocean Research*, 142, 103811. doi: 10.1016/j.apor.2023.103811.

Zhao, L., M. C. Boufadel, T. King, B. Robinson, R. Conmy & K. Lee (2018). Impact of particle concentration and out-of-range sizes on the measurements of the LISST. *Measurement Science and Technology*, 29(5). doi: 10.1088/1361-6501/aab83d.

Zijl, F. & J. Groenenboom (2019). *Development of a sixth generation model for the NW European Shelf (DCSM-FM 100m)*. Technical report, Deltares.

Zomer, J. Y., S. Naqshband, B. Vermeulen & A. J. F. Hoitink (2021). Rapidly migrating secondary bedforms can persist in the lee of slowly migrating primary river dunes. *JGR Earth Surface*, pages 1–20. doi: 10.1029/2020JF005918.

Zomer, J. Y., B. Vermeulen & A. J. F. Hoitink (2023). Coexistence of two dune scales in a lowland river. *Earth Surface Dynamics*, 11(6), 1283–1298. doi: 10.5194/esurf-11-1283-2023.

# Supplementary Materials

Supplementary information, data, and scripts related to each chapter of this thesis can be accessed through the following links:

- Chapter 2
  - supplementary information (https://doi.org/10.1029/2023WR035176)
  - scripts (https://doi.org/10.4121/379d78a3-7370-4171-ae35-a91115f80965)
  - data (https://doi.org/10.5281/zenodo.10002538)
- Chapter 3
  - supplementary information (https://drive.google.com/drive/folders/1S1crCElun8vwLgWyv4piFbRyIaUMXp-?usp=sharing)
  - data (https://doi.org/10.4121/dde430c4-7f9f-4d7b-bff1-d4792e0031f2)
- Chapter 4
  - supplementary information (https://drive.google.com/drive/folders/1S1crCElun8vwLgWyv4piFbRyIaUMXp-?usp=sharing)
  - data will be made available upon publication of the corresponding article (via https://doi.org/10.4121/a02c36b4-e689-4181-87d5-cd8ce3b75579).
- Chapter 5
  - supplementary information (https://drive.google.com/drive/folders/1S1crCElun8vwLgWyv4piFbRyIaUMXp-?usp=sharing)
  - data will be made available upon publication of the corresponding article (via https://doi.org/10.4121/63412419-2502-4b4d-b296-5b30c3bcb157)
- Chapter 6
  - supplementary information (https://doi.org/10.1029/2021WR030329)
  - data (https://doi.org/10.4121/14578749)
- Chapter 7
  - supplementary information (https://doi.org/10.1029/2023JF007340)
  - data (https://doi.org/10.4121/0c6be5a5-2294-4f16-b2ff-cb9ef4826402)

# Nomenclature

**List of abbreviations**

| | |
|---|---|
| 2D | two-dimensional |
| 2DH | two-dimensional horizontal |
| 3D | three-dimensional |
| ADVP | acoustic Doppler velocity profiler |
| ANOVA | analysis of variance |
| BRI | bedform roundness index |
| BTT | bedform tracking tool |
| ETM | estuarine turbidity maximum |
| FM | flexible mesh |
| FTTZ | fluvial-to-tidal transition zone |
| HAD | high-angled dune |
| LAD | low-angled dune |
| LIDAR | laser imaging detection and ranging |
| LOESS | locally estimated scatter plot smoothing |
| LNWL | low navigable water level |
| LSA | bedform leeside angle |
| LTDs | longitudinal training dams |
| MBES | multibeam echosounder |
| PP | primary particle |
| PSD | particle size distribution |
| RK | river kilometre |
| RMSE | root mean square error |
| RWS | Dutch ministry for infrastructure and environment (Rijkswaterstaat) |
| SBES | singlebeam echosounder |
| SFA | bedform slip face angle |
| SPM | suspended particulate matter |
| SPMC | suspended particulate matter concentration |
| SSA | bedform stoss side angle |
| SSC | suspended sediment concentration |
| US | ultrasonic vibrations |
| USPB | upper stage plane bed |

**List of symbols**

| | |
|---|---|
| $\Delta$ | bedform height (in which subscript vRijn, Yalin, Karim, VB refer to the predictors of van Rijn (1984), Yalin (1964), Karim (1995) and Venditti & Bradley (2022), respectively, and subscript d and r refer to dunes and ripples) (m) |
| $\eta_h$ | deviation from h (m) |
| $\eta$ | Kolmogorov length scale (m) |
| $\gamma$ | local topographic leeside angle (°) |
| $\gamma_d$ | calibration constant in the dune height predictor of van Rijn (1984) (-) |
| $\hat{f}$ | predicted hydraulic roughness (-) |
| $\kappa$ | von Karman constant (-) |
| $\lambda$ | bedform length (in which subscript vRijn and VB refer to the predictors of van Rijn (1984) and Venditti & Bradley (2022) respectively, and subscript d and r refer to dunes and ripples) (m) |
| $\mu$ | dynamic viscosity (kg $m^{-1}$ $s^{-1}$) |
| $\nu$ | kinematic viscosity ($m^2$ $s^{-1}$) |
| $\omega_s$ | particle fall velocity (m $s^{-1}$) |
| $\rho$ | density (in which subscript w, s, f and r refer to water, sediment, flocs and the relative submerged density, respectively) (kg $m^{-3}$) |
| $\sigma$ | standard deviation |
| $\sigma_d$ | dimensionless depth (-) |
| $\sigma_g$ | sorting of a PSD (-) |
| $\tau$ | shear stress (N $m^{-2}$) |
| $\tau_c$ | critical shear stress (N $m^{-2}$) |
| $\theta_{red}$ | reduction factor (Lefebvre & Winter, 2016) (-) |
| $\theta$ | dimensionless shear stress $\tau$ (-) |
| $\theta_c$ | dimensionless critical shear stress $\tau_c$ for initiation of motion (-) |
| $\xi$ | transverse bed slope (-) |
| $\zeta$ | correction factor for bimodal sediments (-) |
| A | river cross-sectional area ($m^2$) |
| C | Chézy coefficient, $'$ indicating the grain-related coefficient ($m^{1/2}$ $s^{-1}$) |
| c | filter span in BTT (van der Mark & Blom, 2007) (-) |
| CV | coefficient of variation (-) |
| d | water depth (m) |
| $D^*$ | dimensionless particle size (-) |

| | |
|---|---|
| $D_{\#\#}$ | the $\#\#th$ percentile of the particle size distribution ($\mu$m) |
| $D_{max}$ | local maximum depth (m) |
| $D_e$ | depth excess (-) |
| $D_f$ | floc diameter (m) |
| $D_r$ | regional mean depth (m) |
| f | total hydraulic roughness from pressure slope (-) |
| $f_f$ | form roughness (-) |
| $f_g$ | grain roughness (-) |
| $f_m$ | Darcy-Weisbach fiction factor (-) |
| Fr | Froude number (-) |
| g | gravitational constant (m $s^{-2}$) |
| h | mean water level (m) |
| k | roughness height (in which subscript f, g, p, s and b are roughness height from form roughness, grain roughness, primary dunes, secondary dunes and the total hydraulic roughness, respectively) (-) |
| n | cross-sectional river coordinate (m) |
| $n_{man}$ | Manning's n (s $m^{-1/3}$) |
| Po | span values in BTT (van der Mark & Blom, 2007) (-) |
| Q | river discharge ($m^3$ $s^{-1}$) |
| r | river curvature ($km^{-1}$) |
| $R^2$ | coefficient of determination (-) |
| $R_h$ | hydraulic radius (m) |
| Re | Reynolds number (-) |
| $Re_p$ | particle Reynolds number (-) |
| s | longitudinal river coordinate (m) |
| $S_0$ | bed slope (-) |
| $S_p$ | pressure slope (-) |
| $SS_{tot}$ | total sum of squares (-) |
| SV | span value (-) |
| t | temperature (°C) |
| T | transport stage (subscript VB refers to the definition by Venditti & Bradley (2022) and subscript vRijn to the definition by van Rijn (1984)) (-) |
| u | depth and width averaged flow velocity (m $s^{-1}$) |
| $u^*$ | shear velocity (m $s^{-1}$) |
| $u_c^*$ | critical shear velocity (m $s^{-1}$) |
| W | river width (m) |
| z | bed level (m) |
| $z_0$ | roughness length (m) |

# Acknowledgements

So now you're here at the acknowledgements. I wanna make a little bet. I think at least 95% of you guys went here right away – maybe you've read the summary and looked at the beautiful photographs, but that's kinda it. And that pretty much characterises the PhD pathway. People surrounding you who care a lot about your well-being and support you in any way (and this is amazing, and essential!), but at the same time have no clue what your in-depth topic is about and what you are actually working on. This all makes sense: during the PhD trajectory you push boundaries and become an expert in a very specific field. Such an expert that not even your supervisor can keep up. That can be thrilling, exhilarating, and sometimes a bit lonely. That complex roller coaster was perfectly ameliorated by some amazing people who helped me through, and whom I'd like to thank here.

First of all, my promotor, *Ton*. Your passion and enthusiasm have been both encouraging and refreshing. Your time, support, and critical comments made me into the scientist I am today. You challenged me to make the most out of it, and your unwavering support gave me the confidence to proudly publish this thesis. We could disagree, but eventually we made it through stronger. I really appreciate that everything was possible, as long as the argumentation was sound. My co-promotor *Kryss*, thank you so much for the (mental) support you provided during the last stages of my PhD. I truly enjoyed our monthly talks where we could simply be honest with each other. You always managed to cheer me up. *Suleyman*, although you were only there during the first year of my adventure at WUR, you were an invaluable supervisor. Besides your bedform knowledge, your reassuring presence and ability to comfort me made the transition into a PhD trajectory a whole lot smoother.

*Iris* and *Reinier*, thanks for being my paranymphs. Besides hard work in the mud in the lab, in the mud in Bangladesh, and behind the computer screen, you were indispensable for letting me see the positive side of things.

I'm extremely grateful for the collaboration with my amazing colleagues. You not only made a valuable contribution to my research, but also managed to keep my spirits up. *Dhruv*, I did not know that working together with someone could be so fun and easy. *Reinier*, I'm happy that we did not allow ourselves to talk about work on the highway during our numerous carpool rides, so I could get to know you so well and could enjoy your countless candid comments. *Roeland*, although we only started working together in the final stages of my PhD, I admire your infectious passion for science. *Iris*, I promised that our "body scan" would make it into my thesis, and you will not be disappointed. Thanks for all the songs shared during many hours of shovelling. *Judith*, my only "dune-buddy" here in Wageningen, it was nice to have a colleague around who did not walk away the moment I dropped

some scary question about superimposed dunes or detrending field data. A shout-out to the amazing lab technicians, *David, Nick, and Pieter*. Without your help and know-how multiple chapters of this thesis would not exist. *Paul Torfs*, thanks for your inexhaustible statistics knowledge and your eternal patience in explaining complicated statistics in 'normal people language'. Finally, *Edwin Paree*, I'm very grateful I was allowed to use your amazing pictures throughout my thesis.

Thanks to all other *collaborators* and *co-authors*. Besides providing scientific input to this thesis, working together with you also provided a sparring partner and a feeling of support. I cannot stress enough that collaboration is an essential ingredient for the success of a PhD trajectory. Thanks to all the great people I talked to at conferences, who gave me inspiration, motivation, and that little push to strive for more.

Following up on this, thanks to all *MSc and BSc students*, and especially *Kris, Sanne*, and *Anne*, whom I had the privilege of supervising during their theses. Teaching gives energy, as does being surrounded by motivated students. Additionally, many of your names made it onto my publications, showing your valuable contribution to science!

All ladies from the lady's room (my climbing and boulder partners *Linda and Rahel*, tea lady *Janneke*, *Marjanne, Femke, Tessa, Nazwa, Hadeel*), the blokes next door (*Joris, Jelte*), and my "other hallway buddy" *Steven*, you all taught me how essential real-life contact with colleagues is for creativity, motivation and keeping an open mind. My PhD journey would have been very different without you. I'm not sure if the hours brainstorming thesis titles ("Who's Dune It?", "Breaking Bed(forms)", "Triangle of Sa(n)dness", "Tune the Dune") paid off, but it was hilarious nevertheless. I really appreciate that we could laugh, but also cry together. We celebrated our successes, but also our setbacks, resulting in a beautiful wall full of "PhD art". I genuinely believe that a safe workspace environment is beneficial, if not essential, for scientific progress.

And those good vibes only continued during the many great outings, conferences, field trips, and social activities. I just want to highlight two events, otherwise this acknowledgement section would never end. Thanks to the Tour the PhD-team for the great time I had organising and participating in the Tour the PhD. Secondly, thanks to Iceland's dream team(s) for making these trips memorable - a "safe workplace" takes on a completely different meaning when you're standing next to an erupting volcano!

Mijn lieve *vrienden, Elke, Noor, Anne, de meiden uit Leiden, huisgenootjes, klimmaatjes, kanoteam*, ik kan het zo gek niet bedenken, of jullie stonden voor me klaar. Een klaagverhaal aanhoren, een publicatie toejuichen, of gewoon even zwijgend keihard sporten. Ik ben ontzettend blij en dankbaar dat ik deze ervaring met jullie hebben mogen delen.

*Oom Hans*, het leven overdenken met taartjes en G&T zou ik voor geen goud hebben willen missen, en je positiviteit en vertrouwen in mij zorgen voor dat extra beetje doorzettingsvermogen (en een gevulde maag). *Pappa*, je stond altijd klaar met advies en (wijze) woorden, en ik heb nooit getwijfeld aan het feit dat je apetrots op me bent. Lieve *mamma*, zonder jouw onuitputbare hulp, zowel praktisch, creatief als mentaal, was dit nooit gelukt. Dank voor je vertrouwen in mijn kunnen. En als je nog eens vraagt "wat ik nou in vredesnaam ook alweer doe voor werk", dan wil ik dat met liefde nog eens uitleggen.

My dearest *Wes*, you were an amazing support throughout my PhD trajectory. From English help, to shrimp drawings, to job applications, to 3D print projects, to piecing me back together when I was about to give up. Sometimes you knew better what I needed than I did myself. Thanks for encouraging me to push boundaries, for your confidence, and for your unconditional love and support. I cannot wait to see which amazing things we will achieve in the future.

Sjoukje Irene de Lange
Wageningen, May 2024

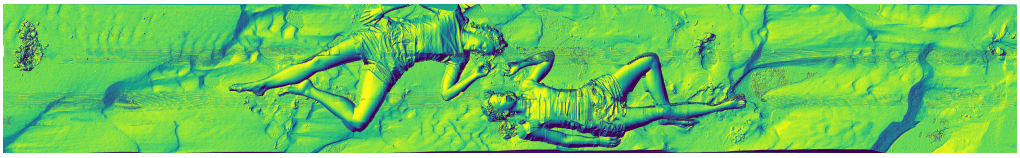

# Statement of authorship contribution

The general research direction was proposed by my promotor Ton Hoitink, and was embedded in the larger project 'Deltas out of Shape'. Based on these plans, I wrote a research proposal including research questions. I wrote the Introduction (Chapter 1) and Synthesis (Chapter 8) with minor suggestions from my (co)promotors. Chapters 2-7 have been written in collaboration with co-authors, and an overview of their contribution is listed alphabetically below. Names have been abbreviated in the following way:

SL = Sjoukje de Lange (WUR)

AW = Anne van der Wilk (WUR)
CC = Claire Casagne (TUD)
DM = Daniel Murphy (SFU)
IN = Iris Niesten (WUR)
JB = Jaco Baas (BU)
KB = Kristian Brodersen (RWTH)
MB = Maximilian Born (RWTH)
PT = Paul Torfs (-)
RK = Ray Kostaschuk (SFU)
RV = Roeland van de Vijsel (WUR)
SV = Sanne van de Veen (WUR)
VB = Victor Bense (WUR)
CH = Christophe Hissler (LIST)
DB = David Boelee (WUR)
DS = Dhruv Sehgal (LIST)
JL = Jasper Lammers (WUR)
JV = Jeremy Venditti (SFU)
KW = Kryss Waldschlager (WUR)
NM = Núria Martínez-Carreras (LIST)
RB = Ryan Bradley (SFU, NHC)
RS = Reinier Schrijvershof (WUR, Deltares)
SN = Suleyman Naqshband (WUR)
TH = Ton Hoitink (WUR)
WA = Waqas Ali (TUD)

**Chapter 2**

| | |
|---|---|
| Conceptualisation: | DS, SL |
| Data collection/assembling: | DS, SL |
| Data analysis: | DS, SL |
| Data interpretation: | DS, NM, SL |
| Drafting of manuscript, visualisation: | DS, SL |
| Revision of manuscript: | CH, DS, NM, SL, TH, VB |

**Chapter 3**

| | |
|---|---|
| Conceptualisation: | IN, SL, TH |
| Data collection/assembling: | DB, IN, JL, SL, SV |
| Data analysis: | IN, SV, SL |
| Data interpretation: | IN, JB, KW, SV, SL, TH |
| Drafting of manuscript, visualisation: | IN, SL |
| Revision of manuscript: | DB, IN, JB, JL, SL, SV, TH |

**Chapter 4**

| | |
|---|---|
| Conceptualisation: | KW, SL |
| Data collection/assembling: | AW, CC, KB, KW, MB, SL, WA |
| Data analysis: | AW, SL |
| Data interpretation: | AW, SL, TH |
| Drafting of manuscript, visualisation: | SL |
| Revision of manuscript: | AW, CC, KW, MB, SL, TH, WA |

**Chapter 5**

| | |
|---|---|
| Conceptualisation: | SL |
| Data collection/assembling: | SL |
| Data analysis: | PT, RV, SL |
| Data interpretation: | PT, SL, RV |
| Drafting of manuscript, visualisation: | RV, SL |
| Revision of manuscript: | PT, RV, SL, TH |

**Chapter 6**

| | |
|---|---|
| Conceptualisation: | SL, SN, TH |
| Data collection/assembling: | SL |
| Data analysis: | SL |
| Data interpretation: | SL, SN, TH |
| Drafting of manuscript, visualisation: | SL |
| Revision of manuscript: | SN, TH |

**Chapter 7**

| | |
|---|---|
| Conceptualisation: | KW, SL,TH |
| Data collection/assembling: | DM, RB |
| Modelling: | RS, SL |
| Data analysis: | RS, SL |
| Data interpretation: | JV, KW, RB, RK, RS, SL, TH |
| Drafting of manuscript, visualisation: | SL |
| Revision of manuscript: | DM, JV, KW, RK, SL, TH |

# List of publications

## **Peer-reviewed journal papers** | In this thesis

de Lange, S.I., Naqshband, S., Hoitink, A.J.F. (2021). Quantifying hydraulic roughness from field data: can dune morphology tell the whole story? *Water Resources Research 57(12).* DOI: 10.1029/2021WR030329.

de Lange, S.I. & Seghal, D., Martínez-Carreras, N., Waldschläger, K., Bense, V.F., Hissler, C., Hoitink, A.J.F. (2024). The Impact Of Flocculation on In Situ and Ex Situ Particle Size Measurements by Laser Diffraction. *Water Resources Research 60.* DOI: 10.1029/2023WR035176

de Lange, S.I., Bradley, R., Schrijvershof, R.A., Murphy, D., Waldschläger, K., Kostaschuk, R., Venditti, J.G., Hoitink, A.J.F. (2024). Dune geometry and the associated hydraulic roughness in the fluvial to tidal transition zone of the Fraser River at low river flow. *JGR Earth Surface 129(2).* DOI: 10.1029/2023JF007340

## **Peer-reviewed journal papers** | Other

de Lange, S.I., Santa, N., Pudasaini, S.P., Kleinhans, M.G., de Haas, T. (2019). Debris-flow generated tsunamis and their dependence on debris-flow dynamics. *Coastal Engineering 157.* DOI: 10.1016/j.coastaleng.2019.103623.

de Lange, S.I., Mellink, Y., Vriend., P, Tasseron, P.F., Begemann, F., Hauk, R., Aalderink, H., Hamers, E., Jansson, P., Joosse, N., Löhr, A., Lotcheris, R., Schreyers, L., Vos, V., van Emmerik, T.H.M. (2023). Sample size requirements for macrolitter characterization. *Frontiers in Water 4.* DOI: 10.3389/frwa.2022.1085285.

Lokhorst, I.R, de Lange, S.I., van Buiten, G., Selaković, S., Kleinhans, M.G. (2019). Species selection and assessment of eco-engineering effects of seedlings for biogeomorphological landscape experiments . *Earth Surface Processes and Landforms 44.* DOI: 10.1002/esp.4702.

de Haas, T., Santa, N., de Lange, S.I., Pudasaini, S.P. (2020). Similarities and contrasts between the subaerial and subaqueous deposits of subaerially-triggered debris flows: an analogue experimental study. *Journal of Sedimentary Research 90 (9), 1128-1138.* DOI: 10.2110/jsr.2020.020.

van Emmerik, T.H.M., de Lange, S.I., Frings, R., Schreyers, L., and H. Aalderink and J. Leusink, Begemann, F., Hamers E., Hauk, R., Janssens, N., Jansson, P., Joosse, N., Kelder, D., van der Kuijl, T., Lotcheris, R., Löhr, A., Mellink, Y., Pinto, R., Tasseron, P., Vos, V., Vriend, P. (2022). Hydrology as a Driver of Floating River Plastic Transport. *Earth's Future 10(8).* DOI: 10.1029/2022ef002811.

van Hateren, T.C., Jongen, H.J., Al-Zawaidah, Beemster, J.G.W., Boekee, J., Bogerd, L., Gao, S., Kannen, C., van Meerveld, I., de Lange, S.I., Linke, F., Pinto, R.B., Remmers, J.O.E., Ruijsch, J., Rusli, S.R., van de Vijsel, R.C., Aerts, J.P.M., Agoungbome, S.M.D., Anys, M., Ramírez, S.B., van Emmerik, T., Gallitelli, L., Chiquito Gesualdo, G., Gonzalez Otero, W., Hanus, S., He, Z., Hoffmeister, S., Imhoff, R.O., Kerlin, T., Meshram, S.M., Meyer, J., Meyer Oliveira, A., Müller, A.C.T., Nijzink, R., Scheller, M., Schreyers, L., Sehgal, D., Tasseron, P.F., Teuling, A.J., Trevisson, M., Waldschläger, K., Walraven, B., Wannasin, C., Wienhöfer, J., Zander, M.J., Zhang, S., Zhou, J., Zomer, J.Y., Zwartendijk, B.W. (2023). Where should hydrology go? An early-career perspective on the next IAHS Scientific Decade: 2023–2032. *Hydrological Sciences Journal 68, 4, 529-541.* DOI: 10.1080/02626667.2023.2170754

van Emmerik, T.H.M., Frings, R.M., Schreyers, L.J., Hauk, R., de Lange, S.I., Mellink, Y.A.M. (2023). River plastic transport and deposition amplified by extreme flood. *Nature Water 1, 514-522.* DOI: 10.1038/s44221-023-00092-7

## Supervised MSc theses that contributed to this thesis

van den Berg, K. (2021). Spatial variation of bedform dynamics in the fluvial to tidal transition zone of the Ganges-Brahmaputra-Meghna delta.

van de Veen, S.H.J. (2022). Bedform geometry in fine sand and coarse silt environments.

van der Wilk, A. (2023). The effect of flocculation on river bedforms.

# Curriculum vitae

| | |
|---|---|
| 25 April 1995 | **Born in Rijnwoude, the Netherlands** |
| 2013 - 2016 | **BSc Earth Sciences** *(cum laude)*<br>Utrecht University, the Netherlands |
| 2017 - 2019 | **MSc Earth Surface Water** *(cum laude)*<br>Utrecht University, the Netherlands |
| 2019 - 2024 | **PhD Candidate**<br>Wageningen University, the Netherlands |

*Netherlands Research School for the*
*Socio-Economic and Natural Sciences of the Environment*

# D I P L O M A

***for specialised PhD training***

The Netherlands research school for the
Socio-Economic and Natural Sciences of the Environment
(SENSE) declares that

## *Sjoukje Irene de Lange*

born on the 25th of April in Rijnwoude, The Netherlands

has successfully fulfilled all requirements of the
educational PhD programme of SENSE.

Wageningen, the 8th of May 2024

Chair of the SENSE board

Prof. dr. Martin Wassen

The SENSE Director

Prof. Philipp Pattberg

*The SENSE Research School has been accredited by the Royal Netherlands Academy of Arts and Sciences (KNAW)*

KONINKLIJKE NEDERLANDSE
AKADEMIE VAN WETENSCHAPPEN

The SENSE Research School declares that **Sjoukje Irene de Lange** has successfully fulfilled all requirements of the educational PhD programme of SENSE with a work load of 50.8 EC, including the following activities:

**SENSE PhD Courses**

- Environmental research in context (2020)
- Research in context activity: Short documentary about fieldwork in Bangladesh (2020)

**Other PhD and Advanced MSc Courses**

- Project and Time Management, Wageningen Graduate Schools (2020)
- Spatial modelling and statistics, WUR (2020)
- Scientific writing, Wageningen Graduate Schools (2021)
- Writing in the Sciences, Stanford University (2021)
- Grip on your career, WUR (2022)
- Delft 3D modelling course, Deltares (2022)

**External training at a foreign research institute**

- Laboratory Education Tour, University of Hull and University of Bangor, the UK (2022)
- Tour the PhD, visiting LIST, KIT, ETH, UoE and UZH (2022)

**Management and Didactic Skills Training**

- Supervising six BSc students and two MSc students with thesis (2020-2023)
- Chair of the organizational committee of Tour the PhD 2022 (2021-2022)
- Teaching laboratory practicals in MSc course 'River Flow and Morphology' (2021)
- Co-convener at EGU 2022 conference (2022)
- Teaching MSc course 'Catchment Hydrology' (2022, 2023)

**Selection of Oral Presentations**

- *Spatial variability of bedforms in the lower Meghna, Bangladesh.* American Geoscience Union (AGU) Fall Meeting 1-17 December, 2020 Online
- *Spatial variability in dune geometry is driven by local hydraulic conditions.* European Geosience Union General Assembly (EGU) 2022, 23-27 May, Vienna, Austria
- *Influence of silt in sand-silt mixtures on dynamic near-equilibrium bedform geometry.* Nederlandse Aardwetenschappen Conferentie (NAC) 2022, 5-6 September 2022, Utrecht the Netherlands
- *Sources of hydraulic roughness in the fluvial-to-tidal transition zone.* Marine and Riverine Dune Dynamics (Marid). 3-5 April 2023, Rennes, France

SENSE coordinator PhD education

Dr. ir. Peter Vermeulen

The research described in this thesis was funded by the Netherlands Organisation for Scientific Research (NWO), within Vici project "Deltas out of shape: regime changes of sediment dynamics in tide-influenced deltas" (Grant NWO-TTW 17062).

Financial support from Wageningen University for printing this thesis is gratefully acknowledged.

Cover design: Photo Edwin Paree, design Sjoukje de Lange, using Adobe Illustrator
Bookmark design: Sjoukje de Lange, Leon Schneider, Maximilian Behnke and Wesley Johnson
Layout design: Sjoukje de Lange, using LaTeX 2ε
Printed by: ProefschriftMaken on FSC-certified paper
The photos on cover and on the chapter pages in this thesis are the exclusive property of Edwin Paree. The images may not be reproduced, copied, downloaded, saved to your computer, transmitted in any form or manipulated without the written permission of Edwin Paree.